University of Sussex

A University of Sussex PhD thesis

Available online via Sussex Research Online:

http://sro.sussex.ac.uk/

This thesis is protected by copyright which belongs to the author.

This thesis cannot be reproduced or quoted extensively from without first obtaining permission in writing from the Author

The content must not be changed in any way or sold commercially in any format or medium without the formal permission of the Author

When referring to this work, full bibliographic details including the author, title, awarding institution and date of the thesis must be given

Please visit Sussex Research Online for more information and further details

Gas-phase Photocatalytic Oxidation of Alkenes Using Nano-structured

Heterogeneous Semiconductor Materials

By

Emmanuel Alhassan Kamba

A thesis presented for the degree of

Doctor of Philosophy (Ph.D.)

School of Life Sciences

University of Sussex

May 2019

Declaration

I hereby declare that this work has not been submitted in any substance to another University

for the award of any other degree or other academic or professional distinction.

Signed……………………….

Emmanuel Alhassan Kamba

"...no matter how thick the cloud is, there is always a space in the sky"

Acknowledgements

I give thanks to God Almighty to whom alone be all glory and honour forever and ever, Amen!

My gratitude goes to The Tertiary Education Trust Fund (TETFund), Nigeria for granting me scholarship for this program. I thank the management of the Federal University, Wukari, Taraba state, Nigeria for making this dream a reality.

Many thanks to my main supervisor Dr. Qiao Chen for his enormous and invaluable support and for taking out time to ensure the success of this research project. I also thank my co-supervisor Dr. Iain Day for his contributions.

I also acknowledge Dr. Deeptima Massey, former Post-Graduate Research Coordinator, School of Life Sciences for her advice and guidance even outside of academic issues. My nano group past and present members: Dr. Giacomo Canciani, Dr. Thomas Draper, Dr. Brnyia Alwhshe, Dr. Amin Qasim, Dr. Fang Yuanxing, Dr. Lee Wei Cheat, Daniel Commanduer, and Munirah Alhar, I thank you all for your efforts and team work. I also want to thank the former MChem students: Ben Fry, Peter Mcnulty and Stella Nikopolouko for their support during their MChem program.

My profound gratitude goes to my lovely wife, Mrs. Maryam E. Kamba (Kantu) and my children Patrick, Hannah and David for your patience. I also appreciate my parents Mr and Mrs. John A. Kamba for their support in many ways. To my brothers and sisters: James, Suzan, Sakaba and Maryam, I say a big thank you for all your prayers. Special thanks to my friends especially Markus Diya Magaji and Patricia Osman for all the concern shown during my hardship.

This work is dedicated to the glory of God!

iv

University of Sussex

Emmanuel Alhassan Kamba

Ph.D.

Gas-phase Photocatalytic Oxidation of Alkenes Using Nano-structured Heterogeneous Semiconductor Materials

Summary

This work focuses on the development of a flow-type photocatalytic reactor and its applications in both photodecomposition of organic air pollutants and photocatalytic conversion of alkenes into industrially important epoxides. Particular importance was given to commercial viability of the developed technologies.

Nanostructured semiconductor photocatalysts including TiO_2, Bi_2WO_6, TS-1 and CeO_2 were synthesised through hydrothermal and sol-gel methods. In addition, several modifications of the materials including doping and coupling with metal ions and metal oxides were performed to enhance their photocatalytic activities. The powders obtained from these syntheses were coated on glass beads through a novel technique with high adherence efficiency. These coated glass beads filled the entire space in the photo-reactor which afforded high packing density. The streamline design of the reactor made it possible for all

the reacting species to be in contact simultaneously, while the transparency of the glass beads provided an excellent UV light penetration to even the innermost part of the reactor.

The functionality of the reactor was first tested by performing photodecomposition of acetone in gas phase. Using commercially available P25, acetone was successfully mineralised in to CO_2 and H_2O.

Photo-epoxidation of propylene was achieved using the designed reactor with increased light intensity. Typical reaction mixture of propylene:oxygen:nitrogen corresponding to the ratio 1:1:15, afforded propylene oxide (PO) in addition to other products such as acetone, acetaldehyde and propanal, observed by Fourier transformed infrared spectroscopy (FTIR) in tandem with gas chromatography mass spectroscopy (GCMS). It was established from the results that coupled Bi_2WO_6-TiO_2 photo-catalysts were preferable for selectivity of PO peaking at 64%. This was achieved in a typical flow reaction for 1hr at the temperature of 345 K at atmospheric pressure under UV_A illumination.

An interesting colour change in the synthesised Bi_2WO_6 nanoflowers was observed during the series of experiments. As such, further study was performed on the photochromic property of the catalyst. Upon exposure to UV irradiation, light-induced photochromism was observed to be highly dependent on the amount of coating on the glass beads; and the colour change from pale yellow to black is reversible. Further test on the effect of photochromic behaviour of Bi_2WO_6 on the photocatalytic epoxidation of propylene was performed. The results revealed enhancement of PO selectivity by 17 %.

The kinetics of the epoxidation of cyclohexene in gas-phase using the product of reaction with a mixture of H_2 and O_2 was investigated. The results showed that the gas-phase reaction mechanism follows the Eley–Rideal mechanism. The physisorbed cyclohexene

reacted directly with the intermediate formed through reaction between Ti base and the OOH species, to produce the cyclohexene oxide. Reaction activation energy was measured to be approximately 31 kJmol^{-1}.

Further experiments focused on *in-situ* reaction of the partial photo-oxidation products of photo-epoxidation of 1-hexene were performed. The exhaust of the photo-reactor was passed directly through methanol which acted as a nucleophile under acidic condition for several hours. This made it possible to establish the features of some of the reactive species formed during the partial photo-oxidation of 1-hexene process, ultimately demonstrating the high versatility of the developed photo-reactor.

Finally, a *"pseudo" in-situ* photo-oxidation of styrene in liquid-phase using NMR spectroscopy was developed. Using molecular oxygen as the oxidant, Co-doped CeO_2 showed the highest conversion of 48% with a selectivity of styrene oxide of 78%. As revealed by the kinetic study in this work, the photo-oxidation reaction proceeded according to Langmuir-Hinshelwood model.

Contents

List of Figures

List of Tables

List of Abbreviations and symbols

°C	-	Degrees Celsius
K	-	Degrees Kelvin
M	-	Moles per litre
wt %	-	Percentage weight
α	-	Absorption coefficient of a material
γ	-	Initial adsorption velocity
E	-	Photonic efficiency
λ	-	Wavelength
$-r$	-	Rate of a chemical reaction
σ	-	Sigma bond
	-	Shielding constant
π	-	Pi bond
ν	-	Frequency
ξ	-	Photonic efficiency of reactions
Φ	-	Quantum yield
A	-	Acceptor molecule
AO	-	Atomic orbitals
ATR	-	Attenuated total reflectance
Btu	-	British thermal unit
$C_{\%}$	-	Percent conversion
CBM	-	Conduction band minimum
CdS	-	Cadmium sulfide

D	-	Donor molecule
D_{avg}	-	Mean crystallite dimension of a crystal plane
DC	-	Direct current
DMF	-	Dimethylformamide
e^-	-	Electron
EDX	-	Energy dispersive x-ray
Eg	-	Band gap energy
EPA	-	Environmental Protection Agency
S_0	-	Ground energy state
FID	-	Flame ionisation detector
FMO	-	Frontier molecular orbital
FTIR	-	Fourier transform infrared
GaAs	-	Gallium arsenide
GaPc	-	Gallium phthalocyanines
GC	-	Gas chromatography
GIAC	-	Gyration induced adhesive coating
h	-	Plank constant
h^+	-	Hole
^{1}HNMR	-	Proton nuclear magnetic resonance
HOMO	-	Highest occupied molecular orbital
HFCs	-	Hydrofluorocarbons
ICDD	-	International centre for diffraction data
InPc	-	Indium phthalocyannines
IPA	-	Isopropyl alcohol

IQE	-	Internal quantum efficiency
ISC	-	Intersystem crossing
k	-	Reaction rate constant
L-H	-	Langmuir Hinshelwood
LUMO	-	Lowest unoccupied molecular orbital
MS	-	Mass spectroscopy
MW	-	Average molecular weight
NIST	-	National institute of statistics
OPD	-	Optical path difference
P25	-	Aeroxide® P25
PbS	-	Lead sulfide
PFCs	-	Perfluorocarbons
PL	-	Photoluminescence
PVA	-	Polyvinyl alcohol
QE	-	Quantum efficiency
rf	-	Radio frequency
RDS	-	Rate determining step
S_{ads}	-	Adsorbed substrate
S_{CO_2}	-	Reaction selectivity for CO_2
SEM	-	Scanning electron microscopy
SF_6	-	Sulphur hexfluoride
TEOS	-	Tetraethyl orthosilicate
TOF	-	Turnover frequency

TON   -   Turnover number

TRI   -   Toxic Release Inventory

TT^iP -   Titanium tetraisopropoxide

UV   -   Ultraviolet

UV_A -   Ultraviolet light ($315 \leq \lambda \leq 400$ nm)

VBM   -   Valence band maximum

Vis   -   Visible

VOCs   -   Volatile organic compounds

XRD   -   X-ray diffraction

Chapter 1: Introduction

In recent years, concerns about climate change and energy security have prodded research and development of more energy efficient technologies in all fields of human endeavour. About 54 % of the world's total energy produced is consumed by the industrial sector.[1–4] However, the amount of fuel used by the industrial sector largely depends on the region as well as country, based on the economic activity and level of technological development. The chemical and petrochemical industry energy demand across the globe is estimated to account for about 10 % of total energy consumption.[5] These industries are also responsible for 7 % emissions of greenhouse gases across the globe, which makes them the biggest contributor to the global industry energy demand.[6–8]

Greenhouse gases are known to trap heat in the atmosphere, which causes a rise in the global temperature. This results in variation of 'normal' atmospheric conditions across the globe, making weather predictions less reliable. CO_2 is the dominant greenhouse gas accounting for 76 % of emission of global greenhouse gases.[8] Fossil fuel and industrial processes have been reported to be responsible for 65 %, while forestry and other land use account for 11 % of the total global CO_2 emissions.[9] As seen in Figure 1.1, other greenhouse gases including methane, nitrous oxide and fluorinated gases contribute 16 %, 6 % and 2 % respectively. Methane is mainly generated from agricultural activities, waste management, biomass decomposition and energy use. Nitrous oxide can be generated from fossil fuel and agricultural chemicals such as fertilizers.[10] Industrial processes and use of products such as hydrofluorocarbons (HFCs), perfluorocarbons (PFCs) and sulphur hexfluoride (SF_6) are all known to contribute to generation of fluorinated gases.[7–9]
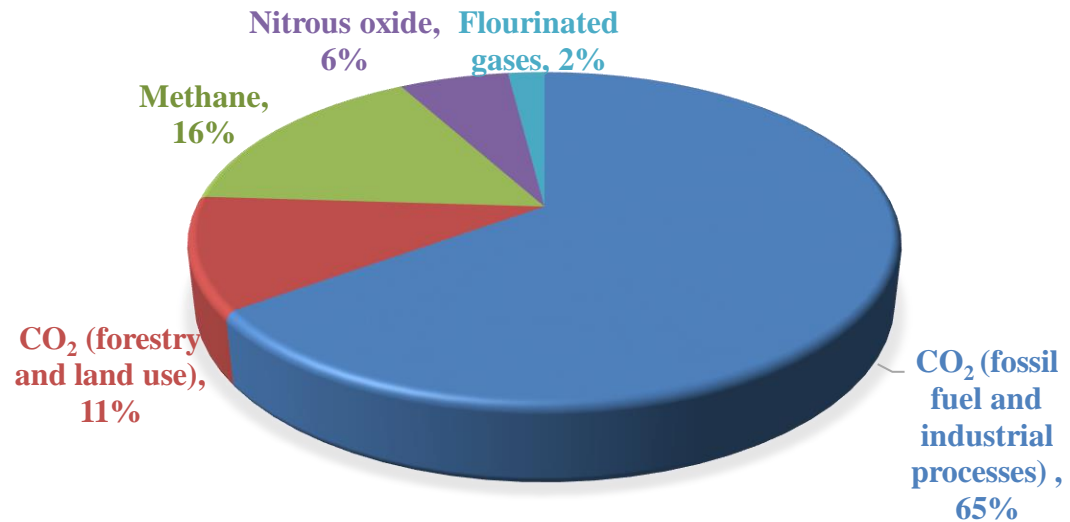
Figure 1.1: Global greenhouse gas emissions[11]

Looking at the dependence of modern global economy on production of finished goods, the high energy demand of industrial sector could be traced. The end products that satisfy human need such as fertilizers, composite items, plastics, cement etc. are products of fundamental chemical syntheses of some basic intermediates.[12] Since the global industrial revolution that began in the 1760s, industries have competed with one another, driven by the global market. As a result, the world has seen unprecedented investments in various processing plants, with the United States of America (USA) and China in the lead.[8,12] The Middle East has also earned global attention due to concentrated deposits of natural gas and oil within the region that has largely contributed in strengthening their economy.[8] It is not surprising therefore, that over the years, the global industrial energy demand was estimated in 2011 to be 40 EJ (1 EJ = 1×10^{18} J).[13] What is more worrying is that the industrial sector energy demand has been projected to increase on an average by 1.2 % annually. That means by the year 2024, the energy demand would be approximately 326 EJ.[14]

Fortunately, since the introduction of green chemistry over two decades now, the amount of chemical waste released to water, land and air has reduced drastically. For example, the United States' Environmental Protection Agency (EPA) Toxic Release Inventory (TRI), shows that between 2004 and 2013 a 7 % decrease in the release of some chemicals such as trichloroethylene, methyl isobutyl ketone and hydrochloric acid.[15] Green chemistry is applied to a wide range of field including the pharmaceutical industry. It provides new approaches for the reduction or elimination of use of solvents, or make them more efficient and safer.[16] Also green chemistry has inspired increase in number of synthetic techniques for the production of petroleum-based chemicals from biogenic sources (mainly plants or waste).[17]

Among the most abundant and important organic products of the chemical industry are the alkenes. Due to heavy dependence on alkenes as key chemicals for the production of economically important polymers such as polyethylene and polypropylene, alkenes are produced in large quantities. As production of alkenes by the petroleum industries is on the increase, the quest to conserve natural resources is also on the increase, which makes it imperative to use such products as starting materials in other industrial processes.[18,19] This is the main objective of this research work. Hence, alkene production and reactivities are discussed in detail in the next section.

1.1. Alkenes and their production

Alkenes are a group of hydrocarbons that contain at least one carbon-carbon double bond. They are sometimes called olefins due to their oily nature.[20] They are used in a wide range of finished goods from rope to car interiors. Due to their resistance to sunlight as well

as relative ease of production, alkenes are very useful.[21] Non-cyclic alkenes have the general molecular formula C_nH_{2n}, while that of cyclic alkenes is C_nH_{2n-n}, where n denotes the number of carbon atoms. The carbon-to-carbon double bond of alkenes displaces two hydrogen atoms. As a result, they do not have the maximum number of hydrogen atoms per carbon, hence they are termed unsaturated. The double bond structure of alkenes makes them chemically different from alkanes. They are more acidic and reactive than alkanes. They also can easily undergo polymerization reactions, a property that makes their industrial applications of high value.[10]

Alkenes are produced by the petroleum industries as by-products through the cracking process.[18] The cracking process involves the breaking up of large molecules of hydrocarbons (mainly alkanes) into smaller and essential molecules with lower viscosity and lower vaporising and igniting temperature. By the application of high temperature and pressure in the absence of catalyst or low temperature and pressure in the presence of a catalyst, the cracking process can be achieved by breaking C-C bonds.[22] The fraction of naphtha or the gas oil, which is a fractional distillation process of crude oil (petroleum), is often the source of the large hydrocarbon molecules.[21] These obtained fractions are in liquid phase, which are then re-vaporised prior to cracking. As no specific reaction occurs during the cracking process, the breaking of the large hydrocarbon molecules are fairly random.[22] As such, a mixture of several smaller hydrocarbons is produced, some of which have C=C double bonds.[21]

By breaking several C-C bonds, additional H atoms are needed to terminate the fragmented hydrocarbon chains. If the H atoms are not available, then either the C=C double bonds or the cyclic C-C bonds have to be formed. Thus, small alkene molecules are formed in the cracking process.

1.1.1 Commercial importance of alkene

Due to the ability of the double-double bond to readily convert to other functional groups, alkenes are important intermediates in the synthesis of polymers, drugs, pesticides, and other valuable chemicals.[23,24] Among all alkenes, ethylene is produced in the largest volume, at around 26 million tonnes yearly as at 2013.[25] About 62 % of the ethylene is polymerized to form polyethylene annually, according to IHS Markit report of 2018.[26] The next largest derivative of ethylene is the ethylene oxide. Ethylene oxide is reported to account for 15 % of the ethylene produced in 2018 and is the primary source of ethylene glycol. The remainder is used to synthesise a wide variety of organic chemicals including ethanol, acetic acid, and vinyl chloride. On a similar note, the heavy demand on the production polypropylene and propylene oxide has caused a surge in the production of propylene. Propylene, which is the second largest volume of chemical produced around the world is the key raw material for the production of a wide variety of organic chemicals.[26] Polypropylene is reported to consume about 65 % of the total propylene produced globally in 2016. Propylene oxide accounted for 8 % while the rest is used to make acetone, isopropyl alcohol, and a variety of other important organic chemicals.[26]
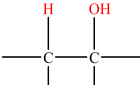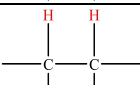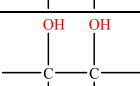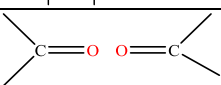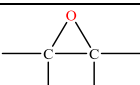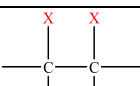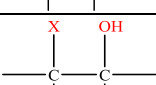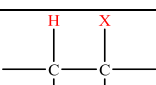
Generally, the largest use of alkenes is for the production of polymers, which are used in consumer products from shoes to plastic bags to car bumpers. An alkene monomer can polymerise by a chain reaction where additional alkene molecules add to the end of the growing polymer chain to form what is known as addition polymer.[27]

1.1.2 Reactions of alkenes

Alkenes tend to undergo various reactions with various reagents under different conditions. Some of the basic reactions of alkenes are displayed on Table 1.1. In general, the

reactivity of alkenes arises from the reactivity of the carbon-carbon double bond. The concept of the functional group helps to organize and simplify the study of chemical reactions. By studying the characteristic reactions of the double bond, it is possible to predict the reactions of alkenes.

Table 1.1: Some reactions of alkenes, examples of co-reactants and the corresponding products. (Ethylene is alkene reactant)

Reaction type	Functional group/co-reactant	Product
Hydration	H_2O	
Hydrogenation	H_2	
Hydroxylation	HOOH	
Oxidative cleavage	O_2	
Epoxidation	O	
Halogenation	X_2	
Halohydrin formation	HOX	
HX addition	HX	

The double bond of alkenes which is also their functional group, consist of a strong σ bond and a weaker π bond. The π electrons have relatively lower bond energy (enthalpy) than the σ bond and as such are easily attracted to a variety of reagents. This results in the breaking

of the π bond and the two carbons form a new σ bond with the reagents as illustrated in Scheme 1.1.

The double bond comprising a σ and a π bond

Broken π bond formed new σ bonds
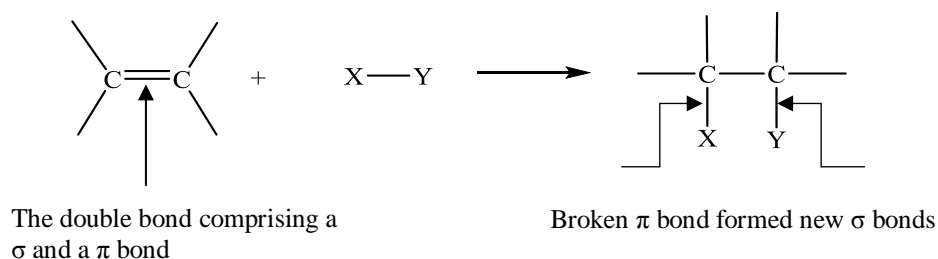
Scheme 1.1: Representation of breaking of π bond to form two new σ bonds upon reacting with reagent termed 'XY'

As π bond is the weaker among the double bond, it is likely to break more easily in a reaction. Because single bonds (σ bonds) are more stable (possess higher bond energy/ enthalpy) than the π bonds, it is expected that the double bond will react and transform the π bond into a σ bond. In fact, this is the most common reaction of double bond. For example, catalytic hydrogenation converts the C=C π bond and the H-H σ bond into two C-H sigma bonds.

There are three major types of alkene reactions: addition, elimination and substitution. During an addition reaction, two molecules combine to form one product molecule. When an alkene undergoes addition, two groups add to the carbon atoms of the double bond, resulting in the carbons becoming saturated. A molecule can also split into two fragment molecules. This is referred to as elimination reaction, and is in many ways, the reverse of addition reaction. In a substitution reaction, one fragment replaces another fragment in a molecule. These major reaction types are illustrated in Scheme 1.2.

Addition

Elimination
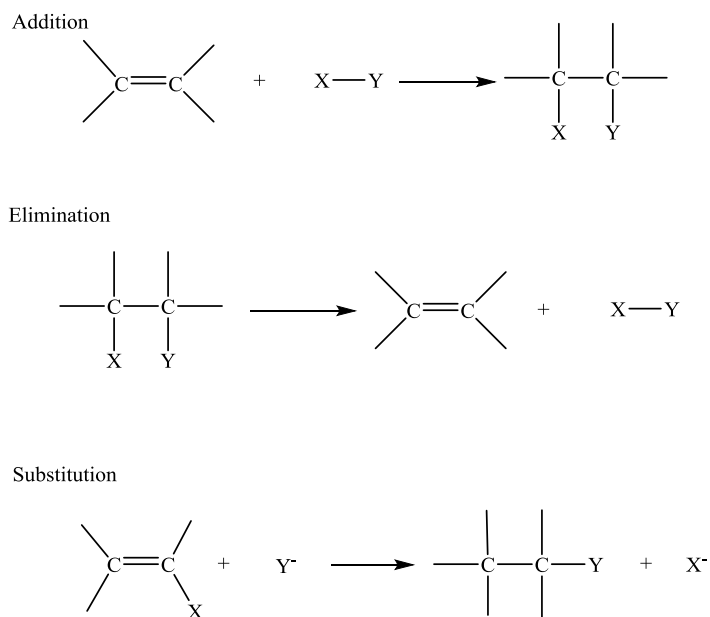
Substitution

Scheme 1.2: Schematic of addition, elimination and substitution reactions of alkene.

Addition reaction is the most common reaction of alkenes, as a wide variety of functional groups can be formed by addition of suitable reagents to the double bonds of alkenes. Due to its relevance to this work, it is discussed in detail.

Alkenes are nucleophilic in nature and would therefore readily react with an available electrophilic reagent.[28] For example, if a reagent like HBr is combined with an alkene, the alkene reacts with the partially positively charged H of the HBr and as a result, a carbocation is formed as shown in Scheme 1.3.
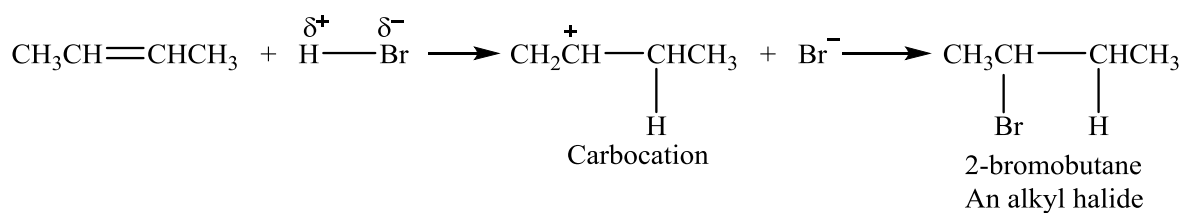
Scheme 1.3: Nucleophilic attraction of an electron-deficient molecule

The carbocation, which is an electrophile in the second step, then reacts with the negatively charged ion to yield an alkyl halide. This type of reaction is referred to as an electrophilic addition reaction since its first step involves the attraction of an electrophile (H^+) by the alkene. This type of reaction is characteristic to alkenes[28] and is therefore discussed in detail in the next section.

1.1.2.1 Electrophilic addition to alkene

In principle, more stable products can be formed by the addition of many different reagents to a double bond; i.e., the reactions are energetically favorable. Some reagents react with C-C double bonds without the aid of a catalyst. To understand what types of reagents react with double bonds, it is important to consider the structure of the π bond. Although the electrons in the sigma bond framework are tightly held, the π bond is delocalized above and below the sigma bond (Figure 1.2). Due to their farther distance from the carbon nuclei, the π bonding electrons are more loosely held. This makes them susceptible to being pulled away by a strong electrophile that has an affinity for the loosely held electrons, resulting in the formation of a new bond. As such, one of the carbon atoms is left with only three bonds and a positive charge.
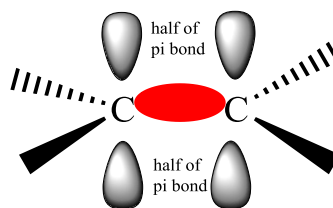
Figure 1.2: Representation of π bond delocalisation above and below the σ bonds (colored red)

The double bond is said to have effectively reacted as a nucleophile, by donating a pair of electrons to the electrophile. In most additions reaction of alkene, a nucleophile attacks the carbocation, resulting in the formation of a stable addition product. The product, contains both the electrophile and the nucleophile bonded to the carbon atoms that were in the double bond. However, for this type of reaction a strong electrophile is required to attract the electrons of the π bond and generate a carbocation in the rate-determining step (RDS). Majority of alkenes reactions are classified under electrophilic additions. There are other several types of additions to the alkenes using a wide variety of reagents including halogens, water, borane, oxidizing agents, and other alkenes; most, but not all, of which will be electrophilic additions.

It is also important to understand the orientation of addition, which helps to determine which part of the reagent adds to which end of the double bond. This is the Markovnikov's rule and it states that *the addition of a proton acid to the double bond of an alkene results in a product with the acid proton bonded to the carbon atom that already holds the greater number of hydrogen atoms*. Many addition reactions of alkenes follow the Markovnikov's rule and they are often referred to as following the Markovnikov orientation and give the Markovnikov product. Other additions to alkenes as well as some examples of this additions are given in the next series of sections.

1.1.2.2 Addition of water: hydration of alkenes

In the presence of a strongly acidic catalyst, an alkene can react with water to form an alcohol. In this reaction, a hydrogen atom adding to one carbon and a hydroxyl group adding to the other. Hydration of an alkene is accomplished by adding excess water to drive the

equilibrium toward the alcohol. The two complementary reactions in an equilibrium will be the hydration and dehydration reactions. As such, they must follow the same reaction pathway, such that the lowest energy transition state and intermediates for the reverse reaction are the same as those for the forward reaction, except in reverse order.[20]

The principle of microscopic reversibility, states that a forward reaction and a reverse reaction taking place under the same conditions (as in an equilibrium) must follow the same reaction pathway in microscopic detail. According to this principle, the hydration mechanism can be written by reversing the order of the steps of the dehydration as seen in Scheme 1.4 below. In the first step, a carbocation is formed by protonation of the double bond. Secondly, the carbocation undergoes a nucleophilic attack by water, and finally, by the loss of a proton, an alcohol is formed.
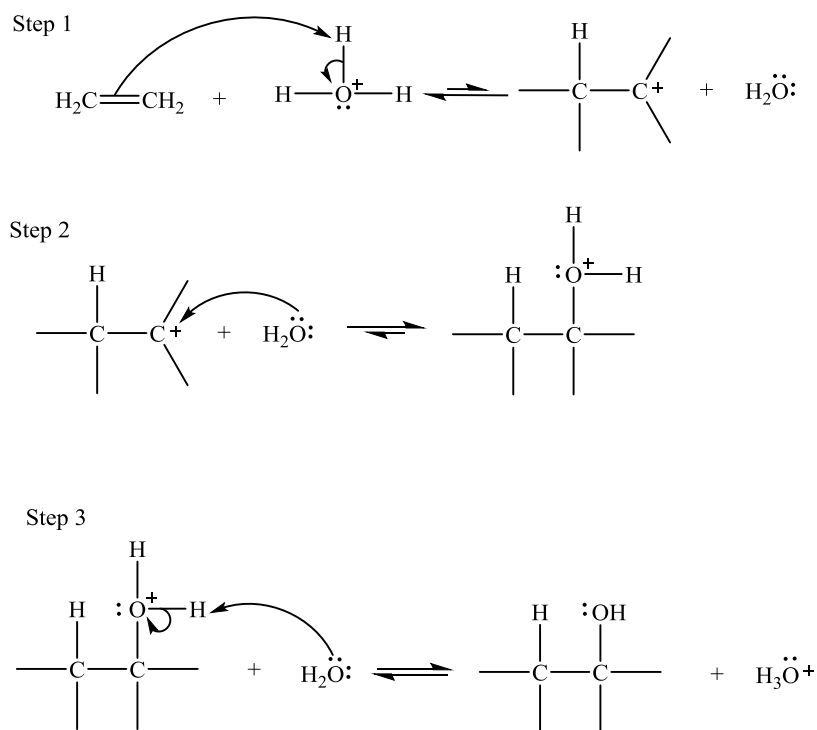
Scheme 1.4: Hydration and dehydration mechanism of alkene

1.1.2.3 Catalytic hydrogenation of alkenes

Hydrogenation of alkene is another form of reduction, where the addition of H_2 across the double bond gives an alkane. The process usually requires a catalyst such as Pt, Pd or Ni. Indeed, for most alkenes, hydrogenation can only take place using hydrogen gas at ambient temperature and pressure due to the presence of a catalyst. Normally, the alkene dissolves in an alcohol, an alkane or acetic acid. By adding a small amount of Pt, Pd or Ni catalyst and shaking or stirring the reaction proceeds. The actual hydrogenation occurs at the surface of the metal, where the liquid solution of the alkene comes into contact with hydrogen and the catalyst.[20]

During catalytic hydrogenation of alkenes, the hydrogen gas is adsorbed onto the surface of the metal catalysts, consequently causing the H-H bond to weaken. In effect, combining H_2 and D_2 in the presence of a catalyst such as Pt, will result in the two isotopes quickly scrambling to produce a random mixture of HD, H_2 and D_2. However, in the absence of a catalyst, no scrambling can occur.
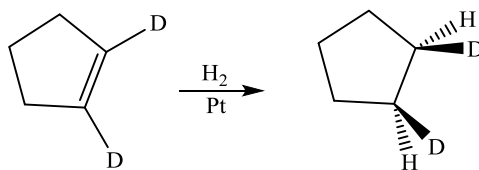
Scheme 1.5: Catalytic hydrogenation of alkene

Scheme 1.5 is an example of hydrogenation of alkene. Here, one face of the alkene (1,2-dideuteriocyclopentene) π bond binds to the catalyst, which has adsorbed hydrogen on its surface. The H inserts into the π bond, and the product is freed from the catalyst. Finally, the two H atoms add to the face of the double bond that is complexed with the catalyst.

1.1.3.6 Addition of halogens to alkenes

The molecule of a halogen (Br_2, Cl_2 or I_2) is electrophilic, which makes it susceptible to a nucleophilic attack resulting in the displacement of a halide ion. For example, in Scheme 1.6, the nucleophile attacks the electrophilic nucleus of one bromine atom, and the other bromine serves as the leaving group, departing as bromide ion. Many reactions including those of alkene follow this pattern. The last reaction in Scheme 1.6 shows how the π electrons of an alkene attack the bromine molecule, removing a bromide ion and forming a three-membered ring with a positive charge (bromonium ion) on the bromine atom.
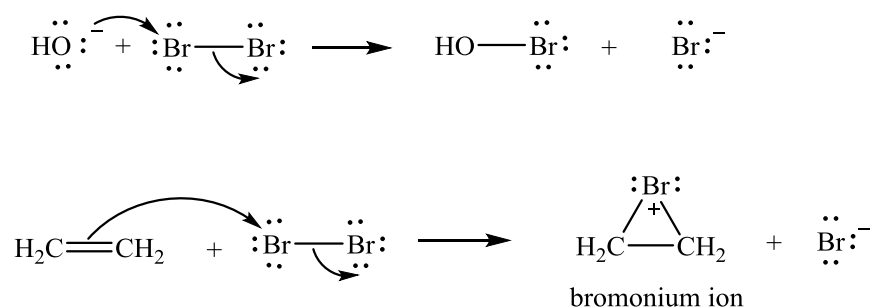
Scheme 1.6: Halogenation of alkene

Contrary to a normal carbocation, all the atoms in a halonium ion such as seen above, have filled octets. However, the three-membered ring has a considerable amount of ring strain, which combines with a positive charge on an electronegative halogen atom resulting in a strong electrophilic halonium. A stable product is obtained when a nucleophile such as a halide ion attacks and opens the halonium ion.

Among the halogens, Cl and Br more commonly add to alkenes using the halonium ion mechanism and produce a stable product. Diiodide products decompose easily, hence is used less frequently.

In alkenes generally, oxidation refers to the reaction that forms carbon-oxygen bonds. As many common functional groups contain oxygen, these reactions are particularly important. Moreover, alkene oxidations are some of the best methods for introducing oxygen into organic molecules.

The reactivities of alkenes presented in this work show that they can be used as starting materials in the synthesis of a great variety of products. Due to the excessive amount of alkenes produced annually across the globe, which contributes to environmental pollution, it becomes important to convert them into other industrially useful chemicals. One of such chemicals is the epoxide. The epoxidation of alkenes forms the basis for this work and so is discussed in detail in the next section.

1.1.3 Epoxidation of alkenes

This is one of the many reactivities of alkenes, the product of which is called an epoxide. Epoxides, also known as oxiranes are versatile intermediates in organic synthesis. They are highly important building blocks for the manufacturing of pharmaceuticals, flavors, perfumes as well as plastics.[29] Epoxides, which are cyclic ethers are made up of three atoms that form triangle. Their basic chemical structure consists of two carbon atoms of a hydrocarbon molecule attached to an oxygen atom as shown in Figure 1.3.
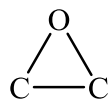
Figure 1.3: Chemical structure of epoxide

Ethylene oxide is the most economically important epoxide used in manufacture of ethylene glycol, antifreeze agents and as fumigant. Across the globe, epoxides are produced in large scale annually. The production of ethylene and propylene oxides have been estimated to reach 28 million tonnes and 18 million tonnes respectively in 2018[30].

Alkenes can be oxidized into epoxides in a reaction that consists of the transfer of an oxygen atom from the oxidizing agent to the alkene. Several methods for synthesising epoxides from alkenes exist. Typically, peroxyacids are used to achieve epoxidation reactions as the oxygen-oxygen single bond of the peroxyacid is weak and can be easily broken.[28] Scheme 1.8 shows an epoxidation reaction process involving an alkene and a peroxyacid.

$$RCH\!=\!\!=\!\!CH_2 \; + \; RCOOH \longrightarrow RCH\!-\!\!-\!\!CH_2 \; + \; RCOH$$
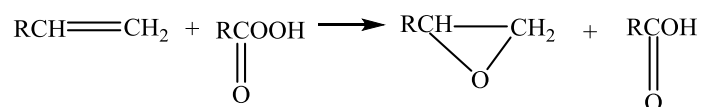
Scheme 1.8: Epoxidation of alkene with peroxyacid

The mechanism for the addition of oxygen to a double bond to form the epoxide begins with the oxygen atom of the OH group of the peroxyacid accepting a pair of electrons from the π bond of the alkene. This results in the breaking of the weak oxygen-oxygen single bond. As in Scheme 1.9, the electrons from the oxygen-oxygen bond are delocalized onto the carbonyl group while the remaining electrons of the OH bond break and add to the carbon of the alkene that becomes electron deficient when the π bond breaks. However, this process is very dated and employs relatively inefficient stoichiometric oxidation chemistry, and

requires a lot of work in order to isolate and purify products. It also suffers low safety and environmental acceptability.
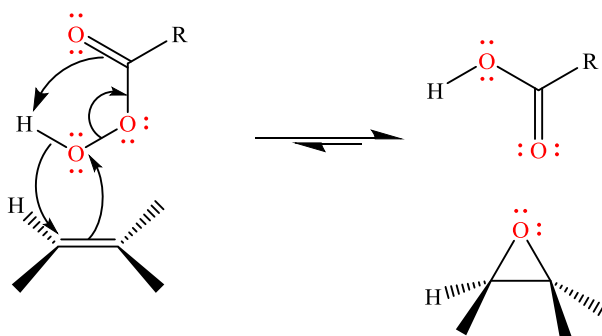
Scheme 1.9: Mechanism for the formation of epoxide with peroxyacid

In addition to the epoxidation of olefins with peroxyacids, several other alternative processes are known and are discussed in the following series of sections.

1.1.3.1 Chlorohydrin process

Alkenes can react either with hypochlorous acid or with chlorine and water to give chlorohydrin, which can be treated with base to yield epoxide. As shown in Scheme 1.10, the epoxide obtained during this process is not formed by direct addition of oxygen but by initial reaction of the alkene with hypochlorous acid.
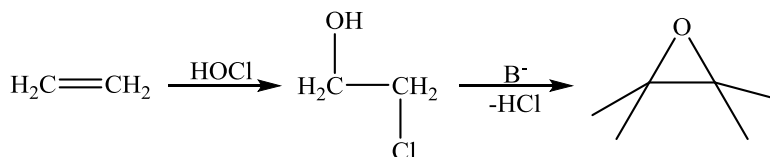
Scheme 1.10: Chlorohydrin process

In a similar fashion, alkene can react with chlorine and water to generate the hypochlorous acid *in situ*. This is an industrial synthetic procedure for the production of epichlorohydrin, which is mainly an intermediate for the synthesis of epoxy resins as well as glycerol.[31] The industrial preparation of epichlorohydrin is in two steps: first allyl chloride is reacted with hypochlorous acid at 30 - 50°C to form dichlorohydrin, which in the second step is reacted with excess calcium hydroxide to yield epichlorohydrin as shown in Scheme 1.11.
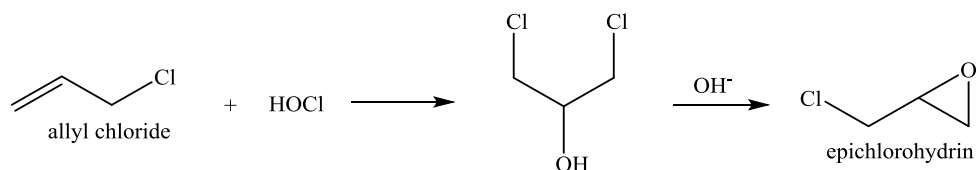
Scheme 1.11 Addition of hypochlorous acid reaction with calcium hydroxide

1.1.3.2 Halcon reaction

The Halcon reaction is another way of producing epoxides. It involves reacting olefins with alkyl hydroperoxides, mainly *tert*-butyl hydroperoxide in the presence of a catalyst such as vanadium, titanium or molybdenum complexes (Scheme 1.12).
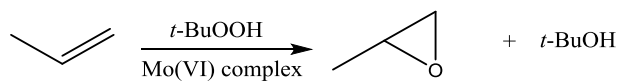
Scheme 1.12 Halcon reaction

Allylic alcohols can be used as starting materials for the Halcon reaction due to the activating and directive influence of OH groups. By using catalytic amounts

of VO(acac)$_2$ and *tert*-butyl hydroperoxide as epoxidation agent, it is possible to obtain high yields as reported by Mimoun et al.[32]

During this reaction, the allylic alcohol first forms a complex with the metal compound in which the allylic alcohol is coordinated to the metal atom through the hydroxyl group. If the alcohol is acyclic, two different epoxides can be formed. As shown in Scheme 1.13, the *(Z)* isomer is preferentially added to the oxygen atom in *anti*-position to the OH group while the *syn* derivative is formed by *(E)* isomer. If however, a cyclic alcohol is used, epoxidation with *tert*-butyl hydroperoxide takes place *cis* to the hydroxyl group.
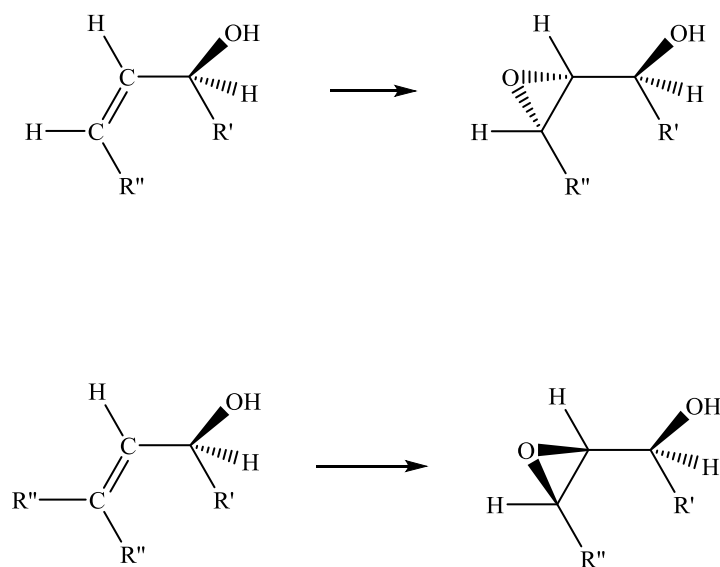
Scheme 1.13: Epoxidation of the *(Z)* and *(E)* isomers

Industrially, this procedure can be applied in the preparation of propylene oxide. Propylene (as well as other olefins) can be reacted with *tert*-butyl hydroperoxide in non-aqueous solvents in the presence of catalytic amounts of V^{5+} or Ti^{2+} complexes.[33]

1.1.3.3 Sharpless epoxidation

The *Sharpless* epoxidation, which is also known as asymmetric epoxidation is another method of preparing epoxy alcohols with high enantiomeric purity. Nevertheless, this reaction is specific for the conversion of allylic alcohols.[34] During *Sharpless* epoxidation of allylic alcohols, tetraisopropoxy titanium is used alongside one of the two enantiomers of diethyl tartrate in catalytic amount, while *tert*-butyl hydroperoxide serves as oxidizing agent and dichloromethane as solvent.
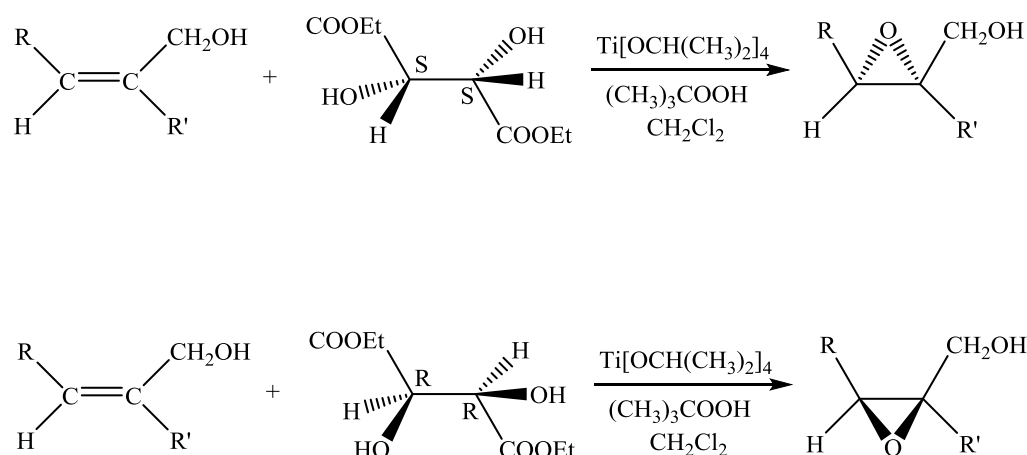
Scheme 1.14: The enantioselective epoxidation of achiral primary alcohols. Chiral primary allylic alcohols preferentially form one of the possible diastereomers.

It is possible to achieve stereochemical control by forming a complex of the titanium compound with the alkene, the tartrate and the peroxide as reported by Heravi et al.[34] As shown in Scheme 1.14, the formation of epoxides with different stereochemistry is possible since the differences in the spatial arrangements of the two enantiomeric tartrates in the complex can allow for this. The overall process begins with the formation of a complex by the catalyst, tetraisopropoxy titanium and diethyl tartrate (+ or -) through rapid ligand

exchange. This can be seen in the transition state shown below, where X could denote CH_3 or H:
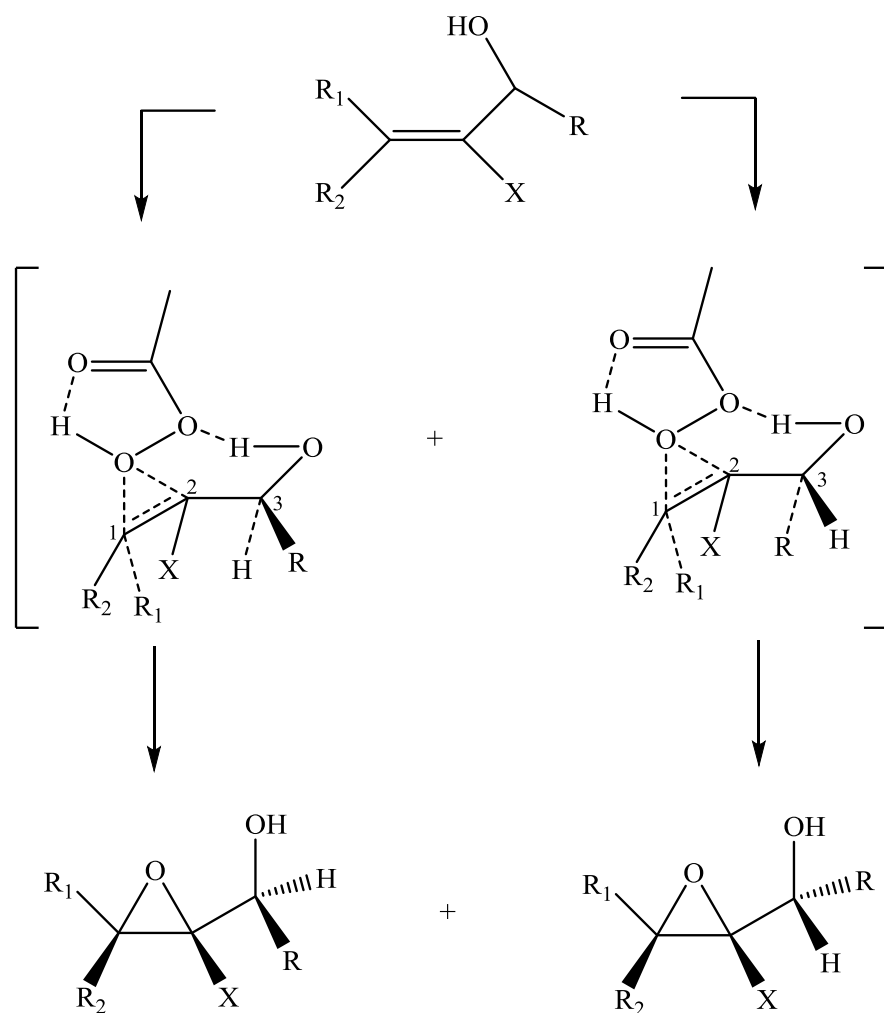
The use of enantiomerically pure diethyl tartrate is crucial for controlling the configuration of the target molecule. As mentioned earlier, the structure of the epoxide formed depends on the enantiomer of the diethyl tartrate used. Generally, enantiomerically pure epoxides are useful as starting materials for various compounds especially those that are optically active. This is because, such epoxides can easily convert to compounds with two adjacent chirality centers due to the fact that they are susceptible to attack by nucleophiles.

Attack by a nucleophilic substance on an epoxide is highly stereoselective. As such, only one stereoisomer can be formed.

The epoxidation of alkenes presented here are only representative examples of the several techniques in the literature. However, green production of epoxide at an industrial scale is still a major challenge.

1.4 Volatile organic compound removal

Although simple alkenes may be emitted from biogenic sources (mainly trees), it was estimated that they account for approximately 7–8 % of anthropogenic non-methane volatile organic compounds (VOCs) emissions.[35] VOCs constitute the major source of indoor air pollution. The presence of VOCs as components of a wide range of domestic products such as cleaning products, paints and varnishes, results in an increase in indoor air concentration. Although, their concentration may be perceived to be low, prolonged exposure can result in adverse health consequence referred to as "the sick building syndrome".[36]The enormous amount of health and environmental threats posed by these compounds has led to various research work to degrade them into less harmful chemicals. Myriads of reports on the oxidation of hydrocarbons, especially VOCs exist.[31,37,38] Currently, different methods of oxidising and degrading various organic compounds including alkenes have been reported. Some of the commonly used methods are: adsorption by activated carbon,[39] biofilteration[40] and thermal oxidation.[10] All these techniques have series of drawbacks. Activated carbon for example merely changes the phase of compounds from gaseous to solid instead of complete mineralisation or destruction. Biofilteration is a very slow process that involves the utilization of microorganisms immobilised on a porous filter bed. Several conditions including optimal microbial environment, large specific surface area, high moisture

retention, high porosity and low bulk density are all required to operate an efficient biofilter reactor.[41] In thermal oxidation, high temperatures ranging from 200°C to 1200°C are required to operate efficiently.[42] These procedures are often performed in a batch system, which means that the amount of the desired product is limited. Moreover, aside their inherent limitations, these techniques are not cost-effective. As such, a more environmentally benign, energy efficient and cost-effective alternatives to the conventional synthetic reactions is required.

By contrast, the use of light to initiate chemical reaction otherwise known as photochemistry is a much milder technique with minimal environmental consequences. Photochemistry gained traction following the establishment of the law of photochemical equivalence by Albert Einstein and Johannes Stark in the early 1900s.[43–45] This law provides a relationship between quantum theory and the effects of photons on chemical reactions. As a result, there has been great improvement in understanding of the molecular adsorption of photons and its effects.

1.5 An overview of electron excitation phenomena

Light can only have an effect on a system if it is absorbed by the system. This is known as the Grotthuss-Draper law.[46] It is the expansion of this law that leads to the modern understanding of photonic excitation of electrons in molecular systems. The excitation of electrons within a molecule is known to occur when the electrons absorb photons. This is accompanied by the transition of the electrons from a low energy ground state, S_0, to a higher energy state. Subsequent processes of the excited electrons eventually results in the loss of energy, which is also known as relaxation and return to the lower energy state.[47] Figure 1.5

Shows the relative energy levels as well as the different processes undergone by theses electrons as presented by Alexander Jabłoṅski in 1933.[46]
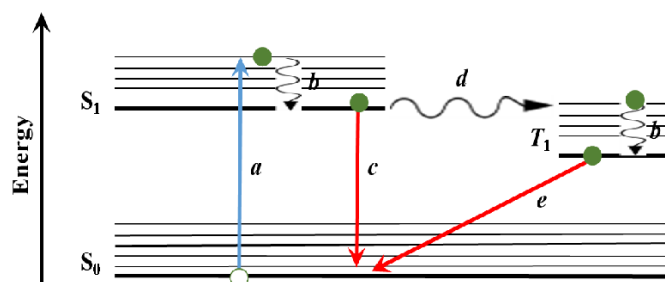
Figure 1.4: Representation of Jabłoṅski diagram revealing the various pathways from by which photoexcited electrons relax.

The absorption of photon by a molecule leads to excitation of electrons from the highest occupied molecular orbital, (HOMO), to an excited state as indicated by *a*, (Figure 1.4). According to Kasha's rule,[46] the excited electrons in a higher energy state undergo a non-radiative internal transition to the lowest unoccupied molecular orbital, (LUMO), indicated by *b*, in Figure 1.4. If the transition of the photoexcited electron is directly to the LUMO, its direct transfer to the lowest vibrational energy state of the orbital will be prohibited as stipulated by Franck-Condon principle. Instead, the electron undergoes a non-radiative decay process to reach the lowest vibrational energy state of the LUMO before further undergoing electronic transitions as indicated by *c* in Figure 1.4. The next process which involves the relaxation of the excited electron from LUMO to the HOMO, can occur by following two different pathways. The more facile pathway is through a radiative decay process from S_1 to S_0 in Figure 1.4. This process is accompanied by emission of excess energy in form of photon through fluorescence as indicated by, *c* in Figure 1.4. However, if the excited electron undergoes a change in spin state from a singlet to a triplet, (T_1), which occur through intersystem crossing (ISC), the second pathway will result as indicated by *d*, in Figure 1.4.

When the electron in T_1 loses energy, it returns to S_0 while emitting photons through phosphorescence indicated by e. There are more excited electrons undergoing fluorescence than those undergoing phosphorescence due to the intersystem crossing occurring in the case the former.[48]

The efficiency of a photochemical reaction can be estimated by determining the quantum efficiency, (QE). QE is defined in terms of the amount of incident light and photo generated electrons over a specific period of time. It can be expressed mathematically as in Equation (1.1).

$$QE = \frac{Photogenerated\ electrons}{Incident\ photons} \qquad (1.1)$$

Although Equation (1.1) is significant, it is mainly applicable to systems where electric currents can be generated by direct light irradiation as in photovoltaic cells. Nevertheless, photovoltaic cells are known to be selective to wavelengths of specific energies. As such, it is important also to determine the internal quantum efficiency, (IQE), which is preferential, owing to the fact that it takes into account only the amount of photons absorbed by a given material. It is worth noting that excited state population is equally significant in photochemical reactions. Photoexcited electrons are required to perform photocatalytic and photosynthetic reactions as would be discussed in subsequent sections.

Light induced photochemical reactions are known to undergo series of different reactions. These chemical interactions between the reacting species was of paramount importance in this work. This is because, toxic compounds are being transformed into less toxic, yet industrially useful chemicals.

Due to the intensive interactions between several chemical species, the overall efficiency of a photochemical reaction could also be limited by the rate of these interactions between reagents. Typically, quantum yield, (Φ) which is the ratio of the number of molecules undergoing reactions to the number of photons absorbed during the photoreaction is used to determine the efficiency of a photochemical system. It is expressed as in Equation (1.2).

$$\Phi = \frac{Molecules\ undergoing\ reactions}{Absorbed\ photons} \qquad (1.2)$$

Photonic efficiency of reactions, (ξ), is preferentially considered since it is often not easy to determine the precise amount of species undergoing reactions experimentally. The photonic efficiency can be defined as the ratio between the number of product molecules to the number of photon absorbed and is expressed using Equation (1.3). The extent of photonic excitation effect in chemical reactions can also be quantified using Equation (1.3).

$$\xi = \frac{Reaction\ products}{Absorbed\ photons} \qquad (1.3)$$

There exist several forms of photochemical reactions which for simplicity can be categorised into two: photocatalysis and photosynthesis.[48]

1.5.1 Organic photosynthesis

Photosynthetic method has been used to perform certain chemical reactions where thermal procedure is prohibited. Photosynthetic technique first came to academic limelight in the late 1960s.[45,49] Since then, there has been many studies performed especially on photosynthetic organic chemistry. Based on the reports on organic photosynthesis, three main types of photoreactions can be identified: radical generation, isomerisation and C-C bond formation.[44]

It is important to understand the basic processes occurring during organic photosynthesis. As such, consideration is given on excited systems in terms of both atomic and molecular orbitals (MO). When a covalent bond is formed, a pair of molecular orbitals is formed by the combination of atomic orbitals (AO) of the individual molecule. The molecular orbitals formed will contain the bonding electrons of the constituting atomic orbitals. The bonding electrons possess different energies, one higher than the other. As such, the formed molecular orbital pairs are referred to as the bonding and anti-bonding molecular orbitals which correspond to lower and higher energy systems. As illustrated in Figure 1.5, two molecular orbitals, which possess lower and higher energies are formed as a result of the linear combination of atomic orbitals (LCAO) in a H_2 molecule.
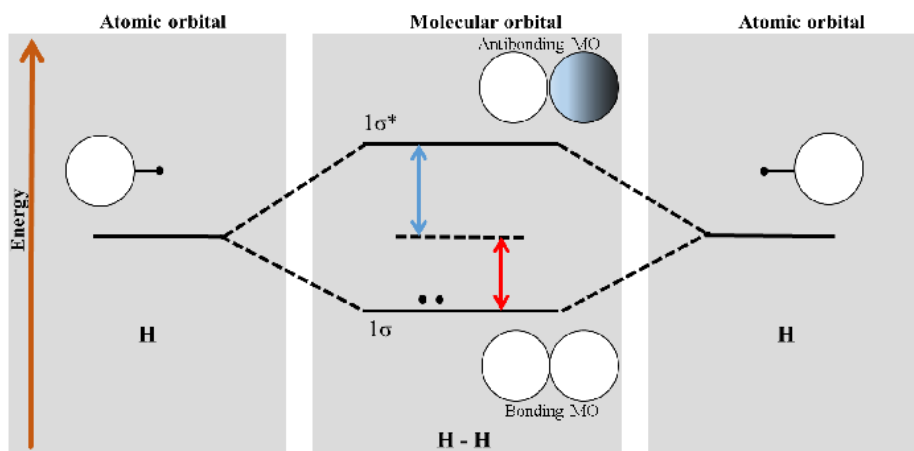
Figure 1.5: Linear combination of atomic orbital of two hydrogen atoms showing the bonding and antibonding MOs formation and the relative energies of individual orbital.

Upon transition of high energy electrons to the antibonding orbitals, several chemical reactions can proceed.[22,44,45] One of the various possible reactions is the photoisomerisation of alkenes. Due to its ability to synthesise chemical species that are thermodynamically unstable, photoisomerisation technique is considered one of the most important techniques. It has been successfully applied in various organic reactions such as the photosynthesis of *cis*-stilbene. This is achieved by irradiation of UV of about 313 nm to the thermodynamically stable *trans*-stilbene. During photoisomerisation, excited electrons transit from S_1 to T_1. As a result, stereochemical rigidity that exists within the excited bond is loss.[43] A *cis* or *trans* configuration can be obtained as electronic decay occurs from T_1 to S_1 resulting in the relaxation of the molecule. Additionally, since the *cis* and *trans* configurations of the molecule are known to exhibit different spectral absorption, one molecular isomer could be selectively excited while the formation of the other is promoted.[50,51] Figure 1.6 shows the various energy positions of electrons during the selective photoisomerisation of stilbene. Note that as the MOs exist in pairs, the low energy bonding orbitals are represented as σ and

π, while σ^* and π^* correspond to high energy antibonding orbitals. During the photonic excitation of stilbene (as other organic molecules), electrons are promoted from the bonding orbitals to the antibonding orbitals. The electronic configuration of the C-C bond during each step of the photoisomerisation process can be seen below the reaction scheme (Figure 1.6).
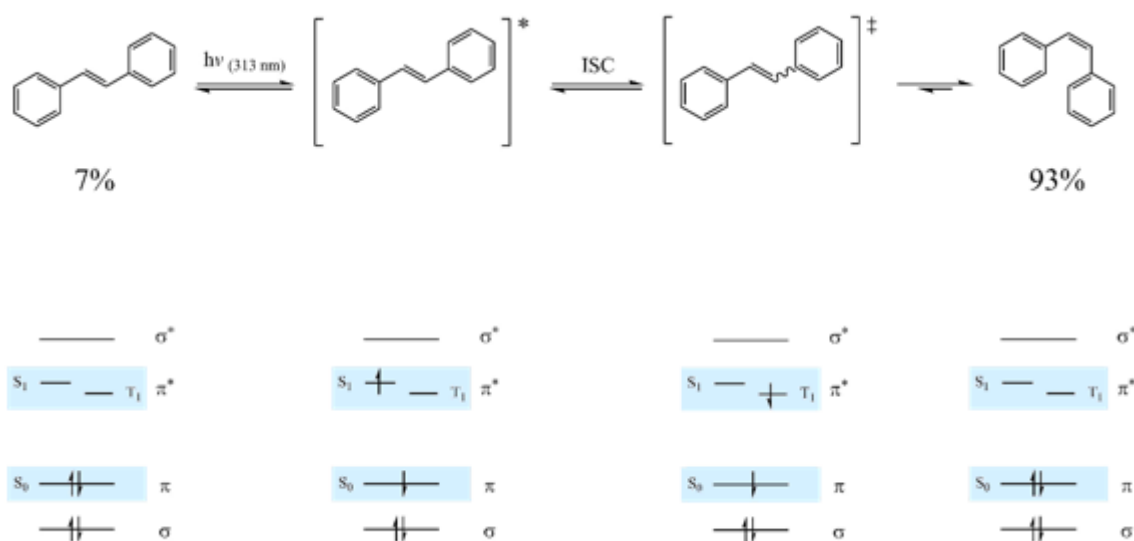
Figure 1.6: Mechanistic pathway showing the selective photoisomerisation of stilbene.

C-C bond formation during photoreactions are numerous. Among the most important ones is the [2+2] cycloaddition of unsaturated molecules such as the alkenes. Photocycloaddition reactions are very important for a number of reasons. For example, photo excitation can lead to easier formation of cyclobutanes systems thereby breaking the thermodynamic barrier that otherwise renders their thermal synthesis difficult.[52] Also, products derived from [2+2] photocycloaddition reactions tend to minimise backward reactions owing to their less absorbing nature relative to synthetic reagents. The ability of the organic compounds to undergo these reactions forms the basis for the development of

purification technique during this work. Decomposition reactions of organic compounds are now known to proceed by interacting with highly reactive radical species that are generated as a result of photonic excitation of photocatalytic materials.

1.5.2 Photocatalytic oxidation

The use of light to excite the electrons of a catalyst leading to a reaction otherwise known as photocatalytic reaction is well known. Photocatalytic oxidation has over the years been keenly studied and interesting successes have been recorded. This method had gained favour by researchers owing to its numerous merits: it is suitable for oxidising both organic[31,36,53] and inorganic[53] compounds, only requires low temperature and pressure and more interestingly, it employs the use of inexpensive, readily available semi-conductor materials such as TiO_2, ZnO, ZnS, CdS, Fe_2O_3, SnO_2 etc.[35,54–57] So far, photocatalytic oxidation has been used to degrade several VOCs in order to improve indoor air quality.[36,58,59] Some of these indoor air pollutants include nitrogen oxides, formaldehyde, carbon oxides, acetone, m-xylene, butylaldehyde, 1,3-butadiene, 1-butanol, toluene and trichloroethylene. These pollutants are known to be carcinogenic, mutagenic or teratogenic.[60–62]

An incomplete photocatalytic degradation of VOCs can result a mixture of undefined products.[63] Han et *al.*[64] identified up to 11 gaseous products including 2-methypropene, acetaldehyde, methylcyclobutane etc. in their photocatalytic oxidation of benzene over TiO_2. Although, all of the by-products which they reported to be probably due to hydrogenation reactions on the surface of the catalyst, are less toxic than benzene, it demonstrates the complexity of the photocatalytic oxidation process. Farhanian and Haghighat[64] investigated the products of UV photocatalytic oxidation of aromatics, alkanes, alcohols and ketones

using a large scale pilot reactor. They observed more products from photocatalytic oxidation of alcohols relative to the other hydrocarbons tested. Two products: formaldehyde and acetaldehyde were formed in all the tested hydrocarbon. Other by-products including propionadehyde and crotonaldehyde were also reported during their study. Such complexity is due to the partial fragmentation and oxidation of the organic molecules. Therefore, the control of the product selectivity from a photocatalytic reaction can be a great challenge and so far there is very limited reported results. In the light of this, a series of selective organic reactions using semiconductor photocatalysts have been developed, which proved to be efficient even if performed in regular glass reactors.

In a typical photocatalytic reaction, the excited photocatalyst react with H_2O and/or O_2 to create reactive radicals. Due the position of the redox potential for H_2O and O_2, normally the photocatalyst with wide band gap are used. Hence, UV irradiation is required. However, large molecules with multiple functional groups can also be directly excited by the UV light. This offers other reaction pathways through photoexcited molecules and results in multiple products through the molecular fragmentation. Semiconductor photocatalyst requires only UV irradiation to be directly excited if organic reactions are to be successful. When high concentration molecular oxygen (O_2) is used, the O_2 can attach to free radical intermediates, resulting in uncontrolled autoxidation products. Meanwhile, the photogenerated hole (h^+) in the semiconductor is highly oxidative. If the organic reactants or their intermediates are directly adsorbed on the semiconductor surfaces, they can also be directly oxidized with little control. For these reasons, it becomes a major challenge to improve the selectivity and yield of photocatalytic reaction. In this thesis, I will try to control the reaction conditions by reducing reaction temperature, managing gas mixture and modifying the surface electronic

structure of the photocatalysts in order to improve the selectivity of the photocatalytic oxidation process for specific reaction.

1.6 Semiconductors as photocatalysts

Photocatalysts are crystalline semiconductor solids that can initiate reactions in the presence of light but are not consumed in the overall reaction.[65] For an efficient photocatalytic reaction, the catalyst needs to be photo-active, and ideally able to be effectively activated by solar light (near-UV light), biologically and chemically inert, photo-stable, inexpensive and non-toxic.

Most of the reported photocatalysts have some limitations. For instance, GaAs, PbS, and CdS readily undergo photocorrosion and are toxic rendering them insufficiently stable for catalysis in aqueous media. ZnO is unstable due to its ability to readily dissolve in water yielding $Zn(OH)_2$ on the particle surface, which renders the catalyst inactive over time.[66] Fe_2O_3, SnO_2, and WO_3 all have a conduction band edge at an energy level below the reversible hydrogen potential.[67,68] So the photo excited electrons from these photocatalyst does not have enough reduction power for water and form the bottleneck for overall process.

In a semiconductor particle, electrons can be excited from a region of highest occupied energy band, also known as the valence band (VB) to that of the lowest unoccupied energy band, the conduction band (CB).[69,70] Normally, the VB states are dominated by the anion species, such as O_2^- in oxides since it is the frontier occupied states, while the CB states are dominated by the empty states of the metal cations. Figure 1.7 illustrates the electronic excitation and transition that occurs within the bands of a semiconductor. For the electrons to be excited, energy must be supplied to the particle. The supplied energy has to be equal to

or greater than the energy gap between the valence band maximum, (VBM), and the conduction band minimum, (CBM).[71–73] This energy gap is also referred to as the band gap, (Eg). Upon excitation of electrons by photons or heat, they transit from the VB leaving a positively charged hole (h^+), to the CB, denoted by a in Figure 1.7. As a result, an electron-hole pair is generated which requires energy to dissociate into free electrons in the CB and holes in the VB. Without the dissociation of the electron-hole pair, they are considered as a single particle known as exciton.
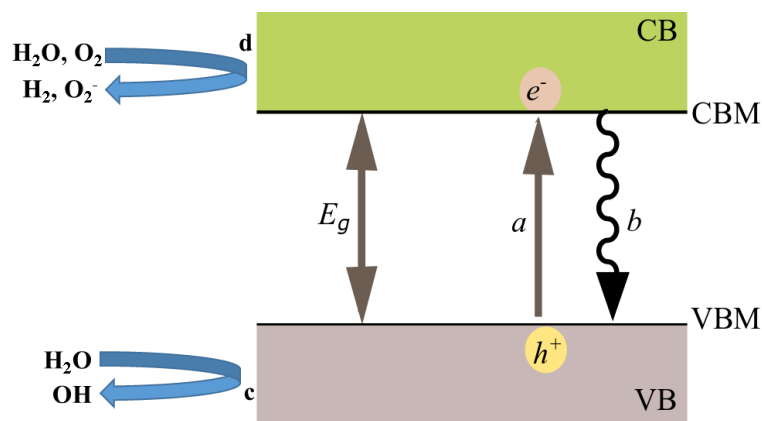
Figure 1.7: Illustration of the band transition during electronic excitation in a semiconductor.

Excitation is determined by the light intensity with appropriate wavelength and material thickness. For a photocatalyst to remain active, it is important that e^-/h^+ pair generated due to photonic excitation are trapped quickly by the targeted molecules. Trapping helps to separate charges and reduce recombination, denoted b. Trapping could also reduce the charge mobility resulting in charge recombination/fluorescence. Finally, the photoexcited electrons and holes travel to the surface of the photocatalyst particle. Such electrons and holes will carry out surface redox reactions if they have sufficient redox potential left. Surface

redox create radicals if H_2O and O_2 are used as the reaction media. In the reaction process, the $^\bullet$OH coming from the oxidation of adsorbed water or OH^- is highly reactive. Similarly, the reducing power of the electrons can induce the reduction of molecular oxygen to superoxide ($O_2^{\bullet-}$). These highly reactive species, $^\bullet$OH and $O_2^{\bullet-}$ demonstrate strong ability to drive organic reactions such as photo epoxidation of alkenes, degradation of micro-organisms[74] as well as organic pollutants. [74,75]

The high charge mobility is an essential property of the semiconductors; hence, their variety of applications in fields of photovoltaics, photodegradation as well as photoelectrolysis.[76–78] The photoexcited electrons will need to travel towards the cathode while the holes need to travel to the surface to facilitate oxidation before the electron and hole recombine. Such traveling within the solid materials will cost energy and reduce the redox potential of the electron and hole. Therefore, if the mobility is not high enough, the overall reaction kinetics will be restricted by the travelling of the electrons and holes.

Generally, the photocatalytic activities of semiconductors depend on their band gaps which is determined by the electronic configuration of the atoms (ions) and the arrangement of the atoms, i.e. the crystal structure. Different semiconductors exhibit different band gaps as shown in Figure 1.8. The lower edge of the CB represented in blue and the upper edge of the VB represented in orange are shown with the corresponding band gap in units of electron volts (eV). Using the vacuum level or the normal hydrogen electrode (NHE) as reference, the various energy scale of the semiconductors are indicated. The standard potentials of several redox couples are also presented on the right relative to the standard hydrogen electrode potential (Figure 1.8).[79]
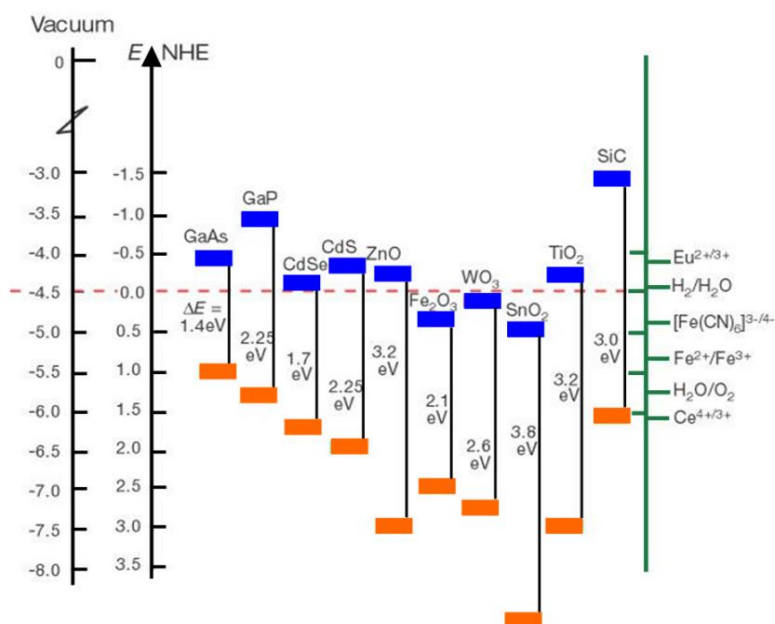
Figure 1.8: Band positions of several semiconductors together with some selected redox potentials measured at pH 7. Adapted from Michael G[79]

Interest in heterogeneous semiconductor photocatalysis has surged over the past decades.[80,81] Fujishima & Honda first demonstrated photocatalytic ability of TiO_2 in their water splitting experiment using UV light and TiO_2 anode in an electrochemical cell.[82] Upon irradiating the TiO_2 electrode, they recorded the evolution of O_2 and H_2 at the TiO_2 electrode and the Pt counter-electrode respectively. This novel observation has sparked unprecedented interest in the semiconductor-mediated chemical utilisation of solar energy conversion. Several applications including CO_2 reduction,[83–87] selective oxidation,[88,89] reduction of nitroorganics,[66,90] removal of toxic ions,[91,92] and C-C bond formation,[93] have been investigated and reported in the literature. Nevertheless, The main areas of research in this field remain in the production of H_2 through photoelectrochemical splitting of water[94–97] and the photocatalytic decomposition of organic pollutants in both residential and commercial areas in air[98,99] and wastewater.[100]

1.6.1 Titanium dioxide photocatalysis

Among the various photo-catalysts currently used, TiO_2 remains one of the preferred. This is because of its hydrophilic properties and its ability to degrade many compounds, both organic and inorganic under irradiation of UV or near UV-light.[101,102] Moreover, due to its appropriate valance band maximum (VBM) and conduction band minimum (CBM) relative to the redox of H_2O and O_2, TiO_2 readily carry out oxidation of most indoor air pollutants at ambient temperature without requiring any chemical additives.[58,103] It is low cost and abundant, since it is readily available as Ti constitutes 0.63 % of the earth's crust. It is environmentally friendly and chemically stable with very little solubility in most of the strong acids or alkalis (except in hot concentrated base, hot H_2SO_4 or HF), thus, the morphology and crystal structures do not change upon activation/reaction. This chemical stability is very important for the long working life of photocatalysts which are subject to constant excitation-reduction oxidation cycles during a photocatalysis process.[66,104] Due to the above merits, there have been reports of several novel heterogeneous photocatalytic reactions using TiO_2 as the photocatalyst for solar cell, photocatalytic hydrogenation and environmental cleanup applications.[58,98,103,105,106]

TiO_2 exists in various crystal phases, but only three are stable and hence are commonly studied. These are: anatase, rutile and brookite.[106,107] They exhibit different crystal structures (Figure 1.9) and therefore different chemical and electronic properties. These three natural polymorphs of TiO_2 are known to be photoactive at different wavelengths based on their respective band gaps: 3.11, 3.06 and 3.30 eV, corresponding to wavelengths of 399, 405 and 376 nm.[78] These band gaps are considered to be fairly wide and are unable to utilise most of the solar spectrum because the majority of the solar energy is in the visible range.
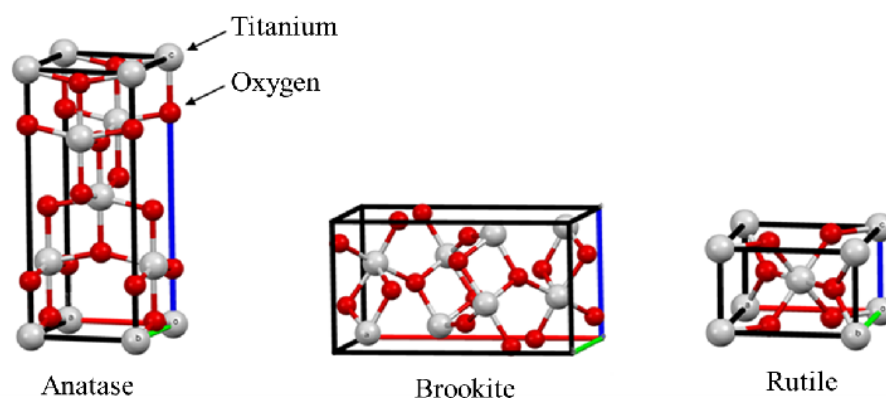
Figure 1.9: Representation of crystal structures of the three main crystal phases of TiO_2

Among the three common phases of TiO_2, brookite has the highest reported photoactivity which perhaps is likely due to its large band gap energy and its ability to form defects easily. These defects are believed to inhibit the recombination of exciton.[108,109] Anatase has been reported to exhibit higher photoactivity than rutile for most reactions.[110] This can be attributed to the higher Fermi level, lower O_2 adsorption capacity and/or higher level of surface hydroxylation of the former over the latter.[110,111] However, there are suggestions that combination of anatase and rutile phases in a given ratio enhances the photoactivity.[1–3,34] Although disputed, the possible reason was that the electron-hole separation efficiency could be improved because of contact between the separate crystalline phases with different positions of Fermi level.[78,107,112]

A highly efficient commercial product of TiO_2 known as P25 is frequently used as a standard in order to assess the photoefficiency of new photocatalyst. [113–117] P25 is a commercially available TiO_2 powder with an anatase/rutile ratio of approximately 3:1 with

consistent photoactivity.[113,114] Ohno *et al.*[118] and Su *et al.*[115] both reported that Aeroxide®

P25 exhibited higher activity than either anatase or rutile alone.

TiO$_2$ was used in most part of this work, either as standalone or modified with other

metal oxides, such as WO$_3$ (Chapter 7). The reason for the choice lies within the fact that the

photocatalyst is one of the most important and popular compounds for a wide variety of

applications.[78,119–122] Although TiO$_2$ has been widely used as photcatalysts, its application in

selective organic reaction is still very limited. This work aims to explore the possibility of

controlling the photocatalytic kinetics in order to obtain industrial important chemicals, such

as epoxides.

The major limitation of using TiO$_2$ as a photocatalyst driven by sunlight is that it does

not absorb visible light due to its wide band gap ($\sim$3.2 eV for anatase and 3.0 eV for

rutile).[110,123,124] It also suffers with the high recombination rate, low charge mobility as well

as uncontrolled photo selectivity.[66]

During photocatalytic oxidation using TiO$_2$ as a photocatalyst, upon irradiation of TiO$_2$

particle, it generates an exciton as expressed in Equation (1.4):

$$TiO_2 \rightarrow e^- + h^+ \tag{1.4}$$

An electron is transferred from the adsorbed molecules H$_2$O or the OH$^-_{ad}$ ion, to the

electron-hole as in Equations (1.5) to (1.7).

$$h^+ + S_{ad} \longrightarrow S^+_{ad} \tag{1.5}$$

$$h^+ + H_2O_{ad} \longrightarrow {}^{\bullet}OH_{ad} + H^+ \tag{1.6}$$

$$h^+ + OH^-_{ad} \longrightarrow {}^{\cdot}OH_{ad} \qquad\qquad (1.7)$$
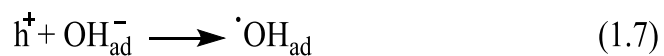
Molecular oxygen in the electron-transfer reaction (Equation 1.8) acts as an acceptor species resulting into a superoxide, $O_2^{\bullet-}$.

$$e^- + O_2 \longrightarrow O_2^{\cdot-} \qquad\qquad (1.8)$$

The subsequent reactions (Equations 1.9 and 1.10) involve the superoxide anions formed in Equation 1.8 yielding hydrogen peroxide as follows:

$$O_2^{\cdot-} + H^+ \longrightarrow HO_2^{\cdot} \qquad\qquad (1.9)$$

$$H^+ + O_2^- + HO_2^{\cdot} \longrightarrow H_2O_2 + O_2 \qquad\qquad (1.10)$$
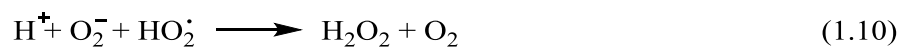
The generated hydrogen peroxide can reversely convert to oxidative ${}^{\cdot}OH$ free radical groups under the light illumination (Equation 1.11).

$$H_2O_2 \xrightarrow{hv} 2\,{}^{\cdot}OH \qquad\qquad (1.11)$$

Finally, the organic molecules in the vicinity of the active radicals are oxidized to form an intermediate (Equation 1.12).

$$^{\bullet}OH_{ad} + S_{ad} \longrightarrow \text{intermediate} \qquad (1.12)$$
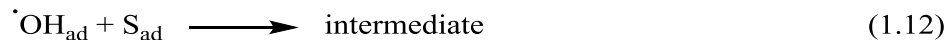
The $^{\bullet}OH$ radicals in Equation (1.12) are very reactive and attack the substrate molecule degrading it into mineral acids including CO_2 and H_2O.[125] Nevertheless, during the above reactions, there is also the tendency that electron and hole could recombine. This phenomenon leads to reduction in photo-efficiency of the photocatalytic oxidation, which corresponds to decreased population of photo excited electrons and holes.[66,125]

Similarly, during the reactions, some of the various intermediates produced have potential of poisoning the active sites resulting in deactivation of catalysts.[119,126] In order to improve the visible light absorption and to improve the charge separation, as well as charge mobility, TiO_2 can be modified by introducing other metal ions (Fe,[75,127] Cr,[128,129] W,[130–132] Rh,[133–135] Al[136,137]) and main group elements (C,[138] N,[139–141] B,[142,143] S,[3,16,144]).

1.6.1.1 Semiconductors-TiO₂ heterojunctions

When a semiconductor forms a heterojunction with TiO_2, the two can be excited, leading to generation of excitons. However, transition process depends on the respective positions of CB and VB of the semiconductors relative to the NHE. Generally, semiconductor-TiO_2 heterojunctions are divided into three categories (Figure 1.10).[145] For the first category denoted C-I, both semiconductors are either n-type or p-type in which CB of TiO_2 is higher than that of semiconductor, X, and at the same time the VB of TiO_2 is lower

than that of X. This means that both CB electrons and VB hole of the TiO_2 would migrate to those of X. An example of X is Fe_2O_3. In the second category, C-II, the electrons in CB of TiO_2 would migrate to that Y, such as SnO, while the holes migrate the opposite direction, from VB of Y to that of TiO_2. This type is more preferable as the excitons are well separated thereby extending the lifetime of the doped catalyst. In the third and final category C-III, the direction of migration of charge carriers is identical to that of C-II. However, there is a huge gap between the CB and VB positions of the two semiconductors, TiO_2 and Z. this implies that a high amount of energy is required to effectively separate and migrate the charge carriers.[145]
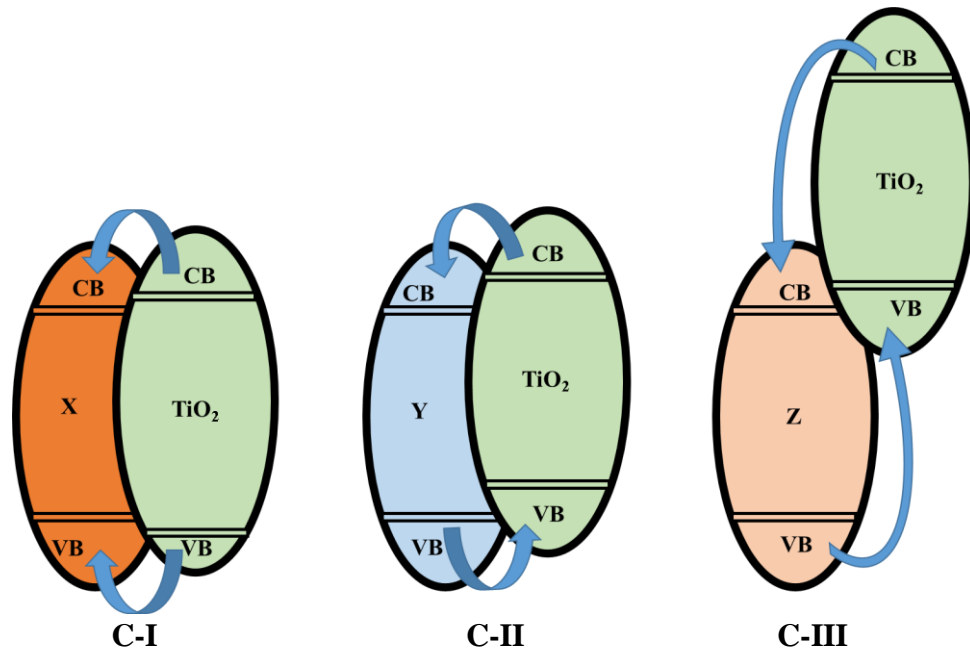
Figure 1.10: Carrier charges migrations between band gap structures of three categories of semiconductor-TiO_2 heterojunctions[145]

There are several reports on heterojunctions between two wide band gap semiconductors such ZnO-TiO_2. Pan *et al.*[145] reported fabrication of TiO_2 nanobelt/ZnO nanorod heterojunction with improved charge separation, which they attributed to decrease in quasi-Fermi energy level. ZnO has a band gap of 3.37 eV[146] which means its CB and VB

potential is slightly more negative than that of TiO_2 (3.2 eV).[147] In heterojunction, the Fermi levels are aligned, and this alignment will determine the relative position of CBM and VBM. Irradiating the heterojunction of these semiconductors generates electrons in the VB, which are excited to the CB and migrate to the CB of TiO_2 owing to the difference in potential between the two semiconductors. This is accompanied by migration of holes from VB of TiO_2 to that of ZnO.[148,149]

In this work, only semiconductors with narrower band gap than TiO_2 were used to achieve partial oxidation of alkenes. This is because such semiconductors are known to be easily photoexcited by solar spectrum ($\lambda \leq 590$ nm). TiO_2-semiconductor heterojunctions were created using Bi_2WO_6 (Chapter 5) and WO_3 (Chapter 7). From economical point of view, the benefit of using semiconductor photocatalyst can be maximised by limiting their choice to only those with band gaps that allow solar photoexcitation.

1.6.2 Bi_2WO_6

Due to its physical and chemical properties, Bi_2WO_6 has attracted attention of researchers significantly. Bi_2WO_6 is desirable also for its ability to effectively drive photocatalytic degradation of organic pollutants as well as water splitting for the evolution of O_2.[72,73,150,151] Its excellent photoactivity could be attributed to the corner–sharing structure of WO_6 octahedron, which is sandwiched between $(Bi_2O_2)^{2+}$ layers. This layered network configuration is known to be enhance the transfer of electrons to the surface of the photocatalyst ultimately suppressing the recombination of photogenerated electron-hole pairs.[71,151–153]

Kudo and Hijii[154] reported photocatalytic evolution of O_2 from $AgNO_3$ solution using Bi_2WO_6. Similarly, Zou *et al.* reported the photoactivity of Bi_2WO_6 for both evolution of O_2 and mineralisation of $CHCl_3$ and CH_3CHO to CO_2 under visible–light irradiation.[153] Many research activities have been performed to study and enhance the efficiency of Bi_2WO_6 photocatalyst. Some example include $F–Bi_2WO_6$,[71] Ce and F co-doped Bi_2WO_6[155] $Co_3O_4–Bi_2WO_6$,[152] $AgBr–Ag–Bi_2WO_6$,[156] $Er^{3+}–Bi_2WO_6$,[157] $Gd–Bi_2WO_6$,[158] $C_{60}–Bi_2WO_6$,[159] $C–Bi_2WO_6$,[155] $Ag–Bi_2WO_6$,[155] etc. Although these composite photocatalysts have demonstrated high photocatalytic activity, they also suffer certain drawbacks. Some contain toxic ions such as Co^{3+}, some contain expensive ions/metals such as Er^{3+}, C_{60}, Ag, while some others are difficult to synthesise. As such, the fabrication of an environmentally benign and economically facile high–efficient Bi_2WO_6–based photocatalysts is still a challenge.

One of the factors that determine the photocatalytic performance of a material is its defect structure. In order to achieve this, some researchers have introduced oxygen vacancies to the photocatalyst framework such as TiO_2 and ZnO.[160–162] Zhu et al.[72] reported successful fabrication of high UV photoactive ZnO and $BiPO_4$ with surface oxygen vacancies. The group observed improvement in the UV photoactivity as well as extended photoresponse wavelength range.

In the present work, Bi_2WO_6 photocatalyst was synthesised and utilised for the photo-epoxidation of propylene. To improve the efficiency of the synthesised material, different molar ratios of TiO_2 were incorporated into the Bi_2WO_6. This afforded improved charge separation as well as enhanced reactant adsorption.

1.6.3 TS-1

Zeolites are a group of inorganic materials with high crystalline nanoporous structures. They have well-defined channels or cavities (of sizes between 0.5 and 2 nm), that are interconnected.[163] Silicalite-1, with an MFI topology structure, is an all-silica zeolite that only contains Si, O and H in the framework. MFI is a framework type derived from ZSM-5 (Zeolite Socony Mobil, with sequence number five), which is a member of the pentasil family of zeolites. The Si atoms of zeolite in the framework can be substituted by metal ions such as V, Mn, Zn and Ti.[164] By incorporating heteroatoms such Ti (and other transition metals), zeolites can exhibit photocatalytic activity.[163] Titanium silicate (TS-1), with the MFI structure is one of the most commonly used zeolites. Due to the substitution of Si atoms with the tetrahedral Ti atoms which allows the transfer of an electron in ligand-to-metal (-O-T), TS-1 exhibits a characteristic absorption band at 225 nm. There have been many researches aimed at studying the photoactivity of TS-1. Lee et al.[165] reported successful photodecomposition of 4-nitrophenol over TS-1 catalyst using 500 W high pressure Hg lamp. Ban et al.[164] also investigated the photocatalytic activity of TS-1 for degradation of monoethanolamine (MEA). In comparison to TiO_2, this group reported that the activity per Ti atom in TS-1 was higher than in TiO_2. They attributed this observation to higher adsorption of MEA on the TS-1 due to its microporous structure.

The use of H_2 and O_2 to form H_2O_2 in-situ over TS-1 is widely investigated. This reaction circumvents the challenges of H_2O_2 decomposition in gas-phase reactions.[166–168] However, to achieve in-situ generation of H_2O_2 with H_2 and O_2 over TS-1, a noble metal such as Au or Pt is added during the synthesis of TS-1.[164,166–169] The noble metal on TS-1 is reported as the active site for the conversion of H_2 and O_2 in to H_2O_2, while the formed H_2O_2 interacts with the TS-1 to form an intermediate, titanohydroperoxyl (Ti-OOH).[168,170] This

procedure was adopted in this work (Chapter 6). H_2 and O_2 were simultaneously introduced into the photo reactor containing Au-TS-1. It was possible to achieve epoxidation of cyclohexene using this technique, hence the validity of the designed photoreactor.

1.6.4 CeO$_2$

CeO$_2$ is one of the widely studied metal oxides that has gained the attention of the academia and industry for decades.[171] Some of its advantages include the Ce^{3+}/Ce^{4+} reduction-oxidation cycle as well as the ability to store oxygen, otherwise known as Oxygen Storage Capability (OSC). The oxidative properties of CeO$_2$ is dependent on the reduction step between Ce^{3+} and Ce^{4+} also referred to as the Ce^{3+}/Ce^{4+} redox cycle.[171,172] This property is mainly caused by its high reduction potential as well as the OSC, the extent of which is a function of the size, morphology, shape as well as surface area of the material.[173] At an average size between 10 and 15 nm, CeO$_2$ nanomaterial exhibits a phenomenon known as quantum confinement effect.[174,175] They also exhibit an appreciable growth of cell parameters owing to the oxygen vacancies present as a result of the increase in number of Ce^{3+}. It has been reported that due to enhancement of the ratio of Ce^{3+} to Ce^{4+}, the OSC can be improved by coupling CeO$_2$ with ions of a transition metal or another rare-earth metal.[176,177] Higher surface energy also plays a crucial role in the enhancement of the material's activity, as it is responsible for the improved activity of the observed (100) surface of cubic CeO$_2$. In descending order, the surface energy of cubic CeO$_2$ is as follows: $(100) > (110) > (111)$.[178] The surface energy, particularly of nanoparticles, represents an important quantity in understanding the thermodynamics of particles. In terms of particle size, different approaches such as, molecular dynamics simulations, ab initio as well as classical thermodynamics

calculations have been used by researchers to predict this quantity. For example, in classical thermodynamics, it is possible to predict change in surface energy since it corresponds to change in particle size. Increase in particle size is accompanied with increase in surface energy and vice versa. This phenomenon is attributed to change in the number of next neighbours of surface atoms as the particle size changes, which leads to partial compensation by a corresponding change in the binding energy between the atoms.[11]

The ability to control some of the most desirable properties of CeO_2 nanostructures has justified their interest over the conventional aggregated nanoparticles. Some of these physicochemical properties include architecture, morphology and growth direction. There exist several morphologies of CeO_2 nanostructures in the literature. Among these, one-dimensional nanorods, aggregates, and wires have drawn a lot of attention owing to their high specificity of both surface area and active crystallography in the direction of growth.[173,179]

1.7 Developing a photocatalytic reactor

For a photocatalytic reaction, a simultaneous continuous contact between the reactants, catalyst and light (photons) is necessary. Several types of photo-reactors have been created and used in the literature some of which include static/batch reactors for gaseous reactants. Solid catalysts were either used as a free powder or immobilised on some support such as quartz wool and mesh etc.[180] Another type of photo-reactor intensively used in the literature is to suspend the powder catalyst in a suitable solvent to form a slurry which is coated on the walls of reactor tube. Photoreactions have also been reportedly performed in a continuous flow system in which the catalyst is immobilised on several materials such as glass rods,[181]

sponge,[182,183] silica gel,[184] activated carbon[185] and a lot more. Although a good combination of catalyst-substrate surface area can be achieved, using the first generation of reactors, the main challenge is the difficulty in separating the catalyst from the reaction mixture, making purification and analysis difficult.

The small the particle, the high the recombination and fluorescence. In addition to the electronic properties of the photocatalysts, the reaction rate is normally determined by the light absorption of the density of surface area. Large surface area allows good contact between the reactants and the photocatalysts. Therefore, many particles at nanometer sizes were used. However, this renders conventional filtration ineffective. Certain coupled catalysts such as Fe_3O_4-TiO_2 core-shell however, can be separated from the reaction mixture using magnetic separation. This type of reactor is used for wastewater treatment especially where post-reaction purification can be carried out easily. For gas phase applications, similar challenge for the collecting particular photocatalysts can be encountered, although the good mixing of light, reactants and catalysts can normally be satisfied. Nevertheless, gas-phase systems are known to suffer loss of surface are, reduced light absorption and penetration, and inhomogeneous illumination. Loss of catalyst and deactivation due to accumulation of less reactive intermediates are also possible issues. [186,107]

For a functional flow reactor, immobilisation of catalyst is required. There are a number of advantages associated with this procedure. The main advantage however, is that the catalyst/product separation problem can be circumvented. Also, different ratios of products could be obtained by simply tuning the flow rate/contact time and it is possible to operate continuously. This type of reactors can be considered suitable for industrial applications for both wastewater systems and large-scale gas phase synthesis.

It is possible to monitor reactions spectroscopically as they proceed in situ.[187–191] Also, considering the fact that catalyst separation is not a problem the reaction products can be easily collected and analysed directly using instruments such as gas chromatograph (GC). Furthermore, only a low radiation amount is required to attain optimal reaction rates in the case of a gas-phase reaction due to low concentrations of substrate (often much lower than in the liquid phase) which makes adsorption negligible.[186] However, since the concentration of gaseous pollutants are typically low (in order of 10^{-9} M)[192,193] diffusion-limitations of reactions,[194] is not an issue for most domestic applications. The major disadvantage of this type of reactor is the low rate of reaction owing to the low concentrations of substrate effectively rendering this reactor type unsuitable for synthetic applications. Interestingly, using an adsorbent catalyst support can improve the performance of this type of reactor as the adsorbent support can increase the concentration of substrate near the catalyst relative to the gas-phase. This act as a storage for the reactants that can diffuse to available active sites on catalyst while preventing the escape of reaction intermediates and driving the reaction to completion. This suggests that choice of support can influence the rates of adsorption, surface diffusion as well as desorption.

In this work, a flow type reactor was designed to achieve a uniform illumination. In order to ensure the catalyst was uniformly distributed across the entire reactor without restricted gas flow or reduced light illumination, powdered photocatalysts were immobilized on glass beads.

1.8 Other photocatalytic applications

1.8.1 Photocatalytic oxidation

No doubt, photocatalytic reactions have now found expression in both the academia and industry. Several photocatalysts have been created and applied for oxidation of organic compounds. Fujihira et al.[70] investigated the effect of the addition of Cu^{2+} and Fe^{2+} on the heterogeneous photocatalytic oxidation of some aromatic compounds in air using powdered TiO_2. They found that the nature and concentration of the added oxidant played a significant role on the ratio of organic products formed. ca. 20 times more increase in the quantum yield of toluene photooxidation was achieved when Cu^{2+} was added than in an additive-free system. Similarly, higher ratio of hydroxylated products (cresols) over side-oxidation products (phenol, benzaldehyde) was also obtained, which suggested a higher production of $^{\bullet}OH$ radicals by the heterogeneous pathway as well as by a Fenton-type reaction.

Dutta et al.[69] studied photocatalytic oxidation of Arsenic (III) in order to provide evidence that $^{\bullet}OH$ is the main oxidant for the oxidation of As (III). They used benzoic acid as a $^{\bullet}OH$ scavenger. The formation of salicyclic acid from the oxidation of benzoic acid by $^{\bullet}OH$ suggested the involvement of $^{\bullet}OH$ in the mechanism of As (III) oxidation. The effect of Fe (III) on As (III) oxidation at different pH values with and without TiO_2 under UV light studied suggested that $^{\bullet}OH$ is the dominant oxidant for As (III) oxidation.

Sclafani et al.[2] studied the influence of Fe^{3+}, Fe^{2+} and Ag^+ on photo degradation of phenol and nitrophenol in anatase and rutile aqueous dispersions. They observed that the low photoactivity of anatase in the absence of oxygen or other electron scavengers increased significantly in the presence of both Fe^{3+} and oxygen, with an optimum value at 0.5mM Fe^{3+}. At higher amounts of Fe^{3+}, the results were unpromising. The rutile, though inactive in the

absence of metal ions, was observed to function effectively in the presence of 0.5mM Fe^{3+}. However, the authors found no effect of Fe^{3+} in deaerated systems. They attributed the enhancement to contributions of the photo-Fenton reaction.

1.8.2 Photocatalytic reduction

Photocatalysis has also been studied extensively in the field of photocatalytic reduction. With tonnes of toxic chemicals in use globally, it becomes inevitable for humans to come in contact with these chemicals, most of which are mutagenic and carcinogenic. An example of such chemicals is the chromium solution. Heterogeneous photocatalytic reduction of chromium with semiconductors such as TiO_2, Pt/TiO_2, ZnO, CdS, ZnS and WO_3 has been widely investigated. Tesla et al.[195] successfully reduced Cr (VI) to Cr (V) to Cr (IV) and to Cr(III) through a one electron transfer process using heterogeneous photocatalysis over TiO_2. Rongxin et al.[196] investigated photocatalytic phenol degradation and Cr (VI) reduction over Elongated TiO_2 nanoparticles with high aspect ratio. Their homemade TiO_2 nanoparticles showed high catalytic activity examined for both photocatalytic phenol degradation and Cr (VI) reduction. Tan *et al.*[197] investigated photocatalytic reduction of selenate Se (VI) ions using unmodified TiO_2 and Ag-loaded TiO_2 (Ag-TiO_2) photocatalysts. They observed that in the presence of formic acid, both photocatalysts were effective in reducing Se(VI). According to this group, the reaction proceeded through the reduction of Se(VI) ions to elemental selenium Se and then to hydrogen selenide gas (H_2Se). Over unmodified TiO_2 photocatalyst, the Se formed from the reduction of Se(VI) was further reduced to Se^{2-} in the form of H_2Se when Se(VI) in solution was exhausted. Using Ag-TiO_2 photocatalysts, the reduction of Se(VI) was accompanied by simultaneous generation of hydrogen selenide gas.

1.8.3 Photocatalytic reduction of CO_2

A promising application for the chemical process of CO_2 reduction is the implementation of artificial photosynthesis through photoreduction. This is by far more environmentally friendly than the conventional energy intensive method. Currently, there are many research works aimed at utilizing the solar energy for direct transformation and storage of chemical energy. The photo reduction of CO_2 with H_2O to produce chemicals, such as methane or methanol (CH_3OH), is an example.

Lui et al.[187] reported CO_2 photoreduction with water vapor using three TiO_2 nanocrystal polymorphs (anatase, rutile, and brookite). They demonstrated the production of CO and CH_4 from CO_2 photoreduction with a remarkable enhancement of up to 10-fold on defective anatase and brookite TiO_2. Wang et al.[198] achieved an efficient photochemical reduction of CO_2 under mild reaction conditions using $ZnCo_2O_4$ nanostructures. Similarly, Li et al.[85] reported an efficient and stable photocatalytic CO_2 reduction process with water over $NaTaO_3$. They achieved this by introducing an electron donor (H_2) into the reaction process. Using $Ru/NaTaO_3$, they demonstrated high activity in CH_4 formation rate (51.8 mol h^{-1} g^{-1}).

Due to ever-growing change in climate, and the need to curb greenhouse gas emission, the photocatalytic reduction of CO_2 has recently seen a surge in interest.[8] Inoue *et al.*[199] successfully reduced CO_2 with H_2O over various semiconductor photocatalysts. Formic acid, formaldehyde and methanol were obtained as products. Li *et al.*[200] achieved photoreduction of CO_2 to CH_4 when they studied the effect of concentrating light and pre-treatment over g-C_3N_4. They attributed the high yield of CH_4 to change in surface oxidation state of the catalyst due to either oxidation of the catalyst or the activation of surface oxygen.

It is important to note that photocatalytic reaction mechanisms are generally very complicated. Several factors have been outlined in the literature that affect the behaviour of the technique. Some of these factors include but not limited to phase and concentration of substrate,[201] catalyst morphology/structure,[202–205] light source,[206,207] humidity,[208–210] O_2 concentration[211–213] and pH.[214–217]There is also the difficulty in detecting reaction intermediate radicals as well as their extent of involvement in the reactions.[218] Kinetics and intrinsic quantum efficiency are often complicated due to competition between substrates.[214,219,220] Although large amount of research has been carried out in the literature as at present on the subject of photocatalysis, there is yet to be a specific guiding philosophy. This can be observed in the amount of inherent problems often arising in reports. Nevertheless, the field of photocatalysis is interdisciplinary, which requires broad background knowledge as well as experience if a meaningful and thorough discussion on the subject matter is to be made.

1.9 Thesis aims

This thesis aimed to design a continuous green chemical process for the epoxidation of alkene with high commercial viability. The technology is operated under low temperature at atmospheric pressure. The heterogeneous design of the reactor eliminated the need for product separation. It does not require any solvent, and oxygen in air can be directly used in combination with H_2 or H_2O (depending on the substrate). The designed technology is highly efficient and selective. Its components are cheap and commercially available which reduces the production costs. It is also effective for total mineralisation of VOCs into CO_2 and H_2O. Partial photocatalytic oxidations can easily be achieved by using an appropriate photocatalyst as well as regulating the flow rate of reactants. This also suppresses the formation of

byproducts as the chemicals have controlled contact time in the photoreactor. It is easy to control reaction temperature, thus providing a reliable kinetic data. Overall, this technology can provide alternative air purification process as well as convert hydrocarbons into useful starting materials for other chemical processes, hence contribute to improving the quality of life.

1.10 Thesis overview

In Chapter 1, general background the major sources of industrial greenhouse emissions such as petroleum industries was discussed. As photocatalytic epoxidation of alkenes was the main application of the designed reactor, it became imperative to refresh memory on the basic chemistry of alkenes and epoxides. An overview of photocatalysis of semiconductors including TiO_2, Bi_2WO_6, TS-1 and CeO_2 as base catalysts as well as their various modification techniques in the literature have been highlighted.

Chapter 2 presented some of the main instruments used for the characterisation of the synthesised photocatalysts as well as those used for product analyses. During catalyst analyses, XRD, SEM, EDX, Integration sphere and BET were used. FTIR, GC-MS and NMR were utilised for the products analyses. The basic principles of operation of these instruments were discussed in this chapter.

Chapter 3 focused on the developmental design of the photo-reactor. Through a complimentary catalyst coating technique designed for this work, all the synthesised photocatalyst powders were immobilised on silicon glass beads. The immobilisation technique is discussed in detail in this chapter. Although, the first reactor designed was effective in decomposing acetone (Chapter 4), it underwent series of modifications in the

subsequent chapters in order to achieve the desired products. Aeroxide P25 was the photocatalyst used in this chapter to test the functionality of the designed reactor.

Chapter 5 contains the photoepoxidation of propylene. Epoxidation was firstly, attempted with our homemade TiO_2. The synthesised catalyst was further improved by coupling with Bi_2WO_6. The epoxidation was achieved with the designed reactor using molecular oxygen as the only catalyst. Also in this chapter, the synthesised Bi_2WO_6 was observed to undergo photochromism during the epoxidation reaction. As such, its effect on the epoxidation of propylene was investigated.

In Chapter 6, a kinetic study was attempted on the photoepoxidation of cyclohexene. A catalyst known in the literature to be effective in the epoxidation reaction of cyclohexene, TS-1, was synthesised and utilised for this purpose. Mixture of H_2 and O_2 was crucial in the photoepoxidation of cyclohexene. Since no epoxide was observed in the absence of H_2, a mechanism was proposed in this chapter. During the kinetic study, the effect of reaction temperature and partial pressure of the reaction gases was investigated.

Chapter 7 presents photoepoxidation of hexene in gaseous phase. Here, pure TiO_2 and WO_3 coupled TiO_2 were utilised for the epoxidation reaction. Further experiments focused on *in-situ* reaction of the partial photo-oxidation products of photo-epoxidation of 1-hexene were performed in this chapter. The exhaust of the photo-reactor was passed directly through methanol, which acted as a nucleophile under acidic condition for several hours. The features of some of the reactive species formed during the partial photo-oxidation of 1-hexene process are discussed in this chapter, hence the versatility of the developed photo-reactor.

Chapter 8 demonstrated another application of the catalyst coating technique. A *"pseudo" in-situ* photo-oxidation of styrene in liquid-phase using NMR spectroscopy was performed and discussed in this chapter. CeO_2 and Co-doped CeO_2 were used as

photocatalysts and molecular oxygen as the oxidant. It was possible to demonstrate in this chapter that the photo-oxidation reaction proceeded according to Langmuir-Hinshelwood model.

The general conclusions of the findings during this work as well as further work are presented in Chapter 9.

Chapter 2: Instrumentation

Different nanostructured materials were prepared in this work according literature reports with modifications. The key instruments utilised in the characterisation of the materials are discussed in this chapter. Powder X-ray diffraction (XRD) was used to study the crystal structures as well as crystal orientation of the materials. Scanning electron microscope (SEM) was used for the study of the morphology of the created materials while their composition was analysed by energy dispersive X-rays spectroscopy (EDX). UV-visible spectrophotometer was employed for the study of the optical properties of the materials while their surface area analysis was performed using Brunauer–Emmett–Teller (BET) analysis.

The products of reaction in this work were analysed using Fourier Transform Infrared Spectroscopy (FTIR), which provided information based on the absorption of infrared light that caused excitation of vibrations of bonds of molecules. Gas chromatography mass spectrometry (GCMS) was also used for separation and detection of reaction products by ionisation of the products as they elute the GC column and the separation of the ions according to their mass-to-charge (m/z) ratio. Finally, Nuclear magnetic resonance (NMR) was used to determine the molecular structure of products of liquid-phase epoxidation reactions.

Here, I will discuss about the principle and application of each instruments used in this project.

2.1 Powder x-ray diffraction

X-ray diffractometer is an essential instrument for identification of crystal structure and orientation of nanomaterials. The technique utilised by this instrument are subject to interference of waves reflected from periodic rearrangement of atoms constituting the crystals. The atoms on the lattice partially refract the X-rays that strike the surface of a crystal structure. As a result, diffraction of waves at certain angles occurs due to constructive or destructive interference.[221] Constructive interference occurs at angle formed by the distance between the crystal planes of the lattice and the wavelength of the X-ray according to Bragg's law:

$$n\lambda = 2dsin\theta \qquad (2.1)$$

Where n denotes an integer number as the diffraction order, λ denotes the wavelength of the x-ray (given by CuK_{α} = 1.54056Å), d denotes the distance between the planes in the atomic lattice and θ denotes the angle of incidence x-ray.
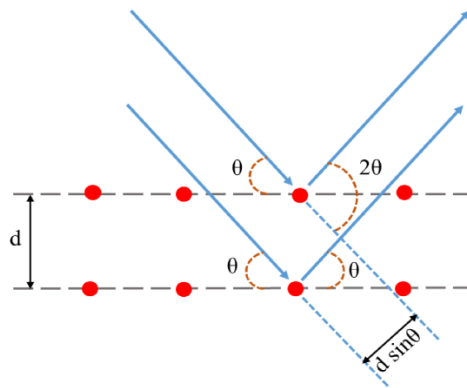
Figure 2.1: A schematic diagram illustrates of Bragg's law.

Figure 2.1 shows a schematic illustration of the diffraction geometry according to Bragg's law. The interaction of x-rays with the atomic planes of crystal can be seen. The emission of the diffracted x-rays at the same angle θ where the incident beam strikes the sample can also be seen in Figure 2.1. As such, in relation to the incident beam, the x-rays are diffracted by an angle value of 2θ. This arrangement is commonly referred to as Bragg-Brentano geometry.

Constructive interference pattern can be built by irradiation of a crystal on all its faces. However, different materials have different crystal structures and so will produce a mixed XRD pattern. The characteristic peaks generated are used for identification of the sample since the peaks positions are determined by the lattice spacing of the sample which is used for calculation of the lattice constants of the nanostructures. Correlating the obtained XRD pattern with the database can also help in identification of the unknown samples. The crystallinity of the sample is typically studied by two different types of XRD: powder and single crystal XRD.

Samples with no known crystalline configuration, and therefore no database entry, can be analysed using both single crystal XRD or powder XRD. However, single crystal XRD is normally more reliable since it involves much more data set. During this technique, all possible orientations of a sample are investigated using a single crystal. Constructive interference spots with 3D orientation are formed in this case from which the base unit cell composing the crystal provides information on the nature as well as the configuration of the studied sample. Due to the time-consuming nature of this technique and the need for large crystals to obtain efficient result, this technique has certain limitation.

Powder XDR on the other hand, is a fast technique compared with the single crystal technique. This technique only studies the diffraction of the incident x-ray along a single axis

of the sample thereby making it much quicker than the single crystal XRD technique. Furthermore, miller indices corresponding to the constructive interferences in a spectrum of a powder XRD can be used for identification of the unknown samples. The miller indices specify directions and planes which could be in lattices or in crystals. The number of indices corresponds to dimension of the lattice or crystal.

In addition, information on the crystallinity of a sample can be obtained by studying the broadness of a diffraction peak. The broadness can be caused by the presence of impurities in the crystalline structure of the sample which leads to distortions in the lattice separation. As a result, the distortions can cause the constructive interference to occur at a slightly different value of θ, resulting in broad diffraction peaks in the XRD pattern. Therefore, sample materials with poor crystals display broad peaks while those with high crystals yield narrow peaks.

The crystal grain size is directly correlated to the XRD peak width. The smaller the width of a peak, the larger its crystal size. The relationship between the peak width and its crystallite size is given by Debye-Scherrer, popularly known as the Scherrer's Equation[76] and is expressed below:

$$D = \frac{K\lambda}{\beta \cos\theta} \qquad\qquad (2.2)$$

where D denotes the size of crystalline domain, K is the shape factor of the sample's crystal lattice (raging between 0.62 and 2.08), λ is the wavelength of the incident x-ray (Cu plate, $\lambda = 1.541$ Å), θ is the Bragg angle of the diffraction peak and β is the full width at half

maximum (FWHM), in radians, of the diffraction peak in consideration of instrument broadening.

In this work, all of the synthesised photo-catalysts were in powder form. All samples were analysed using powder XRD technique in $\theta/2\theta$ mode, on a Siemens Powder D500 diffractometer equipped with Cu X-ray source at the wavelength of 1.541 Å.

2.2 Scanning electron microscopy

The scanning electron microscope is one of the most important instruments used for the visualization of nanostructured materials. It provides information on the morphology of synthesised material. SEM share similarities with optical microscopy (OM) in terms of operation. However, a much higher resolution can be obtained with SEM compared to OM. Unlike OM that uses photon for imaging, SEM uses high energy beam of electrons that interact with atoms of sample. The signals generated due to this interaction are characteristic of the sample's surface composition as well as topography. During this work, tungsten filament was used through thermionic emission to generate high energy electrons accelerated between energy range of 10 and 30 kV under high vacuum condition (10^{-6} to 10^{-10} torr).
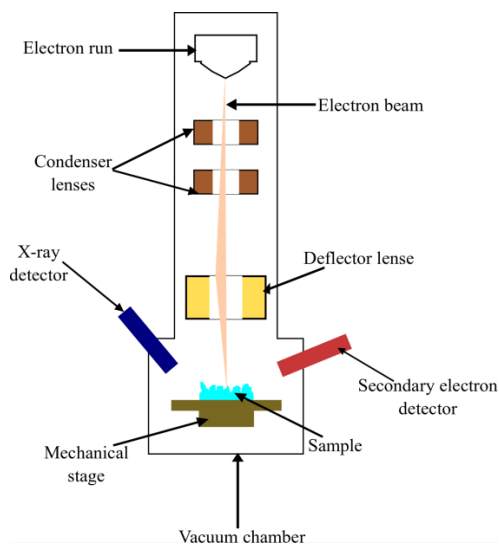
Figure 2.2: Schematic of the scanning electron microscope revealing the main components

The structure of a typical SEM is shown in Figure 2.2. The highly energetic electron beam is finely focused as it passes through a series of electrostatic (condenser) and electromagnetic (deflector) lenses before contacting the sample. The point of contact of the beam on the sample can be controlled by either coarsely adjusting the mechanical stage which holds the sample or by finely shifting the potential on the deflector lens. Upon collision of the electrons on the sample surface, two types of interactions can occur. The interaction of electron that occurs through elastic scattering produces electrons called backscattered electrons. These electrons are reflected from the sample and move in the backward direction, hence, the back scattered electron detectors are positioned almost vertically from the sample stage to maximise detection of these electrons. The intensity of the back scattered electrons is determined by the mass of the atoms in the sample. Heavier elements reflect more electrons. Thus it forms good contrast between heavy (such as metals) and light elements (such as C, N and O). Therefore, it is used to identify metal elements in organic materials,

typical required in forensic analysis. However, back scattered electrons have the high kinetic energy as the incident bean. At higher energy, electrons have large interaction profile as they have large mean free path. Hence the back scattered electrons have large interaction profile as they have large mean free path. Therefore, the back scattered electrons only produce low resolution images. This is one of the reasons why most SEM machines are not equipped with the backscattered electron detectors.

Secondary electron detection is the second form of detection in an SEM. When the incident beam (primary electrons) bombards the surface of the sample, the core electrons on the surface of the atoms of the sample are emitted, leaving a hole at the core level. Upper level electrons will relax and fill this hole which emits energy in the form of X-Ray, determined by the energy difference between the upper level and the involved core level. Such X-ray can excite an upper level electron, which has much lower kinetic energy. The process is called Auger process and the emitted electron is called Auger electron, or the secondary electron, since they were excited through a secondary excitation process. Due to the low energy of the secondary electrons (1-300 eV) they can be easily deflected by applying potential difference. This allows flexibility in positioning the detector that can avoid the back scattered electrons with lower resolution. Typically, the secondary electron detector is mounted horizontally, perpendicular to the back scattering electron detector. Low energy electrons have short mean free path, so the secondary electrons are originated from very small interaction profile. Hence, secondary electrons produce high resolution images. Unlike backscattered electrons that penetrate deep into the sample due to their high energy, typical secondary electrons only shallowly penetrate the sample approximately 10 nm deep.

2.3 Energy dispersive x-ray spectroscopy

SEM instrument can also provide information on the elemental composition of the samples if equipped with an energy dispersive x-ray energy (EDX) detector. This technique adopts the use of x-ray fluorescence. As I have mentioned before, X-ray is emitted during the electron scattering process and the energy of such X-ray is specific to individual element. As such, every individual constituent element of the sample can be identified. It is also possible to obtain quantitative information from EDX using the relative intensity of the X-ray. As a result, the element distribution can be analysed by the technique of element mapping.

During this work, SEM analysis was performed to investigate both the morphology and elemental composition of the nanostructured synthesized materials in Chapters 4 to 7. A Jeol-JSM 820 Scanning Microscope equipped with a cryogenically cooled EDX detector was used for all SEM analyses.

2.4 Diffuse reflectance spectroscopy

One of the desired properties of materials that is essential for generation of charge carriers is the size of its band gap. This property can be measured through a variety of analytical techniques, one of which is the diffuse reflectance spectroscopy. This method was used in this work to study the band gap of the synthesised material.

The conventional technique used in determining the band gap of a material is through ultraviolet-visible (UV-Vis) absorption/transmission spectroscopy. This technique involves monitoring the wavelengths of light absorbed by a given sample. As a result, the minimal

energy required for the photonic excitation of the sample can be determined and presented in form of a spectral pattern.

The technique first developed by Jan Tauc in 1968 is widely used to determine the band gap of a material by applying Tauc's mathematical model which correlates the absorption coefficient of a material and its band gap energy, E_g (Equation 2.3):

$$\alpha h v = A\left(h v - E_g\right)^n \qquad (2.3)$$

where α denotes the absorption coefficient of a sample, $h v$ denotes the energy of incident light, A denotes a proportionality constant of the studied material and n is a constant whose value depends on the studied electronic transition. n has a value of 1/2 and 2 for direct and indirect electronic transitions, respectively.[222]

When Equation (2.3) is applied, the band gap energy of a material can be determined from its UV-vis spectrum by plotting a graph known as Tauc plot. A linear section of the obtained curve of $(\alpha h v)^2$ plotted as a function of $h v$, corresponds to the absorption of the sample. Extrapolating this linear region to the abscissa gives the optical band gap of the studied material.

However, the traditional UV-Vis spectrometry is limited in application as it is only suitable for measuring absorption spectrum of gaseous, liquid, and thin film solid samples. This is so because the absorption spectrum of a sample (and consequently its absorption coefficient) is obtained by monitoring the wavelengths of light transmitted directly through the sample. Therefore, the development of an alternative technique suitable for analysing the band gaps of powders, bulk materials and thick films became necessary, since the light

transmitted through these materials is too weak to measure. Kumar et al. in 1999 determined the band gap of thick films through reflectance UV-vis spectroscopy successfully.[223] This alternative technique involves monitoring the wavelengths of light absorbed by a material through the by analysis of the diffuse reflection of a beam of light from the surface of the material sample. Typically, irradiating light onto a material results in two types of reflection: specular reflection and diffuse reflection. In the case of the former, light incident on a smooth surface directly reflects in a single direction. This type of reflection is limited if the studied materials have uneven surfaces where specular reflection occurs only in small quantities. Unreflected light is either refracted or undergoes internal reflection where it suffers loss of intensity through continuous scattering or emission back into air.

It is the emission of unreflected light that give rise to the second type of reflection, the diffuse reflection. Here, the emitted light moves in several of directions, hence the name diffuse reflection. UV-vis absorption of a material can be determined by monitoring its diffuse reflectance spectrum since the diffusely reflected light will have lost intensity relative to the light absorption properties of the studied material. Using the Kumar et $al.$[223] model (Equation (2.4)), the absorption coefficient of a thin film sample can easily be determined from its diffuse reflectance spectra as follows:

$$2\alpha_\lambda t = \ln(\frac{R_{max}-R_{min}}{R_\lambda-R_{min}})\qquad(2.4)$$

where α_λ denotes the absorption coefficient of the material under study at a given wavelength, t denotes the thickness of the material, R_{max} and R_{min} denote the maximum and minimum

observed reflectance intensity in the spectrum, respectively and R_λ is the reflectance intensity at a given wavelength.[223]

A Tauc plot can be generated by combining Equations 2.3 and 2.4, which can be used to determine the band gap of a sample from its diffuse reflectance.

The intensity of the diffused light might not only be affected by light absorption, but also by the sample morphology, texture, shape and size. In order minimize such sample effects and to maximize light reflection, absorption and diffusion, an integrating sphere is used. Its advantage is that, it can converge the diffuse reflections from across all directions and form a single strong signal that can be detected spectroscopically. The basic principle of operation of an integrating sphere is illustrated in Figure 2.4. It can be seen that to measure the diffuse reflectance of a given sample using this instrument, light is irradiated onto the sample under study through an aperture in the integrating sphere.
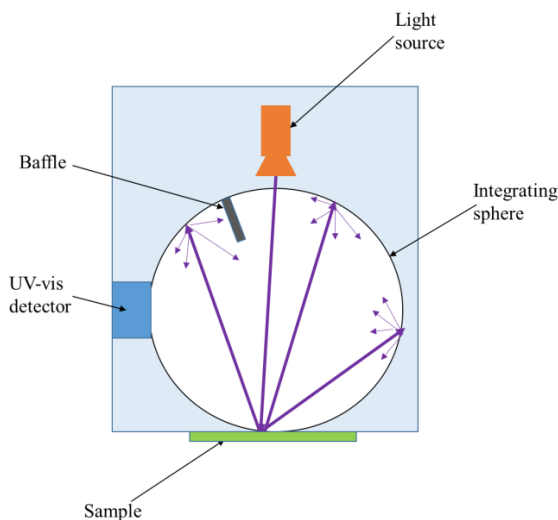
Figure 2.3: Schematic of the operation of an integrating sphere for the measurement of diffuse reflectance of a sample.

When the light beam strikes the sample, it undergoes diffuse reflection, scattering in all directions until collision with the walls of the integrating sphere occur. Further scattering occurs at walls of the integrating sphere owing to the white diffuse reflecting coating of the integrating sphere. As no energy is lost during collision with the walls of the sphere, the concentration of the diffusely reflected light within the sphere is increased and the detector can detect it. Once detected, a spectrum of the diffuse reflectance of the sample, which corresponds to the wavelength of the incident light is produced. A baffle is positioned between the light source and the detector to protect the latter from being 'blinded' by the former.

In this work, diffuse reflectance spectroscopy was used to determine the band gap of the materials synthesised. An Ocean Optics ISP-REF integrating sphere equipped with an inbuilt tungsten-halogen illumination source ($300 \text{ nm} \leq \lambda \leq 1000 \text{ nm}$).

2.5 Fourier transform infrared spectroscopy (FTIR)

FTIR spectroscopy is another technique that shares similarities with UV-Vis spectroscopy. Like UV-vis, IR spectroscopy involves the study of the energies absorbed by materials over a specific wavelength range. FTIR spectroscopy measures the absorption capacities of molecules in the IR region of the electromagnetic spectrum between 2 and 25 µm. The photon energy is much smaller in comparison to UV-vis. The low energy photon is absorbed by molecules. As a result, an excitation in vibrational energy levels within the same electronic state occurs. FTIR can be used obtain preliminary information about the structure of molecules. Such information includes the functional groups and their positions in the molecule or the adsorbed structures of the molecular species. Furthermore, FTIR can

be used to analyse materials in different states (gas, solid, and liquid samples), and can be operated at room and pressure.

Figure 2.4 shows a schematic illustration of an FTIR spectrometer. It can be seen that the instrument is made up of mobile and stationery optical parts. The presence of limited mobile parts seen in the Michelson interferometer in the instrument is perhaps one of the many practical advantages of FTIR.
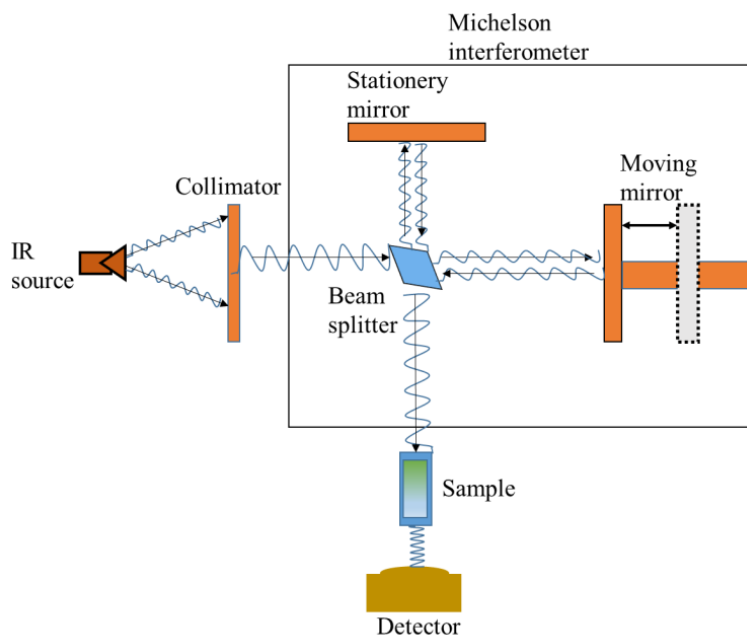
Figure 2.4: Schematic of the principal components of FTIR spectrometer showing the path of a single IR wavelength.

The operation of FTIR spectrometer begins irradiation of infrared from its source heated at 1200 K. The source which is a filament usually made of silicon carbide, emits a full spectrum of IR radiation at this temperature. The emitted radiation is then collimated to minimize spreading of the radiation as it propagates through the spectrometer. After collimation, the IR radiation then enters the Michelson interferometer to carry out oscillating modulation, which is equivalent to the mechanical Fourier transformation. Once in the

interferometer, the radiation comes in contact with the beam splitter which splits into two equal parts. One part is channeled toward the stationery mirror where it is reflected back to the splitter. The other beam part is channeled toward the mobile mirror and also reflected to the splitter. The two reflected beams now at the splitter, are combined to form a single beam which is then directed out of the interferometer.

The path length traversed by the IR radiation is controlled by the mobile mirror which produces a difference in path length known as the optical path difference (OPD). It is this OPD that causes the beam coming from the mobile mirror to undergo constructive and destructive interferences as it meets the beam coming from the stationery mirror. The difference in wavelengths of the combined beams exiting the interferometer results in a display of different maxima at different OPDs, which corresponds to the constructive interference of specific wavelengths. This makes it possible for the interferometer to isolate each wavelength.

The combined beam from the interferometer is channeled toward the sample and passes through. Different design of sample holders can be used according to the state of the sample. Attenuated total reflectance (ATR) is often used for solid and liquid samples, where the sample is placed on a sample plate and pressure applied to it with the help of a pressure lever. This allows the IR reflected through the surface of the sample, which carries the information about absorption. However, in the case of gaseous samples, as in this work, a cylindrical cell of known path length with NaCl, CaF_2 or KBr windows is used. The gas sample is placed in the cell, which is placed within the IR radiation path. The cell can be modified in a continuous gas flow system, with inlet and outlet ports for the gas flow. After passing through and interacting with the sample, the intensity of residual IR beam is measured by the detector and an interferogram is generated. The generated interferogram is difficult to interpret in it its

raw form. As such, a mathematical model called Inverse Fourier Transform is applied to generate a plot of IR spectral absorbance or transmittance versus the beam frequency. The frequency is inversely proportional to wavelength. Generally, IR spectrum is made of a plot of absorbance versus the number of waves per cm, which is also referred to as wavenumber and has a unit of cm^{-1}.

In order to determine the IR absorbance energy of a sample, a background run is made without a sample and the obtained spectrum is compared with that of the sample. To achieve this, the instrument subtracts the spectrum of the blank sample from that of a real sample. Different molecules exhibit different vibrations, hence the IR spectrum of a given sample is a fingerprint of that molecule.

Quantitative data can also be obtained from FTIR spectra. This is achieved by applying the Beer-Lambert law, Equation 2.5, which provides the correlation between the absorbance of the FTIR spectral peaks and the concentration of the sample as follows:[224]

$$A = Ecl \qquad (2.5)$$

where A denotes the absorbance of a given peak in the IR spectrum, E denotes the molar absorptivity of the molecule, c denotes concentration of the sample and l denotes the path length of the IR beam through the sample.

The unknown concentrations of samples can also be determined by calibrating the FTIR peak areas of known concentrations of a given sample.

For alkene samples, various modes of vibration are introduced into the hydrocarbon. These are: C=C stretching vibration, C-H stretching vibration where the carbon atom in the alkene linkage is present also in in-plane and out-of-plane bending of the alkene C=C bond.

In linear unconjugated alkenes, the C=C stretching mode is usually a moderate to weak absorption at 1667-1640 cm^{-1}. In the case of cycloalkenes, the C=C stretch vibration is coupled with the C-C stretching of the adjacent bonds. From Figure 2.5, as the bond angle, α, decreases the interaction becomes influenced. In cyclobutene for instance, the interaction becomes smaller until at a minimum of 90°, whereas in cyclopropane, the interaction increases thus, increasing the absorption frequency.
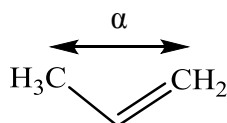
Figure 2.5: C=C and C-C stretch vibration coupling

In this work, FTIR spectroscopy was utilized to analyse gas streams in Chapters 3 to 7. A Perkin Elmer SpectrumOne FTIR spectrometer with a gas phase IR cell equipped with NaCl windows was used to collect IR spectra.

2.6 Gas chromatography-mass spectrometry (GC-MS)

2.6.1 Gas chromatography

One of the ways of investigating the photoactivities of the synthesized catalysts is by monitoring their effectiveness in a reaction. During such reactions, the concentration of all reacting species can be monitored before, during and after reaction. Most often, the chemical reactions contain a variety of substances mixed together that need separation in order to identify and quantify them. Gas chromatography (GC) is one of the most popular instruments used for both qualitative and quantitative analyses of complex chemical mixtures. The technique was first developed by A.T. James and A.J.P. Martin in 1952. Ever

since, GC has gained wide acceptance as an essential tool for analytical chemistry.[225]

In GC, two phases are involved in the separation of compounds or mixtures: the mobile phase and the stationery phase. Upon injection of the sample through the injector port, a carrier gas (usually He, H_2 or N_2) carries the sample through the mobile phase. The mobile phase containing the sample is passed over a stationary phase and then interact with it. They then proceed at different speed, based on the volatility of individual compound and more importantly based on the interaction with the stationary phase. Thus, an effective separation of the different chemicals in the mixture occurs.

The basic components of a GC are shown in Figure 2.6. It comprises a carrier gas source, an injector, through which the sample is admitted into the instrument, a column (housed in an oven) where the separation takes place and a detector. As the carrier gas flows through the GC, a small quantity of sample ($\sim$0.01 - 100 μL for liquids and $\sim$100 μL for gases) is introduced into the system through an injection port. The vaporization of the sample begins in the injector which is maintained at high temperatures.

The vaporized sample is carried into the column by the carrier gas through a split or splitless injection (depending on the concentration of the sample). This allows for the introduction of a controlled fraction of the sample (liquid or gas) into the system while the excess is purged through a separate port (vent) by the carrier gas.
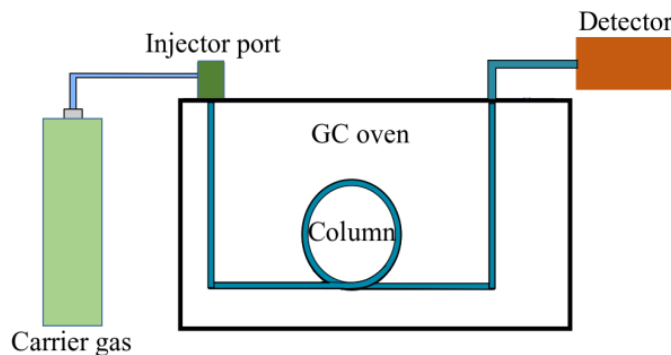
Figure 2.6: Schematic of the basic components of a gas chromatograph.

Once in the column, the sample begins to interact with the stationary phase of the column. GC column is usually made of fused silica (but could be made from other materials), which consists of a stationary phase in form of a liquid coating on the inside of the column. Through adsorption and desorption of the sample within the column, the different chemicals in the sample are separated at different rates. As such, the separated sample components elute the GC column at different times. This time is referred to as the retention time and is usually expressed in minutes (depending on the operating conditions of the GC). The retention times of the sample components and their extent of separation from each other are determined by several factors. These factors include the nature of the stationary phase, the temperature of the GC oven which houses the column and the flow rate of the carrier gas.

Increasing the temperature during GC analysis can reduce the retention time as a result of lowering the rate of adsorption of the sample components onto the stationery phase. So the overall detection time is reduced while the peak resolution is also reduced with certain distortion in the peak shape. Similarly, at low temperature, retention times are longer and

peak resolution could be better. Inconsistencies in the oven temperature can result in some chemical components eluting the column at similar time since their level of interaction with the stationery phase can be affected by temperature differences. In this type of situation, an inefficient separation is obtained. This is the GC oven becomes highly significant as it allows for total control of the column temperature leading to a well separated sample composition. Another factor that affects the retention times of sample components is the nature of the stationary phase within the column. Different compounds interact with the stationery phase in a different way owing to the differences in their properties due to their functional groups. Non-polar molecules will preferentially adsorb on a non-polar stationery phase, and the same applies to a polar molecule as it will be preferentially adsorbed on a polar stationery phase. This means that the choice of column is made based on the nature of the sample in order to achieve an efficient sample separation on a GC machine.

All separated sample components that elute the column are detected by a detector, which is positioned at the other end of the column. GC machine can be equipped with several types of detectors, the choice of which depends on the species to be analysed. During this work, only mass spectrometry (MS) detection method was used.

2.6.2 Mass spectrometry

Mass spectrometer is extensively used in both qualitative and quantitative analyses of organic compounds. This is simply because MS provides a great deal of information about a molecule in comparison to other GC detectors such as the flame ionization detector, (FID). FID is the basic detection method, but it can only measure the concentrations and cannot directly identify the chemical species. So it is used in well-defined chemical systems with known chemical components. The peak retention time can simply be estimated from

standard parameters. Also, FID has limited dynamic detection range defined by the resolution output voltage signal from 1mV to 1000 mV.

Although MS is expensive, it remains a useful tool for identification of chemical species. It measures the mass of the molecule together with its ionisation fragments. It has significantly large detention range starting from several hundred counts, determined by the noise level to millions of counts. Hence, it allows the measurement from very low concentration to very high concentration.

The basic structure of a typical ion trap MS is shown in Figure 2.7. There are several designs available, but all MS machines have three main components. These are: the ion source, where molecules are ionized, the mass selector and the detector.
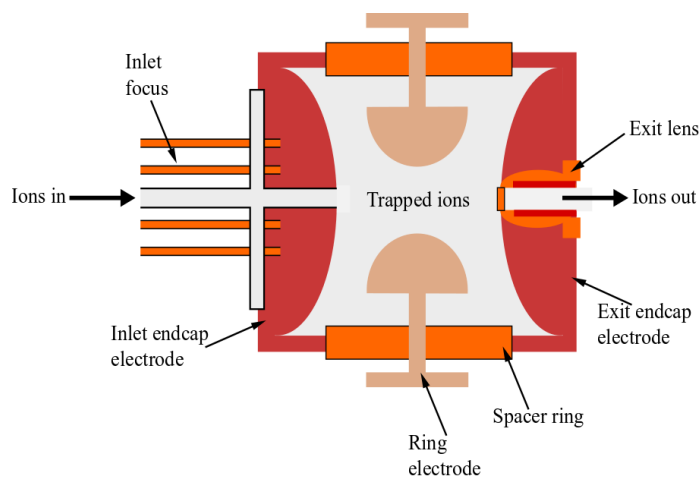
Figure 2.7: Schematic diagram of an ion trap used in GC-MS

Its operation involves ionizing the eluents of GC and separating their ions with respect to their mass-to-charge ratio. One of the ionization techniques used in MS is electron ionization (EI). This technique has gained popularity as an ion source in GC-MS due to its high efficiency and high reliability. GC column eluates are introduced into MS through a

transfer line, and are bombarded with high-energy electrons in the ionization chamber to become ionised. Both the transfer line and the ion source in GC-MS are usually maintained at high temperatures between 250 and 300℃, to prevent condensation of the GC eluates. The high-energy electrons are generated through thermionic emission of a heated filament. The molecules are fragmented into smaller species due to the high energy of the electron beam. Depending on the instrument nature, ions are either formed within or injected into the ion trap assembly from an external source. The trapped ions are then influenced the applied RF potential to perform ion ejection, excitation and mass selective ejection.

The principle of ion transfer under electric and magnetic fields in a vacuum in MS follows the Newton's second law of motion and the Lorentz force law. These laws are expressed mathematically and presented in Equation (2.6) and Equation (2.7) respectively:

$$F = ma \tag{2.6}$$

$$\boldsymbol{F} = q(\boldsymbol{E} + v) \times \boldsymbol{B} \tag{2.7}$$

where F denotes the applied force, q denotes the ion charge, E denotes the influence of the electric field on the ion, a denotes the acceleration of the ion, B denotes the magnetic field and v denotes the ion velocity. Combining Equation (2.6) and Equation (2.7) gives Equation (2.8), which defines the working principle of the mass selector in filtering ions.

$$a\left(\frac{m}{q}\right) = \boldsymbol{E} + v \times \boldsymbol{B} \tag{2.8}$$

Once at the detector, the ions will be collected by a channeltron, a device turning the

ion scattering into electrical pulses. The concentration of the ions is measured from the number of the pulses and correlated to their respective mass-to-charge ratio at a given time. A plot of signal intensity versus the mass-to-charge ratio for a given species, known as a mass spectrum is generated. Due to difference in nature of fragmentation of different species, different mass spectra are generated for different species. By comparison with the mass spectrum database, the unknown chemical species can be identified. The concentration of the unknown can also be determined by measuring the peak area for specific species.

Another important aspect of a MS worthy of mention is its vacuum system. MS instruments only function efficiently when equipped with vacuum pumps. This is important since the average free path of ionic molecules in air is very low. In addition, the ionisation filament would have a very short lifetime if the vacuum is poor. As such, high vacuums (low pressure = high vacuum) are required in MS to ensure the detection of the ions. The presence of a vacuum system in GC-MS contributes to the cost of the instrument as it is often coupled with expensive vacuum pumps such as the turbomolecular pumps.

The molecular ion peak of alkenes is typically distinct due to the double bond location. This can be attributed to the ability of alkenes to produce stronger molecular ion peaks than alkanes as a result of the lower ionization energy of a π electron than a σ electron. Double bonds can easily migrate upon ionization, which makes it almost impossible to determine isomers. For acyclic alkenes, it is especially difficult, as the double bond tends to migrate during fragmentation. It is easier in the case of cyclic alkenes since the location of the double bond is readily evident due to presence of strong tendency to undergo allylic cleavage without necessarily suffering any double bond migration. Double bond can also be fixed in a position through conjugation with a carbonyl group.

Acyclic alkenes are known to form clusters of peaks at 14 units interval, in which the

C_nH_{2n-1} and C_nH_{2n} peaks have higher intensities than those of C_nH_{2n+1}.[225]

In this work GC-MS was used extensively to monitor the photo-oxidation products over various catalysts in gas flow reactors, as discussed in Chapters 5 to 8. A Varian gas chromatograph, CP 3800 equipped Saturn 2000 mass spectrometer was used. The GC was equipped with two different columns to achieve separation of products. In Chapter 5, a PLOT column, Rt-QS-BOND 30 m x 0.53 mmID x 20 µm was used. The MS (detector) end of this column was coupled with 25 cm of a 0.25 mmID x 0.25 µmdf column using a RESTEK siltite micro union to trap the particles coated within the PLOT column and prevent contaminating the MS trap assembly. A Restek RXI-5ms column 30 m x0.25 mmID x 0.25 µmdf was used in Chapters 6 and 7. Helium was used as a carrier gas. Samples were injected into the GC columnusing an automated split injection with a split ratio of 100, an injection volume of 0.2 µl and an injector temperature of 250℃. MS was performed by EI in combination with a quadrupole mass selector. The MS scanned the mass region between 40 and 300 m/z (amu/e) for a total of 22 minutes with a 0.5 minute solvent delay.

2.7 Proton nuclear magnetic resonance

Nuclear magnetic resonance (NMR) is another important analytical tool for identification of organic compounds. It is useful for quality control as well as research for determination of the chemical content, purity and molecular structure of a given sample. Like IR or UV, it operates under the principle of absorption of electromagnetic wave. As illustrated in Figure 2.8, a sample can absorb electromagnetic radiation in the radio frequency (rf) region, under appropriate conditions in a magnetic field. The absorbed electromagnetic radiation is characteristic to the sample.

Powerful electromagnet
or superconducting magnet

Radio frequency
input oscillator

Sample tube

Radio frequency
output receiver/detector
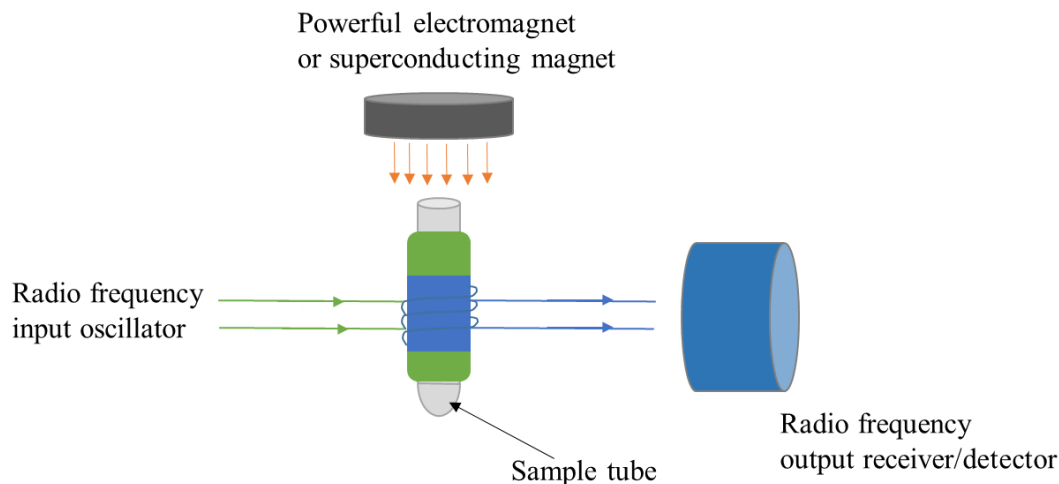
Figure 2.8: Illustration of Fourier Transform NMR showing direction of magnetic field perpendicular to rf

However, absorption is a function of certain nuclei within the molecule of a sample. All nuclei are known to be charge carriers, which causes them to spin on the nuclear axis resulting in the generation of a magnetic dipole moment along the axis. The angular momentum of the spinning charge is often described in terms of quantum numbers, I, which have values expressed in increment of ½ (i.e 0, 1/2, 1, 3/2…). When I is zero it indicates no spin occurs. The generated dipole has an intrinsic magnitude, which is expressed in terms of nuclear magnetic moment, μ. The atomic mass and atomic number can be used to determine the spin number, I. As such, it is easy to obtain the spectra of some nuclei such as $^{1}_{1}H, ^{3}_{1}H, ^{13}_{6}C, ^{15}_{7}N, ^{19}_{9}F, ^{31}_{15}P$, owing to their ½ spin numbers as well as a uniform spherical charge distribution. Examples of some nuclei and their spin number are displayed on Table 2.1.

Table 2.1: Spin numbers of selected nuclei according to their atomic mass and numbers

Spin number, I	Atomic mass	Atomic number	Example
Half-integer	Odd	Odd/even	$^{1}_{1}H\left(\frac{1}{2}\right)$, $^{17}_{8}O\left(\frac{5}{2}\right)$, $^{15}_{7}N\left(\frac{1}{2}\right)$
Integer	Even	Odd	$^{2}_{1}H(1)$, $^{14}_{7}N(1)$ $^{10}_{5}B(1)$
Zero	Even	Even	$^{12}_{6}C(0)$, $^{16}_{8}O(0)$, $^{34}_{16}S(0)$

However, if the *I* value of a nucleus is equal to or greater than one, the nucleus will have a non-spherical charge distribution. This results in generation of an electrical quadrupole moment that affects the relaxation time. Consequently, broadening of signal peaks and coupling with neighboring nuclei are affected. The orientation of a nucleus in a magnetic field is determined by its spin number, and is expressed as $2I + 1$.

A proton has a spin number ½, which according to Figure 2. 9 represents two energy levels labeled α and β. In the lower energy level, there is a higher proton population (*N*) in accordance with Boltzmann distribution.
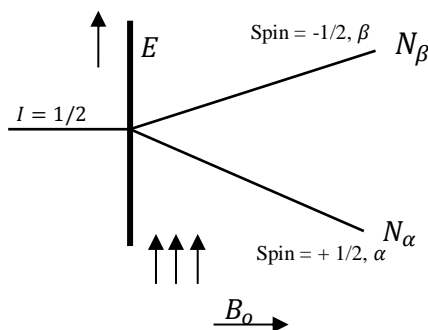
Figure 2.9: Two proton energy levels, from quantum mechanics, in a magnetic field of magnitude B_o. The direction of the magnetic field (↑↑↑) is up, parallel to the ordinate, and Bo increases to the right.

The change in energy between α and β spin states is given by:

$$\Delta E = \frac{h\gamma}{2\pi} B_o \quad (2.9)$$

where h denotes Planck's constant, which as shown Figure 2.9, states that ΔE is directly proportional to the applied magnetic field, $\boldsymbol{B}_0$, since the other parameters are all constants. γ, called the magnetogyric ratio is the proportionality constant between the magnetic moment, μ and the spin number, I and is expressed as:

$$\gamma = \frac{2\pi\mu}{hI} \quad (2.10)$$

Upon establishing two energy levels for the proton, energy in form of rf radiation (υ_1) can be applied in order to initiate transition between the two energy states in a stationary magnetic field of strength, $\boldsymbol{B}_0$. The rf radiation and magnetic field of strength are related as shown in Equation (2.11):

$$\upsilon_1 = \frac{\gamma}{2\pi} \boldsymbol{B}_0 \quad (2.11)$$

Since

$$\Delta E = h\upsilon \quad (2.12)$$

υ_1 is expressed in units of megahertz (MHz). Thus, a frequency of 100 MHz in a magnetic field strength of 2.35 tesla (T) is necessary to bring a proton into a state of resonance. The state of resonance is that in which a proton absorbs energy and transits from lower energy

level, or α spin state to higher energy level, or β spin state. At this point a signal corresponding to this transition is measured and a spectrum is obtained for the nucleus.

Among the various spectra of nuclei commonly used in NMR, the ^{1}H and ^{13}C dominate. In this work, only the proton NMR was studied for the determination of photo-oxidation products of styrene.

2.7.1 Chemical shift

This is the difference in the resonant frequency of a nucleus relative to a reference signal. Under the influence of a magnetic field, electrons are known to circulate around a nucleus, which results in the generation of their own local magnetic field in the opposite direction to the applied field. As such, the nucleus is said to be shielded to a very small extent by its electron cloud. The density of this cloud varies with the chemical environment. The absolute resonant frequency of the transition between energy states depends on the effective magnetic field surrounding the nucleus. The level of electron shielding as well as the chemical environment of nuclei determine the effect of this field on the nuclei. Thus, information on the chemical environment of a nucleus can be obtained from its resonant frequency. However, certain factors such as electronegativity, ring current (also referred to as anisotropy) as well as bond strain associated with a nucleus, can cause a higher resonant frequency.

$$v_{eff} = \frac{\gamma}{2\pi} \boldsymbol{B}_0 (1 - \sigma) \quad (2.13)$$

Equation (2.13) can be used to determine the effective frequency at resonance, v_{eff}, where

σ denotes the shielding constant with value proportional to the degree of shielding. At a given

value of $\boldsymbol{B}_0$, v_{eff} is less than the applied frequency v_1. The degree of shielding depends on

the thickness of the electron cloud circulating the nucleus. The degree of shielding of a proton

of a carbon atom depends on the effect induced by the other group attached to the carbon

atom.

As the chemical shift is the difference in the absorption of a particular proton relative

to that of a reference proton, the choice of reference is important. Tetramethylsilane (TMS)

is traditionally used as the proton reference compound. This is because of the many plausible

advantages that render this compound suitable. Some of the advantages include being

chemically inert, volatile, solubility in most organic solvents and symmetrical (Figure 2.10).

Its protons are more shielded than those of almost all other organic compounds. As a result,

TMS yields a single, sharp and intense absorption peak which has been assigned a chemical

shift of zero.

$$\begin{array}{c} CH_3 \\ | \\ H_3C - Si - CH_3 \\ | \\ CH_3 \end{array}$$
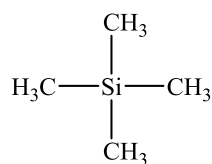
Figure 2.10: Chemical structure of TMS

Deuterated chloroform ($CDCl_3$) is another reference compound, often used as a solvent.

It has a chemical shift of 7.26 and 77 for ^{1}HNMR due to normal chloroform impurity and

^{13}CNMR respectively. Chemical shifts can be expressed in dimensionless units, which does

not depend on the applied frequency using the Equation (2.14):

$$\delta = \frac{(frquency\ of\ signal - frequency\ of\ reference)}{frequency\ of\ spectrometer} \times 10^6 \qquad (2.14)$$

where δ is expressed in units of parts per million (ppm).

The concept of electronegativity is a good guide for determination of chemical shift of a proton. Proximity of a proton to an electronegative substituent provides information on the electron density around the proton. For example, the high electron cloud in TMS renders its protons highly shielded owing to the electropositivity of silicon relative to carbon.

NMR was used in Chapter 8 of this work to analyse reaction products of styrene photo oxidation over CeO_2. This reaction was carried out in liquid phase in order to test the stability of the coating technique.

This Chapter presented an overview of the scientific instrumentations used in this work for characterising nanostructured photocatalysts as well as those for analysing chemical species from the photocatalytic reactions. The design and construction of gas phase photocatalytic reactors will be discussed in the next Chapter.

Chapter 3: Photo reactor design and setup

3.1 Introduction

For a photocatalytic reaction, a simultaneous contact between the reactants, catalyst and light (photons) is necessary. In order to minimise the $e-/h^+$ recombination rate, the catalyst particles must be sufficiently small (tens of nanometres),[187] which renders conventional mechanical filtration ineffective. Certain coupled catalysts such as Fe_3O_4-TiO_2 core-shell however, can be separated from the reaction mixture using magnetic separation. This type of reactor is used for wastewater treatment especially where post-reaction purification can be carried out easily. For gas phase reaction applications, it is possible to monitor reactions spectroscopically as they proceed in situ.[187–191] However, the catalysts have to be immobilised in order to achieve homogeneous illumination. Meanwhile, the supporting medium needs to be transparent to avoid light absorption and blocking by the solid substrates. The chemical reactants and products can be effectively separated from the immobilised catalysts which is essential for a flow reactor.

Several types of photo-reactors have been created and used in the literature. Some of which include closed static reactors for gaseous reactants and solid catalyst which is either used as a free powder or immobilised on some supports such as quartz,[226] wool,[180] mesh[227] etc. However, the light illumination in such photoreactors is less homogeneous. In order to overcome this problem, photo-reactors with powdered catalyst suspended in a suitable solvent to form a slurry or (usually) coated on the walls of reactor tube have been developed.[228,229] In such situations, the light illumination is improved, but the contact between the gaseous reactants and catalysts is significantly reduced.

Photoreactions have also been reportedly performed in a continuous flow system in which the catalyst is immobilised on several materials such as glass rods, mesh, sponge, silica gel, activated carbon and a lot more. To maximise the contact between reactants and catalysts without sacrificing the light illumination.

Since the concentration of gaseous pollutants are typically low (in order of 10^{-9} M)[192,193] diffusion-limitations of reactions,[194] are not an issue for most domestic applications. Interestingly, using an adsorbent catalyst support can improve the performance of the photoreactor as the adsorbent support can increase the concentration of substrate near the catalyst relative to the gas-phase. This acts as a storage for the reactants that can diffuse to available active sites on catalyst while preventing the escape of reaction intermediates and driving the reaction to completion. This suggests that choice of support can influence the rates of adsorption, surface diffusion as well as desorption.

For a functional flow reactor, immobilisation of catalyst is required. There are several advantages associated with this procedure. The main advantage is that the catalyst/product separation problem can be circumvented. Different ratios of products could be obtained by simply tuning the flow rate/contact time and it is possible to operate continuously. This type of reactors can be considered suitable for industrial applications for both liquid and gaseous samples. Nevertheless, in gas-phase systems, catalyst/substrate contact area is reduced which is a drawback, although the light illumination is maximised. Loss of catalyst and deactivation due to accumulation of less reactive intermediates are also possible issues.[186,107]

3.2 Catalyst support

Different supports have been reportedly used from different applications. Some of the popular ones include wire mesh,[186,55,230]fibres,[82] Raschig rings (pieces of tube of similar length and diameter used as a packed bed in columns),[186,231]silica gel[231,232]and glass beads.[233] The first two have been applauded for providing adequate contact area, but are limited in application as they must be designed specifically to fit appropriately-sized reactors. They also suffer from low UV/Vis transmittance in comparison with glass supports. These drawbacks render there supports less efficient. The latter three supports are more advantageous as they exist as several separate aggregates which are more convenient to transport, store, transfer as well as re-use. They are also more flexible in terms of reactor shape/size. Using glass as support tend to increase the radiation path length leading to improved contact with the catalyst and therefore improved quantum efficiency.[234]

Before finally settling for the choice of glass beads as the appropriate support for this work, a computational simulation was considered. Using Flowsquare Flow Dynamic Simulation Software, 2D flow dynamic simulations were carried out, taking into account the experimental gas flow rate and temperatures. In comparison to use of glass rods as catalyst support. Although the gas flow is much more effective for the glass rod system, the gas molecules will not have sufficient contact with the catalyst. This can be seen in the cross-sectional image of gas flow simulation in Figure 3.1, which leads to generation of a laminar flow around the surface of the glass rods. The flow velocity is reduced at the glass rod interface, which means that only limited number of molecules of the gaseous substrate actually come in contact with the catalyst (Figure 3.1A).
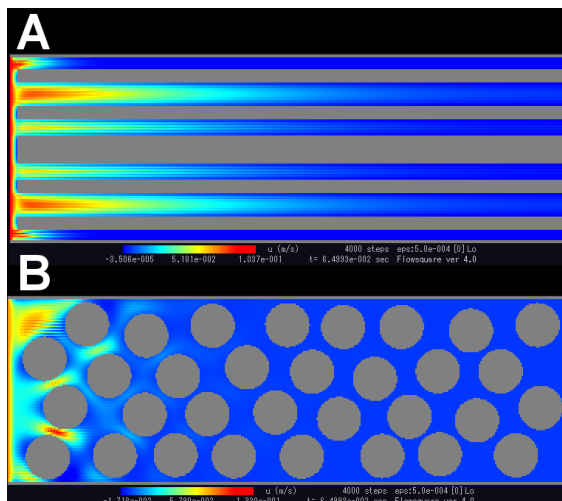
Figure 3.1: Flow dynamic simulations results showing the velocity of the gas flow. The 2D cross-sections of the photo-reactors over (A) glass rods (250 mm long and diameter of 0.5-2 mm) and (B) glass beads (diameter of 1-1.5 mm), both coated with TiO_2 catalysts are shown.

However, in a spherical system, a turbulent flow is observed when gases meet the catalyst. As shown in Figure 3.1B non-preferential flow paths are taken by the gases while maintaining a homogeneous velocity throughout the cross section of the entire reactor. The close packed coated glass beads form the hexagonal arrangement which force the gas molecule moving between the gaps. The size of the spheres determines the volume of space between the spheres. For large spheres, the flow is fast and the contact duration is short. For small spheres, the contact duration can be significantly increased. In this way it is possible to achieve a greater contact between the gases and the catalyst considering that the velocity at the surface of the catalyst is closely like that of the bulk of gas. In their calculations, Patil and Lidbury[235] observed a turbulent flow pattern when they investigated fluid flows in a randomly packed porous reactor beds. This is consistent with the observation made in this work which is particularly important for the epoxidation of alkenes as it provides a good contact between all the reacting species.

3.3 Catalyst immobilisation

In order to achieve high analytical simplicity as well as industrial relevance, a flow-type reactor for gas-phase photoreaction was developed and used in this work. To achieve this, immobilisation of catalyst was necessary. There are several methods for this in the literature, most of which involve immobilising pre-synthesised catalyst in powdered form. It involves making a suspension/slurry of the powdered catalyst followed by dipping[226,236,237] or spraying[230,238] on to the support. Often the suspension is an aqueous,[230,119] or organic solvent.[239] To improve the dispersion of particles, use of surfactants as well as sonication have been reported.[240] There has also been report of catalyst and certain supports synthesised simultaneously.[241] Dip coating was considered unsuitable for the glass beads support used in this work due to the difficulty to achieve uniform coating. As established in our group, when removing the glass beads from the suspension, the solvent tends to dislodge the catalyst to the bottom of the beads leaving the top with less amount of catalyst. If a thick suspension is used, it could be difficult to achieve thin layer coating. This can create a barrier for achieving a sufficient catalyst/light contact. Moreover, the adherence of the catalyst on the glass beads support may be weak, making it difficult to handle.

It has been reported that in the presence of surface OH group on glass surfaces, catalyst tend to bind more stronger.[236,242] Pre-treatment of the glass support with NaOH can lead to an increase in density of the OH group on the support.[192] The adherence stability can also be enhanced by using organic coupling agents in the surface treatment which is then followed by a calcination at high temperature.[196,243] However, the drawback with this procedure is that at high temperature catalyst may suffer a change in phase and it is likely that transference of ion between catalyst and support may occur.[240] Light transmittance can also be inhibited if the catalyst is loaded in excess leading to a reduced efficiency.[244,245]

As it has already been established that dip-coating method of immobilizing catalysts has a number of drawbacks hence, less efficient, a new and reliable *Gyratory-Induced Adhesive Coating (GIAC)* technique was used throughout this work since the glass beads (soda-lime glass beads; 1.0-1.5mm diameter, Glass Sphere S.R.O) offer the advantages mentioned above. Prior to pre-treatment, the glass beads were washed with acetone (Fisher Scientific) and then refluxed for 2 hours in 6M NaOH (Fisher Scientific). The glass beads were rinsed with deionised water until the washings were neutral, then rinsed with ethanol and allowed to dry in air. This was followed by weighing to account for any loss in mass that could have resulted from the base treatment. The glass beads were then left in a rotating drum overnight with appropriate amounts of catalyst (TiO_2) to give loadings of 1-7 $mg_{catalyst}/g_{beads}$, followed by a second weighing to check the catalyst loading.

The success of this novel catalyst immobilization technique can be seen on the Scanning Electron Micrograph (SEM) images in Figure 3.2. A stable, well-dispersed and controllable catalyst loading was achieved. The 1 mg/g coating was the most homogeneous among the various catalyst loading amounts studied. An increase in size of the aggregates of the catalyst as loading amount was increased was observed under SEM (Figure 3.2). A noticeably denser coating was also observed because of the base treatment initially carried out on the glass beads (Figure 3.3). It can be physically observed that the base treatment influenced adherence of the catalyst on to the glass beads due to increased OH density as mentioned earlier.
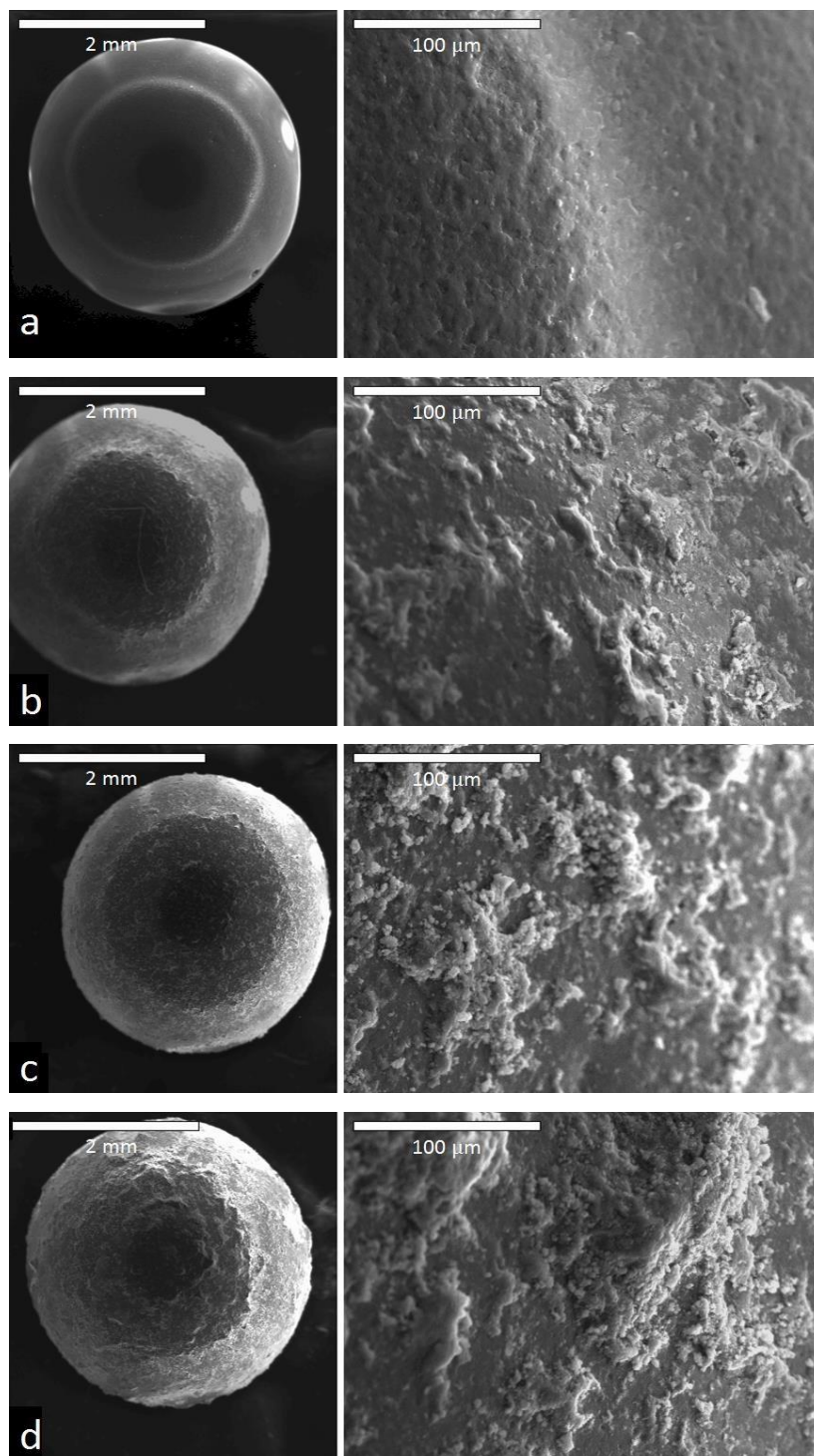
Figure 3.2: Glass beads coated using the GIAC method as observed under SEM.
(a) 1 mg/g; (b) 3 mg/g; (c) 5 mg/g; (d) 7 mg/g

Figure 3.3: Comparison of the coating density (0.3 mg/g) with and without prior base treatment. Left to right: uncoated bead, bead coated without prior base treatment, bead coated with the standard GIAC method.

Only a negligible amount of the catalyst was left in the GIAC apparatus after performing coatings of up to 5 mg/g suggesting that an excellent adherence stability was achieved. Above this coating amount, significant amount of catalyst left over was noticed indicating overload of the catalyst on the glass beads surface.
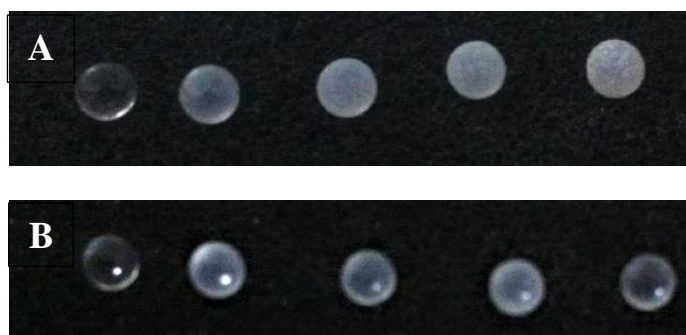
Figure 3.4: Glass beads of Figure 3.2 before (A) and after (B) mechanical abrasion, in the same order. Catalyst loading from left to right are: 0,1, 3, 5 and 7 mg of TiO_2 per g of glass beads. The 7 mg/g loading showed a noticeably lower stability than the others.

A stability study performed on the coated glass beads showed that much of the coated catalyst of more than 5 mg/g would detach from the beads surface by simple mechanical abrasion between a finger and thumb. It can be seen from Figure 3.4 the visual similarity of the resultant coatings to the 1 mg/g loading. This suggests the 1 mg/g loading was the most suitable for repeated handling and use; and therefore, the most suitable for industrial applicability. However, the 1 mg/g loading was the least active during photo-decomposition of acetone test in Chapter 4 of this work. Interestingly, the highest loading studied here i.e. 7 mg/g was not the most active which can be attributed to increased opacity of the coating.

3.4 Photo-reactor design considerations

Ideal reactors are normally referred to model reactors that have been simplified by making various approximations. Usually, by these approximations, it is possible to describe or predict the behavior of the reactor with simple mathematical expressions. There are basically three types of reactors:[180,246] the batch reactor, the continuously stirred tank reactor (CSTR) and the plug flow reactor (PFR). However, during this work, only the PFR was considered as most of the reagents used were in gaseous phase.

One of the important parameters to determine during the design of a reactor is the mole balance. In batch reactors, it can be used to determine time required to convert a given amount of reactants into products. For a flow reactor, the mole balance gives information about the reactor volume required. Typically, the mole balance can be expressed as in Equation (3.1):

$$n_{j0} - n_j + G_j = \frac{dN_j}{dt} \qquad (3.1)$$

where n_{j0} and n_j denote the molar flowrate of species j as it goes in and out of the reactor respectively, G_j denotes the rate of generation of j through chemical reaction and N_j denotes the number of moles of component j accumulated in the reactor. All variables are expressed in units of moles per second, except N_j, which is in the unit of moles. G_j is equivalent to the typical concept of chemical reaction rate. For reactants, G_j is negative, while for products, G_j is positive. The quantity of accumulated chemicals in a flow reactor, N_j, is determined by the gaseous volume and the adsorption behaviour of the gaseous chemicals.[247] Equation (3.1) is useful for mole balancing within the reactor volume where all other system parameters such as temperature, concentration distribution and photo illumination are considered uniform. As such, it is possible to determine the rate of production/generation, G_j in a reaction over a specific volume, V, using the rate of formation of j, r_j, as follows:

$$G_j = r_j V \qquad\qquad (3.2)$$

Generally, PFRs are designed for gas phase reactions and are often packed with catalyst. The reactants are fed continually into a tube (usually cylindrical), at one end while the products are withdrawn continually. As the reactant stream flows through the reactor, reaction proceeds. The amount of reactants that react depends on the length (size) of the cylindrical tube. In order to achieve the desired conversion, the contact time between the reactants and catalysts need to be optimised. The specific volume, V, is defined by total gas volume within the reactor and is the difference between the total volume of the reactor and catalysts volume. If average radius of glass beads is r, the total number of beads is N, which are installed in a glass tube with inner diameter of R and length of L, the specific volume is defined as follows:

$$V = \pi R^2 L - \frac{4}{3} N \pi r^3 \qquad (3.3)$$

If the glass beads is closely packed, the maximum packing density is 74% with 26% of volume counted for the empty space between spheres. Hence, the maximum number of the glass beads can be calculated by:

$$N = \left. 0.74\pi R^2 L \middle/ \frac{4}{3}\pi r^3 \right. = 0.555 R^2 L r^{-3} \qquad (3.4)$$

For a fixed dimension of glass reactor, the smaller glass beads will need larger number of beads to fill the space. Meanwhile, the gas volume can be calculated as:

$$V = 0.26\pi R^2 L$$

This indicates that the specific volume is not affected by the dimension of the glass beads and is only determined by the volume of the glass reactor. The specific volume is important since it directly affects the contact time between the reactants and catalyst. The contact time, t, can be calculated as the follows:

$$t = V\!/\!F \qquad (3.5)$$

where F is the gas volume rate. If the reactant gas is diluted by inert gases of x vol %, the true contact time is:

$$t = {Vx}/{100F} = 2.6 \times 10^{-3} \pi x R^2 L F^{-1} \tag{3.6}$$

The contact time is the time allowed for reactant to react on catalyst surface. Hence it is directly proportional to the conversion. By increasing the diameter or the length of the photoreactor, the conversion is expected to increase. However, if the diameter is increased too much, a uniform gas flow cannot be maintained and therefore, it will be less effective for the increase in conversion. Although the total specific volume is affected by the beads dimension, individual space surrounded glass beads is proportional to r^3. The total surface area of the beads within the reactor can be calculated using Equation (3.7):

$$S = 4N\pi r^2 \tag{3.7}$$

with N defined in Equation (3.4), the Equation 3.4 can be simplified as:

$$S = 2.22\pi R^2 L r^{-1} \tag{3.8}$$

Therefore, the total surface area of the beads is inversely proportional to the dimension of the beads. This suggests that smaller beads will offer larger number of catalytic centre and result in higher conversion. So, both the contact time and surface area are important to affect the reaction efficiency in a flow reactor. The contact time suggests how long the reactant will stay in contact with catalyst while surface area indicates how many reaction centers are available for reactions. For a slow reaction with high reaction barrier, increase in the contact time is essential to increase the conversion. For smaller beads flow reactor, higher gas flow

rate can be achieved, since there is higher number of reaction centers. However, if the catalyst is too reactive or the product is also reactive, longer contact time can result in the decrease in selectivity and yield.

A CSTR can be considered as operated under steady-state conditions of a PFR reactor. The starting and shutting down of the PFR are not considered for analysis when sizing the reactor. A few assumptions are often made during modelling of a PFR, one of which is the well-mixing of reactants.[246]But this is only applicable in a radial direction, where it is usually assumed that no gradients of composition or temperature is in the radial direction.[247] The spherical glass beads used to pack the reactor developed in this work means that this condition is met since the flowing reactants are scattered through closely packed spheres. As such, the velocity distribution within the reactor was considered constant. That means, it is better to approximate under turbulent flow conditions. Similarly, it can be assumed that no axial mixing occurs, which allows for the omission of terms due to dispersion as well as diffusion in the mole balance.
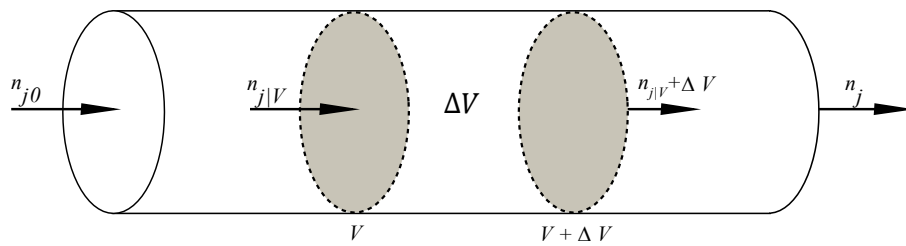
Figure 3.5: Mole balance of component j in a differential segment of ΔV

At steady state, the part of the reactor labeled ΔV in Figure 3.5 shows the part with uniform distribution of both temperature and reactants. From Figure 3.5, the mole balance

can be determined between the region ΔV. If there is no chemical accumulation within the volume of ΔV, Equation (3.3) then applies as follows:

$$n_{j|V} - n_{j|V+\Delta V} + r_j \Delta V = 0 \qquad (3.9)$$

Taking the limit as $\Delta V \to 0$, then the reaction rate, r_j, is defined as:

$$r_j = \frac{dn_j}{dV} \qquad (3.10)$$

Therefore, for a reaction $A \to B$, the volume of reactor, V_1 required to decrease n_{A0} to n_{Af} can be determined as follows:

$$dV = \frac{dn_A}{r_A} \qquad (3.11)$$

Taking the boundary conditions of the reactant, A, $n_A = n_{A0}$ when $V = 0$ (corresponding to the inlet) and $n_A = n_{Af}$ when $V = V_1$(corresponding to the outlet) gives:

$$\int_0^{V_1} dV = V_1 = \int_{n_{A0}}^{n_{Af}} \frac{dn_A}{r_A} = \int_{n_{Af}}^{n_{A0}} \frac{dn_A}{-r_A} \qquad (3.12).$$

For a 1st-order reaction, $-r_A = kC_A$ and $n_A = vC_A$ was obtained, where v is the flowrate of A, then Equation (3.12) becomes:

$$V_1 = \int_{n_{Af}}^{n_{A0}} \frac{dn_A}{kC_A} = \frac{v}{k} \int_{n_{Af}}^{n_{A0}} \frac{dn_A}{n_A} \tag{3.13}$$

Equation (3.13) can be integrated to give:

$$V_1 = \frac{v}{k} ln \frac{n_{A0}}{n_{Af}} = \frac{v}{k} ln \frac{C_{A0}}{C_{Af}} \tag{3.14}$$

The molar flowrates for reactant A and product B as a function of the reactor volume follows exponential behaviour and can be represented on a plot as in Figure 3.6. As can be seen here, for a reaction A to B each mole of A consumed results in the formation of one mole of B. As such, the total molar flowrate is kept constant. If however, the reactor is not isothermal, the dependence of v on T also needs to be considered.[247]
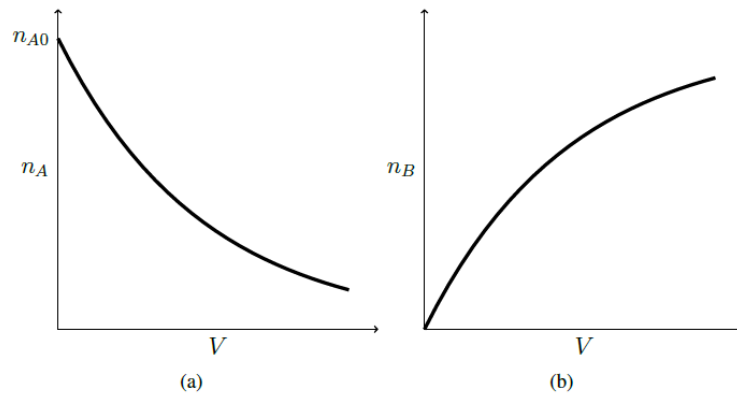
Figure 3.6: Molar flowrate of component A and B as a function of volume in a PFR.

3.4.1 Construction of photo-reactor

Flow reactors with immobilised catalysts have been reported to perform optimally for gas-phase photoreactions.[234,248] However, the efficiency can be achieved by careful design

as well as selection of a number of reactor parameters which include source of UV light, reactor configuration, lamp location, type of catalyst, distribution and impregnation of catalyst and more importantly, interaction between the light, catalyst and reacting substrate.

The choice of a gas-phase, flow-type reactor was necessary in this work as most of the oxidations of organic molecules were carried out in gas-phase. More importantly, the gas phase reactor is highly compatible with photocatalytic reactions, since the light can illuminate the whole reaction vessel uniformly. The reactors used in this work were similar to that of Verbruggen *et al.*[233] but independently modified. The reactor (Figure 3.7) consisted of a quartz tube (400 mm length, 24/28 mm internal/external diameter) surrounded with 8 cold-cathode fluorescent UV_A lamps (wavelength 365.44 nm) each being; 305 mm length and 4.0 mm diameter. Another lamp was placed in the centre of the reactor tube making it 9 lamps each having peak intensity of 22.6 mW power output. The reactor was filled with glass beads covered with coated catalyst. Both ends of the reactor were sealed with rubber bungs which were pre-installed with steel tubing (6 mm external diameter) plugged with quartz wool, to give appropriate gas inlet/outlet. All connections were sealed with epoxy glue for achieving airtight connections. Aluminium foil was then wrapped round the reactor to avoid the escape of the UV radiation. The dead reactor volume was calculated to be approximately 56 cm^3.

3.4.2 Photo-reactor illumination

The source of illumination in photoreactions is very important as it can influence the activity of the catalyst. A UV light source with a wavelength less than 388 nm is required to overcome the large band-gap of TiO_2 in order to generate charge separation, which is fundamental in the process of photocatalysis.
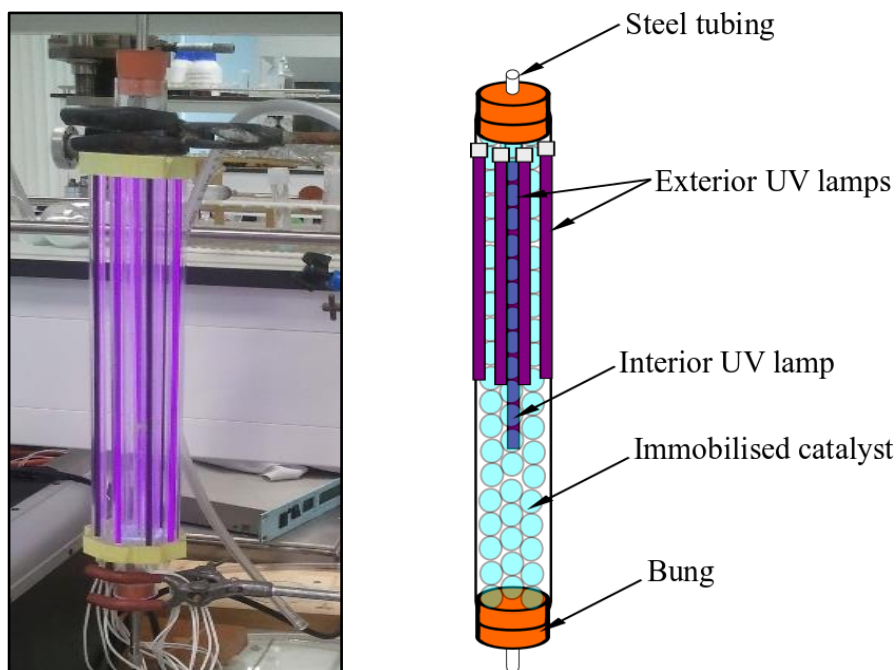
Figure 3.7: Image (left) and schematic diagram (right) of the designed photo-reactor showing all its components. The lower part is exposed for illustration

Traditional mercury UV lamps have high intensities, but heat up very rapidly, as such they require special cooling in order to maintain the photocatalyst temperature,[55,249] although it may only have a negligible effect.[250] Cold-cathode fluorescent lamps, on the other hand, only warm up slightly after a prolonged illumination period. They were therefore considered more suitable for use in this work as they are generally suitable for compact, annular flow reactors. It can be seen from Figure 3.7 that a fully illuminated photoreactor design was achieved.

3.5 Conclusion

In this Chapter, a new catalyst immobilization technique with high catalyst-support adherence efficiency have been demonstrated. The key equations used for the design of the photoreactor were derived. The reactor was designed to achieve a uniform irradiation field

that affords a plausible control over the average light intensity. The success of the design will produce more reliable experimental data and provide a more simplified photocatalytic process. A promising industrial implication is envisaged when an excellent catalyst adherence on the glass beads with high stability was achieved with the lowest catalyst loading amount.

Chapter 4: Photo-oxidation of acetone

4.1 Introduction

The photocatalytic degradation process of volatile organic compound (VOCs) is widely investigated. Considering the health hazards associated with prolonged exposure to VOCs, it becomes increasingly important to degrade them, especially in less ventilated environments. Acetone is one of the commonly used solvents in a wide range of products such as paints and varnishes. It is also used widely as a cleaning liquid especially in laboratories. Due to its high volatility, acetone can easily compromise indoor air quality. As it is known to potentially cause nose, skin and lung irritation,[251] it becomes significant to convert it into less hazardous compounds such as CO_2 and H_2O. In order to develop the application of VOC treatment for environmental protection, photocatalytic decomposition of acetone was carried out in our gas flow photocatalytic reactor designed in Chapter 3. Using standard, commercially available P25 as photocatalyst, acetone was successfully decomposed into CO_2 and H_2O.

4.2 Introduction of acetone in the gas stream

Following a modified procedure reported by Stengl *et al.*[60] 5 ml of acetone in liquid form was placed in a Dreschel bottle under a continuous gas stream. Using compressed air as carrier gas at a flow rate of 4.31 ± 0.51 Lh^{-1}, the acetone was introduced to the reactor.
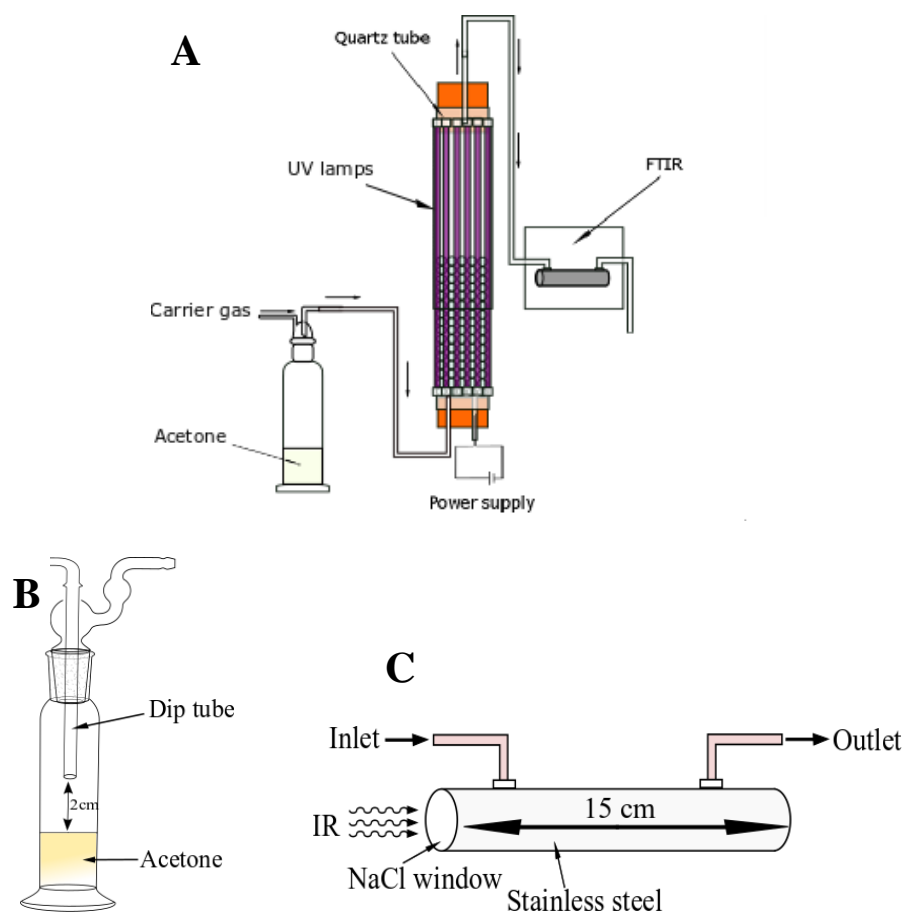
Figure 4.1: (A) Schematic diagram showing the experimental set up, (B) the setup for the Dreschel bottle and (C) FTIR sampling cell.

Due to the high volatility of acetone, the inlet concentration was controlled by maintaining the dip tube in the Dreschel bottle at 2 cm above the liquid to diffuse the acetone vapour, shown in Figure 4.1B. The vapour was collected by the outlet tube on the top. In this arrangement, if the dip tube is moved closer to the liquid level, the acetone vapour concentration will increase and vice versa. If the dip tube is below the liquid level, the concentration of acetone in the mix will be too high for the photoreactor and detection. The true concentration of acetone introduced in the flow reactor was measured by FTIR where

the gas stream was passed through a gas sampling cell mounted in the optical pathway of the FTIR (Figure 4.1A). The length of the sampling tube is fixed at 15 cm, which was made from stainless steel tube. Either NaCl, KBr or CaF_2 discs were used as IR windows, see Figure 4.1C. After balancing the adsorption equilibrium by the photoreactor and catalysts in the dark, the lights were turned on and the acetone and CO_2 concentrations were monitored. By monitoring these concentrations, it was possible to gain insight in to the photo-degradation kinetics of acetone by TiO_2 photocatalysts, thus confirming the functionality of the designed reactor.

4.3 Results and discussion

4.3.1 Effectiveness of acetone photo-degradation

For the environmental treatment, VOCs have to be mineralized into CO_2 and H_2O without trace of organic fragments. Otherwise, such fragments might cause more hazardous than the original VOCs. By applying UV illumination on the photoreactor fed with acetone and air, CO_2 concentration was increased immediately. The transient plot for the CO_2 concentration with light on and off is shown in Figure 4.2. No CO_2 was observed in the absence of either light or catalyst. Hence it confirms the nature of photocatalytic mechanism (Scheme 4.1).

Verbruggen et al.[233] reported similar increase in CO_2 concentration in their study of the photodecomposition of acetone. When the light is switched on, the initial concentration slowly increased to the saturation concentration, while the gas flow is constant. This suggests that the created CO_2 might be adsorbed by the catalysts until the surface is

saturated. By increasing the reaction temperature, the adsorption can be reduced and one might expect a faster increase in the CO_2 concentration.
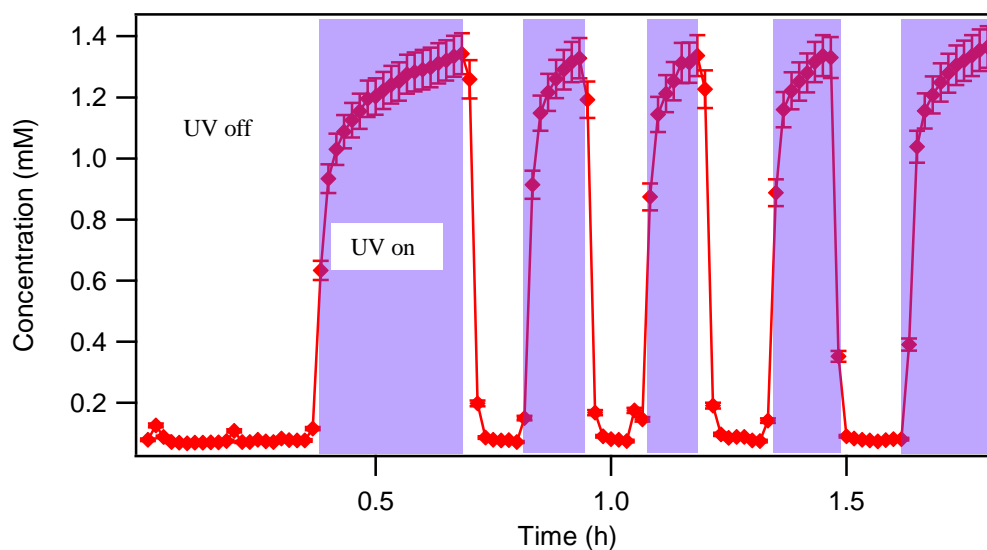
Figure 4.2: Concentration of CO_2 in a gas stream containing acetone versus flow time with the UVillumination on and off.

The sharp drop of CO_2 concentration when light was switched off possibly reflects the decaying kinetics of the excited states in TiO_2 and desorption kinetics of the adsorbed CO_2. As the desorption is normally slower, hence the decrease of CO_2 when light is off is dominated by the slow desorption kinetics alone. Another likely reason for the decrease in CO_2 concentration is that, upon switching the light off, the production of CO_2 ceased. Since the IR cell had open ends, it is likely that the accumulated CO_2 within the cell was replaced by fresh unreacted acetone. This is possible as the instrument scanned the content of the cell at regular interval of 3 or 5 min. throughout the reaction, which is enough time to flush the

cell in a continuous flow system, hence the observed sharp drop in CO_2 concentration in Figure 4.2.
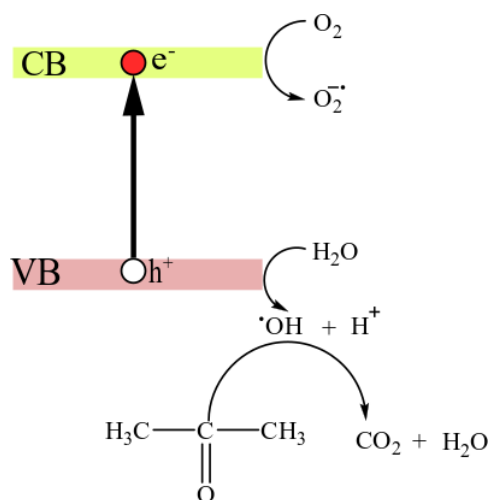
Scheme 4.1: Mechanism for the photocatalytic decomposition of acetone

The experimental data provide important information that will help to propose the mechanism of acetone photo-degradation under TiO_2 (P25), UV_A and O_2. The initial photochemical steps result in the generation of $\cdot OH$ radicals as described in Scheme 4.1. This was then followed by abstraction of hydrogen from the acetone molecules to initiate the decomposition process leading to the formation of acetonyl radical as in Equation 4.1:

$$\cdot OH \; + \; CH_3COCH_3 \longrightarrow \; \cdot CH_2COCH_3 \; + \; H_2O \tag{4.1}$$

Through diffusion controlled process, the formed acetonyl radical can react with oxygen to form a peroxyl radical (Equation 4.2).

$$\cdot CH_2COCH_3 \ + \ O_2 \ \longrightarrow \ \cdot OOCH_2COCH_3 \qquad (4.2)$$

The next step is the radical-radical reaction (Equation 4.3), which is followed by β-scission (Equation 4.4).

$$2\cdot OOCH_2COCH_3 \ \longrightarrow \ 2\cdot OCH_2COCH_3 \ + \ O_2 \qquad (4.3)$$

$$\cdot OCH_2COCH_3 \ \xrightarrow[\beta-\text{scission}]{} \ HCHO \ + \ \cdot COCH_3 \qquad (4.4)$$

The formaldehyde formed in Equation (4.4) is then oxidised to formic acid in three reaction steps (Equations 4.5 – 4.7).

$$HCHO \ + \ H_2O \ \longrightarrow \ CH_2(OH)_2 \qquad (4.5)$$

$$HOCH_2OH \ + \ \cdot OH \ \longrightarrow \ \cdot OCH_2OH(HO\dot{C}HOH) \ + \ H_2O \qquad (4.6)$$

$$\cdot OCH_2OH(HO\dot{C}HOH) \ + \ O_2 \ \longrightarrow \ H\dot{O}_2 \ + \ HCOOH \qquad (4.7)$$

It has been reported that at low concentrations, formic acid can scavenge OH radicals more efficiently than acetone due to the high rate constant of the reaction process in Equation (4.8).[252]

$$\cdot OH \ + \ HCOOH \ (HCOO^-) \ \longrightarrow \ H_2O \ + \ \cdot COOH \ (\cdot COO^-) \qquad (4.8)$$
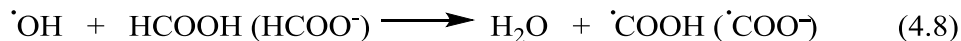
The $\cdot$COOH radical can then be oxidised to CO_2 (Equation (4.9)).

$$\dot{C}OOH(\dot{C}OO^-) \ + \ O_2 \ \longrightarrow \ CO_2 \ + \ H\dot{O}_2 \ (\dot{O}_2^-) \qquad\qquad (4.9)$$

As it has been established that the concentration of CO_2 in the gas stream is as a result of the complete mineralization of acetone by TiO_2 photocatalyst, it became necessary to evaluate the effect of catalyst loading on the glass beads by monitoring the increase in CO_2 concentration for different catalyst loading. This is the focus of the next section.

4.3.2 Effects of catalyst loading

The quantity of catalysts loaded on each beads could affect the photocatalytic reaction rate. At lower loading, there is not enough TiO_2 particles to be excited and to contact acetone, so the overall reaction rate will be low. At higher loading, each bead will absorb more photons and will result in insufficient, un-uniform light illumination. As a result, the reaction rate will also be reduced. Hence an optimum catalyst loading exists which balances the light illumination and contact with reactants. In order to find the optimum loading, the reaction rate was measured as a function of TiO_2 loading.

Here the reaction rate was determined at constant gas flow and light illumination. The CO_2 production rate, r_{CO_2}, was calculated as the product of the gas flow rate, f, and the CO_2 concentration, $[CO_2]$, shown in Equation (4.1). The CO_2 concentration was determined by the FTIR signal intensity at 2300 cm^{-1} calibrated with known CO_2 concentration. The intensity of the CO_2 under dark condition was also subtracted. Similar method was used for measuring the acetone flow rate. By considering the contributions of gas flow rate to the concentration, the flow rate of CO_2 makes a better representation of CO_2 production in comparison with to the molar concentration, since the molar concentration can be affected

by overall gas flow rate, hence the reason for this approach.

$$r_{CO_2} = f\,[CO_2] \qquad\qquad (4.1)$$

The rate of CO_2 production obtained from the photodecomposition of acetone with different loadings of TiO_2 is presented in Figure 4.3. During this measurement, the acetone was fed at the rate of 2.8 mmolh^{-1} and air flow rate is maintained at 4.3 Lh^{-1}. The reaction was carried out at near room temperature as the cold cathode lamps increase temperature very slowly to 63 $^{\circ}$C.
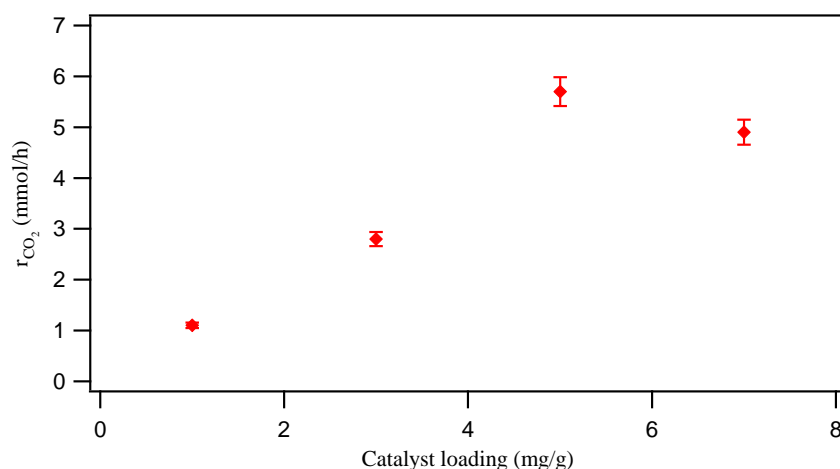
Figure 4.3: CO_2 production rates from the photodecomposition of acetone at different catalyst loading.

As shown here, there was a proportional increase in the production of CO_2 with increase in TiO_2 loading. This observed increase in CO_2 production continued until a maximum rate of 5.75 ± 0.07 mM$_{CO_2}$h^{-1} was achieved with a catalyst loading of 5 mgg$^{-1}_{beads}$. Loading greater than 5 mgg^{-1} showed a decrease in CO_2 production rate which can be attributed to reduced light/catalyst contact. In this case, only catalyst closest to the

light source became activated as the coating was too thick. Excess catalyst loading resulted in enhanced local UV adsorption and potentially, increased the surface area as well as active sites for the photocatalytic decomposition of acetone. An optimum catalyst loading of 5 mg/$g_{beads}$was found to be the best TiO_2 loading for maximum efficiency of photodecomposition of acetone under the studied conditions.

4.3.3 Decomposition of acetone

To study the photodecomposition process of acetone, the flow rate of acetone with and without light was monitored. As can be seen in Figure 4.4, upon UV illumination a rapid initial increase in concentration of acetone was observed until a steady state was reached; during which the acetone adsorption and decomposition was balanced on the catalyst surface. When the UV irradiation was turned off, the photodecomposition process became halted which resulted in a slow rise in concentration of acetone until another steady state was reached. The increase of acetone concentration at the beginning of light on and slow increase after light is off suggests there are significant effects of adsorption. The illumination of light cause the desorption of acetone and when light is off, the feed acetone is adsorbed back on the catalyst surface.
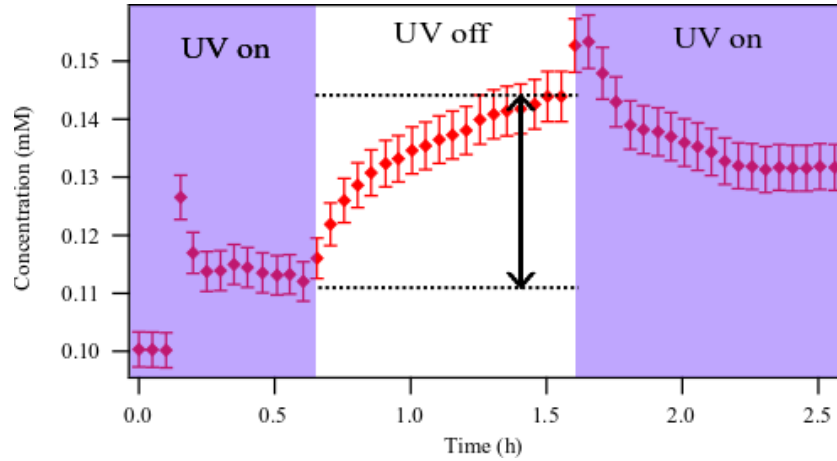
Figure 4.4: Acetone concentration in the presence and absence of UV illumination using 5 mg/g catalysts. The initial acetone concentration was regarded as the background and has been subtracted.The difference between the two steady state concentrations used to determine the decomposition rate of acetone is shown by the dotted lines and arrow.

The actual concentration of photodecomposed acetone [A], is given by the difference between the concentrations in dark and under illumination, $[A]_{dark} - [A]_{UV}$. Knowing the gas flow rate, f, allows to determine the rate of decomposition of acetone, $-r_A$ using Equation 4.2.

$$-r_A = f([A]_{dark} - [A]_{UV}) \tag{4.2}$$

In this study, the gas flow rate was 4.3 mMh^{-1} and $[A]_{dark}$ is 0.145 mM while $[A]_{UV}$ is 0.113 mM, reading from Figure 4.4. Thus the acetone decomposition rate is 0.14 ± 0.02 mM/h.

The decomposition efficiency can also be characterised using the concept of conversion. Conversion is defined by the ratio between the decomposed acetone [A] and the inlet concentration $[A]_{dark}$ using Equation 4.3.

$$Conversion \% = \frac{[A]_{dark} - [A]_{UV}}{[A]_{dark}} \qquad (4.3)$$

In the present work conversion of 22 % was achieved for the photodecomposition of acetone, based on the values of $[A]_{dark}$ and $[A]_{UV}$ from Figure 4.4.

Higher conversion value has been reported for photodecomposition of acetone. Žabová and Dvořák[253] reported 35 % conversion of acetone in their study on the photodecomposition of acetone in gas-phase over Degussa P25. They attributed the higher conversion rate to their TiO_2 immobilisation substrate (polystyrene mesh) which allowed for a significant increase in gas-catalyst contact area with respect to the glass beads used in the present study. However, the ease of handling catalyst makes the GIAC technique used in this work a more industrially viable choice.

The photocatalytic mineralisation of acetone to CO_2 is known to proceed through various stable chemical intermediates and the mechanism largely depends on the experimental conditions. Several routes have been proposed in the literature for the photo conversion of acetone, many of which show that acetone undergoes several chemical transformations before finally mineralizing completely.[254] However, there is likelihood that many partial oxidation products were formed considering that during photodecomposition of acetone, the initial oxidation steps are more kinetically favoured rather than total mineralization.[186,107,233] The partial oxidation products include many carbonyl moieties such as acetic acid,[186,255] formic acid,[256] and mesityl oxide[190,256,257]. Most of them are easily oxidized. In this experiment, variation in CO_2 produced was also monitored as shown in Figure 4.5. The maximum production rate of CO_2 was found to be $1.31 \pm$ mMh^{-1}. This makes it 9.4 times as much as the corresponding decomposition rate of acetone (0.14 ± 0.02 mM/h).
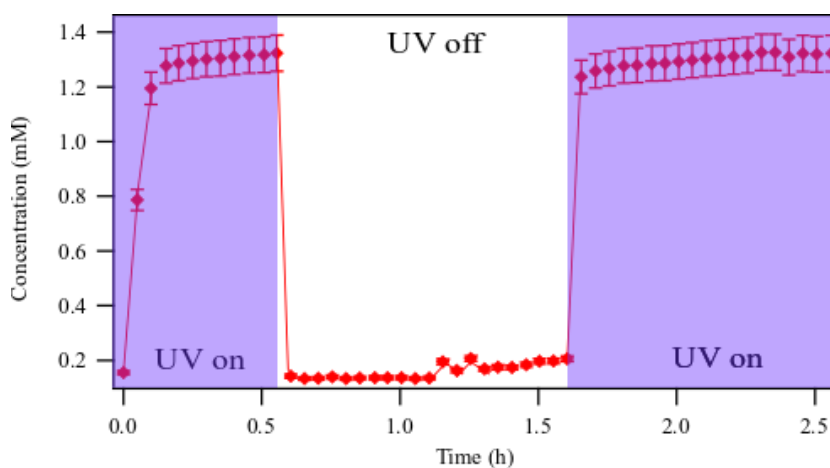
Figure 4.5: CO_2 concentration from acetone decomposition with and without UV illumination during the photodecomposition process

Due to stoichiometric ratio (1:3) between acetone and CO_2, it would be expected that the CO_2 concentration would only be 3 times of decomposed acetone. The higher than expected CO_2 concentration suggests there are other factors affecting the CO_2 concentration. The possible reason for this is that there are significant amount of organic species, including acetone, and its partial oxidation products such as acetic acid,[186,255] formic acid,[256] and mesityl oxide[190,256,257] adsorbed in the photoreactor. They are then gradually released after being oxidized into CO_2, since the reaction was carried out at room temperature. The adsorption behaviour was confirmed with the initial increase in the acetone concentration when light was switched on. At room temperature, such adsorption is inevitable. As such, the parameter of conversion could underestimate the performance of the TiO_2 photoreactor. A high temperature measurement could eliminate the adsorption and could give more accurate result.

The existence of intermediates could interfere with the measuring of acetone concentration. The extinction coefficient of these species will not be the same as that of

acetone, consequently the carbonyl peak area can increase by unknown amounts due to contribution of the intermediates. As such, the observed reduction in the concentration of acetone could be overestimated.

Verbruggen *et al.*[233] reported similar results where concentrations of produced CO_2 exceeded the complete mineralisation of the photo decomposed species. They also suggested that the deposition of organic residue on the photocatalyst surface may be responsible for the high concentration of CO_2.

Further experiments were performed to investigate the extent of carbonaceous deposition on the surface of the catalyst. The amount of CO_2 output was measured under UV illumination without the input of acetone immediately after the decomposition of acetone. It can be seen in Figure 4.6 that by switch on the UV light, the concentration of CO_2 rose rapidly despite the absence of acetone in the system. This observed CO_2 formation must have resulted from the oxidation of adsorbed carbonaceous species. After reaching its peak at 3.5 mins, the concentration of CO_2 decreases slowly as the adsorbed carbonaceous species became depleted. The maximum production rate of CO_2 was measured to be 0.90 ±0.09 mMh^{-1}.
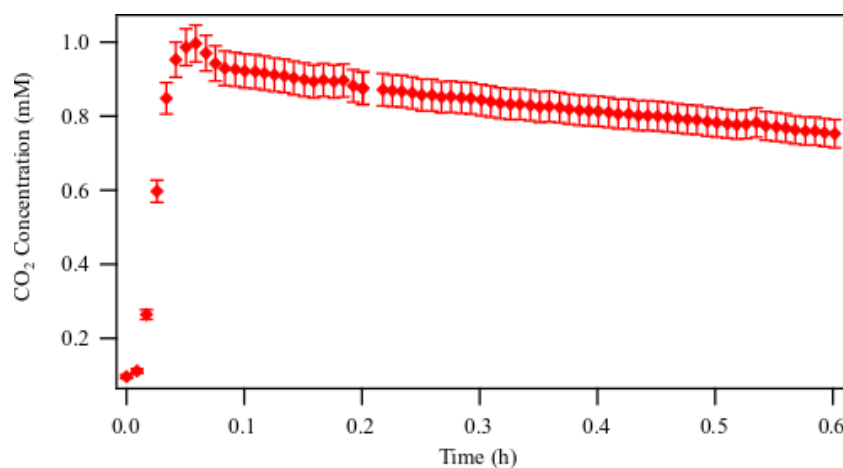
Figure 4.6: CO_2 concentration developed during the photocatalytic decomposition of carbonaceous residues on the TiO_2 under UV illumination with a clean gas in a flow reactor.

Having realised that CO_2 production is contributed from the decomposition of supplied acetone and the adsorbed organic species, it is possible to evaluate the net contribution of CO_2 production from the decomposition of acetone. From Figure 4.5, the maximum CO_2 production rate is about 1.31 mMh^{-1}. This value is reduced to 0.90 mMh^{-1} without acetone, in Figure 4.6. Hence, the net contribution to the CO_2 production from acetone decomposition is 0.41 mMh^{-1} (1.31 mM/h-0.90 mMh^{-1}). From Figure 4.4, the acetone decomposition rate was found to be 0.14 mMh^{-1}. In comparison with the CO_2 production rate of 0.41 mMh^{-1}, the stoichiometric ratio of 3 for CO_2 vs acetone is almost satisfied. Thus, it is much more accurate to calculate the conversion directly from the acetone concentrations. However, it is difficult to get meaningful kinetic data from the CO_2 production rate, since it is distorted by the adsorption. This also confirms that the excess amount of CO_2 produced during the photodecomposition reaction of acetone can be ascribed to the decomposition of accumulated carbonaceous species on the catalyst surface together with the decomposition of acetone. Extended photodecomposition of acetone beyond 20 h also provided an evidence of carbon deposition resulting in discoloration of TiO_2 catalyst coated glass beads, shown in Figure 4.7.

Figure 4.7: TiO_2 coated glass beads before (left) and after (right) photodecomposition reaction of acetone. Yellowish discoloration is due to accumulated carbonaceous species on TiO_2 surface.

However, irrespective of the complexity associated with quantifying photocatalytic decomposition of acetone, it is comforting to know that a successful photodecomposition at a constant rate of 0.14 ± 0.02 mMh^{-1} was achieved during this work. Interestingly, this value far outweighs the concentrations of acetone within domestic environments (2.2 - 9.9 nM).[192,193]Therefore, the photo-reactor so developed in this work can serve as a potential ambient air acetone removal system.

4.4 Conclusions

In this chapter, the gas-phase, flow-type photo-reactor was successfully tested for photodecomposition of acetone. The immobilisation method (GIAC) developed in Chapter 3 is indeed complementary and simple to implement. By utilising a highly active, inexpensive commercially available photocatalyst (Aeroxide® P25) it was possible to achieve acetone decomposition. The streamline design of the reactor made it possible for all the reacting species to be in contact while the transparency of the glass beads provided an excellent UV light penetration to even the innermost part of the reactor, hence the observed high photo activity. The formation of CO_2 from carbonaceous species adsorbed on the surface of the catalyst during the photodecomposition reactions have been observed. Prolonged illumination in the absence of reactant (acetone) can easily deplete the deposition of these accumulated carbonaceous species and release more active sites for the adsorption of substrate.

Since records have shown that the levels of indoor acetone pollution are typically in orders of magnitude lower than the concentrations used in this chapter, the designed reactor can therefore be a plausible initial step for the development of air purification devices.

Chapter 5: Photo-epoxidation of Propylene

The photo activities of some photo-catalysts including TiO_2, Bi_2WO_6 and Bi_2WO_6-TiO_2 (in various mixing ratios) were evaluated for photo-epoxidation of propylene. The photocatalytic epoxidation reaction was performed in gas-phase under atmospheric pressure. The reaction products, reaction kinetics and reaction selectivity were monitored by using inline analysis of FTIR combined with GC-MS in tandem. Typical reaction mixture of propylene:O_2:N_2 with ratio of 1:1:15 was used as the feeding gas. Propylene oxide (PO) in addition to other byproducts such as acetone, acetaldehyde and propanal were observed.

It was established that Bi_2WO_6-TiO_2 photo-catalysts were more preferable for better selectivity of PO with the best value of 64 %. Under the studied conditions, the selectivity of products was also observed to be very stable. The temperature effects on the photocatalytic epoxidation reaction were also studied. The change of the reaction temperature influences the product distribution significantly. Highest selectivity was found to be in the temperature range of 335-345 K, which was attributed to the inhibition of transformation into propionic acid. However, by increasing the reaction temperature further, the reduction of reaction rate was observed. This suggests that the reactions occurred on the surface of the catalysts. As the temperature increases the residence time of the reactant on the catalyst decreases, hence the surface concentration decreases. This results in decrease in overall reaction rate.

The photochromic behavior of the Bi_2WO_6 and Bi_2WO_6-TiO_2 was investigated. Upon UV illumination, Bi_2WO_6-TiO_2 appeared darker than Bi_2WO_6. This observation is attributed

to the contributions of TiO_2 as a result of defects formation on TiO_2 surface. The darkened Bi_2WO_6-TiO_2 composite enhanced the selectivity of PO by 17 %.

5.1 Introduction

Epoxidation of propylene (PR) among other alkenes is an important chemical reaction in the chemical industry. This is so because the corresponding epoxide, propylene oxide (PO) is an important intermediate for a variety of chemical processes. For instance, PO is used in the production of polyurethane, PR glycol as well as some fumigants. With several million tons produced around the globe annually, PO is ranked among the most useful chemical products in the chemical industry.[258] Conventionally, PO is produced in the industry through a process known as peroxidation using peroxy acid[259] as well as chlorohydrin.[260] The details of these reactions were discussed in Chapter 1. Unfortunately, these procedures produce large amount of undesired by-products as well as toxic chlorinated organics.[261] Fundamentally, both reactions utilize free radical oxidants. There has been reports of successful epoxidation of allylic olefins with water as the only by-product over titanium silicalite (TS-1) catalyst in the presence of H_2O_2 as oxidant.[261,258,262] In recent times, there have been a lot of effort put into developing some core industrial processes such as the hydrogen peroxide to propylene oxide (HPPO) process for the production of PO.[262] The high pressure and reliance on availability of H_2O_2, associated with these processes renders them expensive to run. The use of bimetallic-supported catalysts with Pd and Pt where O_2 and H_2 are used to generate H_2O_2 in-situ have also been reported.[263] Similarly, Au doped TiO_2 has shown some interesting result in the generation of H_2O_2 in-situ for photocatalytic oxidation reactions.[264,241] In such cases, H_2O_2 is dissociated over the catalyst to create hydroxyl radicals. However, the

inefficiency of the direct oxidation of PR with molecular oxygen has placed a demand for continuous research. So far, selectivity of PO has only been improved by modifying the catalyst significantly, through processes such as addition of alkaline earth promoters, salt and chlorine.[265,260,258]

In order to overcome these challenges researchers are shifting attention toward the field of photocatalysis as an alternative. During the photocatalyic process, either hydroxyl radicals or superoxide radicals can be formed using H_2O and O_2 as the source. If the reaction can be driven by solar energy directly, extra saving on the energy costs will be more beneficial. Considering that sunlight is a renewable source of energy capable of sustaining several chemical transformations through photocatalysts. With our photocatalytic approach, the use of H_2O_2 can be completely eliminated. Nguyen et al.[266] investigated the photo-epoxidation activity of a series of photocatalysts including SiO_2, TiO_2, V-Ti/MCM-41, V_2O_5/SiO_2, Au/TiO_2 and TS-1. They report a PO selectivity of 47 % over V-Ti/MCM-41. Pichat et al.[29] also investigated PO production over a series of semiconductor oxide photo-catalysts and reported PO selectivity dependence on the catalyst. They obtained CO_2 and water over TiO_2 while SnO and ZrO_2 produced other partial oxidation products including acetone, ethanal and acrolein alongside PO. Use of supported systems have also been reported to improve PO selectivity. [267,268] Yoshida et al.[269] studied over 50 different silica-supported materials in their photocatalytic epoxidation of PR and found that Bi-, Zt- and Ti-based catalysts produced the highest yield for PO. Recently, Bi-based materials have seen surge in interest as promising photocatalyst for various applications. A number of these materials including $BiVO_4$, Bi_2MoO_6, Bi_2WO_6, and $Bi_2W_{1-x}Cu_xO_{6-2x}$ have been reported to exhibit high photocatalytic activity.[241,270–272]

Indeed, Aurivillius-based compounds are known for their interesting properties. They were first reported by a Swedish chemist, Bengt Aurivillius in 1949. They exhibit high oxide ion conductivity owing to their layered perovskite structure. They have a general formula $(Bi_2O_2)^{2+}$ $(A_{n-1}B_nO_{3n+1})^{2-}$, where n denotes the number of BO_6 octahedral.[273] Bi_2WO_6 is apparently the most studied among this group. It exhibits hybridisation between O 2p and Bi 6s orbitals in its valence band (VB) which contributes to its high photocatalytic activity through first, electronic transitions under visible light to the W 5d orbitals in its conduction band (CB); and secondly, the mobility of holes is highly favoured due to the large dispersion in the VB.[274] Due to its interesting properties and displayed photocatalytic activity, several attempts have been made to modify the structure of Bi_2WO_6 in order to control some of its physical features including morphology and crystal size. As such, several 3D-hierchical architectures have been synthesised and studied, many of which showed enhanced photocatalytic activity. Moreover, an improved configuration has been reported by coupling Bi_2WO_6 with other materials such as TiO_2. Murcia López et $al.$[275] reported an enhanced activity with coupled Bi_2WO_6/TiO_2 heterostructure in their photodegradation of Rh B study.

As such, in this work we aimed to develop a direct gas-phase photo-epoxidation of propylene under mild conditions with emphasis on the selective production of PO using molecular oxygen as the only oxidant as shown in Equation (5.1) below:

$$+ \, 1/2 \, O_2 \xrightarrow[\text{Mild conditions}]{\text{Photo-catalyst}} \qquad \qquad (5.1)$$
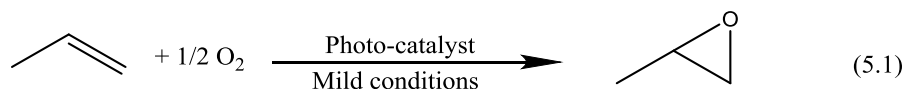
The main objective of this chapter is to investigate the efficiency of a promising photo reactor designed and discussed in Chapter 3 of this work; and a photo-catalyst in the direct gas-phase photo-epoxidation of propylene under mild conditions. Using hydrothermal synthesis, different photo-catalysts including Bi_2WO_6 and several coupled Bi_2WO_6/TiO_2 heterostructures were synthesised. Each photocatalyst powder was coated on glass beads according to procedure in Chapter 3 of this work and tested for photo-epoxidation of propylene. Furthermore, the effects of temperature and propylene to oxygen ratio were also investigated. The optimal reaction conditions were determined by comparing the selectivities of PO for different catalyst modifications.

5.2 Experimental

5.2.1. Preparation of photo-catalysts

Bi_2WO_6 was synthesised using a modified procedure reported by Amano et $al.$[276] The bismuth solutions was made by dissolving 0.1 mol $Bi(NO_3)_3 \cdot 5H_2O$ (Alfa Aesar) in 10 ml glacial acetic acid (BDH) and the tungsten solution was made from 0.05 mol $Na_2WO_4 \cdot 2H_2O$ (Agro Organics) in 90 ml water. The bismuth solution was then added dropwise to the tungsten solution whilst stirring. The milky suspension was stirred for further 1 hour. An aqueous solution of sodium hydroxide (1.0 mol L^{-1}) was added to adjust the pH of the suspension to 9. The suspension was then transferred to a hydrothermal vessel where it was heated at 140 °C for 20 hours. The suspension was filtered under vacuum and rinsed several times with deionised water and dried in an oven at 80 °C for 4 hours. The powder was then ground and calcined at 300 °C for 4 hours.

Bi$_2$WO$_6$-TiO$_2$ was prepared using the same synthesis procedure as above for the preparation of the Bi$_2$WO$_6$ precursor. TiO$_2$ precursor was prepared as follows: 0.1 mL of distilled water and 10 mL of isopropanol were mixed. The small amount of water was used to control the speed of hydrolysis and particle sizes of the Ti species. The solution was added dropwise to a mixture containing 2.5 g of titanium (IV) isopropoxide (TT^{i}P) (Agros Organics) as the Ti source dissolved in 10 mL of isopropanol (VWR Chemicals). The solution was stirred in an oil bath holding at 80 °C for 18 hr. An amount of 6 mL of acetyl acetone was then added to the TiO$_2$ sol to delay the hydrolysis. The final TiO$_2$ sol solution was incorporated into the milky suspension of Bi$_2$WO$_6$ under vigorous magnetic stirring for 1 hr, followed by hydrothermal synthesis at 140 °C for 20 hr. The suspension was filtered and rinsed with deionised water and dried in an oven at 80°C for 4 hours. The baked powder was then ground and calcined at 300 °C for 4 hours. The procedure was repeated with different weight ratios of TiO$_2$ to make 10, 30, 50 and 70 wt. %. Based on the concentration of TiO$_2$, the obtained Bi$_2$WO$_6$/TiO$_2$ powders were labelled as B-X/TiO$_2$, where X represents the TiO$_2$ weight percentage. TiO$_2$ was also synthesised alone according to above procedure for comparison.

5.2.2 Characterization techniques

The morphological analysis of the synthesised nanostructure during this study was carried out using a scanning electron microscope (Jeol, JSM 820). The various dimensions of the created nanostructures were measured from SEM images using the Image J analytical software. The band gap of the nanostructure was determined using an integrating sphere (Ocean Optics ISP-REF) equipped with an inbuilt tungsten-halogen illumination source (300

nm $\leq \lambda \leq$ 1000 nm). The Tauc relation was applied in the determination of the band gap of the studied materials from their UV-Vis diffuse reflectance spectra. Powder X-Ray Diffraction (Siemens D500 diffractometer) was used for crystalline structure determination and calculation of crystal domain sizes. A Cu X-ray source was used which emits the X-ray at wavelength of 1.54 Å. The diffraction data were assigned to known crystalline phases by comparing with those of ICDD database. Brunauer-Emmett-Teller (BET) specific surface area was measured using nitrogen adsorption at 77 K on a JW-BK122W BET surface area and pore size analyser.

5.2.3 Direct gas-phase photocatalytic epoxidation of propylene

All photocatalytic epoxidation experiments were conducted in a flow reaction set up. Typical reaction gas mixture was $PR:O_2:N_2$ = 1:1:15 at a gas hourly space velocity (GHSV) of approximately 6000 h^{-1} under atmospheric pressure. The GHSV was defined as the ratio of volumetric flowrate of the gaseous feed in cubic meter per hour to the volume of the rector in cubic meter. During each run, the photo-catalyst was immobilised on glass beads at a loading of 5 mg/g according to the procedure discussed in Chapter 3. The packed catalyst coated beads were brought in contact with the reacting gaseous mixture through the reactor inlet (Figure 5.1) under the illumination of UVA. In order to maximize uniform illumination, the entire walls of the UV chamber was covered with aluminium foil. The photo-reactor was placed on an aluminium block installed with heating cartridges (Figure 5.1) and thermocouples in order to measure the effect of temperature of the photoreactor. The heating system was controlled with phase angle power regulator to give accurate power control. The cold cathode lamp will also heat up photoreactor to the temperature of 335 K, which is the

lowest temperature that can be achieved without additional cooling. Photoreaction study was carried out at the temperatures of 335, 345 and 355 K.
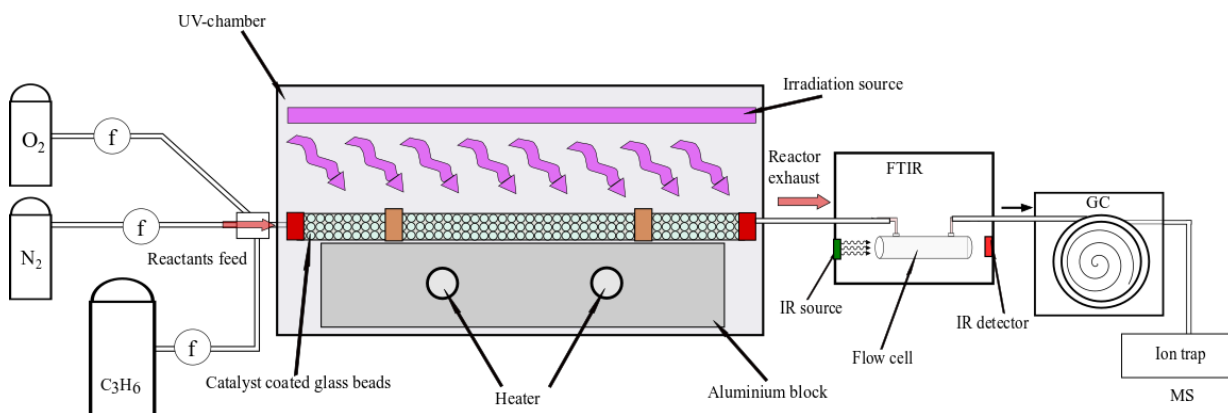
Figure 5.1: Experimental set up for propylene epoxidation reactions

Propylene, oxygen and nitrogen was mixed together in a mixing chamber before passing over the catalyst. The exhaust from the reactor was analysed directly using a purpose-built Fourier Transform Infrared Spectroscopy (FTIR) flow cell mounted with NaCl windows and a Gas Chromatograph Mass Spectrometry (GCMS) auto-sampling system developed in this work (Figure 5.2); which were controlled by automated system softwares. The GCMS and FTIR were connected in tendam. So data was collected from both instruments simultaneously.

PerkinElmer Spectrum One FTIR was used to analyse the concentration of reactants and products. The alkene peak was measured from 1695-1600 cm^{-1} while the CO_2 peak area was measured between the ranges of 2390-2230 cm^{-1}. Also, the peak between 3170-2820 cm^{-1} which is a common peak for the C-H stretch was monitored for changes. The detection limit for the FTIR was found to be approximately 3 μmol dm^{-3}.

Varian CP-3800 gas chromatograph was used to separate the compounds and a Varian Saturn 2000 mass spectrometer (MS) was used to analyse the separated products. For separation of epoxidation products of propylene, a PLOT column, Rt-QS-BOND of 30 m length, 0.53 mm internal diameter and a film thickness of 20 µm was used. The end of this column was coupled with a piece of column of 25 cm length, 0.25 mm internal diameter and 0.25 µm film thickness using a RESTEK siltite micro union, before connecting to MS. This was to trap the particles coated within the PLOT column and prevent contaminating the MS ion trap assembly. A carrier gas of helium was used at a flow rate of 100 mlmin^{-1}. The MS detector scanned from 20 to 300 m/z. with a delay of 1 s for each scan using electron ionisation (EI) method.
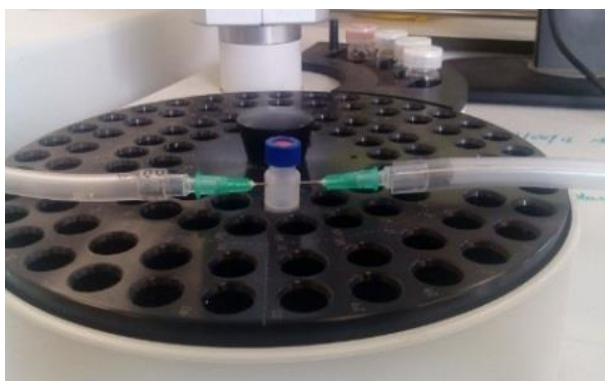
Figure 5.2: Auto-sampling vial modification

The flow rates of the reactant gases were controlled with rotameters before feeding into the reactor. It was possible to continuously monitor changes in concentrations of all chemicals as a function of time after every 5 minutes of reaction. Before the light illumination, the flow and the concentration were stabilised to avoid the disturbance of concentrations due to adsorption and desorption.

The following Equations (5.2)–(5.4) were used to define PR conversion, PO and CO_2 the selectivities respectively, for the reaction.

$$\text{PR conversion } = \frac{\text{mole of inlet PR} - \text{mole of outlet PR}}{\text{mole of inlet PR}} \times 100 \text{ \%} \tag{5.2}$$

$$\text{PO selectivity} = \frac{\text{moles of outlet PO}}{\text{mole of inlet PR} - \text{mole of outlet PR}} \times 100 \text{ \%} \tag{5.3}$$

$$CO_2 \text{ selectivity} = \frac{(\text{moles of outlet CO2})/3}{\text{moles of inlet of PR} - \text{moles of outlet PR}} \times 100 \text{ \%} \tag{5.4}$$

5.3 Results and discussions

5.3.1 Photo-catalyst characterization

The synthesised catalysts, Bi_2WO_6, Bi_2WO_6-TiO_2 and pure TiO_2 were characterised by XRD analysis, shown in Figure 5.3. The obtained diffraction peaks were analysed with the ICDD database in order to assign them. The Bi_2WO_6 only displayed russellite phase (JCPDS 39-0256). The broadness of the diffraction peaks of Bi_2WO_6 indicates poor crystal structures.
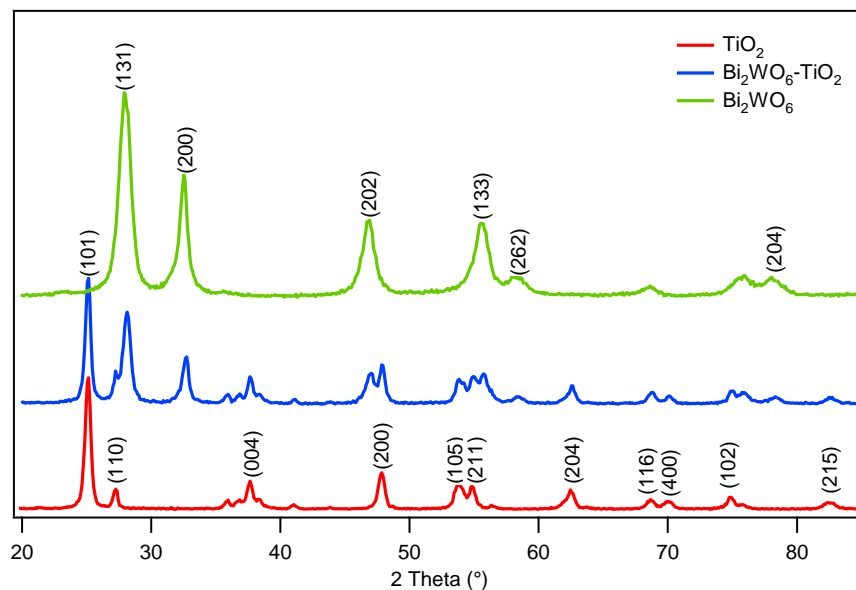
Figure 5.3: XRD spectra of Bi_2WO_6, Bi_2WO_6-TiO_2 andTiO_2.

The crystal sizes of the prepared Bi_2WO_6 were determined using the Scherrer's equation. The FWHM of the strongest (131) peak at 28.8^o was analysed. The crystallite size of 65 nm was obtained. Bi_2WO_6-TiO_2 composite displayed additional peaks associated with anatase phase of TiO_2 (JCPDS 21-1272). The peaks from Bi_2WO_6 are generally broader than those from the TiO_2. Using the Scherrer's equation, the crystallites of TiO_2 were determined to be 28 nm. In all cases, TiO_2 showed only anatase phase without rutile phase.

Tauc plot generated from the UV-Vis reflectance spectra of the synthesised Bi_2WO_6-TiO_2 composite photo-catalysts is shown in Figure 5.4. The linear nature of the Tauc plot, suggested that the materials are semiconductive with indirect band gap. In such case, the excitation and electron-hole recombination will need additional momentum borrowing from the vibration of the atoms. Moreover, it was possible to determine from the plot that the created Bi_2WO_6-TiO_2 nano crystals possessed a band gap of 2.89 ± 0.05 eV. The pure

Bi$_2$WO$_6$ powder was used as reference material and similar band gap was found to be 2.95 $\pm$ 0.02 eV) which is consistent with the reported literature value.[155] The band gap energy from our nano crystals are slightly higher, which might be related to the crystal domain sizes. When the crystals become smaller, the quantum confinement effects will increase the band gap, as observed in quantum dots.
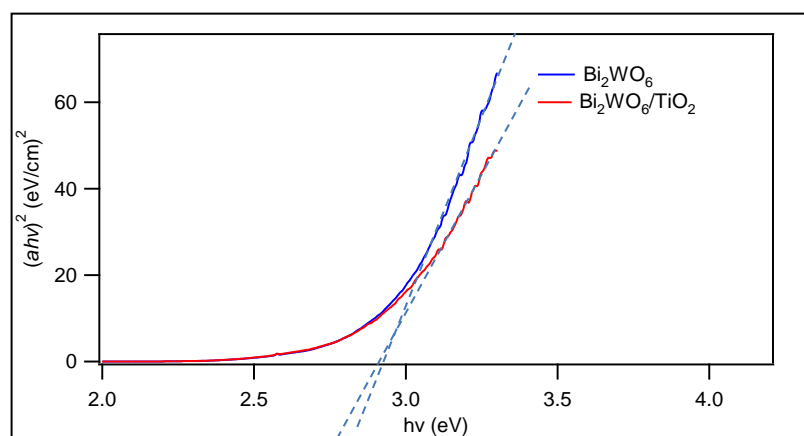
Figure 5.4: Tauc plot of the diffuse reflectance spectra of Bi$_2$WO$_6$ and Bi$_2$WO$_6$/TiO$_2$ Nano materials. The linear portion shown in blue segmented lines indicate the extrapolation of the nanostructures' band gaps.

SEM images of hydrothermally synthesised Bi$_2$WO$_6$ (Figure 5.5) show that the bismuth tungstate has formed a powder with an average particle size of 2 µm. Under closer inspection, it was possible to observe the formation of uniformly shaped and sized nanostructures (Figure 5.5 A). The nanostructures are known in literature as "nano flowers"[276,277] or "nano flakes"[278] and are composed of nano sheets. These nano sheets are centred on a nucleation site to produce this flower like structures, the size of which depends on the mixing ratio of the reacting species and are well documented in literature. Amano *et al.* reported similar hierarchical structure of the nano flakes aggregates and attributed it to strong acidity caused by the hydrolysis of Bi (NO$_3$)$_3$.[276] Figure 5.5 B shows a magnified single Bi$_2$WO$_6$ particle

with a flower-like morphology believed to form through the Ostwald-ripening mechanism.[241,274,276,279] However, as expected the sharpness of the nucleation sheets decreased as the concentration of TiO_2 within the framework increased (Figure 5.5 C-E). The most obvious alterations in morphology was observed in the case of B50-TiO_2 (Figure 5.5 E) where a structure more closely related to TiO_2 was obtained which clearly shows disappearance of the 3D hierarchical architectures. This suggests that incorporating TiO_2 into Bi_2WO_6 tends to inhibit the growth of nano-flower structures, thus no Ostwald-ripening took place in this case as a result. On the other hand, by loosing the flaked crystal features, the surface of the nanoparticles becomes much more fragmented which could offer larger surface area with higher density of catalytic centres.
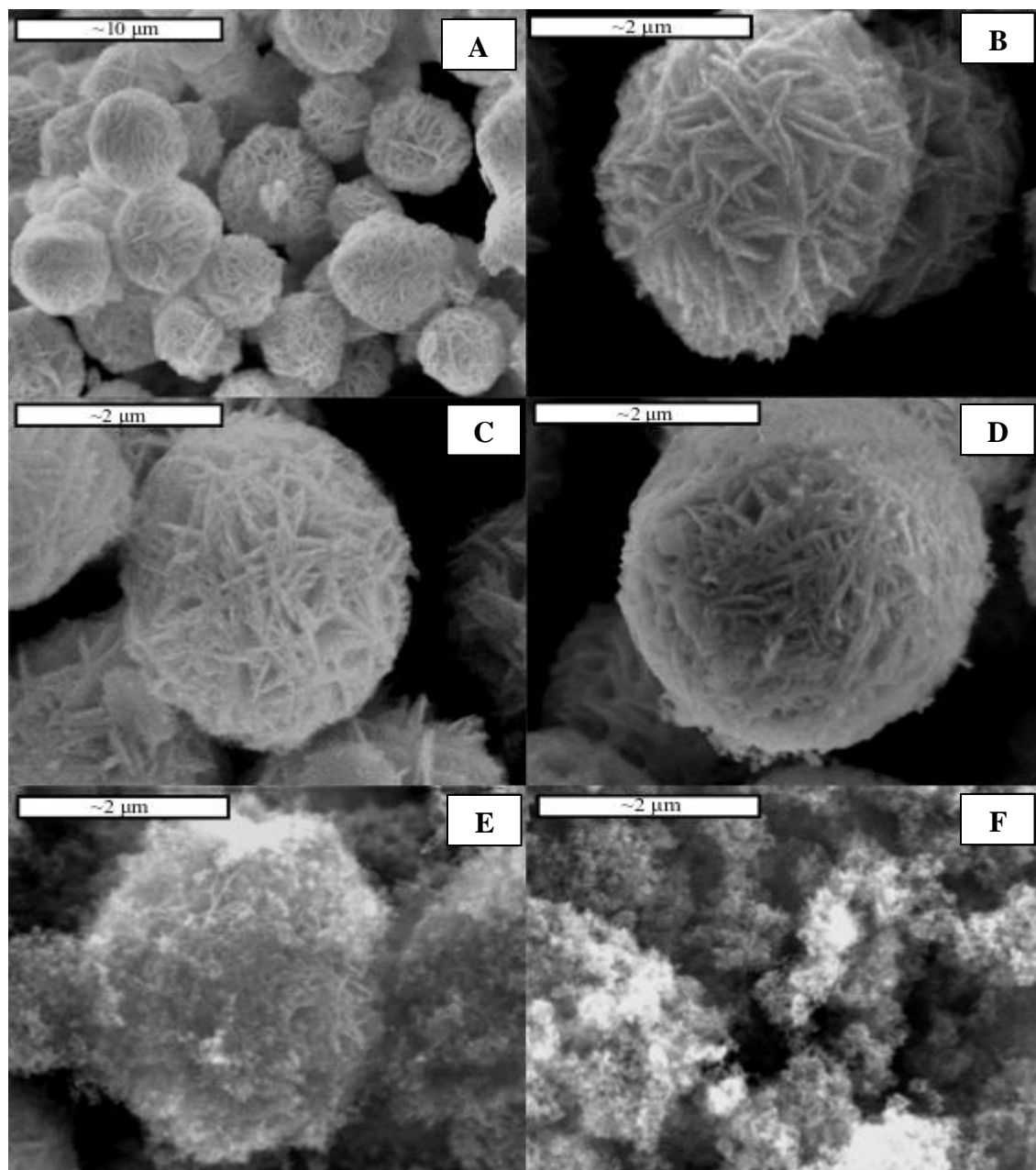
Figure 5.5: SEM images of hydrothermally synthesised Bi_2WO_6 Nano flowers: (A) Uniform distribution of Nano flower balls of pure Bi_2WO_6; (B) Higher magnification of (A); (C) B-10/TiO_2; (D) B-30/TiO_2; (E) B-50/TiO_2 and (F) TiO_2.

The surface areas of the synthesised catalysts are represented on Table 5.1. It can be seen here that the heterostructures of composite Bi_2WO_6-TiO_2 materials presented higher surface area than either pure TiO_2 or Bi_2WO_6. However, the respective surface areas are not

likely to remain the same after coating the catalysts on the glass beads. As such, the surface areas values of the catalysts presented here were considered of less effect on the overall photocatalytic activity. Murcia-Lopez et al.[241] have reported a remarkable decrease in the surface area of their catalyst supported on glass sphere compared to unsupported catalyst.

Table 5.1: Surface areas of the catalysts as determined by BET

Entry	Catalyst	BET surface area (m^2g^{-1})
1	TiO_2	36.1
2	Bi_2WO_6	37.8
3	$B-10/TiO_2$	47.2
4	$B-30/TiO_2$	51.3
5	$B-50/TiO_2$	59.7
6	$B-70/TiO_2$	49.3

5.3.2 Growth mechanism of Bi_2WO_6 Nano-flower.

In order to monitor the crystal-growth mechanism of the Bi_2WO_6 nano-flower, samples were taken by interrupting a fresh hydrothermal synthesis reaction and were characterized by SEM (Figure 5.6). It was possible to observe changes in the formation of nano-flower in the white precipitates prepared according to procedure in section 5.2.1 at ambient temperature. After an hour of hydrothermal reaction, some irregular shaped aggregates of nano-flower less than 2μm in diameter were observed (Figure 5.6 A). 2 hours later, slight reduction in size of the particles was observed (Figure 5.6 B). Uniformly shaped spherical particles decorated

with surface flakes were formed only after 5 hours of reaction (Figure 5.6 C and D). The diameter of the sphere is about 4 μm. From higher magnification images in Figure 5.6 D the characteristic nucleation sheets (platelets) were clearly observed. There were no further development of the nanoparticles for hydrothermal reaction beyond 5 hours. The SEM observation indicates that the synthesised nano-flower spherical particles were formed by starting from the core and through crystal plane-selective growth continued to increase in size. This observation agrees with finding of Amano *et al.*[276] and is contrary to some suggestions that the formation was through aggregation of individual rectangular platelets. For less than 5 hours of reaction, the completed spherical particles were not formed due to the incompletion of hydrolysis of bismuth salt.
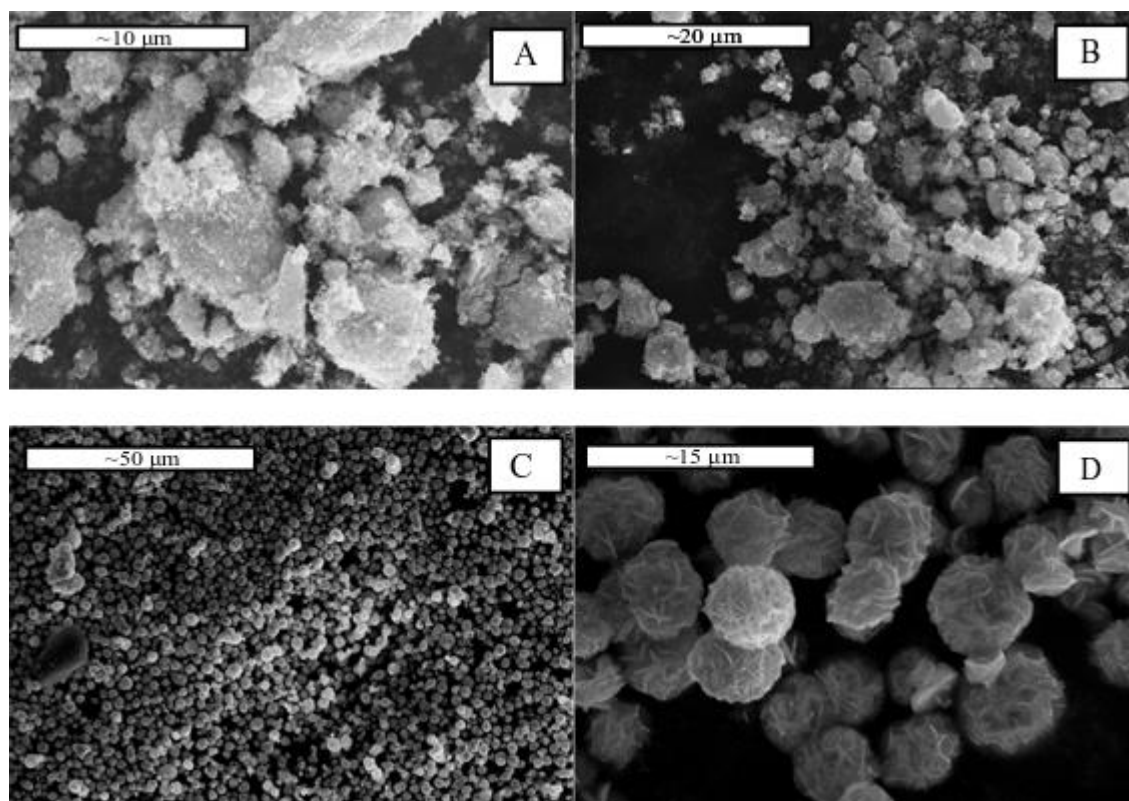
Figure 5.6: SEM images of time dependent growth of Bi_2WO_6 after hydrothermal synthesis for: (A) 1 hr., (B) 2 hr. (C) and (D) 5 hr.

In general, an anisotropic crystal growth such as observed here is achieved as a result of additives being selectively adsorbed on to specific sites.[276,280] Consequently, isotropic crystal growth becomes significantly suppressed. The anisotropic growth of crystals observed here could be as a result of the presence of acidic aqueous medium as well as adequate amount of tungsten precursor, as required for the formation of Nano-flower particle from cores.[274] Furthermore, it is well known that a diffusion-limited growth condition is also required in order to form a multi-branch aggregates of polycrystals.[276]

It has been reported that the formation of spherical particles decorated with nano flakes is the result of Ostwald ripening process. Small crystals have large population of surface atom which is easier to dissolve. It was observed that after 5 hours of reaction, smaller particles formed after 2 hour reaction disappeared to form the larger crystals as illustrated in Figure 5.7. This is the Gibbs-Thomson effect which is expected during nucleation, growing and coarsening processes.[281] The spherical appearance of the nano-flower is attributed to formation of minimization of the surface free energy.[276,282]
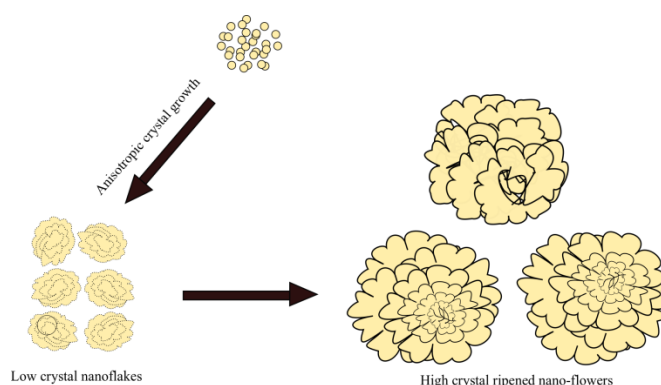
Figure 5.7: Schematic illustration of formation process of Bi_2WO_6 nano-flower.

The mechanism of formation of Nano-flower ball particle is considered to occur in two stages. First, anisotropic crystal growth and secondly, Ostwald ripening process, depending on the overall concentration of dissolved starting materials and the changes they undergo during crystallization.[276,280,283–285]

5.3.3 Direct gas-phase photocatalytic epoxidation of propylene

During the epoxidation experiments, no activity was observed in the absence of either photo-catalyst or UV illumination suggesting that the epoxidation reactions over the studied photo-catalysts were mainly photocatalytic. TiO_2 is known for its ability to completely mineralise VOCs to CO_2 as was also observed in this work. Due to the high sensitivity of FTIR to CO_2, it was used to analyse CO_2 concentration. GCMS was used for analysis of reactants and product. The FTIR spectra in Figure 5.8 shows the formation of CO_2 as reaction progressed. At steady flow of reactant mixture, gradually increased CO_2 peak was observed when the reaction was illuminated, and the intensity of the peak increased as the reaction time increased (Figure 5.8 A). No such increases were observed without illumination suggesting the significance of light to the oxidation. The high intensity of the CO_2 peak observed suggest complete oxidation of PR to CO_2 as was expected of TiO_2. However, this was not the case when Bi_2WO_6 was coupled with TiO_2 catalyst. When Bi_2WO_6 was incorporated into the catalyst, only a small amount of CO_2 was observed over the same reaction time (Figure 5.8 B) indicating partial oxidation of PR. Figure 5.8 C shows the plotted peak areas of CO_2 peak (at 2300 cm^{-1}) for pure TiO_2 and B-50/TiO_2.
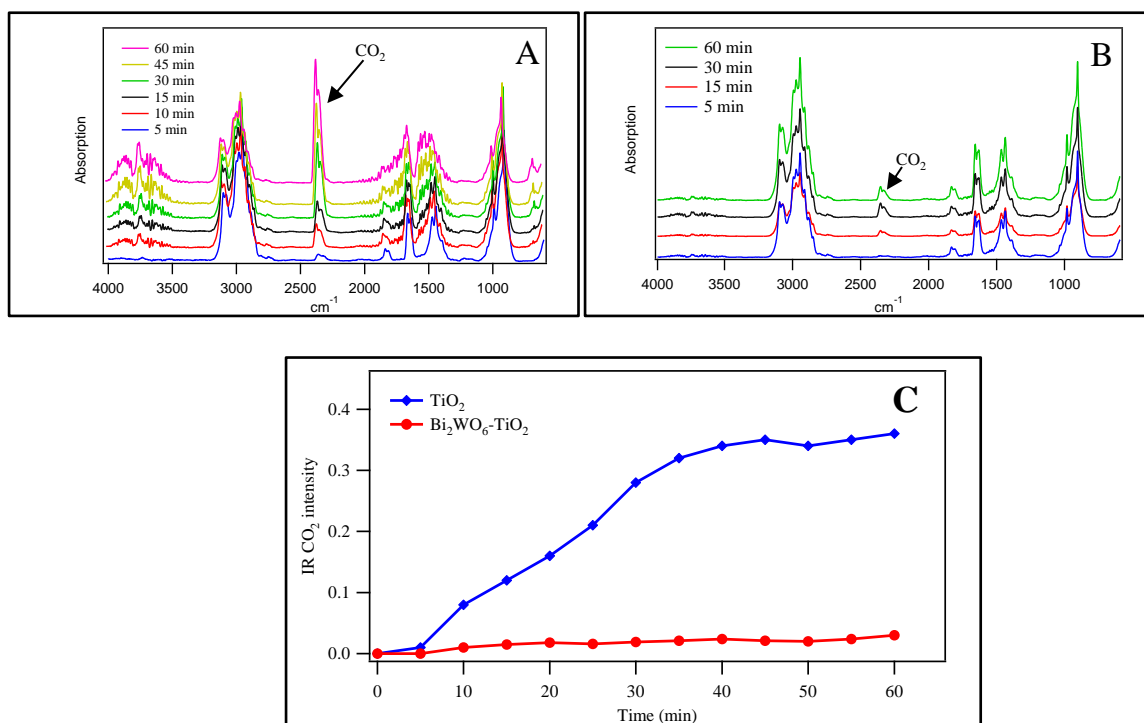
Figure 5.8: FT-IR spectra of the beginning of the flow reaction with (A) TiO_2 and (B) B-50/TiO_2. The IR intensities of the produced CO_2 are shown in (C).

The results of photo-epoxidation of PR with molecular oxygen over the studied photo-catalysts in a flow reactor at mild conditions are summarized in Table 5.2. Pure Bi_2WO_6 showed higher PR adsorption in the dark compared to TiO_2. In the case of composite materials, the adsorption increased significantly with no much of a difference between them. This can be ascribed to the increased surface area observed during the BET analysis, presented in Table 5.1.

Table 5.2: PR adsorption and conversion during the epoxidation reaction

Entry	Catalyst	PR	
		Adsorbed (μmol g^{-1})	**Conversion** (%)
1	TiO$_2$	0.03	0.6
2	Bi$_2$WO$_6$	0.039	0.4
3	B-10/TiO$_2$	0.051	1.6
4	B-30/TiO$_2$	0.058	2.5
5	B-50/TiO$_2$	0.083	4.1
6	B-70/TiO$_2$	0.089	3.4

The co-existence of Bi$_2$WO$_6$ and TiO$_2$ in the growth solution has significant effects on the growth of nano crystals resulting in fragmented structures with high surface areas. PR adsorption was considered the combination of physical and chemical adsorptions on the photo-catalysts, which largely depends on surface area as well as TiO$_2$ content. Due to the presence of nucleation sheets on the surface of the Bi$_2$WO$_6$ catalyst which is expected to increase the surface area of the catalyst, a substantial amount of propylene was adsorbed.

PR was observed to attain conversion up to 4.1 % while PO selectivity was up to 64 % with B-50/TiO$_2$ catalyst. Other products observed alongside PO include acetone and acetaldehyde.

The TiO$_2$ synthesised in this work showed high photo-oxidation activity. The conversion of PR was 0.6 % with CO$_2$ as the major product (selectivity 86 %), while no PO was observed (Figure 5.9 A). Excess production of CO$_2$ can be attributed to the successive photo-oxidation of oxygenated by-products. As expected, the more favourable photo-catalyst was the coupled Bi$_2$WO$_6$-TiO$_2$ (Figure 5.9 B). B-50/TiO$_2$ achieved the highest PO selectivity (64 %) while less than 10 % was observed for B-10/TiO$_2$. From Figure 5.9 C, it can be seen

that PO was the dominant product over B-50/TiO$_2$ photocatalyst. All combinations of photo-catalysts were active and stable for the production of PO.
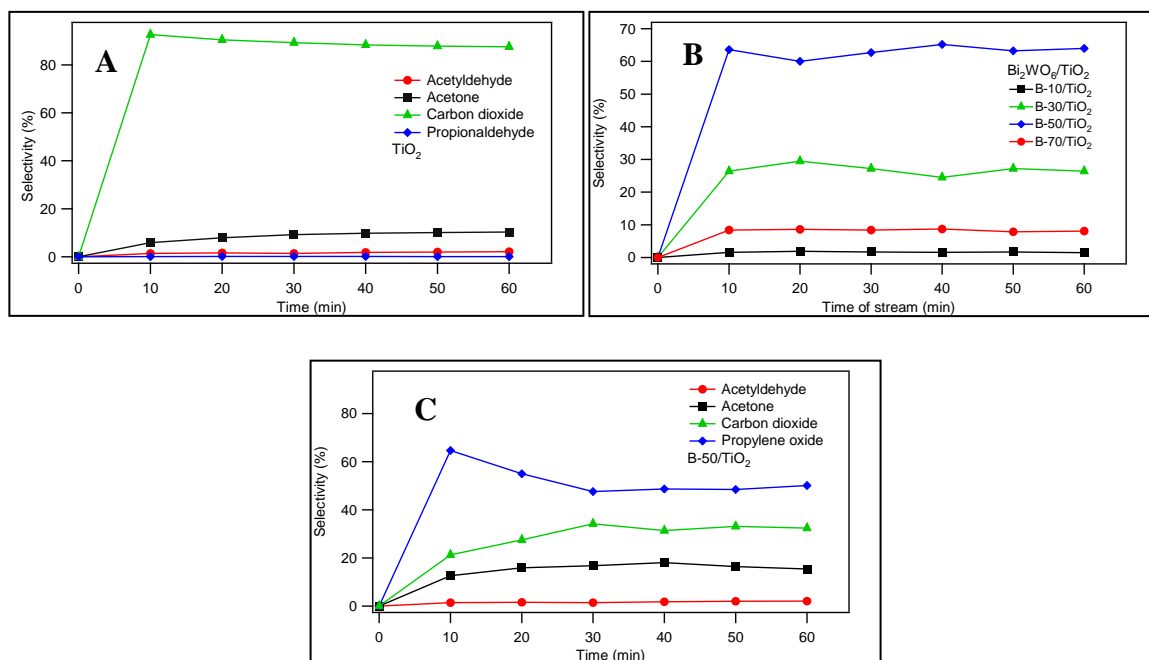
Figure 5.9: The time-dependent behaviour of selectivity of products over: (A) TiO$_2$, (B) PO selectivity over Bi$_2$WO$_6$/TiO$_2$ and (C) B-50/TiO$_2$.

The different types of products obtained with the Bi$_2$WO$_6$-TiO$_2$ composite catalyst suggests that there are different active sites on the catalysts. In other words, the active sites are specific for the formation of products. The low production of CO$_2$ in the presence of Bi$_2$WO$_6$ indicates a decrease in the active sites of the TiO$_2$ where majority of the CO$_2$ is formed (Figure 5.9 C). The selectivity of acetone doubled from 9 % to 18 % when B-50/TiO$_2$ was used (compare Figure 5.9 A with 5.9 C). Increase in acetone suggests that more active site for its production were introduced by Bi$_2$WO$_6$. Indeed, considering that the CBM of TiO$_2$ is more negative than CBM of Bi$_2$WO$_6$,[241] the photo excited electrons will transfer from the TiO$_2$ to the Bi$_2$WO$_6$ (Figure 5.10). The less negative CBM of Bi$_2$WO$_6$ will reduce the

possibility of superoxide radicals near the interface between TiO_2 and Bi_2WO_6. As the highest formation of CO_2 was only observed from pure TiO_2, and high PO selectivity from composite Bi_2WO_6-TiO_2, it is possible that the superoxide radicals are responsible for the complete mineralisation of PR. Hence, the Bi_2WO_6-TiO_2 interface plays an important role in the formation of PO. On the other hand, small band gap of Bi_2WO_6 (2.89 eV) can offer a combination of mild redox power, which is responsible for the formation of organic intermediates.[156]
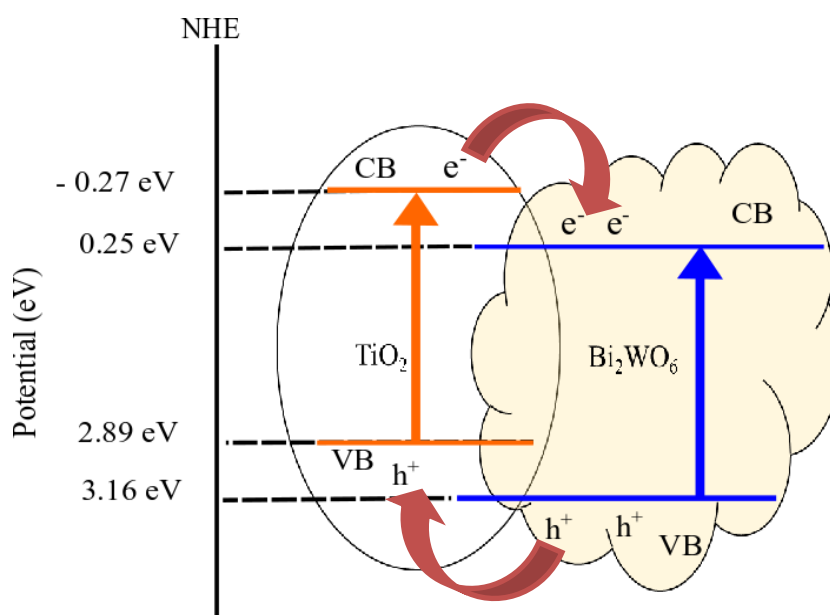
Figure 5.10: A schematic of electron transfer between conduction bands of the Bi_2WO_6-TiO_2.

$$\text{Photocatalyst} \xrightarrow{h\nu} e^- + h^+ \qquad (5.5)$$

$$O_{2(g)} \longrightarrow e^- + O_2^-_{(ads)} \qquad (5.6)$$

$$O_2^-_{(ads)} + h^+ \longrightarrow 2O_{(ads)}^* \qquad (5.7)$$
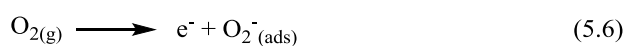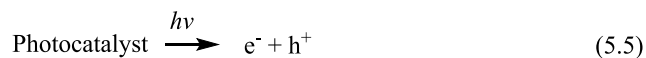
Adsorbed O_2 is reduced to superoxide, $O_2^{\bar{}}$, as it traps the photo induced electron as shown in Equation (5.5). Due to the stable nature of $O_2^{-}{}_{(ads)}$ species, it is not directly involved in the process. Atomic oxyradicals which are formed during the reaction between the $O_2^{-}{}_{(ads)}$ and the positively charge hole (Equation 5.6), are the active species.[278,286]

$$(5.8)$$
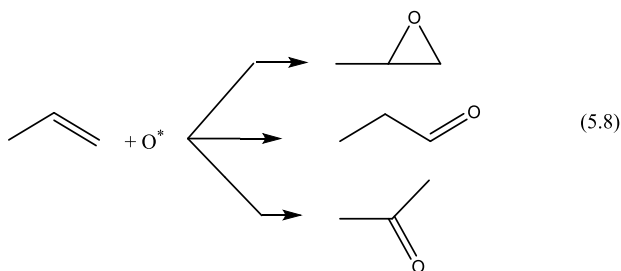
It is well established in the literature that approximately 80 to 90 % of the reaction products are known to be formed when the surface atomic oxy-radicals react with propylene in the epoxidation reaction shown in Equation (5.8). [287–290] In other word, the amount of PR converted as well as the type of product obtained depend on the concentration of oxy-radicals present in the reaction. The oxy-radicals in turn depend on the interaction of a superoxide with a hole, which is generated as a result of photonic excitation.

5.3.4 Effect of reaction temperature on photo-epoxidation

In order to elucidate how temperature affects the photo-epoxidation reactions, experiments were performed at different temperatures. Figure 5.11 shows high stability in the selectivity of products on stream as well as similarity in time-dependent behaviour of the photocatalytic epoxidation reaction. The selectivities of products gradually increased with rise in temperature. This is consistent with the Eley-Rideal mechanism for epoxidation. It

does not need the adsorption of PR for epoxidation. But it also reduce the adsorption on TiO_2 and B_2WO_6/TiO_2 interface. Overall selectivity is determined by both the Langmuir-Hinshelwool mechanism on TiO_2 defects, where the adsorbed PR and adsorbed O_2 reacted to form CO_2 and H_2O, and the Eley-Rideal mechanism on the B_2WO_6/TiO_2 interface where the adsorbed O_2 reacted with PR in a non-thermal surface reaction. According to Langmuir Hinshelwood mechanism, two adsorbed molecules on neighboring sites can react as biomolecules on the surface of the catalyst. Eley-Rideal on the other hand describes reaction of an adsorbed molecule with a gaseous molecule within the vicinity.[229,231,291]

At low temperature, the adsorption on TiO_2 defects result in increased photo oxidation and reduced selectivity. Although PO was the dominant product when the reaction temperature was increased from 335 K to 345 K, there was a slight increase in concentration of acetone and alcohol (Figure 5.11(a)–(c)). Further increase in temperature to 355 K showed a substantial amount of increase in propanal concentration while that of PO remained constant. This suggests that temperature can affect the adsorption and desorption of the PR and reaction products respectively on the photo-catalyst. Increasing the temperature would inhibit the process though, since adsorption itself is an exothermic process. Nevertheless, high temperature favours desorption process as it is an endothermic process. However, when the temperature rose above 345 K, a slight decrease in selectivity of PO was observed (Figure 5.11 b). This decrease is attributed to increased competition of multiple reactions towards different products as is widely accepted that upon irradiation of a photo-catalyst with UV, several reactions occur leading to generation of active species. This observations agree with the result obtained by Nguyen *et al.*[292]in their study of the effect of temperature on the photocatalytic epoxidation of propylene with O_2 over V-Ti/MCM-41 photocatalyst.
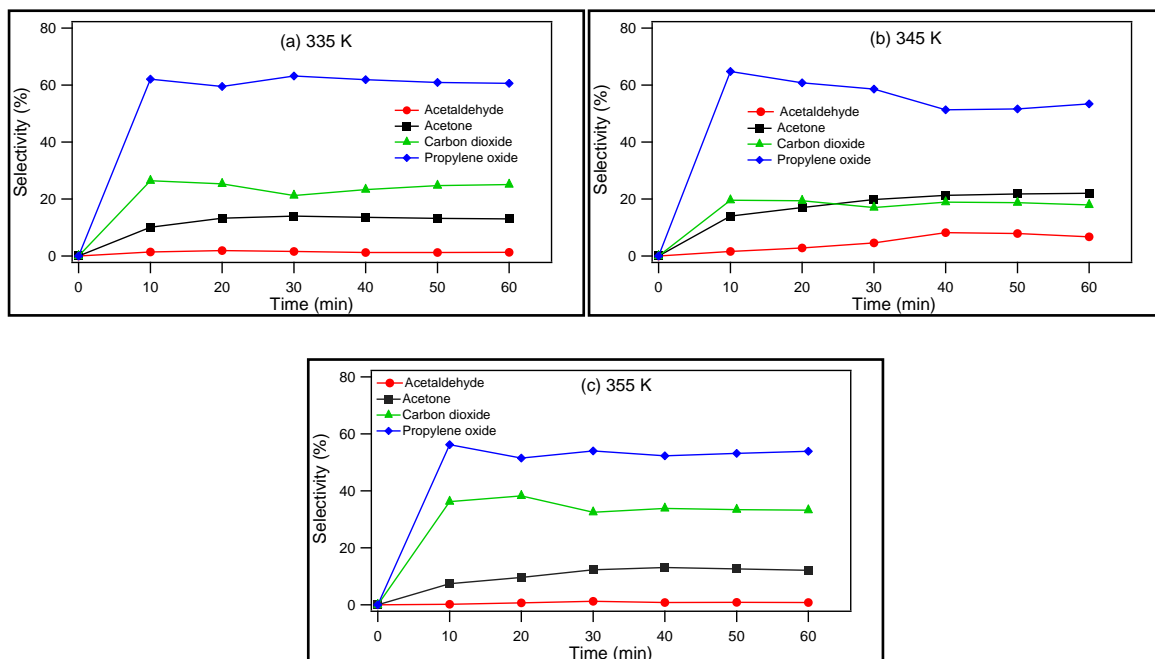
Figure 5.12: The selectivity of epoxide products on stream for different temperature conditions using B-50/TiO$_2$: (a) 335 K, (b) 345 K and (c) 355 K. Selectivity for PO was not affect by temperature, hence an Eley-Rideal mechanism.

Photo-reactions are generally known to proceed without requiring any form of heat because of photonic activation. However, Kim and Lee[293] investigated the effect of pH and temperature on photocatalytic degradation of organic compounds using carbon-coated TiO$_2$. They concluded that, since there was no true activation energy, in photo-reaction, thermal activation energy was not required to activate the reaction. [293] Therefore, the desorption rate of the final product was the limiting step while apparent activation energy tends toward the heat generated as the products were adsorbed within the range of medium temperature.[293,294] Simply put, increasing the temperature enhances efficiency of the photo-catalytic reaction by increasing desorption of reaction products which in turn releases more active sites for more reactions. However, increasing the temperature could cause difficulty in adsorption of PR on photo-catalyst consequently reducing the efficiency of the reaction. This could account for the observed efficiency decline at temperatures higher than 345 K.

5.3.5 Changing reactants concentration

Further investigation on the effect of propylene/oxygen ratio was also carried out by increasing the flow of O_2 and decreasing that of N_2 in the feed while retaining the overall reaction flow rate. Using B-50/TiO$_2$ and keeping the other reaction conditions constant, 4 different ratios were studied as shown in Figure 5.12.
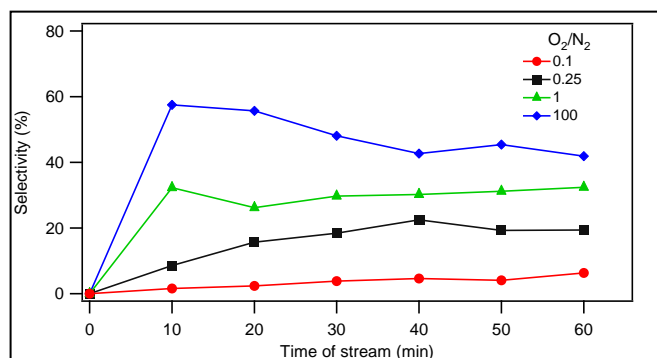
Figure 5.12: The effect of concentration of oxygen on PO selectivity with B-50/TiO$_2$.

It can be seen that mixing the two gases at a ratio of 100, afforded the optimum selectivity of PO. As the concentration of O_2 in the system increased, the selectivity of PO increased. However, decrease in the O_2 concentration i.e. at a higher concentration of N_2, total oxidation was favoured resulting in higher CO_2 production. Although the results of preliminary experiments during this study, using air as oxidant has not been presented, no PO was observed under this condition. Interestingly, at low concentration of O_2 in the ratio of 0.1, the results obtained were not too different from that of the stoichiometric ratio for attaining conditions for oxidation.[295] This result shows the significant role played by O_2 in the overall epoxidation reaction.

5.4 Photochromism of Bi_2WO_6

Upon irradiation of the coated sample of Bi_2WO_6 on the glass beads support with UV light, a dramatic change of colour from bright yellow to black was observed (Figure 5.13).

Figure 5.13: Colour change observed before (left) and after (right) the reaction

Although the colour change was only slightly grey after 15 min of illumination, it became progressively darker as the reaction continued. Figure 5.14 shows from left to right the change in colour observed after 15, 30 and 60 min of reaction respectively. Darkened UV-irradiated Bi_2WO_6 coated on glass beads kept in the dark tend to change colour from black to grey. However, upon re-illumination with UV light, the sample turned black again. This shows that the photochromic phenomenon here is easily reversible; going from coloured to bleached states could be achieved several times.[296]

Figure 5.84: Progressive colour change observed after 30 min of coating of the catalyst

The effect of change in color of catalyst observed during the photo-epoxidation reaction was investigated. Using B-50/TiO_2, under continuous UV illumination and constant flow of N_2 at 1.2 L/h for 60 min, the reactor was purged until no peak signal was observed on either FTIR or GCMS. When the catalyst had turned completely black the reactant feed was introduced into the reactor while maintaining the same reaction conditions. It can be seen from Figure 5.15 that relative to the results in Figure 5.9, using black beads resulted in an increase in selectivity of PO by 17.2 %. Carbon dioxide, acetone and acetaldehyde were all observed to decrease by 25 %, 77 % and 86% respectively.
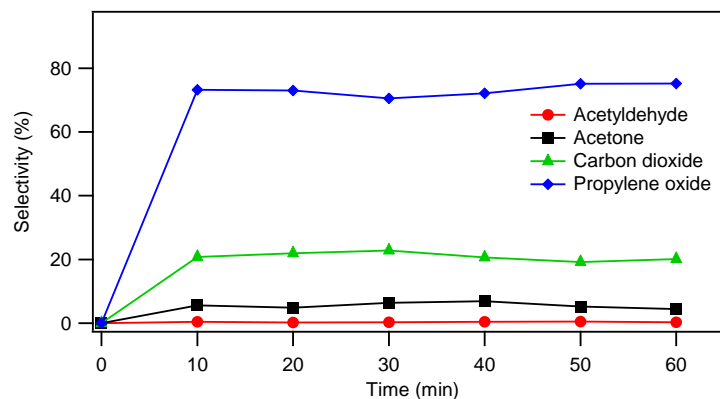
Figure 5.15: Effect of photochromism of Bi_2WO_6/TiO_2 on the selectivity of products of photo-epoxidation of PR using B-50/TiO_2.

The increase in PO selectivity shows that darkened Bi_2WO_6-TiO_2 is more effective for the production of PO in comparison to pristine (undarkened) Bi_2WO_6-TiO_2. This shows that black Bi_2WO_6-TiO_2 can effectively suppress the formation of by-products, hence promote the formation PO. Although pure Bi_2WO_6 coated on glass beads turned dark upon UV illumination, the result was not as dark as the Bi_2WO_6-TiO_2 composite as seen in Figure 5.16. It can therefore be assumed that TiO_2 played a role in the chromism behaviour, while still retaining its activity as seen in the selectivity of CO_2 (Figure 5.15).

Figure 5.16: Comparison of chromism activity between pure Bi_2WO_6 (left) and Bi_2WO_6-TiO_2 (right), both on glass beads exposed to UV illumination for 1hr.

The observed increase in the selectivity of PO over darkened Bi_2WO_6-TiO_2 could be attributed to defect formation within the band gap of Bi_2WO_6. Such defects effectively reduce the band gap causing the Bi_2WO_6 to turn into grey color.[297] Such defects can trap photo-excited electrons and decrease their reduction power, since the defect level is below the CBM of the Bi_2WO_6. The consequence of the decreased reduction power is that the reaction pathways for the formation of organic intermediates is closed and therefore, the PO selectivity is further increased. Indeed, photo-induced defect on semiconductors is a known phenomenon. It has been reported that light induces defects formation on the surface or subsurface of a photocatalyst by trapping photogenerated charge carriers and excitons.[298] Based on this mechanism, it is possible to establish that TiO_2 is responsible for the PR mineralisation, Bi_2WO_6 is responsible for the formation of organic by-products and the Bi_2WO_6-TiO_2 interface is responsible for formation of PO as illustrated in Figure 5.17. Hence, we can propose that an ideal catalyst for epoxidation of PR must have maximum Bi_2WO_6 interface with minimum isolated TiO_2 and Bi_2WO_6 phases. To achieve this, the catalyst must have smaller particle sizes with the maximum coupling between Bi_2WO_6 and TiO_2. Alternatively, if Bi_2WO_6 is in excess, the isolated TiO_2 phase can be reduced and CO_2

formation can be minimized. If in such case, Bi_2WO_6 is reduced either by chemical or physical methods, the PO selectivity could also be increased. The chemical reduction methods could involve adding reduction agents during the formation of Bi_2WO_6 or calcinating the Bi_2WO_6 in the presence of H_2, CO or alcohol. Physical methods include the photo-dichroism or calcinating the Bi_2WO_6 under vacuum.
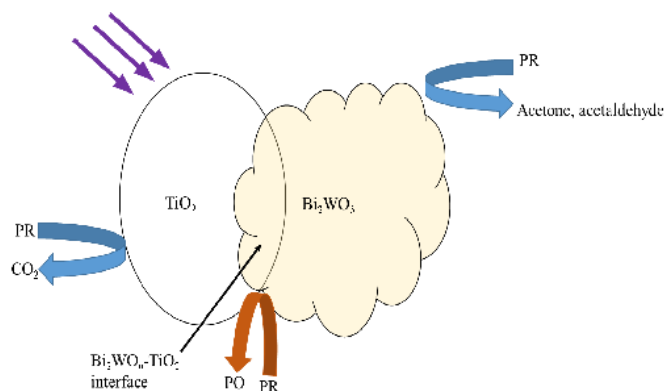
Figure 5.17: Illustration of the active sites for the formation of products of photo-oxidation of PR over Bi_2WO_6-TiO_2 composites.

The mobility and separation of charge carriers is a key factor in photocatalysis. To elucidate the higher efficiency of dark Bi_2WO_6-TiO_2 composite for the formation of PO, this factor was considered during this present work and is discussed in the next section.

5.5 Optical properties of Bi_2WO_6-TiO_2

By studying the optical properties of Bi_2WO_6-TiO_2, it was possible to establish the cause of its high efficiency toward the production of PO. Photoluminescence (PL) was utilized for this study as the emission spectra could be used to investigate the efficiency of charge carrier transfer and separation.[299] PL emission results from the recombination of the

free carriers. By exposing Bi_2WO_6-TiO_2 (white) to UV illumination for 0 min, 30 min and 60 min followed by PL analysis (at emission wavelength 350 nm), it was possible establish the results in Figure 5.18. It can be seen here that the intensity of broad peak of Bi_2WO_6-TiO_2 was reduced as illumination time increased (as it progressively became darker). It could be assumed that as Bi_2WO_6-TiO_2 changed color into black, it resulted in blocking of the fluorescence transmission and increased light scattering. Hence the decrease in intensity at 30 and 60 min.
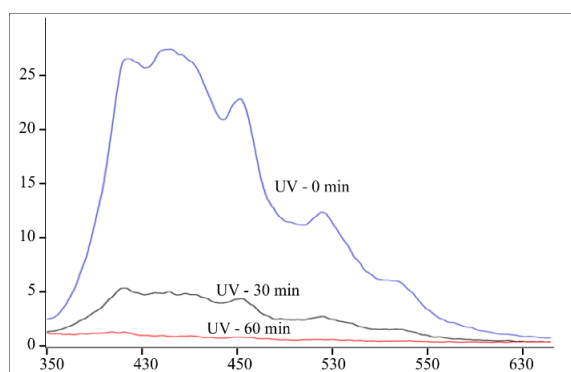
Figure 5.18: PL spectra of the Bi_2WO_6-TiO_2 (emission wavelength at 350nm) under UV illumination at 0 min, 30 min and 60 min.

In order to compare the behaviors of the three catalyst under PL, the same experiment as above was repeated. By applying PL emission wavelength at 406 nm, the results in Figures 5.19-5.21 were obtained for Bi_2WO_6-TiO_2, Bi_2WO_6 and TiO_2 respectively. The emergence of a new peak at $\lambda = 613$ nm was observed for Bi_2WO_6-TiO_2 and Bi_2WO_6, but not for TiO_2. As the time for UV illumination increased from 30 to 60 min, the intensity of the peak at $\lambda = 613$ nm for Bi_2WO_6-TiO_2 was increased and stable which was consistent with the appearance of color changed into black. Meanwhile, the phenomenon was also observed for Bi_2WO_6. Through the calculation of the intensity ratio of the new peak at $\lambda = 613$ nm to the peak at $\lambda = 485$ nm (which was identified as peak due to the glass beads and was used as an internal

reference), the ratio in Bi_2WO_6 was much lower than that in Bi_2WO_6-TiO_2 (Figure 5.19 and 5.20). Although TiO_2 could not be excited at the wavelength of 406 nm, the higher intensity of peak at $\lambda = 613$ nm for Bi_2WO_6-TiO_2 further confirms its role in promoting the chromism of Bi_2WO_6. The higher intensity of peak at $\lambda = 613$ nm also confirms defects formation on the surface of the black Bi_2WO_6-TiO_2 catalyst, hence its high efficiency in photo-epoxidation of PR to PO.
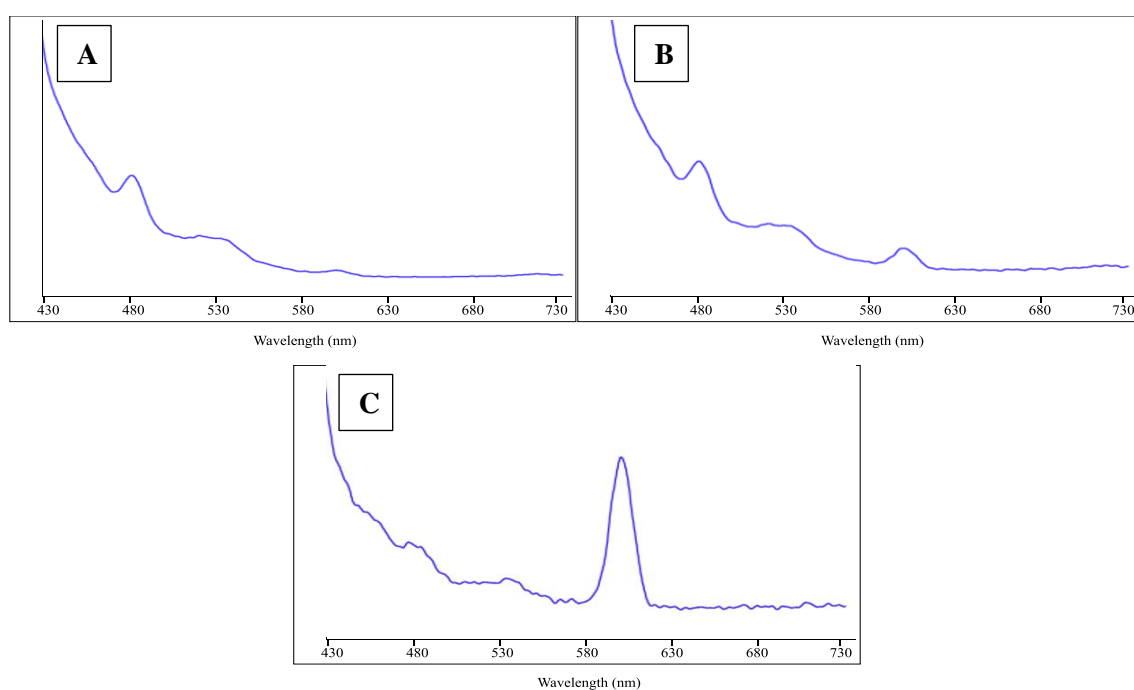
Figure 5.19: PL spectra of the Bi_2WO_6-TiO_2 under UV illumination (A) 0 min, (B) 30 min, and (C) 60 min (emission wavelength at 406 nm).
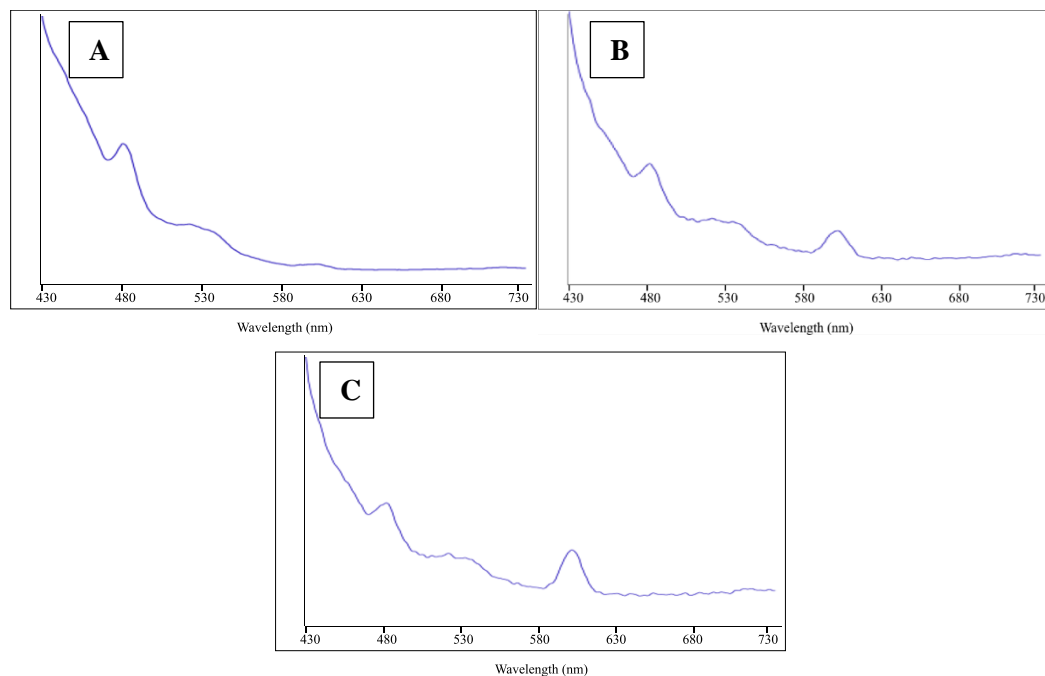
Figure 5.20: PL spectra of the Bi_2WO_6 under UV illumination (A) 0 min, (B) 30 min, and (C) 60 min (emission wavelength at 406 nm).
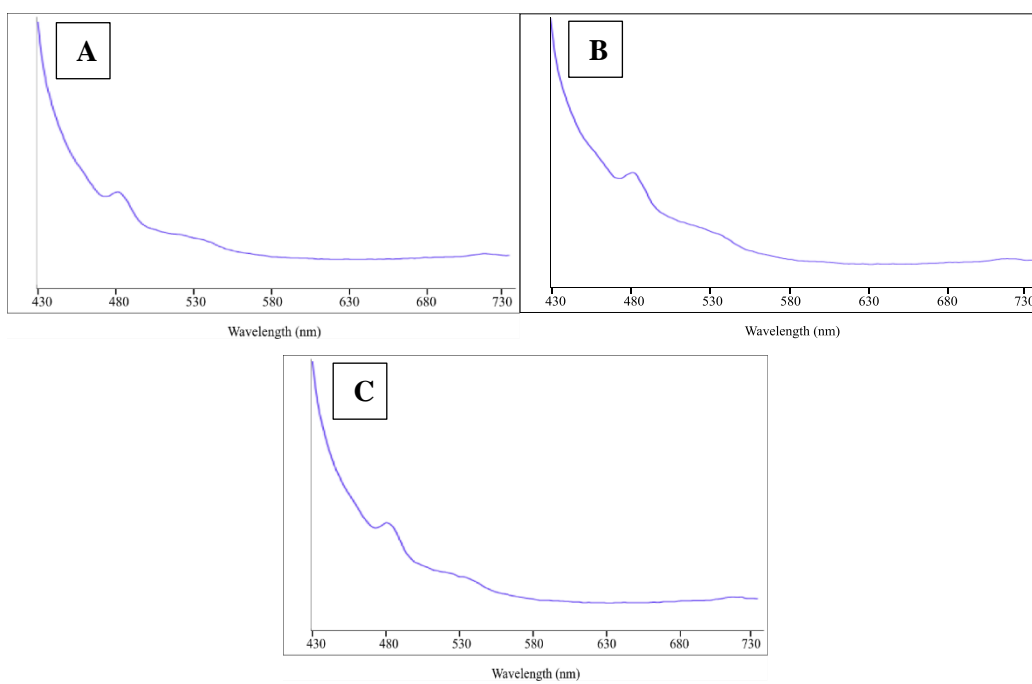
Figure 5.21: PL spectra of the TiO_2 under UV illumination a) 0 min, b) 30 min, and c) 60 min (emission wavelength at 406 nm).

5.6 Conclusions

In this chapter, TiO_2, Bi_2WO_6 and Bi_2WO_6/TiO_2 were synthesised through hydrothermal reaction. The catalysts were then coated on glass beads and used in a direct photo epoxidation process to produce PO from PR. This study shows that even though TiO_2 has high photocatalytic activity, it is not ideal for partial oxidation of propylene to PO under the studied reaction conditions. Instead, it completely mineralised the reactant into CO_2 and H_2O as the main reaction products. Bi_2WO_6-TiO_2 composite material demonstrated efficiency of photo epoxidation process. The high PO selectivity observed with this catalyst relative to pure Bi_2WO_6 showed that the interface between Bi_2WO_6 and TiO_2 is the main active site for PO formation. Hence the wider the interface, the more the active sites. This was demonstrated in the concentration of Bi_2WO_6 and TiO_2 in the composite material. The highest PO selectivity was achieved with B-50/TiO_2 which had the widest Bi_2WO_6-TiO_2 interface. The photo catalytic epoxidation of propylene can be performed at room temperature as the reaction can be initiated by photons. However, when the effect of temperature on the photocatalytic epoxidation of propylene over the studied photo catalyst was investigated, it was revealed that there exists an optimum temperature that favours the production of PO, 345 K. The results obtained in this work also show that the effect of temperature on the photo-epoxidation reaction temperature is two-fold. While increase in temperature accelerates surface reaction, it can also lead to decrease in the adsorption of reactants on the surface of the photo-catalyst.

Bi_2WO_6-TiO_2 powdered samples coated on glass beads changed colour from pale yellow to black within an hour of reaction. The presence of TiO_2 in the Bi_2WO_6-TiO_2 plays an important role in the dichroism of the catalyst. The darkenend catalyst was more efficient in the selectivity of PO largely due to photo-induced defect formation in the composite

material. This was confirmed by photoluminescence analysis. The results in this study show that Bi_2WO_6-TiO_2 can be alternative photo-catalyst for the effective production of PO under mild and more environmentally friendly way.

Chapter 6: Kinetic Study of Photo-epoxidation of Cyclohexene in Gas-Phase

The efficiency of the photo-reactor designed in Chapter 3 was further tested in studying the kinetics of the epoxidation of cyclohexene in gas-phase. H_2 and O_2 gases were used as redox agents. Titanium dioxide (TiO_2) and Titanium silicate (TS-1) were prepared and used as photocatalysts. Stable production of cyclohexene oxide was achieved with the TS-1 while only total mineralisation to CO_2 was achieved with the TiO_2. The kinetic analysis conducted here showed that the gas-phase reaction mechanism follows the Eley–Rideal mechanism. Gas phase cyclohexene reacted directly with the intermediate formed through reaction between Ti base and the hydroperoxyl species, to produce cyclohexene oxide. Thus, this step was considered the rate-determining step. The effect of temperature was investigated at various partial pressures of individual gas reactant. An approximate value of 31 $kJmol^{-1}$ of activation energy was achieved. No epoxide was produced in the absence of H_2 under the experimental conditions studied here. Total mineralisation of cyclohexene to CO_2 was observed when O_2 was used alone in the system.

6.1 Introduction

Choice of oxidant during epoxidation reactions of alkenes is often seen as a challenge for this process. While molecular oxygen remains the ultimate oxidant, a lot has been done to minimise the total mineralisation through the use of other oxidants such as H_2O_2, H_2O and

in some cases, air. However, other factors such as the environmental hazards, selectivity of desired products and chemical costs come into play when the choice for the type of oxidant is made.[300] Hydrogen peroxide has been used extensively for epoxidation of alkenes owing to the fact that it only produces water as a by-product.[301,302] Higher olefins such as 1-hexene have been converted to their corresponding oxides using H_2O_2.[303] Such reactions are typically performed in liquid phase using batch reactor setup, in which the overall reactivity of the catalyst can be influenced by the solvent used, which adversely affects the selectivity of products. Separation of product can also be a challenge.[304–306] The effect caused by solvent type can be due to its hydrophilic and hydrophobic interaction with the catalyst, oxidants and the alkene undergoing reaction.[304] However, reactions such as this, can also be performed in gas-phase with higher reaction rates, high selectivity and high reaction stability at higher operating temperature and pressure. Furthermore, it is possible to avoid leaching of the active sites, which is a typical challenge in liquid-phase when gas-phase is used.

In gas phase, H_2O_2 can be directly produced by catalytic reaction of H_2 and O_2 in the presence of Au-doped Ti.[264] The H_2O_2 is produced on the Au particles while the epoxidation reaction occurs on the Ti active sites. It was believed that the H_2O_2 was converted to the hydroperoxyl species on the nearby Ti sites in the form of Ti-OOH.[170] However, most of the thermal alkene epoxidations have to use H_2O_2 as the main oxidant. The challenge in the use of H_2O_2 as an oxidant is to maximise the formation of epoxides without mineralisation of the alkenes.[307] By using H_2O_2 in a gas-phase directly in the epoxidation process, the decomposition of alkenes can be minimised according to the report by Klemm *et al*.[308] In another report by Ferrandez *et al*.[309] an epoxidation rate of 10.5 kg_{po} kg_{cat}^{-1} h^{-1} and selectivity of 90 % was achieved when H_2O_2 vapour was used alongside TS-1 to convert propylene to propylene oxide.

In this chapter, kinetics study of cyclohexene was carried out with emphasis on the mechanism of gas-phase epoxidation using H_2 and O_2 to form hydroperoxyl species through photoexcitations over TS-1 photocatalyst. The direct epoxidation of alkene, using the co-reactants H_2 and O_2 and oxygen is highly selective over gold-titania based catalysts and has gained considerable attention in the past decade.[170] Although this catalytic reaction has been investigated extensively, the mechanism is still not well understood.

Hydroperoxyl formation can occur by protonating a superoxide radical.[310] The supplied O_2 is adsorbed on the photocatalyst and is reduced by the photo-generated electrons to form superoxide radicals. The adsorbed H_2 is oxidised by the photogenerated holes and forming protons. This proton reacts with the nearby superoxide radicals to form hydroperoxyl species ($HO_2^{\bullet}$), which was stabilized by attaching to the transition metal ion, Ti^{4+} and forming Ti-OOH.[311] The resulting Ti-hydroperoxyl (Ti-OOH) complex reacts with alkenes to form corresponding epoxide. Similar reactions in the literature show that a number of oxidation pathways exist which inhibit the selectivity of cyclohexene oxide.[312–315] In this work, I will try to establish the mechanism for the photocatalytic epoxidation with H_2 and O_2 based on the kinetic measurements.

6.2. Experimental details

6.2.1. Preparation of TS-1

TS-1 was prepared hydrothermally, through wetness impregnation using a modified procedure reported by Deng *et al*.[316] and Zhang *et al*.[317] The catalyst was prepared in stages described in the following subsections.

6.2.1.1 Sol-gel preparation

Sol-gel was prepared by hydrolysing tetraethyl ortho-silicate (TEOS, 98 %, Acros) with 0.05 M hydrochloric acid (HCl, 32 %, AnalaR) under magnetic stirring at room temperature. The mol ratio used was 1:4 of HCl:TEOS. Separately, titanium (IV) chloride (TiCl$_4$, Sigma Aldrich) and isopropyl alcohol (IPA, Fisher Scientific) in a ratio of 15:2 of IPA:TiCl$_4$ were mixed, stirred and added dropwise to the silicate-acid solution under continuous stirring. The silicalite and Ti mixture were then mixed by adding the former in to the latter under stirring. The obtained sol was allowed to age for 1 h at room temperature.

6.2.1.2 Gelation

The prepared sol-gel from above was transformed to a solid cogel by dropwise adding 10 mL 20 % solution of tetrapropylammonium hydroxide (TPAOH, Sigma Aldrich). However, the gel point obtained depends on the amount of base added. The product obtained was then dried in an oven at 60℃ overnight.

6.2.1.3 Wetness impregnation

The impregnated gel was transferred to a Teflon autoclave and heated at 120°C under auto-geneous pressure for 24 hr. The product was cooled at room temperature and the crystals were filtered using vacuum filter, washed with water and dried under ambient temperature. The final product was then calcined at 550°C for 24 hr in air. 87 % yield of the final product was obtained based on the amount of TiO$_2$ and SiO$_2$ in the starting materials.

6.2.2. Characterization

XRD patterns were obtained using a Siemens powder X-500 diffractometer. SEM analysis of the synthesised TS-1 was performed using a Jeol-JSM 820 Scanning Electron Microscope. Elemental analysis was performed using a Leica Stereoscan 420 Energy Dispersive X-ray Spectroscopy. The surface area BET measurements were performed on JWK-B122 surface area and pore size distribution analyser 77 K.

6.2.3. Cyclohexene epoxidation reactions

The schematic for the gas-phase epoxidation kinetic studies is shown in Figure 6.1. A similar setup as used in chapter 5 was also used here but with additional attachment for the H_2 source. The reactor consisted of a quartz tube plugged at both ends for inlet and outlet of reactants and products respectively. All photocatalytic reactions were performed in a flow system under various conditions. TS-1 and P25 TiO_2 were used as the catalysts. The catalyst was immobilised on glass beads following the detailed procedure in chapter 3 of this work. Hydrogen was supplied from a hydrogen generator (SPE300HC Hydrogen Generator, Union Space Int'l Ltd.) and mixed directly with pure oxygen in a round bottomed flask that was stocked with quartz wool to ensure adequate gas mixing. The gas mixture was fed directly to the catalyst coated glass beads. Cyclohexene was admitted into the reactor in gaseous phase by placing liquid cyclohexene (5mL) in a Dreschel bottle where nitrogen gas was used as a carrier gas to deliver gaseous cyclohexene into the reactor at a total flow rate of 1.4 ± 0.2 Lh^{-1} controlled by rotameter. At this point, the concentration of cyclohexene was monitored through the FT-IR/GCMS tandem analysis. All standard reactions were performed under ambient conditions. The boiling points of cyclohexene and cyclohexene oxide are 83ºC and

130ºC, respectively. In order to minimise deposition of chemicals in transfer tube, all the connection tubings, particularly the outlet tubings, were shortened as much as possible. Upon attaining a steady state flow in the reactor, i.e. at adsorption desorption equilibrium, UVA lamps were turned on to initiate the photoreaction. Changes in concentration of cyclohexene as well as the products formed were monitored in a tandem FTIR-GCMS analysis, similar to the one we described in previous chapters. The outlet of the reactor was connected to the IR sampling cell with NaCl windows which was in turn connected to a modified GCMS auto-sampler (Figure 5.2). FTIR and GCMS data were collected every 3 min. This sampling frequency is restricted by the retention time of the targeted chemicals in the GC.
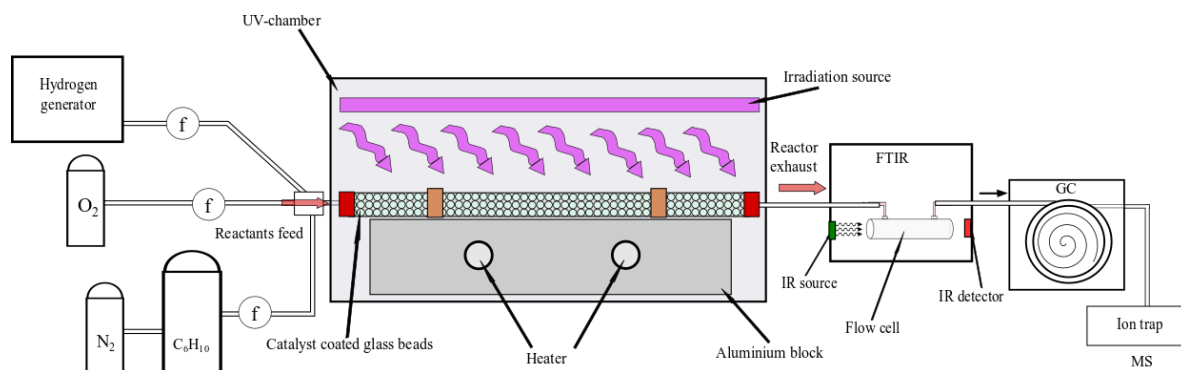
Figure 6.1: Experimental set up for gas-phase cyclohexene epoxidation with H_2 and O_2.

The epoxidation products were separated using an Rxi-5Sil MS fused silica column with total length of 30 m. The inner diameter of the column is 0.25 mm while the film thickness is 0.25 μm. The column was engineered to be a low-bleed GC-MS column. The column was set at a pressure of 10 psi for the carrier gas and a constant temperature of 130°C, similar to the boiling temperature of cyclohexene oxide. The gaseous mixtures were introduced to the GC through auto-injection at a fixed interval of 3 min. A carrier gas of helium was used at a flow rate of 100ml/min. Data was collected for at least 1 h under each

set of conditions to allow attainment of steady state concentrations of the products. During the kinetic studies, the effect of partial pressure of individual reactant was studied. Since all reactants were delivered in gaseous phase there was no consideration to the possibility of condensation of reactants in transfer line when determining the partial pressures. In a typical photo-epoxidation reaction, the partial pressures of the reactants were: 3 kPa, 5 kPa and 20 kPa for cyclohexene, hydrogen and oxygen respectively. 5mg of catalyst per gram of glass beads was found to be ideal for this reaction.

6.3. Results and discussion

6.3.1 TS-1 characterisation

The XRD pattern of the TS-1 sample prepared by the hydrothermal method is shown in Figure 6.2 in the *2θ* ranging from 5 to 40º. The diffraction peaks at *2θ* = 7.8°, 8.8°, 23.1°, and 23.9° match well with the characteristic MFI-type structure of TS-1. A typical silicate-1 exhibits an amorphous crystallite in its XRD pattern even if it contains low amounts of Ti. Depending on the content of Ti in the framework, TS-1 shows well defined diffraction peaks typical of MFI topological structure. [165] The high crystals of TS-1 may be attributed to the linear increase in the unit cell parameter and volume relative to Ti content in the framework as suggested by some literature reports.[318–320] It can be seen in Figure 6.2 that the TS-1 synthesised during this study exhibited high phase purity, judging by the appearance of the characteristic peaks above.
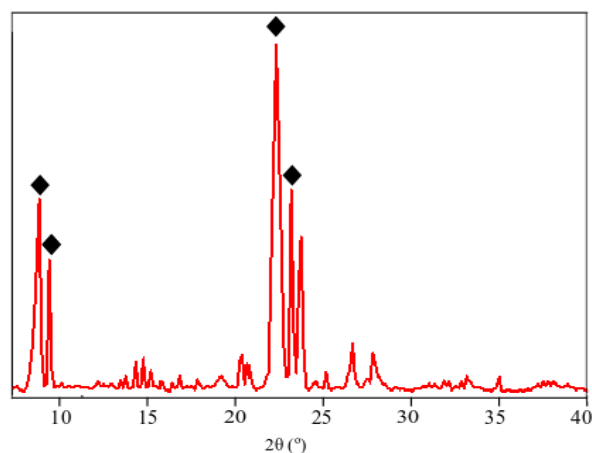
Figure 6.2: XRD pattern of TS-1

SEM image of synthesized TS-1 is shown in Figure 6.3. It has a particulate morphology with particles diameter of about 150 nm. Different morphologies of TS-1 have been reported in the literature. For instance, Zhao *et al.*[321] reported a spherical morphology of nanosized crystallites without characteristic hexahedron configuration.
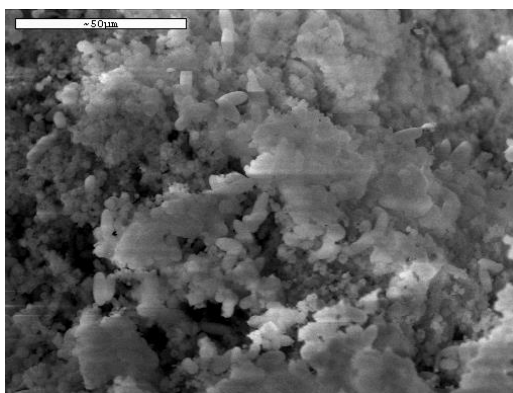
Figure 6.3: SEM image of synthesised TS-1 showing grain-like particles.

To further verify the composition of the synthesised TS-1 in this work, EDX analysis was performed and the result shown in Figure 6.4. It can be seen that the composite consisted of Ti, Si and O. The additional peak with high intensity is ascribed to C, which was used as support material during the EDX analysis.
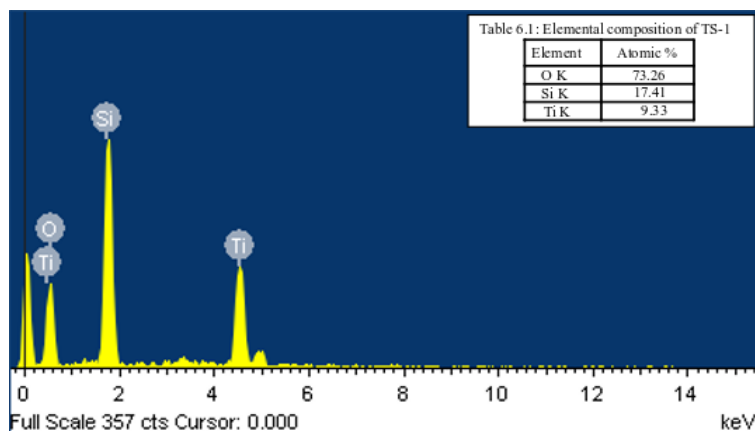
Figure 6.4: EDX showing elemental composition of the synthesised TS-1

The atomic percentages of the constituent elements are given on the inset Table 6.1. These values agree with the ratio (2:1, Si:Ti) of the input chemicals during the synthesis of the catalyst, hence confirming the purity of the catalyst.

6.3.2 Gas-phase cyclohexene epoxidation

One of the major challenges associated with using hydrogen peroxide in gaseous phase is its tendency to decompose under thermal condition.[322] Studies on its decomposition rates show that the nature of the material used for the reaction plays a vital role on the rate of decomposition. Satterfield *et al.*[323] reported that the decomposition rate is higher when metals are used compared to when borosilicate or quartz. This knowledge was an advantage in this work as it provided the basics for the use of quartz tube packed with catalyst coated glass beads, hence the stability of the hydroperoxyl species was improved. In this work, hydroperoxyl species are expected to be formed on the catalyst as the product of the reaction between H_2 and O_2. It is important that these hydroperoxyl species are able to react with

cyclohexene as soon as it was formed, due to its limited lifetime. To verify that both H_2 and O_2 was responsible for the epoxidation of cyclohexene, studies were performed by altering the partial pressure of individual species during photoreaction. First, the partial pressure of O_2 was reduced by half while that H_2 was kept constant. It was not surprising to see that the conversion of cyclohexene decreased by 80% and zero conversion was achieved when no O_2 was supplied to the system. Without H_2, total oxidation of cyclohexene was observed, as CO_2 was the main product and no epoxide was observed across the photocatalysts tested. This indicates that H_2 is responsible for the selectivity cyclohexene epoxidation while O_2 is responsible for the conversion of cyclohexene. It is also important to mention at this point that no reaction was observed in the absence of either catalyst or light.

To study the intrinsic behaviour of the catalyst , the reactants' stoichiometry should not limit the reaction under specific conditions of differential conversion.[324] Therefore, it was of high significance to ensure that the hydroperoxyl species was constantly formed on the active sites of the catalyst for the production of Ti-OOH complex and subsequent conversion of cyclohexene.[325,326]

The conversions and selectivities of cyclohexene and products respectively were quantitatively determined. Turn over frequency (TOF) was determined according to the mole of cyclohexene oxide produced per mole of Ti per second and was used to represent the product formation rate. No epoxide was made under standard conditions of reaction with TiO_2, and only CO_2 remained the dominant product with a selectivity of 96% while ketone and alcohol were formed with selectivities of 2.8 and 1.2 % respectively.

TS-1 showed activity towards formation of cyclohexene oxide with selectivities of 38.1 %. Unfortunately, the cyclohexene oxide selectivity obtained during this work was lower than the reported value in the literature. Kwon et al.[327] recorded up to 74.1 % of cyclohexene

oxide selectivity with their mesoporous TS-1. However, their experimental conditions were more complex than those used in this chapter. This group used temperature range between 120°C and 160°C at 50 ml/min, while a milder temperature ranging from 60°C to 80°C at 20 ml/min (1.4 L/h) was used in this chapter. Nevertheless, the use of O_2 and H_2 to generate in-situ reaction intermediates remains advantageous over the use of more expensive H_2O_2, which can also decompose easily resulting in undesirable products.[325]
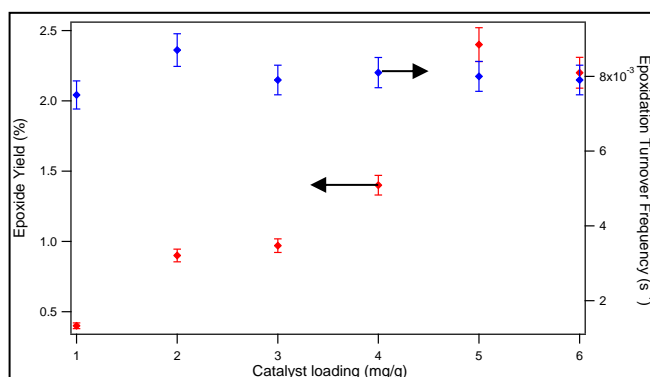
Figure 6.5: Cyclohexene oxide yield (red diamonds) and TOF (blue diamonds) under different catalyst (TS-1) loading.

TS-1 was tested in different amounts to study the effect of catalyst loading on the photoepoxidation of cyclohexene. Figure 6.5 shows that the yield of cyclohexene oxide increased while TOF remained unchanged with increase in the catalyst loading. The highest yield for cyclohexene oxide was achieved at the optimal catalyst loading of 5 mgg^{-1} and the yield was reduced as the loading was increased to 6 mgg^{-1}. Meanwhile, the cyclohexene oxide yield decreased from 2.39 % (at 5 mgg^{-1}) to 2.2 % (at 6 mgg^{-1}). Such decreases could be related the increased diffusion path length as the thickness of the catalyst increases. The TOF is directly determined by the surface concentration of the hydroperoxyl. As TOF is

independent of TS-1 loading, it suggests that the epoxidation happens on the surface of the TS-1 catalyst, so the thickness of the TS-1 film is not affecting the reactivity. The effective surface area can be increased by using smaller glass beads as supporting media. So, it is possible to increase the epoxide yield using smaller beads. In Chapter 3, I have established that the total beads surface area is inversely proportional to the radius of the beads. By reducing the radius by half, one can expect to double the yield. These results are in agreement with those reported by Kwon *et al.*[324] in their cyclohexene epoxidation reaction over mesoporous TS-1. Contrary to the findings of Ferrandez *et al.*[309] where they found the conversion is relatively independent of the amount of TS-1 used. They ascribed their observation to the limited amount of the H_2O_2 present in the system due to its rapid decomposition. In both examples, H_2O_2 was used as oxidant.

6.3.2.1. Stability

The stability test was performed by measuring the formation of cyclohexene oxide at the optimal catalyst loading of 5mgg^{-1} up to six hours of reaction.
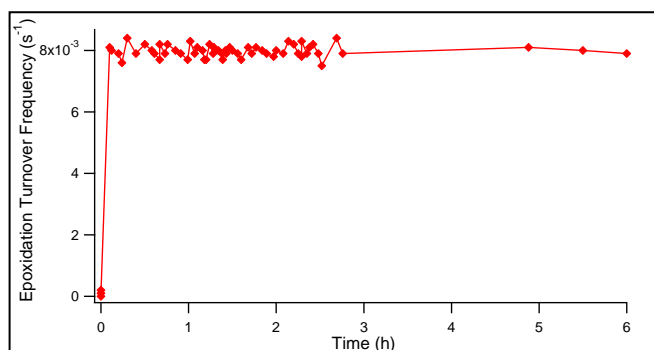
Figure 6.6: Gas-phase cyclohexene epoxidation turnover frequency over time with 5 mg of TS-1 and total flow rate of 2.8 Lh^{-1}

Figure 6.6 show that a steady TOF was maintained with no sign of degrading, suggesting that the catalyst was remaining active. Contrary to the findings on Au-doped TiO_2 which was deactivated within a short period of reaction time, the TS-1 used in this work proved to be stable with no observable sign of deactivation over the period of the reaction. Although still a subject of debate, the rapid deactivation in Au-doped TiO_2 is widely believed to be due to the generation of H_2O_2 which oxidizes surface Au atoms.[328]

6.3.2.2. By-products

During the gas-phase epoxidation of cyclohexene with hydroperoxyl radicals formed on titanium silicate catalyst (TS-1), high selectivity towards cyclohexene oxide was observed. Only negligible amount of the ring-opening products, such as 1,2-cyclohexanediol was observed and so was not considered in determining the yield of epoxide. Ketone and alcohol were also formed only in small quantities. This observation agrees with reports on liquid phase reactions under similar conditions.[304,329] Some reports suggested that epoxidation reaction proceed through a simple electrophilic oxygen transfer while others reported that an allylic oxidation proceed through a radical pathway.[330,302,315] Similar observation was made by Klemm *et al.*[308] in their study of propylene epoxidation over TS-1 catalyst and H_2O_2.[308] The details of the epoxidation mechanism and competitive pathway for byproducts will be discussed later.

6.3.3.1. Temperature effect

The dependence of the production rate of the epoxide on temperature was investigated in order to study the possible reaction mechanism and to evaluate the reaction activation

energy. With light on, the reactor will reach a stable temperature of 335 K over a period of 1 hr. The reactor temperature was then controlled by applying heat on a purpose-built aluminium block. This way, the maximum temperature of 433 K can be achieved. Here, we use TOFs for cyclohexene oxide to represent the reaction rates. A single set of reaction parameters showed a typical Arrhenius kinetics, as expected. However, adjusting the in-flow of reactants into the reactor resulted in different trends in the apparent activation energy. In general, by increasing the partial pressure of all reactants, including cyclohexene, H_2 and O_2, the reaction rates increase, as observed from Figure 6.7. All the Arrhenius curves show a negative gradient, which suggests a positive reaction energy barrier. However, by changing the cyclohexene partial pressure from 1 to 5 kPa, there was no significant change of the activation energy with an averaging value of 15.03 kJmol^{-1}, shown in Figure 6.7A. On the other hand, for both H_2 and O_2, the changing of their partial pressure could affect the apparent activation energy, shown in Figures 6.7B and C. For H_2 gas, the change of the partial pressure from 2 to 6 kPa, the activation energy increases from 22.4 to 12.46 kJmol^{-1}. Less effects on the activation energy was observed for O_2 gas pressure.
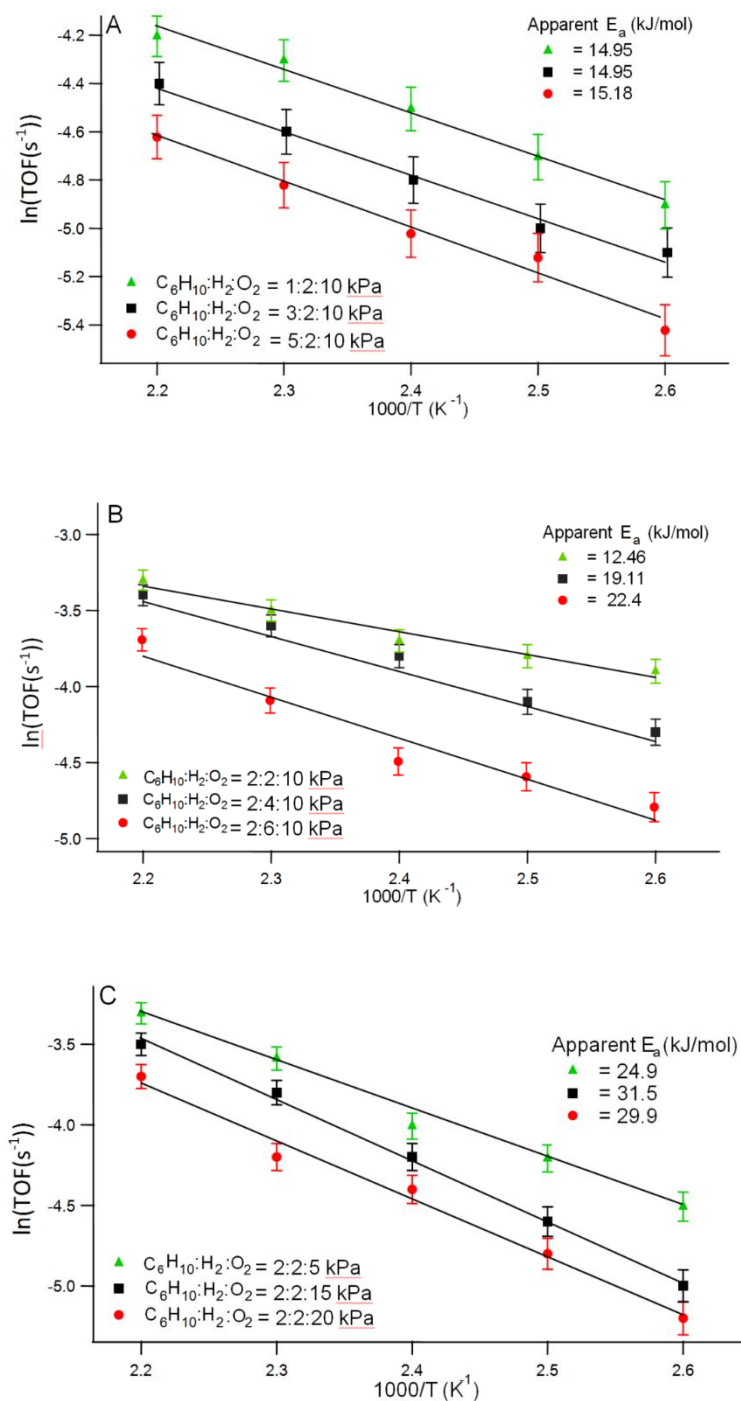
Figure 6.7: Temperature dependence of cyclohexene oxide production rate with different partial pressures of reactants over TS-1 photocatalyst loaded at 5mgg^{-1}.

Such observation, suggests that the final step of epoxidation of cyclohexene is probably elementary single step, while the reaction of H_2 and O_2 are less simple and likely to involve

multiple steps. In principle, it is impossible to have H_2 and O_2 directly reacting with cyclohexene on TS-1 surface under light illumination, since it involves the simultaneous collision of three chemicals on the same site on the solid surface. Thus, as suggested from literature[331] and described in the introduction of this chapter, H_2 and O_2 must be adsorbed on the TS-1 surface, dissociate and photocatalytically form the critical intermediate of hydroperoxyl species, OOH. The importance of hydroperoxyl in the epoxidation of alkenes on catalst surface has been well established in the literature.[34,166,169,170,331] This species is assumed to be stabilized by attaching to the Ti cations, denoted as Ti-OOH.[170] As such, the reaction kinetics is related to the partial pressure. The Arrhenius behaviour as a function of cyclohexene partial pressure suggests that cyclohexene can be oxidized by the formed Ti-OOH directly in a single step. So, it is likely that the reaction follows the Eley-Rideal mechanism in which an adsorbed chemical reacts with a gas phase molecule. The adsorption of water on active sites of the catalyst is competing with the formation of Ti-OOH. Increasing the reactor temperature however, would cause a decrease in the amount of water adsorbed consequently, increasing the number of sites available for the formation of hydroperoxyl species. Hence the TOF for cyclohexene oxide increased as the reaction temperature increased.

6.3.4. Reaction mechanism

The oxidation of alkenes to corresponding epoxides using a Ti-based catalyst and hydrogen peroxide is widely reported to proceed through two major pathways. First, the reaction between Ti site and the hydrogen peroxide species which results in the formation of

a titanium-hydroperoxo complex (Ti-OOH) and secondly, the closer oxygen atom to the Ti in the Ti-OOH is transferred to the alkene resulting in the formation of the epoxide.[327,303,332]

$$Catalyst \xrightarrow{h\nu} e^- + h^+ \qquad (6.1)$$

$$O_2 + Catalyst \longrightarrow O_2\,(ads) \qquad (6.2)$$

$$e^- + O_2\,(ads) \longrightarrow O_2^{\cdot-}(ads) \qquad (6.3)$$

$$2h^+ + H_2 \longrightarrow 2H^+ \qquad (6.4)$$

$$O_2^{\cdot-}(ads) + H^+ \longrightarrow Ti\text{-}OOH \qquad (6.5)$$
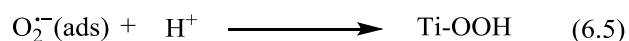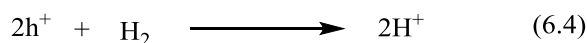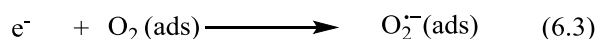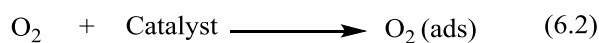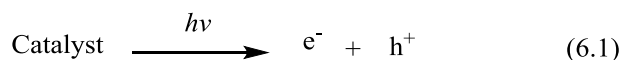
In this work, the overall reaction begins by illumination and generation of photoexcited electrons (e^-) and holes (h^+) (Equation 6.1). O_2 is adsorbed on the surface of the catalyst (Equation 6.2). The adsorbed O_2 was then reduced to superoxide radical O_2^- (Equation 6.3). Meanwhile H_2 is oxidised to proton (Equation 6.4). Although it is difficult to confirm whether H_2 was adsorbed on the surface before oxidation, the result proton is very likely attached to the nearby O atoms in the silicate, forming OH groups, holding by the relative weak hydrogen bond. The proton will react with the superoxide radicals to form hydroperoxyl species, OOH attached to the Ti^{4+} metal ions (Equation 6.5). Obviously, without H_2, the photoexcited hole (h^+) will oxidise the alkene instead which will lead to the fragmentation and mineralization of alkene, rather than epoxidation. In this work, no epoxide was formed in the absence of H_2 and no significant amount of alkene was observed to adsorb on the active site of the catalyst (perhaps due to its low BET surface area ($21\ m^2g^{-1}$)). The structure of Ti-OOH intermediate is proposed in Scheme 6.1.

The formed surface Ti-OOH complex reacted with gas phase cyclohexene to form the cyclohexene oxide as shown in Scheme 6.1. Therefore, the epoxidation of cyclohexene under our experimental conditions is an Eley-Rideal type.[303] This result is similar to the liquid-phase epoxidation reported by Sever and Root when they carried out a DFT study of the epoxidation of ethylene using a Ti-based catalyst in the presence of H_2O_2.[332] The desorption of the epoxide results in regeneration of the active sites, ultimately inducing a recycled competitive adsorption of water and hydroperoxyl species onto the active site.[333]
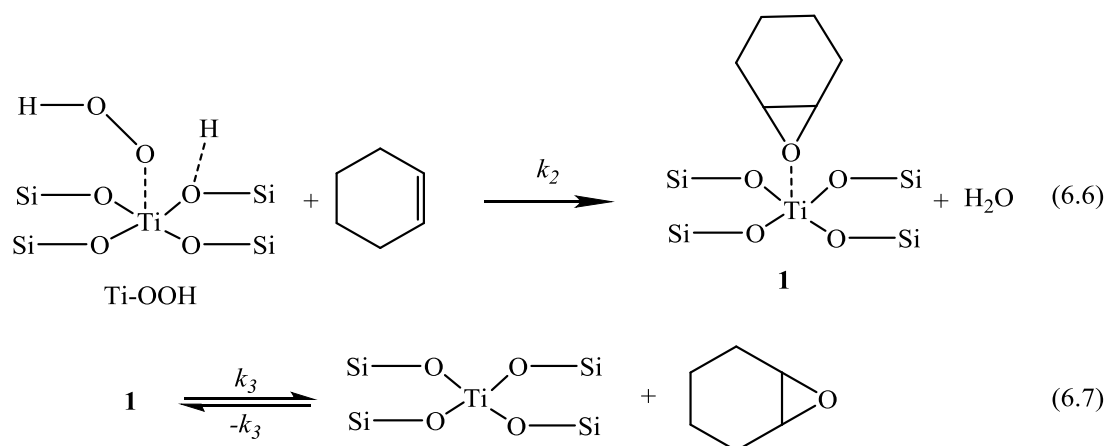
Scheme 6.1. Proposed reaction mechanism for cyclohexene with Ti-OOH species.

Following the proposed mechanism, it is possible to establish the reaction kinetics. Here we assume the O_2 is adsorbed on the Ti^{4+} site while H_2 is attached to the SiO sites. So there is no direct competition for the adsorption of O_2 and H_2 on TS-1 surfaces. However, if element transition metals, such as Pd or Pt, are used, both O_2 and H_2 will adsorbed on the same sites and directly react them to form water. I also assumed that the redox of the adsorbed O_2 and H_2 are relatively efficient and are not rate limiting steps.

$$\theta_O = \frac{K_O P_{O_2}}{(1 + K_O P_{O_2})} \qquad (6.8)$$

$$\theta_H = \frac{K_H P_{H_2}}{(1 + K_H P_{H_2})^{\frac{1}{2}}} \times \frac{1}{[1 + (K_H P_{H_2})^{\frac{1}{2}}]} \qquad (6.9)$$

Gases, such as O_2 and H_2, are normally weakly adsorbed on silicate surface, due to their non-polar nature.[331] Hence at low gas pressure, the adsorption likely follows the Langmuir isotherm. The equilibrium is described in Equations 6.8 and 6.9, where θ_O and θ_H are the surface coverages for O_2 and H_2. P_{O_2} and P_{H_2} are the partial pressures for O_2 and H_2. K_O and K_H are the Langmuir constant for O_2 and H_2 on TS-1 surface. For H_2, a dissociative adsorption on the silicate is calculated. The reduced O_2 and oxidised H will react to form hydroperoxyl species. Assuming an equilibrium is reached with steady state concentration of Ti-OOH, its concentration can be expressed as:

$$\theta_{\text{Ti-OOH}} = k_{OH} \theta_O \theta_H \qquad 6.10)$$

where k_{OH} is the equilibrium constant for the formation of Ti-OOH, which includes the redox process and protonation of superoxide radicals. Equation 6.10 can be extended as:

$$\theta_{\text{Ti-OOH}} = \frac{k_{OH} K_O P_{O_2}}{(1 + K_O P_{O_2})(K_H P_{H_2})^{\frac{1}{2}}} \times \frac{1}{[1 + (K_H P_{H_2})^{\frac{1}{2}}]P_C} \qquad (6.11)$$

Therefore, the reaction rate for the epoxidation of cyclohexene can be described as:

$$r_e = k_e \theta_{TiOOH} P_C$$

$$= \frac{k_e k_{OH} K_O P_{O_2}}{(1 + K_O P_{O_2})(K_H P_{H_2})^{\frac{1}{2}}} \times \frac{1}{[1 + (K_H P_{H_2})^{\frac{1}{2}}] P_C}$$

$$= \frac{k_e k_{OH} K_O P_{O_2}}{(1 + K_O P_{O_2})(K_H P_{H_2})^{\frac{1}{2}}} \times \frac{1}{[1 + (K_H P_{H_2})^{\frac{1}{2}}] P_C P_{O_2}} \qquad (6.12)$$

where P_C is the partial pressure of cyclohexene. Here, I have also assumed that the formed epoxide will desorb from the site immediately without competitively disturbing the adsorption equilibrium of hydroperoxyl species. If this condition is not satisfied, significant amount of mineralization will happen and large quantity of CO_2 will be formed.

Equation 6.12 is a typical formula for the Eley-Rideal type reaction. It is clear, that for cyclohexene, the apparent rate constant is defined as:

$$k_C = \frac{k_e k_{OH} K_O P_{O_2}}{(1 + K_O P_{O_2})(K_H P_{H_2})^{\frac{1}{2}}} \times \frac{1}{[1 + (K_H P_{H_2})^{\frac{1}{2}}]} \qquad (6.13)$$

which is independent of P_c. Therefore, the calculated activation energy is independent of P_c, as we observed from the Arrhenius plots in Figure 6.7A. However, for O_2, the apparent rate constant is defined as:

$$k_O = \frac{k_e k_{OH} K_O P_{O_2}}{(1 + K_O P_{O_2})(K_H P_{H_2})^{\frac{1}{2}}} \times \frac{1}{[1 + (K_H P_{H_2})^{\frac{1}{2}}] P_C} \qquad (6.14)$$

It clearly demonstrated that the apparent rate constant is also affected by the O_2 partial pressure P_{O_2}. Therefore, the obtained activation energy can be a function of P_{O_2}, as we have observed from Figure 6.7C. Similar behaviour could be analysed for H_2, although its kinetics is more complicated, since it follows a dissociative adsorption.

6.4. Conclusions

A successful demonstration of epoxidation of cyclohexene over TS-1 and hydroperoxyl under UV illumination was achieved. Under the experimental conditions, no cyclohexene oxide was produced over TiO_2 even in the presence of H_2 and O_2. TS-1 produced cyclohexene oxide with high stability only when H_2 and O_2 were simultaneously present in the reaction system. No epoxide was formed in the absence of H_2. The gas-phase epoxidation of cyclohexene is believed to follow the same type of mechanism as that proposed for the liquid-phase reaction, known as the Eley–Rideal mechanism. The reaction between superoxide and hydrogen formed the hydroperoxyl which reacted with the Ti site of the catalyst to form the Ti-OOH complex. Other forms of active oxygen and peroxo species may be generated within the reaction system from the presence of H_2 and O_2, and as such, new reaction pathways resulting in the generation of different products may be possible. The effect of temperature and partial pressure was investigated, and the true apparent activation energy was determined to be 31.5 kJmol^{-1}. The results obtained in this work provide the possibility of utilizing H_2 and O_2 for various oxidation reactions at elevated temperatures.

Chapter 7: 1-Hexene Photo-Epoxidation in Gas Flows

The photo-reactor design technology was tested for photo-epoxidation of 1-hexene in gas flow system. A chemical synthetic reactions application was also attempted. Photo-epoxidation of 1-hexene and nucleophilic ring opening of 1,2-epoxyhexane under acidic condition was investigated. During these studies, various partial photo-oxidation products were formed from the conversion of 1-hexene. The light induced epoxidation potential of TiO_2 was first tested by photo-catalytic oxidizing 1-hexene. WO_3-coupled TiO_2 was also used to engineer the band gap of TiO_2. The chosen photo-catalyst was immobilized on glass beads as discussed in more details in chapter 3. It was possible to establish oxidation rates of 0.12 ± 0.02 mmolh^{-1} for 1-hexene with TiO_2/WO_3 (4 mol %). 1,2-epoxyhexane was successfully synthesized from 1-hexene achieving 15.9 % conversion and 41 % and 54 % selectivity for the 1-hexene, 1,2-epoxyhexane and CO_2 respectively when H_2O/O_2 was used as oxidant. Selectivity of 96 % and 97 % for CO_2 were achieved with air and O_2 respectively. Further experiments focused on the *in-situ* reaction of the partial photo-oxidation products of the photo-epoxidation of 1-hexene were performed. The exhaust of the photo-reactors was passed directly through methanol which acted as a nucleophile in the presence of concentrated sulphuric acid for 24 hours after which the products were separated, treated and analyzed. This made it possible to establish the features of some of the reactive species formed during the partial photo-oxidation of 1-hexene process, ultimately demonstrating the high versatility of the photo-reactor so developed.

7.1 Introduction

The photo activity of TiO_2 in decomposing organics is a well-known reaction.[104,114,334] Upon irradiating TiO_2 with UV light, high energy electrons and holes are generated which then react with adsorbed O_2 and H_2O on the surface of the semiconductor. As a result, highly reducing and oxidising species ($O_2^{\bullet-}$ and $OH^{\bullet}$) are formed.[59] These highly oxidising species are responsible the total photo-mineralization of organic molecules.[104] TiO_2 gained the attention of both academia and industry due to its numerous advantages such as high chemical stability as well as the ability to be activated by light.[104] The major drawback in using TiO_2 however, is its high light energy requirement to activate and the photocatalytic decomposition techniques often used with it end in complete mineralisation of the organics to form CO_2. Consequently, from a chemical perspective, production of CO_2 poses another challenge, as the stability of the produced CO_2 is so high that it does not take part in further reactions without supplying more energy to the system.[104,82,335] However, overcoming this challenge can be achieved by conducting partial photo-oxidation of organic molecules through for instance, coupling of TiO_2 with a lower band gap semiconductor such as WO_3. Previous reports show that during oxidation process, the initial steps occur faster than the decomposition steps. The non-selective behavior of TiO_2 activated photo-oxidation of organic molecules in the presence of O_2, is known to be due to the several individual decomposition steps that occur at different rates, and are essential to achieve total mineralisation of a molecule.[336] For this reason, a gaseous flow reaction system is advantageous as the created products in addition to CO_2, get to be separated from the catalyst before they undergo any total mineralization. A number of researchers have reported this observation where several partial photodecomposition products were formed under

controlled reaction processes. Ren *et al.*[337] and Taffarel *et al.*[338] all reported similar scenario while analysing photodecomposition of styrene.

Another strategy for controlling partial photo-oxidation products is the modification of the flow rate. This simple technique can be used to adjust the contact time between the reacting species within a photo-reactor, which will ultimately reduce complete photo-mineralisation.[254] Other modifications controls include adjusting the reactants concentrations and the overall reaction temperature, both of which have been reported to enhance the production of partial photo-oxidation intermediates.[39,340] Murcia-López *et al.* reported that by varying both the reaction temperature and the propylene/oxygen ratio in the gas stream, the production of propylene oxide in their reactor increased by 10 %.[240] They further modified the photocatalyst through doping and as a result enhanced the selectivity of propylene oxide. Similarly, Nguyen et al. modified their TiO_2 by doping with Au and used it to study photo epoxidation of propylene. Their report showed that as a result of the modification, 54 % selectivity of propylenene oxide was achieved against the use of pure TiO_2.[266] Furthermore, the epoxidation of 2-hexene was shown by Ohno *et al.*[341] to be performed both stereoselectively and stereospecifically which achieved high selectivity, thus showing the viability of the technique as a precursor generating procedure. In this chapter, a new photo-reactor was designed and used to study photo-epoxidation of 1-hexene in gaseous phase over TiO_2 and WO_3-coupled TiO_2. The pure TiO_2 used was commercial Degussa P25. By bubbling O_2 directly into H_2O as an oxidant, it was possible to suppress the formation of CO_2 while enhancing epoxide formation according to Scheme 7.1.

$$H_2O + O_2 \xrightarrow[\text{Catalyst}]{hv} \underset{\text{radicals}}{\text{Intermediate}} \xrightarrow{\text{1-hexene}} \text{Epoxyhexane} \xrightarrow{OH^{\cdot}} CO_2$$
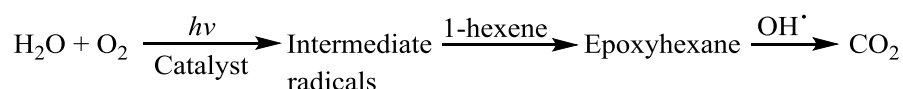
Scheme 7.1: Reaction pathway for photo-catalytic epoxidation of 1-hexene

The relative stability of photogenerated epoxide species are known, although the high reactivity of the various products of partial oxidation implies that many important unidentified compounds are often not collected directly during photocatalytic gas phase reactions. Therefore, during this set of experiments, a tandem system was set up to achieve a nucleophilic ring-opening of 1,2-epoxyhexane product formed during the reactions. GC-MS data analysis showed that the one-pot reaction mixture connected to the outlet end of the reactor, effectively utilized the partial photo-oxidation products in a synthetic reaction.[341]

7.2 Experimental section

7.2.1 Catalyst preparation

WO_3–coupled TiO_2 was prepared using a modified procedure reported by Guangjuan *et al.*[342] 1 g titanium tetrachloride ($TiCl_4$, 99.9 %, Sigma Aldrich) was dissolved in 15mL of isopropyl alcohol (IPA, Fisher Scientific) and vigorously stirred for 30 min. Separately, 0.028 g sodium tungstate ($Na_2WO_4 \cdot 2H_2O$) was dissolved in 20 mL de-ionised water and then added dropwise into the first solution while stirring. A few drops of $NH_3 \cdot H_2O$ was then added dropwise to adjust the pH of the solution to 8. The final solution was stirred continuously for 1 h then transferred to Teflon tube and submitted for hydrothermal treatment for 48 hours at 120°C. The resulting product was washed with DI water followed by ethanol several times. Finally, it was dried at 90°C for 15 min, and ground into powder using porcelain mortar and pestle. The obtained powder (60 % yield) was then calcined at 550 C for 2 h in an open furnace. The final product was 4 mol % WO_3 coupled TiO_2 which was denoted WO_3(4 %)-

TiO$_2$ in this theses. For comparison, commercially available P25 (Aeroxide) was also tested. The characterization techniques in this chapter are similar to those used in previous chapters.

7.2.2 Photo-epoxidation of 1-hexene

The 1-hexene oxidation reaction was performed using the modified reactor set up used in previous chapters of this work. Similarly, catalyst immobilisation technique used in Chapter 3 was adopted here. The method used for introducing cyclohexene in to the reactor was also adopted in this Chapter. 20 ml of liquid 1-hexene was placed in a Dreschel bottle and allowed to continuously flow in vapour phase using nitrogen as the carrier gas. Oxygen was bubbled directly into H$_2$O and moisture, which served as the oxidant was delivered simultaneously into the reactor as the 1-hexene, at a fixed flow rate of 2.1 ± 0.51 mmolh^{-1}. These steps were repeated prior to each run. By maintaining the length of the Dreschel bottle's dip tube at 2 cm above the liquid, it was possible to ensure a stable flow at constant concentration of 1-hexene in the gas stream.

After attaining a steady state flow through the photo-reactor, the lights were turned on and the reactor exhaust passed through FTIR gas-phase flow cell to monitor changes in concentrations of reactants and products.

A PerkinElmer Fourier Transform Infrared Spectroscopy (FTIR) was used to measure the concentration of 1-hexene and the products of the reaction. The CO$_2$ asymmetric stretch peak area was measured between wavelength of 2390 and 2230 cm^{-1}. The C=C stretching mode of linear alkene (1-hexene) was measured around 1640 cm^{-1}, which is common to monosubstituted alkenes. C-H stretching vibration was looked at from 3170-2820 cm^{-1}, which is a common to peak for hydrocarbons.

7.2.3 Synthetic trapping and ring opening reaction

Since the high reactivity of some of the partial photo-oxidation products that made it almost impossible to trap chemically, such products can be involved in other "pseudo" *in-situ* photo reactions within the exhaust of the photo-reactor. In this section, the epoxyhexane formed *in-situ* during the photo-epoxidation of hexene was first trapped in toluene by directly bubbling the reactor exhaust into 30 mL of the trap solvent for 24 h, after which eluents were collected for GC-MS analysis.
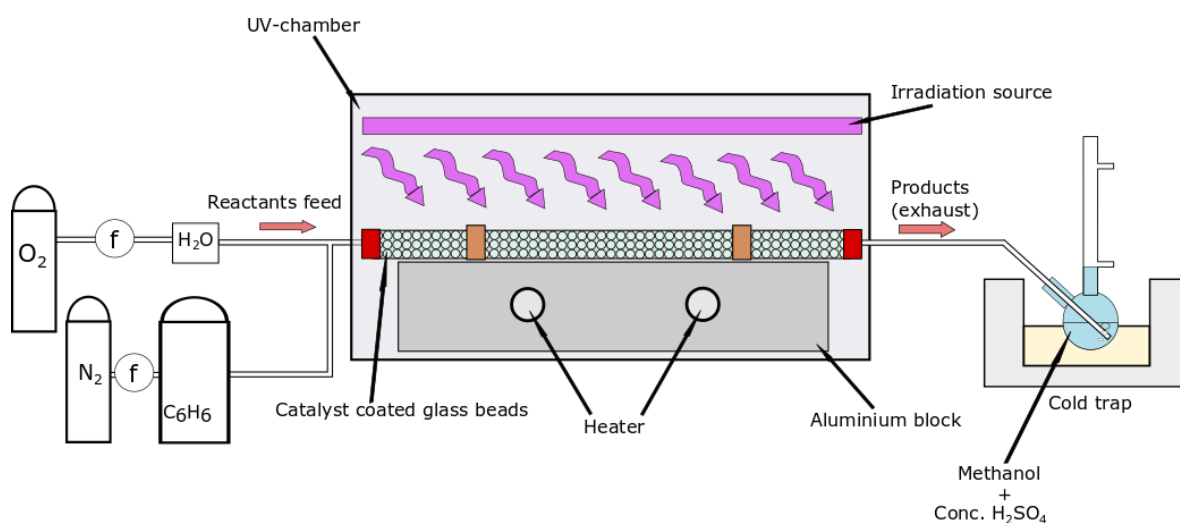
Figure 7. 8: The experimental set up for the chemical trapping of the exhaust of the photo-epoxidation reactions of hexene in gas streams.

7.2.3.1 Synthetic ring opening under acidic condition

During the synthetic trapping, the epoxide formed *in-situ* was used as the starting material under acidic condition to produce two product mixtures. Under this condition, 2 drops of concentrated sulphuric acid were added to 10 ml of methanol, which acted as a nucleophilic reagent in a 20 mL round bottomed flask, placed in an ice bath as shown in

Figure 7.1. At steady state flow with illumination, the exhaust stream from the reactor was bubbled directly through the content of the flask for 48 hours. Loss of trapping agent was minimized by placing a condenser through the second neck of the round bottomed flask. It is expected that the epoxide produced during the partial photo-oxidation of 1-hexene would undergo ring opening reaction as it is formed. After 48 h reaction time, the mixture was washed with 10 mL of saturated sodium bicarbonate solution (obtained by dissolving 10 g of $NaHCO_3$ powder in 100 mL of H_2O at ca. 80 ^{o}C) using a separating funnel (Figure 7.2 A). The products then were extracted from the aqueous solution and washed with double portions of 10 mL diethyl ether, followed by draining off and combining the ether layers together. The organic solution was then dried with magnesium sulphate and the liquid was carefully decanted into a round bottomed flask. Finally, using a rotatory evaporator, the organic extract was dried by immersing the flask in water at room temperature until a dry yellowish brown residue was obtained (Figure 7.2. B). The residue was dissolved in acetonitrile and analysed using GC-MS.

Figure 7. 9: The extraction process of epoxidation reaction (A) and the residue obtained after rotatory evaporation (B)

A Varian CP-3800 gas chromatograph was used to separate the compounds and a Varian Saturn 2000 mass spectrometer was used to analyse the separated products. The GC was mounted with Rxi-5Sil MS 30m x 0.25mm ID x 0.25µm df column. An appropriate method was developed for this analysis in order to achieve good separation of the products. Helium was used as carrier gas at a flow rate of 40 ml/min. A high injector temperature of 220 ℃ was maintained to ensure that no condensation occurred in the injector. The samples were injected through autoinjection mode, maintaining 0.2 µl as injection volume with a split ratio of 30. The initial GC oven temperature of 50 ℃ was held for 4 min then ramped to 200 ℃ at the rate of 50 ℃min^{-1} and held for another 4 min. Finally the oven temperature was ramped to 270 ℃ at 50 ℃min^{-1} and held at this tepmrature for 4 min. The MS was performed through EI, scanned between 20 and 250 m/z for 21 min. with a delay of 3.5 min.

7.3 Results and discussion

7.3.1 Catalyst characterization

In order to monitor changes in phase of the as-prepared WO_3-coupled TiO_2, XRD data was used. The monitored diffraction peaks revealed particle sizes 9.6 nm, based on the Scherrer's equation. It can be seen from Figure 7.3 that the diffraction peaks of the WO_3(4 %) TiO_2 exhibited both anatase and rutile phases which appears similar as compared with the structure of P25 powder. The characteristic diffraction peaks were observed to broaden as the calcination temperature was increased, which indicates a decrease in the average size of the TiO_2 anatase crystals. It also suggests that coupling TiO_2 with WO_3 could prohibit phase transformation as well as control the growth of the catalyst crystallites.[81,109,342]
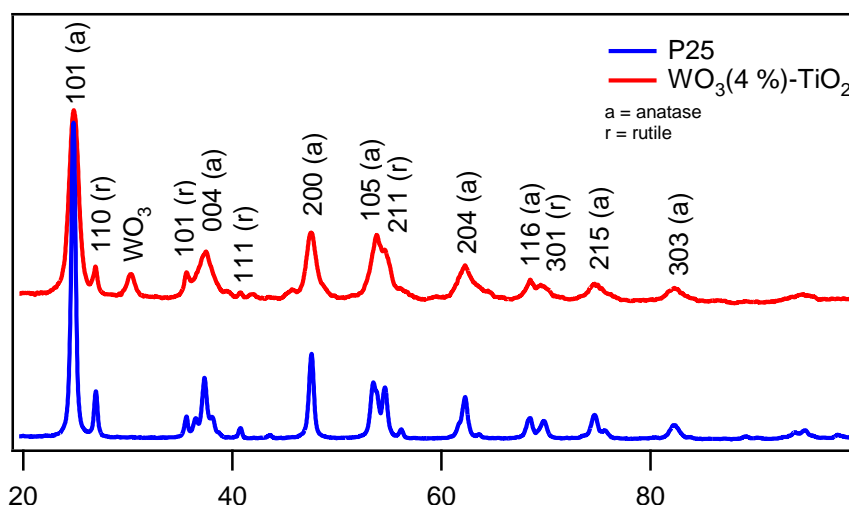
Figure 7. 10: XRD patterns of TiO_2/WO_3 nanocomposites

The XRD patterns shows that the coupling amount of WO_3 was sufficient enough to be detected by the XRD thus implying that all the W^{6+} may have been absorbed into the titania lattice replacing the Ti^{4+}. If this assumption were true, then W–O–Ti bonds would be

formed or located at interstitial sites as suggested by Jingxia *et al.*[343] Inability to detected

WO_3 in similar material has been reported and attributed to either of these assumptions: (1)

The WO_3 was present in an amorphous phase or (2) it was well dispersed on the TiO_2 surface.

Sajjad et al.[109] reported that only when the concentration of the WO_3 was increased to 6 mol

% from 1 mol % did the crystals become obvious. This signifies that the minimum required

amount for the formation of a monolayer was reached, hence the appearance of the

peaks.[343,342] Interestingly, in this work, WO_3 diffraction peaks were visible at 4 mol %. As

such, only EDX analysis was further performed. All the constituent elements of the coupled

material were visible on EDX spectrum as shown in Figure 7.4.
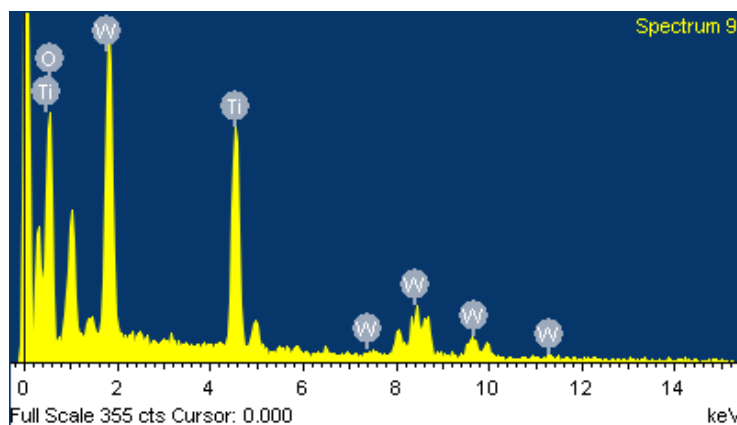
Figure 7.11: EDX of WO_3(4 %)-TiO_2show the elemental composition of the coupled material

7.3.2 1-hexene photo-epoxidation product analysis

7.3.2.1 FTIR analysis

During the IR analysis, the C-H stretching band of $=CH_2$ groups at 3087 cm⁻¹ and the

C=C at 1646 cm⁻¹ were used to identify alkene (1-hexene). The CH_2 stretching mode were

ascribed to the peaks at range 3000 cm^{-1} and 2700 cm^{-1} while those below 1500 cm^{-1} were considered for bending vibration mode.[60,61] The selected peaks were observed increasing and decreasing as the reaction proceeded with time. Peaks at 1415 cm^{-1}, 1260 cm^{-1} and 843 cm^{-1} were all observed to increase in intensity as time of reaction increased while peaks at 1829 cm^{-1}, 1647 cm^{-1}, 994 cm^{-1} and 632 cm^{-1} were observed to decrease accordingly. The photo-oxidation became stable and no other changes were observed after 1.5 h. Figure 7.5 shows the IR spectra of epoxidation reaction using P25 while maintaining other reaction condition as mentioned above. It can be seen that a steady increase in the intensity of the peaks was observed upon irradiation. This was expected due to desorption of molecules adsorbed on the surface of the catalyst as light is shone.[291,344] It can also be seen from Figure 7.5, the emergence of a new peak at 2380 cm^{-1} which is attributed to CO_2.[344] Indeed, TiO_2 is widely known to mineralise alkenes (and other organic compounds) into CO_2 and H_2O.[101,345,346] Nguyen et al. reported 74.4 % selectivity of CO_2 and 0 % propylene oxide in their photocatalytic epoxidation of propylene with P25. In Figure 7.6, the IR spectra of 1-hexene epoxidation with 4 mol % WO_3 coupled TiO_2 is shown.
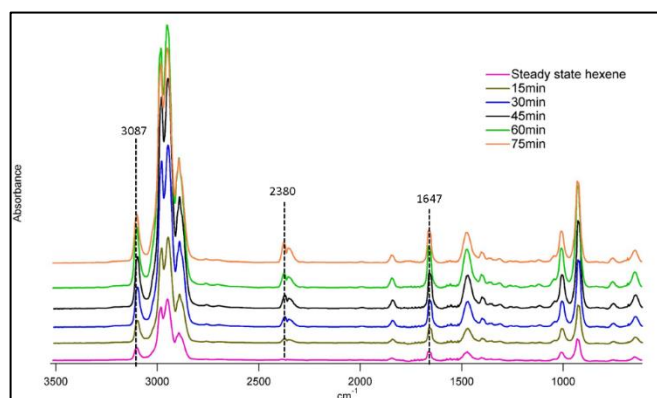
Figure 7. 12: FTIR spectra of epoxidation reaction 1-hexene with P25

The emergence of new peaks at 3048 cm^{-1}, 1415 cm^{-1} and 1260 cm^{-1} can be seen. However, the steady state spectrum of the epoxidation reaction was compared with that of a standard 1,2-epoxyhexane, and a remarkable resemblance was observed, hence confirming the identity of the reaction product. This further shows the reliability of the designed reactor for epoxidation of 1-hexene.
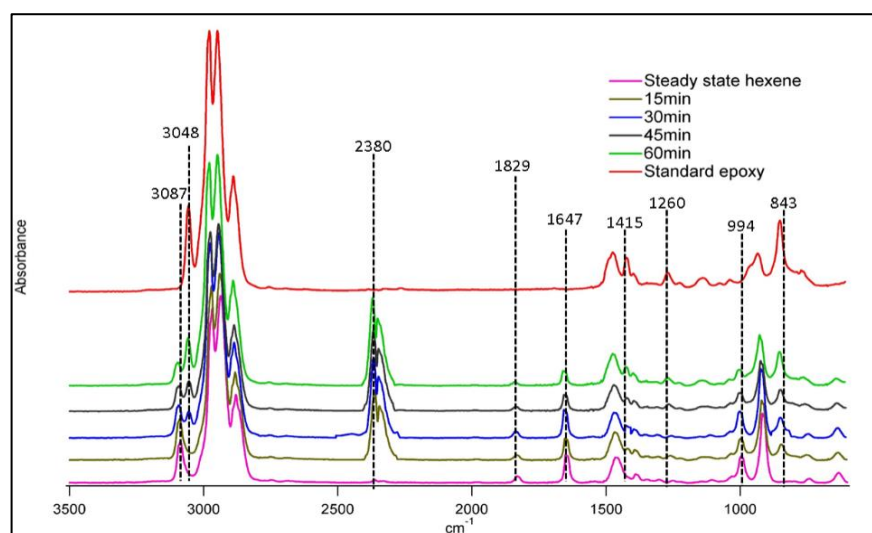
Figure 7. 13: IR Spectral of oxidation of 1-hexene with WO$_3$(4 %)-TiO$_2$

Among the various functions of catalyst coupling agents, their ability to lower the band gap of the core material (through interstitial band gap states) is of paramount importance. This is because the amount of energy necessary to activate such materials is reduced. WO$_3$ has been widely used to improve the photo-activity of TiO$_2$ in various forms. When used as dopant, i.e. present in TiO$_2$ in amounts ranging from 0.1-1 mol %, it acts as an electron trap. When TiO$_2$ is excited by photons of appropriate wavelength (< 387 nm), photo generated charge carriers are produced. However, in the presence of WO$_3$, the two materials become excited when irradiated. As such, the conduction band of WO$_3$ which is lower than that of TiO$_2$ becomes a trap for the photo-generated electrons in the conduction band of TiO$_2$. As

the photo-generated holes accumulate in the valence band of TiO_2, the rate of recombination of these charge carriers is effectively reduced, thereby enhancing the efficiency of the coupled material. As similar transition of the photo-generated holes to the valence band of WO_3 is not energetically favourable, the formation of more hydroxide radicals become enhanced. Also, the increased amount of adsorbed water in the system means that the holes are captured in oxidative reaction to produce hydroxide radicals which eventually oxidise the alkene into epoxide.

Although, no literature report exist to the best of the author's knowledge, on the use of WO_3 coupled TiO_2 for alkene epoxidation, it is assumed that the improved efficiency of the coupled material is based on certain factors: the surface adsorption was increased due to increased surface acidity. WO_3 is known to be about 15 times more acidic than TiO_2[342], thus coupling the two promotes their affinity to OH^- and H_2O on the surface leading to formation of more OH radicals. Similarly, the coupled WO_3-TiO_2 tend to have more affinity toward the molecules of the reactant. In terms of coupling amount, different reports exist each having ideal mixing ratio for the studied compound. Sajjad *et al.* [109] found that 4 mol % WO_3 on TiO_2 yielded the highest adsorption and photocatalytic activity on decomposition of methylene orange and phenol. Guangjuan *et al.*[342] reported that the highest reaction rate for the degradation of rhodamine blue was achieved with 3 mol % WO_3 on TiO_2. However, there are also reports where 1 mol % displayed the photodecomposition of contaminants. Bellardita *et al.*[347] and Song *et al.*[102] both observed highest photo degradation efficiency at 1 mol % of WO_3 dopant. These observations have been attributed to some factor including increase in life span of exciton[347] as well as the bathochromic shift caused by the WO_3 doping.[102] Nevertheless, in this work, only mixing ratio was tested in order not to deviate from the objectives of the chapter.

7.3.2.2 GC-MS analysis

After 1.5 h of reaction, the reactor exhaust was trapped in a Tedlar gas sampling bag from which a sample was manually injected in GC-MS. Four main peaks were shown at 1.31, 1.65, 2.00 and 2.58 minutes as in Figure 7.7. These observed peaks were identified using the NIST MS database.
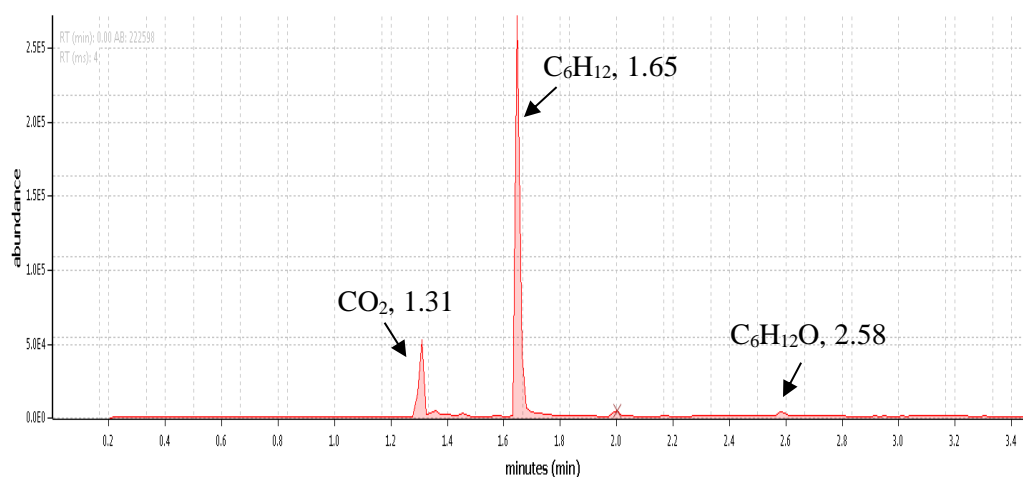
Figure 7. 14: Gas chromatogram of the reactor exhaust trapped in a Tedlar gas sampling bag using $WO_3(4 \%)$-TiO_2 The retention time of the main peaks in the spectrum has been marked.

The peak at retention time 1.31 minutes was ascribed to carbon dioxide. It is worth noting that this peak had the highest intensity apart from that of the reactant hexene (at retention time of 1.31 min) suggesting that it is the main product of this reaction. This also show that the photooxidation rate of 1-hexene over the studied catalyst occurred at a fast rate which leads to the formation of a relatively stable product. The MS match for the peak at retention time 1.31 min is shown in Figure 7.8. From the molecular ion peak at 44 m/z, compound can be confirmed to be CO_2 and it is consistent with NIST database for CO_2.
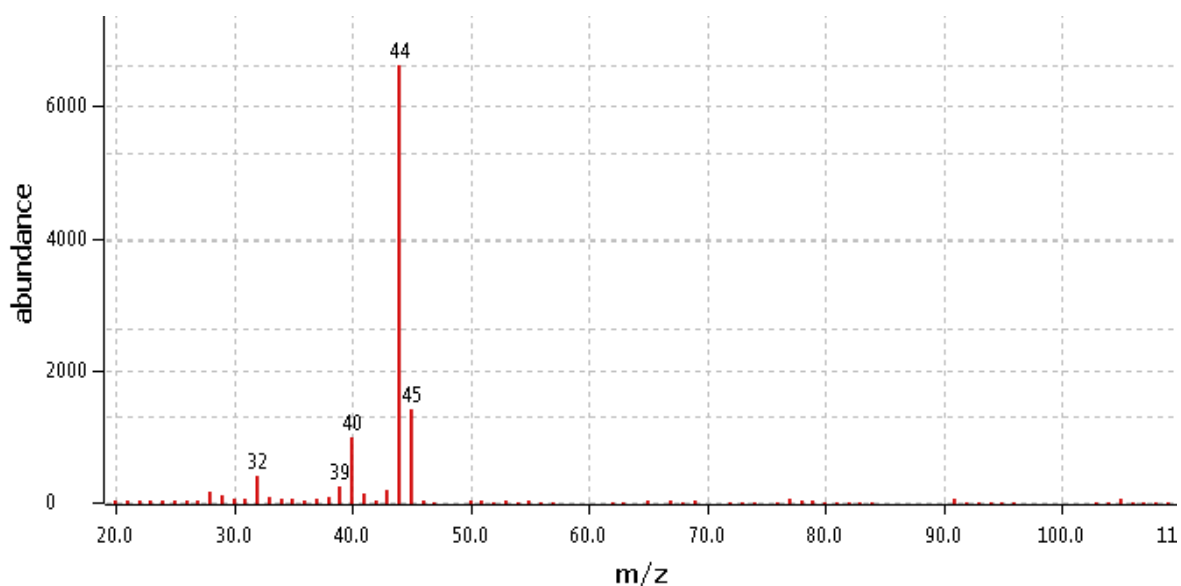
Figure 7. 15: Mass spectrum of the peak at 1.31 minutes from the gas chromatograph of the partial photo-oxidation products of 1-hexene

At retention time 2.58 min, a very low intensity peak appeared in the gas chromatogram of the trapped reactor exhaust using $WO_3(4\ \%)$-TiO_2. This peak was attributed to 1,2-epoxyhexane, and its mass spectrum (Figure 7.9) correlates to that of epoxyhexane in the NIST database. This observation is further supported by reports of academic studies that showed that 1-hexene has tendency to photocatalytically convert into its corresponding epoxide.[348–350]
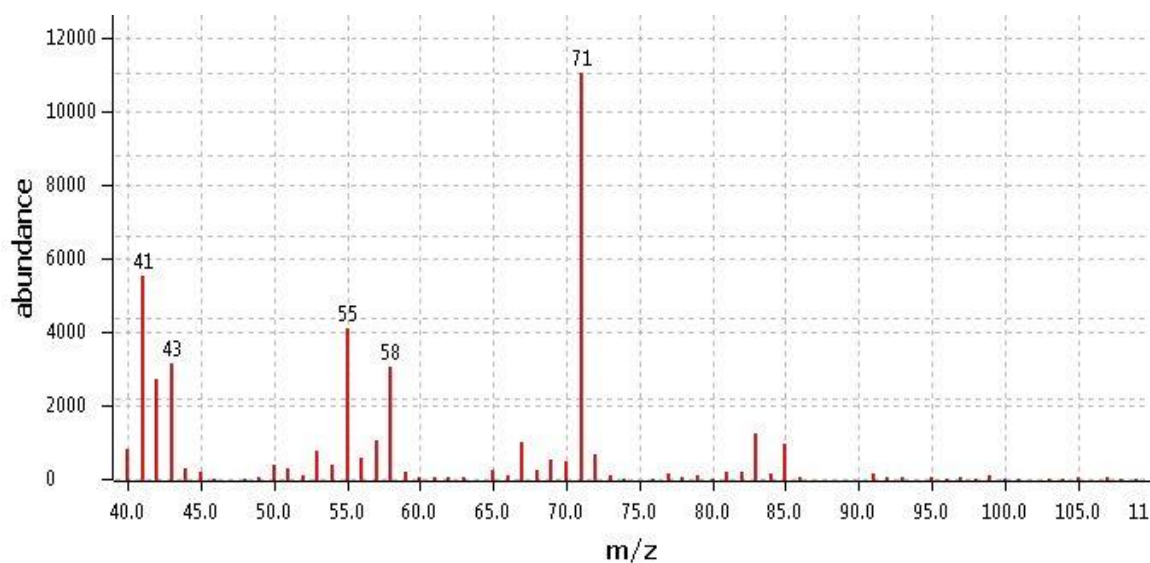
Figure 7. 16: Mass spectrum of the peak at 2.58 minutes from the gas chromatograph of the partial photo-oxidation products of 1-hexene.

At exactly 2.00 min, another peak appeared which has intensity approximately similar to that of epoxyhexane. This peak which barely appears but identifiable by the NIST database as 2-hexenal. The appearance of this molecule suggest that during photo-epoxidation reactions, a double bond migration occurred on the organic species, as also reported by Pillai and Sahle-Demessie.[351] The mass spectrum of the peak is shown in Figure 7.10, which correlates with the NIST MS database, thus confirming the formation of the compound.

Although there may be other molecules produced during the reaction, which may not be detected by the GS-MS due to their low concentration or unstable nature, their presence could be traced partially through chemical reactions.
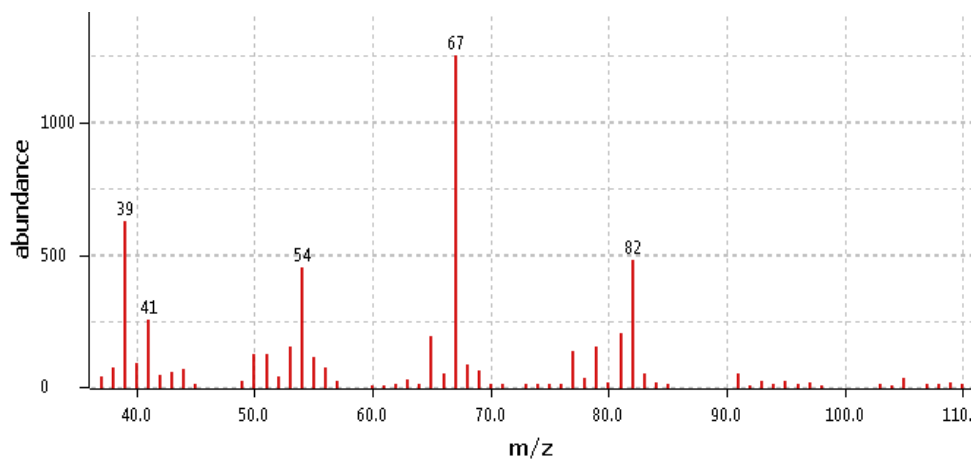
Figure 7.17: Mass spectrum of the peak at 2.00 minutes from the gas chromatograph of the partial photo-oxidation products of 1-hexene.

The residue obtained through the ring opening reaction of epoxyhexane was dissolved in acetonitrile. The gas chromatograph of the result is shown Figure 7.11. It can be seen that three major peaks were obtained at 4.10, 5.16 and 5.34 minutes. The peak at 4.10 min is due to the solvent, acetonitrile. It eluted earlier due to its lower boiling point and higher volatility relative to the other two species. The observed delay of up to 4.10 min was as set in the GC analysis method. Figure 7.12 shows the mass spectrum of the peak at 4.10 min, which further confirms its identity as it correlates with MS database.
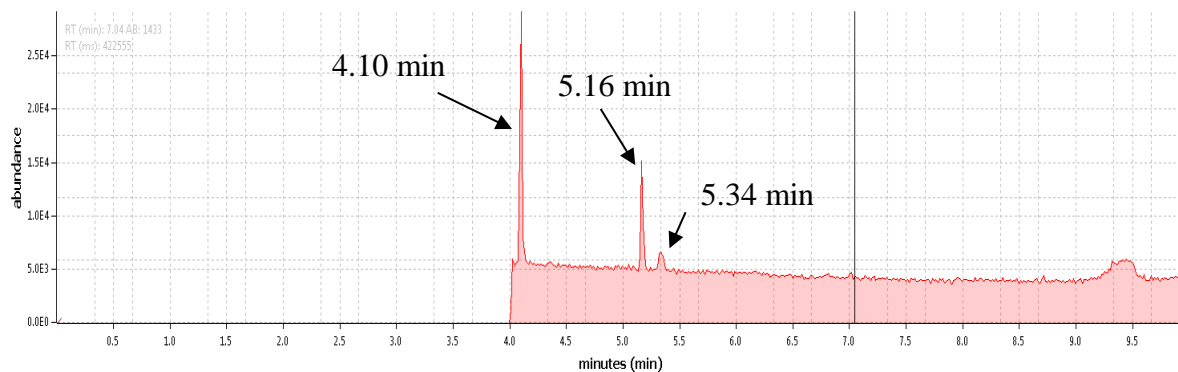
Figure 7. 18: Gas chromatogram of the dissolved residue of epoxyhexane ring opening in acetonitrile
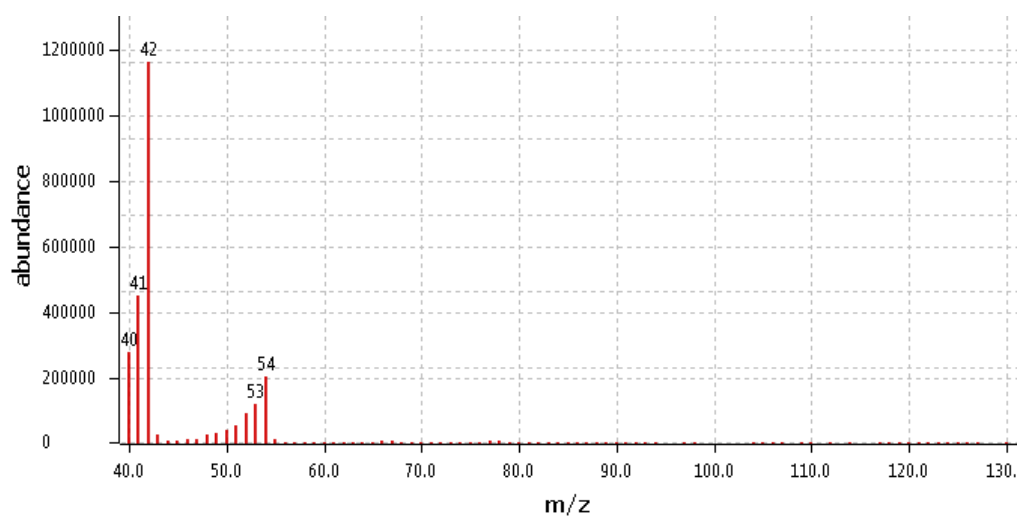
Figure 7. 19: Mass spectrum of the peak at 4.10 minutes

Unfortunately, the two species at retention times 5.16 and 5.34 minutes did not find any match in the available NIST database. As these peaks were not observed in the gas chromatograph of acetonitrile, they are most likely the products of the ring opening reaction.

From the proposed mechanism (Scheme 7.1) for the photo-epoxidation of 1-hexene,

the possible formation route for the epoxide precursors can be seen. Moreover, during the *in situ* nucleophilic ring opening reaction of epoxide using methanol as nucleophile, a preferential methoxy substitution was expected to occur at the most substituted carbon of the epoxide ring.[349] In terms of regioselectivity, where two or more different constitutional isomers could be formed, the nucleophile is expected to attack the most hindered carbon in an S_N1 reaction.[349,352] As such, one of the products is formed preferentially. This could be the reason for the observed high intensity of the peak at retention time 5.16 min relative to that at 5.34 min (Figure 7.11).
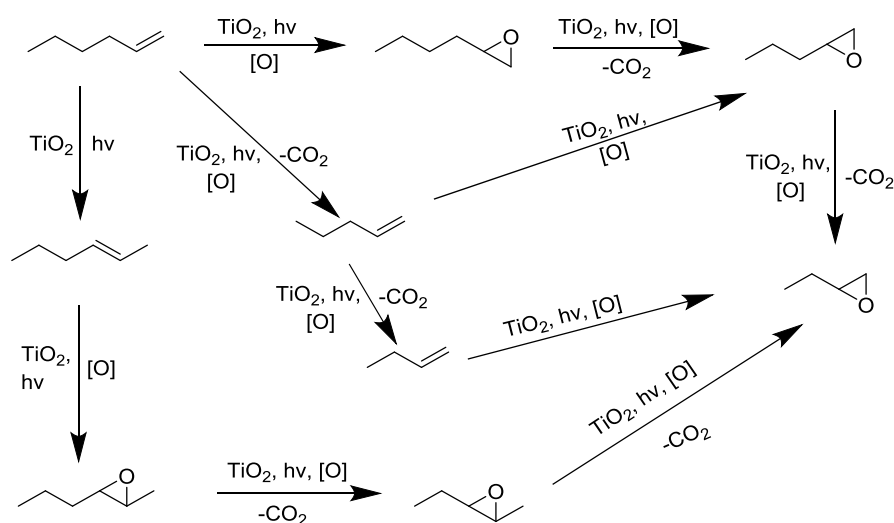
Scheme 7.1:   Proposed scheme for the formation of the epoxide precursors from 1-hexene. [O] = oxidant/O_2.

In Scheme 7.2, the step-by-step acid catalysed ring opening of epoxide leading to the formation of a product is shown. In the presence of an acid, the epoxide oxygen is protonated to create a leaving group, step 1. In step 2, the C-O bond breaks, creating a partial positive charge on the most substituted carbon due to carbocation stability. The nucleophilic CH_3OH

then attacks the electrophilic carbon in step 3. This step prevents the formation of a complete

carbocation intermediate. As the C-O bond still is yet to break completely, the O prevents

attack from the front leading to preferential attack from the back as seen in step 3.
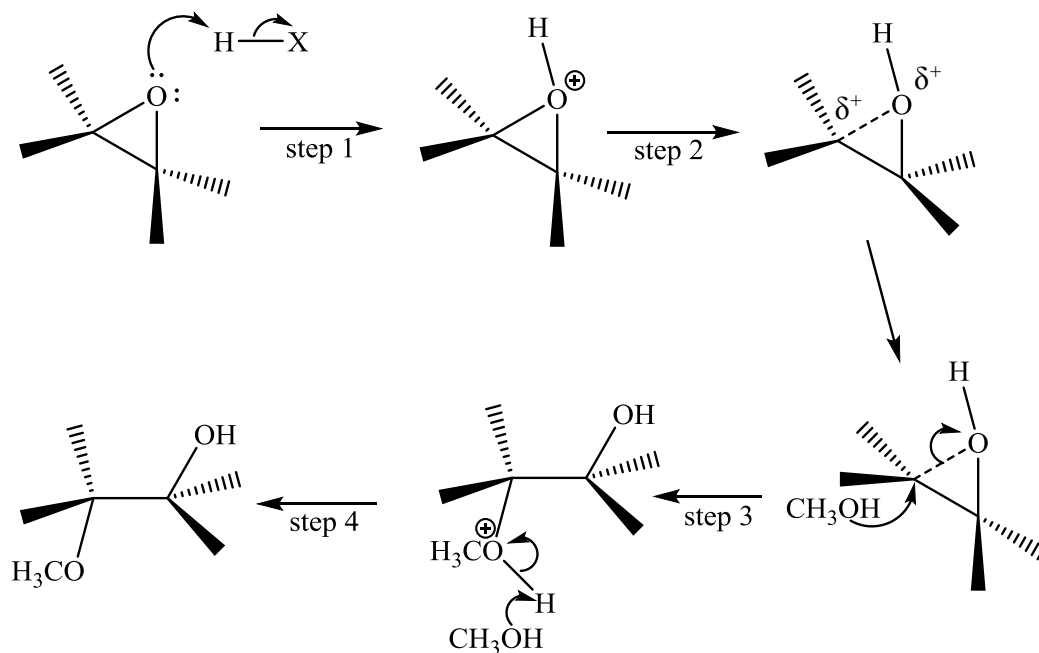
Scheme 7.2: The Schematic of a nucleophilic ring opening of epoxide in an acid catalysed reaction with methanol

As no matching species were found for these newly created molecules either on the

spectra of standard samples or the NIST database, attempts were made to identify them using

basic knowledge. It can be seen from Scheme 7.2 that the two species are likely to be some

compounds with molecules that contain OCH_3.
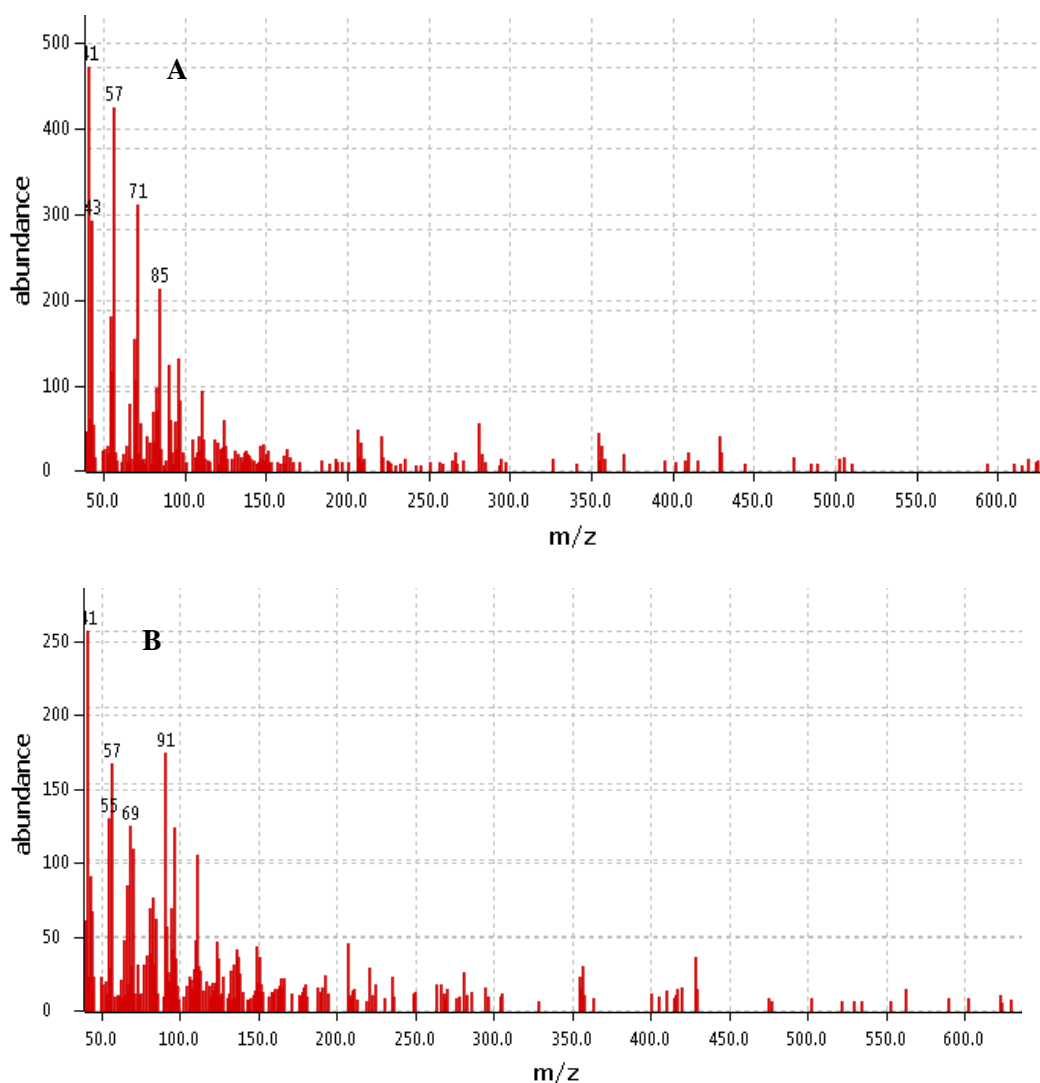
Figure 7. 20: Mass spectra of peaks at retention times 5.16 min (A) and 5.34 min **(B)**

Figure 7.13, shows the MS of species at retention times 5.16 min (A) and 5.34 min (B). A close look at the MS spectra of these unknown species A and B, shows that they contain odd m/z peaks which implies fragmentation by loss of CH_2.[107] Moreover, both have a difference of >14 amu between the fragments in their MS spectra suggesting that both molecules are sourced from molecules that only differed from each other by a CH_2 group. Therefore, considering the ring opening reaction of epoxide (Scheme 7.1), it becomes apparent that the two unknown species are products of the ring opening reactions of epoxide.

Photo-oxidation of organics over TiO_2 based materials is known to lead to gradual fragmentation of the molecules, hence the observed difference of CH_2 group between the epoxides formed *in situ* (Scheme 7.1). Nevertheless, it is worth mentioning that even though the photodecomposition of organics over TiO_2 has been widely studied, the reaction is perceived to proceed in a complicated manner. Several different pathways have been proposed in the literature. The proposed scheme in Scheme 7.2 is only considered as a potential mechanism for this reactions which is still open to further research.

7.4 Conclusions

In this chapter, the designed reactor has successfully demonstrated capability for photo-epoxidation reaction. During this study, 1-hexene was successfully converted to epoxyhexane through photo-epoxidation reaction using WO_3 coupled TiO_2. Whereas TiO_2 was effective in mineralizing 1-hexene to CO_2, addition of WO_3 to TiO_2 resulted in partial oxidation of the substrate.

This shows that several important chemical compounds can be synthesized using simple, less energy demanding system such as the one used in this chapter. Although the designed photo-reactor could be optimized to enhance the product yield, the simplistic design and operation of the reactor makes it industrially attractive. Other side products were also formed alongside the desired epoxide. Some of these products were envisaged to be very unstable or very low in concentration which made them difficult to detect. Two novel compounds were successfully synthesized when the exhaust of the photo-reactor was reacted directly with a nucleophilic methanol catalyzed by acid. Although these compounds were not identified due to the NIST database, their sources as well as molecular structures could be

suggested based on MS data. Only a handful of information about the synthesis procedures for these two structures seem to exist and sadly, they are overly complicated. Therefore, the reactor design technology presented in this chapter offers a potentially low cost synthetic procedure for species that are difficult to synthesise non-photocatalytically.

Finally, the photo-reactor designed in this study could be significantly improved if it will be applied to industrial scale. Nevertheless, photocatalytic reactions remain environmentally benign, cost effective, alternatives to conventionally high energy systems. It is therefore imperative that the designed reactor is potentially an initial step towards the manufacture of more sustainable chemical industry.

Chapter 8: NMR Study of Photo-Oxidation of Styrene

In this chapter, CeO_2 and several Co metal ion doped CeO_2 were synthesised through hydrothermal method and tested for photocatalyzed oxidation of styrene. The characterisation data obtained on XRD, EDX and SEM showed the formation process of the synthesised nanoparticles of various sizes as well as the structure of the crystals. Catalyst immobilisation technique utilised in previous chapters of this thesis was adopted to perform a *"pseudo" in-situ* photo-oxidation of styrene using NMR spectroscopy. Using molecular oxygen as the oxidant, 0.3 mol % Co-doped CeO_2 showed the highest conversion of 45 % while the selectivities for styrene oxide and benzaldehyde were 38 % and 51 % respectively. As revealed by the kinetic study in this work, the photo-oxidation reaction proceeded according to Langmuir-Hinshelwood model. The synthesised catalyst showed high stability and reusability over several photo-oxidation cycles. CeO_2 is indeed a promising catalyst ideal for photo-oxidation reactions to produce styrene oxide.

8.1 Introduction

As the demand for new techniques for screening semiconductor photo-catalysts keep rising, a significant amount of research into this field are also increasing. The use of oxides of rare-earth metals is yet another significant area that has received much attention due to the attractive properties such as optical and magnetic properties[176] of these materials. This group of materials has also demonstrated appreciable catalytic properties. One of the highly studied is cerium oxide (CeO_2). CeO_2 is one of the widely used rare-earth metal oxides that has gained the attention of the academia and industry for decades.[171] Some of its advantages include the Ce^{3+}/Ce^{4+} reduction-oxidation cycle as well as the ability to store oxygen, otherwise known as Oxygen Storage Capability (OSC). The oxidative properties of CeO_2 is dependent on the reduction step between Ce^{3+} and Ce^{4+} also referred to as the Ce^{3+}/Ce^{4+} redox cycle.[171,172] This property is mainly caused by its high reduction potential as well as the OSC, the extent of which is a function of the size, morphology, shape as well as surface area of the material. At an average size between 10 and 15 nm, CeO_2 nanomaterial exhibits a phenomenon known as quantum confinement effect.[174,175] They also exhibit an appreciable growth of cell parameters owing to the oxygen vacancies present as a result of the increase in number of Ce^{3+}. It has been reported that due to enhancement of the ratio of Ce^{3+} to Ce^{4+}, the OSC can be improved by coupling CeO_2 with ions of a transition metal or another rare-earth metal.[176,177] Higher surface energy also plays a crucial role in the enhancement of the material's activity, as it is responsible for the improved activity of the observed (100) surface of cubic CeO_2. In descending order, the surface energy of cubic CeO_2 is as follows: (100) > (110) > (111).[178] The ability to control some of the most desirable properties of CeO_2 nanostructures has justified their interest over the conventional aggregated nanoparticles. Some of these physicochemical properties include architecture, morphology and growth

direction. There exist several morphologies of CeO_2 nanostructures in the literature. Among these, one-dimensional nanorods, aggregates, and wires have drawn a lot of attention owing to their high specificity of both surface area and active crystallography in the direction of growth.[173,179] However, only the aggregate morphology was synthesised in the work due to its certain advantages that have been outlined in the literature. Due to its porous structure and high surface area an enhanced contact between the catalyst and the substrate can be achieved. Moreover, a significant decrease in sintering could be achieved due to the porosity created when aggregates are stacked randomly.[179,353–355] Effectively, decreasing sintering leads to sustenance of surface area which otherwise would be reduced at higher temperature. One of the methods for synthesising aggregate CeO_2 is the hydrothermal method. However, in order to achieve precision in width size, aspect ratio as well as accessible surface active sites, a lot is still required to be done. Nevertheless, high level of control could be achieved when a suitable precursor, a suitable reaction medium and conditions are carefully chosen.

Styrene epoxidation reaction is one of the most important chemical reactions in the chemical industry. Due to its commercial value, styrene oxide is extensively used as an intermediate for production of variety of pharmaceutical and fine chemical products. It is normally synthesised using two principal methods. The first is the use of a suitable base to de-hydrochlorinate styrene chlorohydrin while the second method involves the use of H_2O_2, organic peracids or urea-H_2O_2 to oxidise styrene.[354,355] Unfortunately, neither of these methods is environmentally or economically friendly due to the use of hazardous chemical substances. In order to synthesise styrene oxide in a "greener" way, the use of heterogeneous photo-catalyst and molecular oxygen could be employed for the oxidation reactions. In spite of the efficiency of CeO_2 as a catalyst, only a few reports have been made about it.

In this chapter, hydrothermal method was utilised to synthesise CeO_2 and Co metal ion doped CeO_2 nanostructured photo-catalyst. Another application of the catalyst coating technique has been further demonstrated in this chapter, this time in a liquid phase. NMR screw cap tube was utilized as the reaction vessel which allowed for the use of economical quantities (1 mL) of reactants. This novel technique is a possible quick technique for screening of a variety of organic reactions.

8.2 Experimental

All reagents used in this chapter were used as supplied. No further treatment was performed on any chemical.

8.2.1 Preparation of CeO_2 catalyst

Hydrothermal method was used to synthesise CeO_2 aggregate according to modified procedure reported by Pal *et al.*[356] 1 g of cerium (III) nitrate hexahydrate ($Ce(NO_3)_3 \cdot 6H_2O$, Aldrich Chemicals) was pre-mixed with 10 mL ethylene glycol. 0.3 M ammonium hydroxide was added dropwise until a pH of 7 was achieved. A straw yellow mixture was obtained which was stirred vigorously for 3 h. The final mixture was transferred to a Teflon vessel and an autoclave, placed in an oven for hydrothermal synthesis at 120 °C for 24 h. When the autoclaves have cooled down to room temperature, the formed precipitates were separated by centrifuging and vacuum filtering, washed thoroughly with de-ionised water followed by ethanol and dried at 80 °C for 12 h. The final dried powder was then calcined at 500 °C for 6 h.

8.2.2. Preparation of Co doped CeO$_2$

1 g of Ce(NO$_3$)$_3$·6H$_2$O was pre-mixed with 10 mL ethylene glycol. 0.2 g of cobalt (II) nitrate hexahydrate (Co(NO$_3$)$_2$·6H$_2$O, 97.5 %, AnalaR) was dissolved in 15 mL ethanol and added to the first mix under magnetic stirring. 0.3 M ammonium hydroxide was added dropwise until a pH of 7 was achieved. The obtained mixture was stirred vigorously for 3 h. The final mixture was transferred to a Teflon vessel and an autoclave, placed in an oven for hydrothermal synthesis at 120 °C for 24 h. When the autoclaves have cooled down to room temperature, the formed precipitates were separated by centrifuging and vacuum filtering, washed thoroughly with de-ionised water followed by ethanol and dried at 80 °C for 12 h. The final dried powder was then calcined at 500 °C for 6 h.

The same general procedure as above was followed for preparing different mol ratio of cobalt metal ion doped-CeO$_2$. The various doping amount and their allocated their names in the thesis are displayed on Table 8.1. The characterisation techniques in this chapter are same as the ones used in the previous chapters of this work.

Table 8. 1: Amount of Co in Co doped-CeO$_2$

Entry	Amount (mol %)	Thesis allocated name
1	0.0	CeO$_2$
2	0.1	Co(0.1)-CeO$_2$
3	0.3	Co(0.3)-CeO$_2$
4	1.0	Co(1.0)-CeO2

8.2.3 Preparation of catalyst loaded NMR Tubes

Considering the success achieved for photo-epoxidation of alkenes in gas-phase in the previous chapters of this work, it became imperative to further study the efficiency of the developed catalyst coating method of this work in a liquid-phase. Using a novel technique,

NMR screw cap tube was used as the reactor as seen in the set-up shown in Figure 8.1 (left). Catalysts synthesised in sections 8.2.1 and 8.2.2 were individually immobilised on glass beads according to the procedure in Chapter 3 of this work and placed in a 600 MHz frequency, 7 in. and 5 mm outer diameter screw cap NMR tube (Wilmad). A piece of quartz wool was placed before the catalyst coated beads to keep the latter from falling to the lower part of the tube as doing so may obstruct the NMR reading.
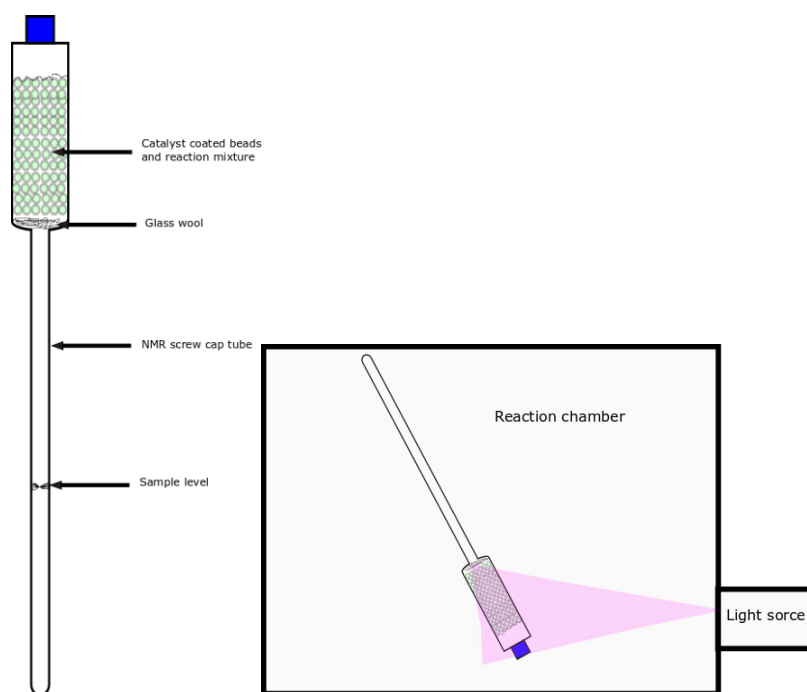
Figure 8.1: NMR tube assembly (left); reaction set-up (right)

8.2.4 Styrene catalytic oxidation reaction

When the reactor in Figure 8.1 was ready for reaction, the reactants were added as follows: separately, 1.5 mL of chloroform-d was placed in a GC autosampling vial and 20 uL of styrene was added and thoroughly shaken to homogeneity. The solution was then transferred to the NMR tube assembly with the aim of a syringe. A bleed needle was inserted

through the septum on the screw cap to reduce pressure build-up during this process. 5 mL of molecular oxygen was also pumped into the reaction set-up as the oxidant. The tube was then inverted to allow contact between the reacting species and placed in a crosslinker UV chamber and irradiated with 2.0 mWcm^{-2} of light from a xenon light source as shown in Figure 8.1 (right). NMR analysis was performed periodically after every 10 min of illumination by taking the reactor and keeping it vertical for a couple of minutes to allow the liquid drain to the bottom of the tube, then placed in a 600 MHz Varian NMR. This was repeated until no further changes in the NMR spectra was observed. The cycle was performed for all the catalysts.

8.3 Results and discussion

8.3.1 XRD analysis

The XRD patterns of the CeO_2 nanoparticles are shown in Figure 8.2. A well resolved diffraction peaks for CeO_2 corresponding to a standard data JCPDS 34-0394 can be seen.
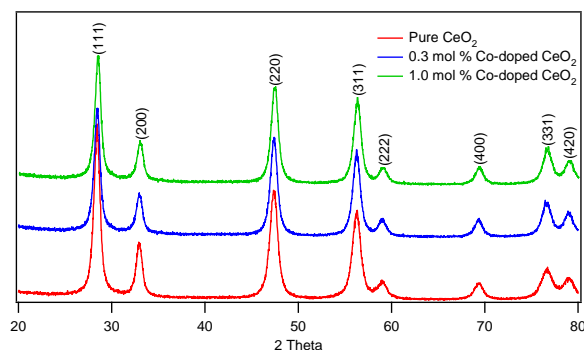
Figure 8.2: Powder XRD patterns of synthesized pure and cobalt impregnated CeO_2 NP

No observation was made for peaks associated with cerium hydroxide. This suggests the direct formation of crystalline CeO_2 particles from the cerium nitrate precursor solution. Interestingly, the peaks intensity ratio of 0.5 was achieved for the (200) and (220) crystals of CeO_2 nanoparticles. Ideally, the peaks intensity ratio should be 0.6.[357] This observation shows specificity in the growth direction of the crystals of the CeO_2 nanoparticles synthesised and is well documented in the literature.[356,358] Using Scherer's Equation, it was possible to determine the average sizes of the crystallites considering the broadness of the diffraction peak (111). As the calcination temperature was increased the average crystallite sizes also increased as displayed on Table 8.2. It can also be seen on Table 8.2 that the crystals of the CeO_2 nanoparticles synthesised were longer than those of bulk CeO_2. This is consistent with the findings of Pal et al. which they attributed to be due to grain surface relaxation (that plays a vital role in the line broadening which results in reduction of the dislocation density[359]) as well as the presence of Ce^{3+}, which leads to a high redox potential of CeO_2 nanocrystals.[356]

Table 8.2: The crystallinity and unit cell parameters of the synthesised catalysts

Entry	Sample	S_{BET} (m^2g^{-1})	Crystallite size (nm)
1	CeO_2	47.21	6.28
2	Co(0.1)-CeO_2	52.47	7.45
3	Co(0.3)-CeO_2	51.41	7.78
4	Co(1.0)-CeO_2	64.12	7.86

As Ce^{4+} is being replaced with Ce^{3+}, due to the higher atomic radii of Ce^{3+} an enhancement of the crystal lattice of the CeO_2 nanoparticles can be observed according to Vegard's rule. The XRD patterns of Co–CeO_2 (Figure 8.2) was not different from that of pure CeO_2 as expected, since dopants usually have no effect on XRD pattern.[360] There was

no additional peak corresponding to cobalt oxide even though the catalyst was calcined at 500 °C. This can be attributed to the low amount of the material present in the final Co-CeO$_2$ material. Another possible reason is that the Co was uniformly dispersed in the overall material.

Nevertheless, relatively lager crystals size and unit cell parameters were obtained for pure CeO$_2$ compared to Co-CeO$_2$ which shows that a successful incorporation of Co ions unto the CeO$_2$ crystal structure was achieved (Table 8.3).

8.3.2 SEM analysis

The synthesised CeO$_2$ and its dopants were further characterised by SEM as shown in Figure 8.3. The SEM images of the CeO$_2$ show an irregular shaped material of micro-meter length. The observed morphology of CeO$_2$ did not show any significant change with calcination. Similarly, due to low amount of dopant used in the syntheses of Co doped CeO$_2$ no difference was observed in the morphology of the base CeO$_2$. As such, EDX analysis was performed to ascertain the presence of Co ions in the finished material (Figure 8.4). The elemental composition data on Table 8.1 shows the presence Co up to 0.5 wt % with 0.44 at %.
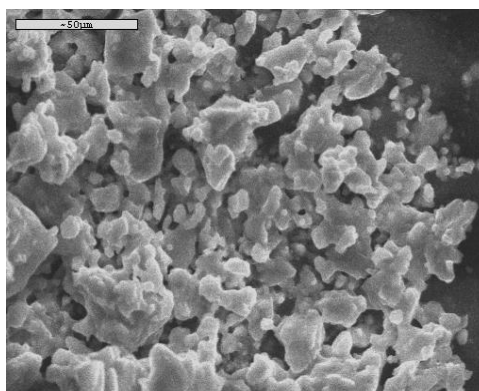
Figure 8.3: SEM images of as-synthesized CeO$_2$
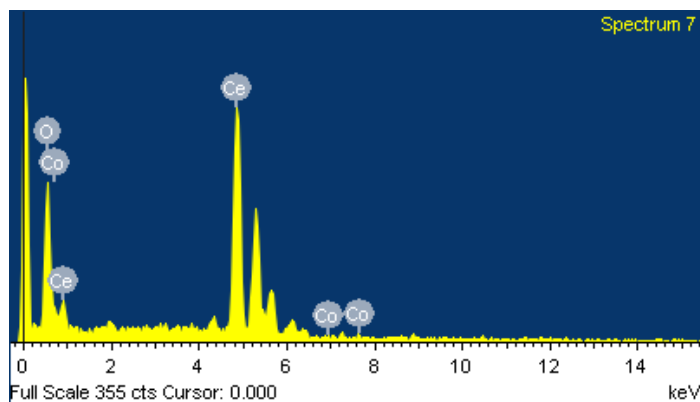
Figure 8.4: EDX spectrum of 0.3 mol % Co-CeO$_2$

Table 8.1: Elemental composition of synthesised Co(0.3)-CeO$_2$

Element	Weight%	Atomic%
O K	22.36	71.42
Co K	0.51	0.44
Ce L	77.14	28.14
Totals	**100.00**	

Conventionally, synthesis of CeO$_2$ nanoparticles is performed through the formation of cerium carbonate or hydroxide intermediate which often result in low formation of product and is not time efficient.[173,361] Here, a direct formation procedure was adopted by using cerium (III) nitrate hexahydrate which under hydrothermal condition nucleates to form CeO$_2$ nanoparticles during the initial reaction. Ethylene glycol also played a vital role in CeO$_2$ particles formation as it provided a platform upon which the CeO$_2$ particles grew. Ethylene glycol has been reported to play a role in morphology control[146] as well as crystal growth direction.[202] Weng et al[357] explained that when poly ethylene glycol is used, at the initial stage of CeO$_2$ growth mechanism, nanoparticles independently arrange themselves in such a way that their crystallographic orientation is the same. After that, the particles combine at a

planar interface that result in a decrease in the surface energy. As also observed by Pal et al. the (100) corresponds to the binding of the nanoparticles on the chains of poly ethylene glycol which led to surface energy reduction. This was followed by the enlargement of the particle and eventual oriental attachment on the next available reactive surface (110).[356] Upon poly ethylene glycol removal, (100), which is the highly energetic surface became highly exposed. On the other hand, when ethylene glycol is used, the particles tend to form an agglomerate by dehydrating and then condensing to form particles with an irregular shape due to the presence of hydroxyl group on the CeO_2 surface. This explain the morphology of the CeO_2 nanoparticles obtained in this work.

8.3.3 Catalytic activity study

Although the aim of this chapter was to test the coating technique discussed in Chapter 3 of this work using NMR analysis, it became imperative to test the catalytic activity of all the synthesised CeO_2 nanoparticles. As such, analysis was carried out to study the photo activities of the synthesised catalysts by plotting the concentration profile of styrene as well as those of styrene oxide and benzaldehyde. This data was generated by taking 2 ul of the NMR reaction tube after each round of illumination, using a micro syringe. The eluent was injected in to GCMS and corresponding peak of species were analysed. It can be seen from the GCMS data in Figure 8.5 that all the catalysts were active toward photooxidation of styrene. Figure 8.5 (A) shows the normalised styrene concentration data according to catalysts and time of reaction. It can be seen here that the highest decrease in styrene concentration which corresponds to conversion of 45 % was achieved with Co(0.3)-CeO_2. However, the highest increase in concentrations of styrene oxide was achieved with Co(1.0)-

CeO$_2$ which corresponds to selectivity of 61%. These modified CeO$_2$ catalysts performed better than pure CeO$_2$ with respect to conversion and selectivity.

The incorporation of cobalt to the CeO$_2$ catalyst showed an improved activity which can be attributed to an increase in the sites vacancies as a result of enhanced number of Ce^{3+} ions which in turn increases the number of active sites to adsorb more oxygen molecules.[356] On the other hand, increasing the amount of Co to make 1.0 mol % Co-CeO$_2$, showed a decrease in conversion of styrene and selectivity of benzaldehyde. This is probably due excess un-bonded Co ions which could cause surface deactivation.[362] Nevertheless, pure CeO$_2$ achieved the lowest conversion and selectivity showing clearly the superiority of Co impregnated CeO$_2$, which is most likely due to three major factors as outlined by Pal *et al.*: increased surface area, increased number of Ce^{3+} ions as well as revealed surface of active (100). This observation is in agreement with the literature.[176,356,359,362]
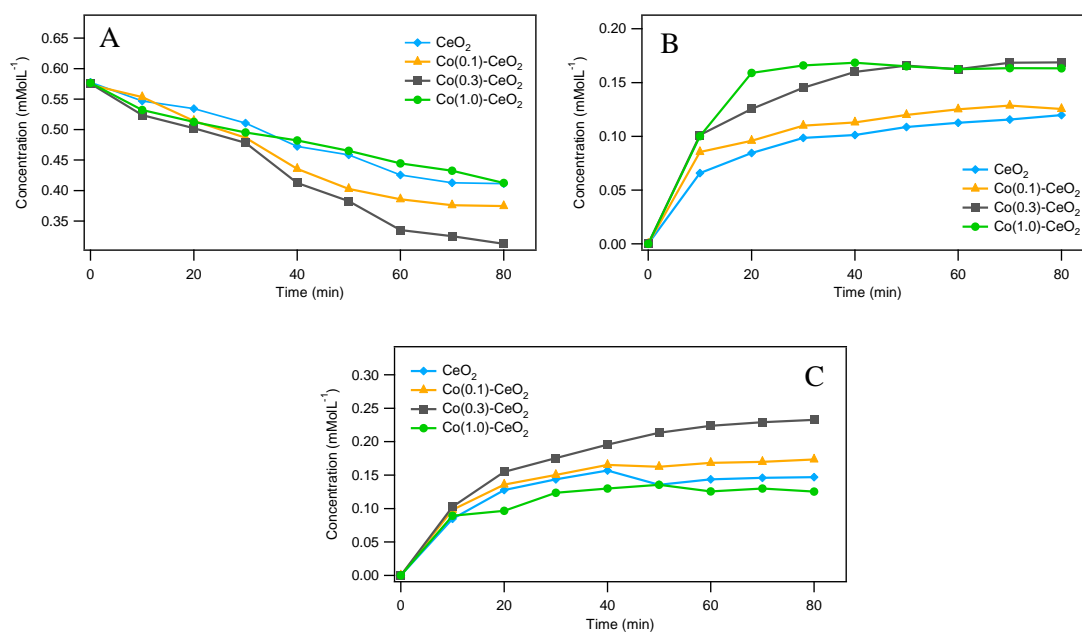
Figure 8.5: Concentration profile for styrene (A), styrene oxide (B) and benzaldehyde (C) obtained for the oxidation of styrene with O$_2$ over all the synthesized CeO$_2$ based catalysts.

8.3.4 NMR analysis

Figure 8.6 represents the distribution and allocation of protons according to their electronic environments. The position of a proton on the structure determines whether its peak will appear at a high or low shift relative to a reference. The number of peaks in the NMR spectrum is equal to the number of protons (or other atoms) in the molecule. Also the proximity of a proton to an electronegative atom or multiple bond leads to a peak appearing more downfield. Since ^{1}H-NMR spectrum produces peaks according to this classification, it became imperative to identify these individual peaks and their sources from the three major molecules present before (Figure 8.6 (A)) and after (Figure 8.6 (B & C)) reaction. Identification of all peaks was further confirmed by considering their multiplicity as well as by comparing with ACD/I-Lab database.

(A)   (B)   (C)
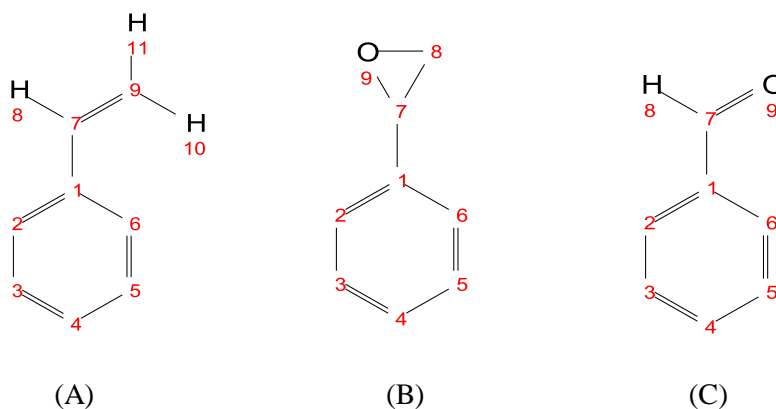
Figure 8.6: Schematic representation of electronic environments of H atoms within the molecules of (A) styrene, (B) styrene oxide and (C) benzaldehyde.
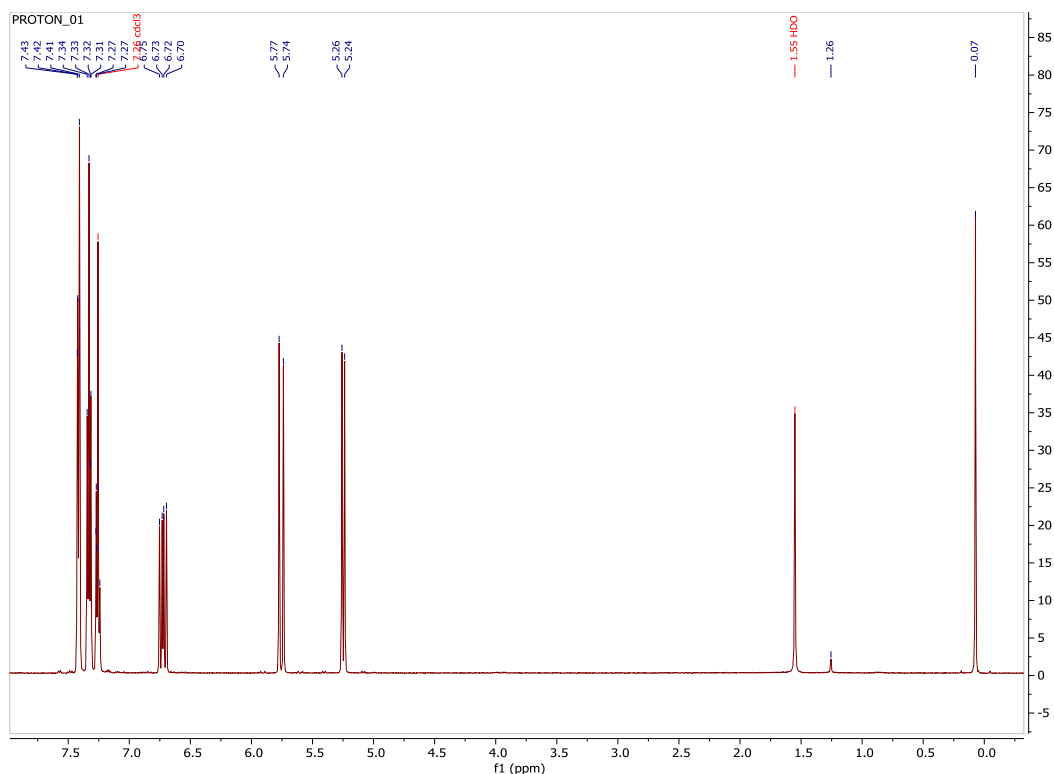
Figure 8.7: ^{1}H-NMR of reaction mixture before illumination

Figure 8.7 shows the ^{1}H-NMR spectrum of reaction mixture before reaction (irradiation). The peaks at 1.2 and 1.55 ppm are likely due to impurities in the mixture. At 5.2, 5.7 and 6.66 ppm, the peaks correspond to H in the electronic environments labelled 11, 10 and 8 respectively, in Figure 8.6 (A). The multiplet peak at 7.23 corresponds to the CDCl$_3$. However, several peaks appeared almost overlapping with the solvent peak at 7.23 ppm. These peaks are attributed to the aromatic ring with protons labelled 1 to 6 in Figure 8.6. After every 10 min of reaction, NMR analysis was performed until no further changes were observed in the NMR spectra. Figure 8.8 (A) shows the ^{1}H-NMR of photo-reacted styrene using Co(0.3)-CeO$_2$. As can be seen here, spectrum 7, which is the initial reaction spectrum at time 0 min. shows peaks similar to those in Figure 8.7. This implies that no reaction took place in the absence of light. After 10 min of reaction, new peaks appeared between 2.0 and

4.0 ppm which were absent before illumination (Figure 8.8, spectrum 6). Similarly, further

downfield at 10.2 ppm another new peak appeared which can be attributed to protons labelled

8 in Figure 8.6 (C). The downfield appearance of this peak is due to the proximity of the

protons to a double bond as well as O (a highly electronegative atom).[363] This peak has been

identified as benzaldehyde. [364]
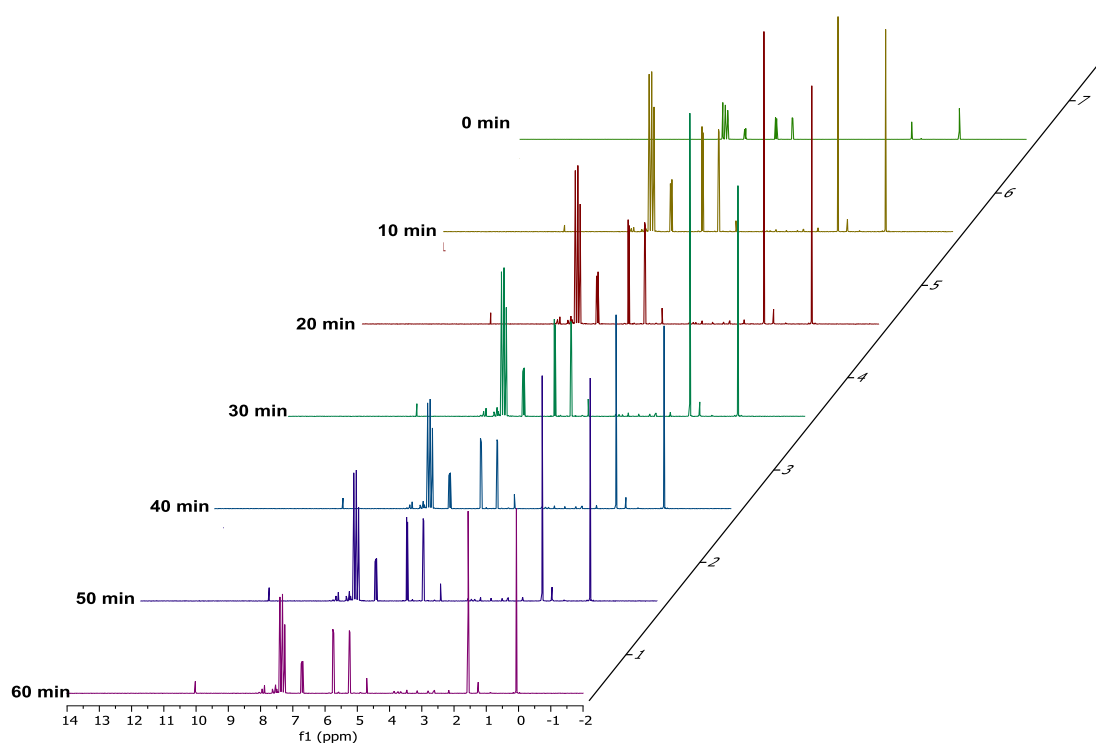
Figure 8.8: Full spectra of ^{1}HNMR of styrene epoxidation after irradiation at 10 min interval for 60 min.
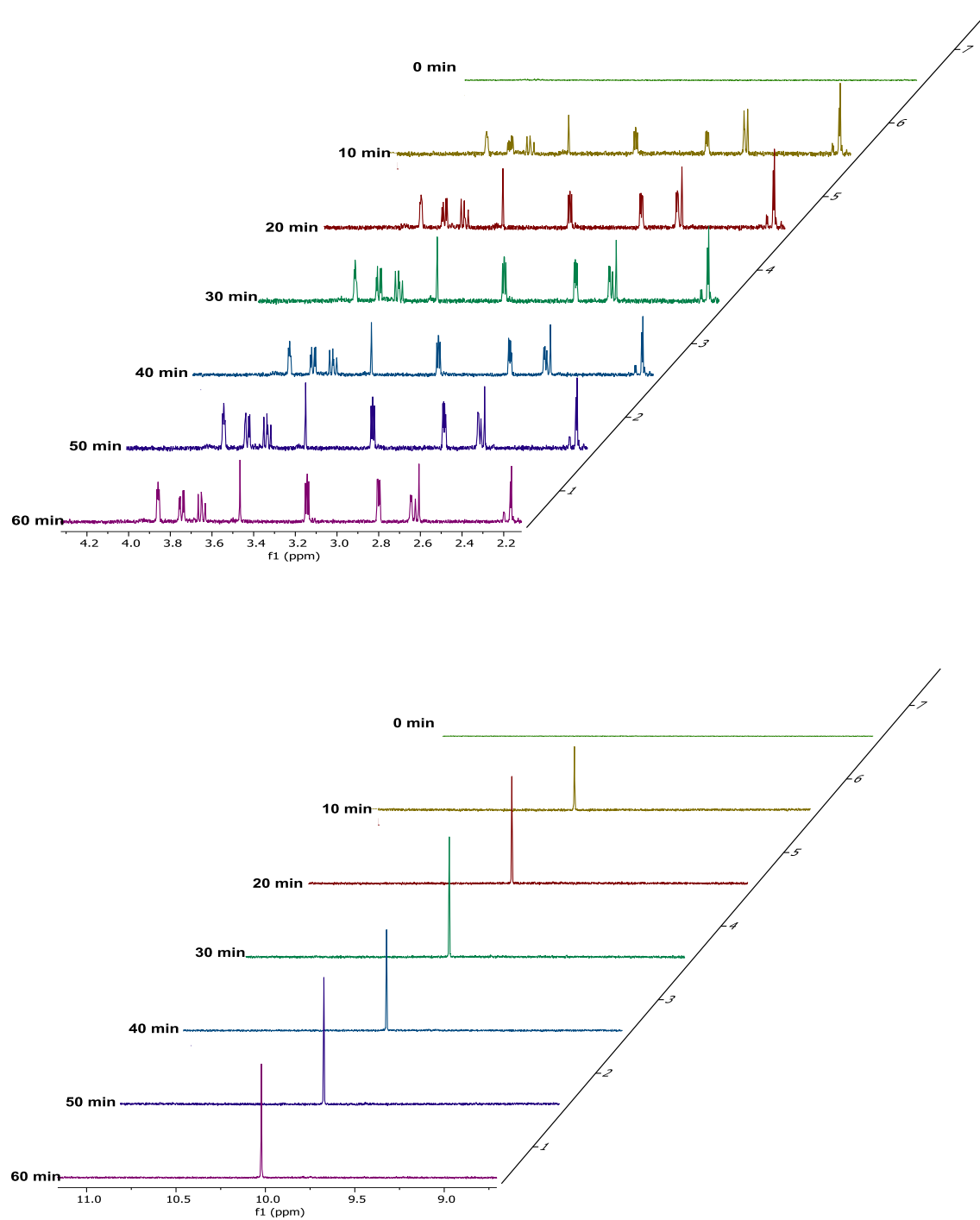
Figure 8.9: Zoomed in ^{1}HNMR of styrene epoxidation showing (A) peaks due to styrene oxide and (B) peak at 10.2 ppm, due to benzaldehyde

From Figure 8.9 (A), the emergence of new peaks after reaction can be seen. All the peaks which were absent at 0 min reaction time, appeared after 10 min of reaction. No other different peaks were observed after this time. This shows that only one type of reaction occurred in the system and the products did not suffer any form of decomposition. The emerged peaks were also observed to retain their intensity between 20 and 60 min of reaction. Only a slight increase in intensity was observed from 10 min to 20 min of reaction, which can be ascribed to initial product formation process. Similarly, the proton peak at 10.2 ppm remained stable within the reaction period tested (Figure 8.9 B). Figure 8.10 shows peaks at 2.80, 3.15 and 3.86 ppm which have been ascribed to protons of styrene oxide in chemical environments labelled 8, 8 and 7 respectively. These were identified by first stacking the spectrum of a standard styrene oxide with that of reaction after 60 min.
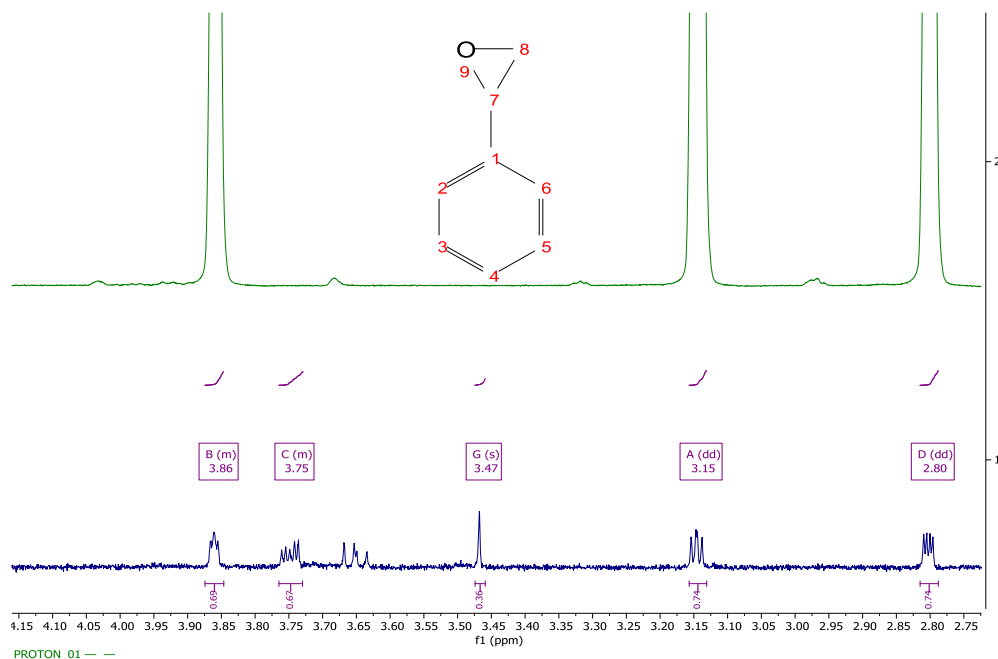
Figure 8.10: Comparison between NMR spectra of standard styrene oxide (green) and reaction product at 60 min (blue).

The multiplicity of the selected peaks in Figure 8.10 further confirms the identity of the product. By determining the coupling constant of the selected peaks, it can be seen that peaks at 2.80 and 3.15 ppm are doublets. Also, form the coupling constant, peak at 3.86 ppm is a multiplet. Considering protons at C labelled 8 in the styrene oxide structure, their neighbouring proton at C labelled 7 is 1. As such, applying the *N+1* rule results in 2, hence the doublet peaks observed at 2.80 and 3.15 ppm. Similarly, applying this rule to peak at 3.86 ppm gives a multiplet. Other peaks whose identity could not be confirmed by NMR were also observed. Around 3.47 ppm a singlet, around 3.63 ppm a singlet, around 3.67 ppm a singlet and around 3.75 ppm a multiplet.

8.3.5 Kinetic considerations

The oxidation reaction of styrene can be summarised in Equation (8.1) as follows:

$$(8.1)$$
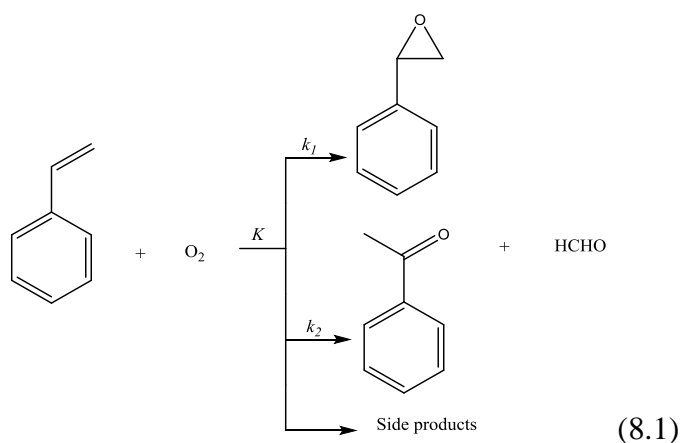
where the rate constants K, k_1 and k_2 were estimated at different reaction temperatures. Using the Arrhenius Equation, $K = Ae^{-Ea/RT}$, the plot of ln K, ln k_1 and ln k_2 against 1/T (Figure

8.11) showed linear relationships. From these plots, the activation energies Ea for styrene, styrene oxide and benzaldehyde were determined to be 12.87 kJmol^{-1}, 8.52 kJmol^{-1} and 11.96 kJmol^{-1}, respectively.
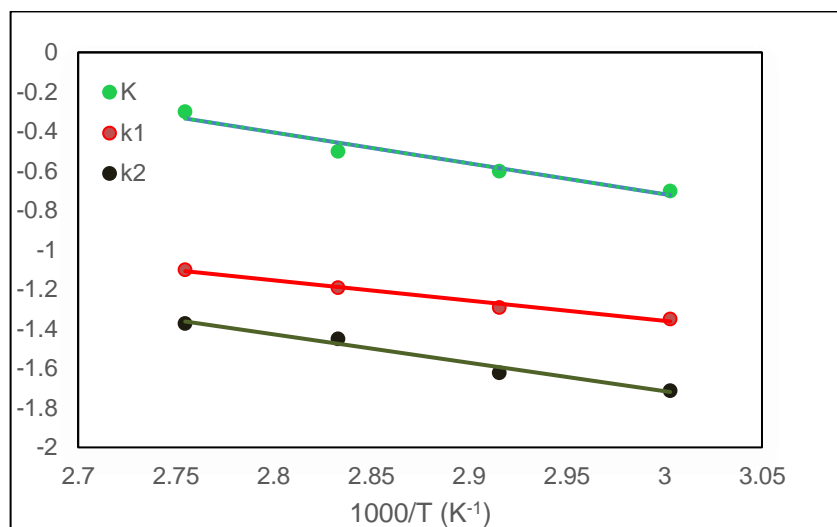
Figure 8.11: Arrhenius plot of photo oxidation of styrene over Co(0.3)-CeO$_2$ catalyst.

From the Arrhenius plots, the activation energy of benzaldehyde is greater than that of styrene oxide. This implies that production of benzaldehyde is favoured at higher temperature more than styrene oxide. This observation is contrary to the findings of Zhang *et al.*[365] where they reported higher activation energy for styrene oxide. At lower temperatures, the cleavage of C=C occurred easily while at higher temperatures epoxidation competes more preferentially.

The linear relationship obtained in Figure 8.11 strongly suggests that the photocatalytic oxidation of styrene preformed here using molecular oxygen as the oxidant and CeO$_2$-based nanoparticles as catalyst proceeded according to Langmuir-Hinshelwood model which

means that reaction occurred at the surface between adsorbed styrene and oxygen as illustrated in Scheme 7.1.

8.4 Reaction mechanism

Several possible reaction routes have been proposed for heterogeneous photo-catalysed oxidations in the presence of molecular oxygen, out of which two models are widely used. Mars-van Krevelen and Langmuir-Hinshelwood mechanisms have helped to identify the reaction pathways which is essential in understanding the overall reaction mechanism. According to Mars-van Krevelen model, the oxidation process occurs by loss of O on the surface of catalyst which is then replaced by molecular oxygen. However, the model assumes the reaction can proceed significantly in the absence of O since the lattice O of the catalyst surface is responsible for the reaction. The Langmuir-Hinshelwood model on the other hand describes the reaction where the substrate adsorbed on one site and O adsorbed on a different site of the catalyst react. Since O was an essential reagent in this work as no product was made without it, it is therefore apparent that the photo catalysed oxidation of styrene studied here followed the Langmuir-Hinshelwood model. However, more investigations need to be carried out to confirm this claim.
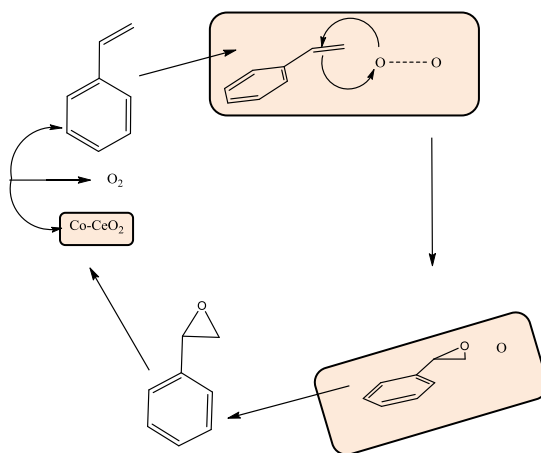
Scheme 8.1: Proposed probable reaction mechanism of styrene oxidation with O_2 over synthesized CeO_2 NW based catalyst.

Scheme 8.1 shows a proposed mechanism for the epoxidation reaction of styrene. It starts by adsorbing styrene onto the surface of the catalyst (CeO_2-based nanoparticles) as a result of p-interaction associated with aromatic ring.[366] Then follows the adsorption of oxygen onto the surface of the catalyst. On the surface of the CeO_2 nanoparticles, some sites become vacant as a result of the formation of Ce^{3+}. It is these vacancies that are occupied by molecular oxygen.[76] Eventually, the adsorbed species (styrene and oxygen) interact together to form the product styrene oxide. The other oxygen atom is left to either interact with Ce^{3+} and participate in the redox cycle or interact with another molecule of styrene. [366]

8.5 Conclusions

In this chapter, another application of the catalyst coating technique has been demonstrated. CeO_2 and Co-CeO2 nanoparticles were successfully synthesised, characterised and tested for photocatalytic oxidation of styrene. The nanoparticles powder with highly exposed active (100) surface were coated on glass beads and placed in an NMR

tube to make a simple photo reactor. In order to improve the efficiency of CeO_2 nanoparticles in photo-oxidation of styrene, different amounts of Co ions were added as dopant owing to the wide knowledge of Co complexes as efficient catalysts for selective oxidation of alkenes.[362]

The photo catalytic experimental results showed that the catalysts have high activity towards oxidation of styrene using molecular oxygen as oxidant. $Co(0.3)$-CeO_2 showed the highest conversion of styrene peaking at 45% while the highest selectivity of 61 % for styrene oxide was obtained with $Co(1.0)$-CeO_2. The kinetic study performed revealed that the reaction agrees with Langmuir-Hinshelwood model based on which a proposal for the possible reaction mechanism was made. The technique developed in this work can serve as a quick screening technique for both catalysts and oxidation of organic materials in the presence of molecular oxygen.

Chapter 9: Conclusions and Further Work

9.1 Conclusions

A gas-phase flow-type photo-reactor was developed during the present work. A new and complementary catalyst immobilization technique was developed. By deriving and applying the key equations for the reactor design, an excellent catalyst/reactant/light contact was achieved. The designed photoreactor was tested using a standard, inexpensive and commercially available TiO_2 P25 coated on silicone glass beads. Under mild reaction conditions, it is possible to achieve photodecomposition of acetone into CO_2 and H_2O . The effect of catalyst loading investigated during the pilot tests of the reactor revealed an optimum catalyst loading is required to achieve high decomposition and production rates for reactants and products respectively. Under the study conditions during this work, 5 mg/g of catalyst loading gave the highest CO_2 production rate of 5.75 ± 007 mMh^{-1} and acetone decomposition rate of 0.14 ± 0.02 mMh^{-1}. This shows that the designed reactor has capability of photodegrading organic pollutants.

Also during the present work nanostructured semiconductor photocatalysts including TiO_2, Bi_2WO_6, TS-1 and CeO_2 were synthesised through hydrothermal and sol-gel methods. In order to enhance the photocatalytic activity of the catalysts were modified through doping with metal ions such as Co, which was used in Chapter 8 as a dopant on CeO_2. The powders obtained from these syntheses were coated on glass beads through a novel technique with high adherence efficiency. The adherence of the catalyst on glass beads depend on the concentration of OH radicals on the glass support. The streamline design of the reactor made

it possible for all the reacting species to be in contact simultaneously, while the transparency of the glass beads provided an excellent UV light penetration.

Using Bi_2WO_6 and $Bi_2WO_6–TiO_2$ composite as photo catalysts, epoxidation of propylene was achieved using the designed reactor. Using reaction mixture of propylene:oxygen:nitrogen corresponding to the ratio 1:1:15, it was possible to produce propylene oxide with high selectivity of 64 % over B-50/TiO_2. The enhanced photocatalytic activity of B-50/TiO_2 has been ascribed to its large $Bi_2WO_6–TiO_2$ interface.

$Bi_2WO_6–TiO_2$ and Bi_2WO_6 are excellent photochromic materials. They turn from a bright yellow color to a black color. The amount of TiO_2 catalyst present in the $Bi_2WO_6–TiO_2$ play an important role the photochroism of Bi_2WO_6 by introducing extra defects at the interface of the composite. The selectivity of PO was 17 % higher when a darkened composite was used. This increment in selectivity was attributed to the trapping of photo excited electrons by the formed defects. This consequently decrease the reduction power of these electrons resulting in change in reaction pathway that produces organic intermediates. This leads to enhanced selectivity of PO. The photoluminescence results also supports the likelihood of photo induced defects in $Bi_2WO_6–TiO_2$, hence its higher activity.

The gas-phase photo-epoxidation of cyclohexene using a mixture of H_2 and O_2 was investigated. The kinetics results showed that the gas-phase reaction mechanism follows the Eley–Rideal mechanism. The physisorbed cyclohexene reacted directly with the intermediate formed through reaction between Ti base and the OOH species, to produce the cyclohexene oxide. Reaction activation energy was measured to be approximately 31 kJmol^{-1}.

The designed reactor was also used for the photo-epoxidation of 1-hexene. By bubbling the exhaust of the photo-reactor as starting material, directly through methanol which acted as a nucleophile under acidic condition for several hours. This made it possible to establish

the features of some of the reactive species formed during the partial photo-oxidation of 1-hexene process.

Finally, the catalyst coating technique was tested in a liquid phase. Using CeO_2 as photocatalyst, photo-oxidation of styrene was performed through NMR spectroscopy. Using molecular oxygen as the oxidant, Co-doped CeO_2 showed the highest conversion of 48% with a selectivity of styrene oxide of 78%.

It can therefore be said that during the present thesis it was possible to design a gas phase reactor which proved to be efficient for photo-degradation of organic pollutants as well as photo-epoxidation of alkenes. In addition to air purification potential of the designed reactor, it can also be a means for novel organic synthesis.

9.2 Further work

First, several optimization procedures can help greatly in choosing the best conditions for optimum results. Time did not allow for such optimization during this thesis work. Such optimisations should include flow rates, temperature, partial pressure, surface are of catalyst coated on the glass beads as well as ratio of components in case of composite materials. The relationship between these parameters should also be determined. Nevertheless, initial steps have been taken during this work. Novel, more efficient photocatalysts the will utilize visible light should be synthesised and applied to the GIAC coating technique. By using smaller glass beads, less than the ones used here (1.0-1.5 mm diameter) the surface area of the catalyst on glass beads may be improved. The synthetic route presented in Chapter 7 has great industrial potential application especially for novel materials whose starting material are not easy to come by. As such, efforts should be made to isolate and identify reaction products as well as their formation pathways. This case other instruments liquid chromatography be used. Choice

of photocatalyst should be efforts should be made to isolate and identify the two novel synthetic products created in order to ascertain their mechanistic formation pathways. This could be performed through a variety of techniques amongst which liquid chromatography and cryogenic distillation. Once a solid understanding of the underlying processes is achieved, the photosynthetic reactor can be developed further in order to study its effectiveness as a synthetic flow reactor for the formation of rare organic molecules.

Concentration of oxidising agents (such as O_2) in the gas streams should be controlled. As suggested in this work, changing the catalyst's specific properties may positively improve the selectivity of the desired product.

Through these modifications, it may be possible to obtain a second generation of photo-catalysts. These materials would greatly improve the overall performance of the designed photoreactor for photocatalysis.

References

1   Y. Jiang, P. Zhang, Z. Liu and F. Xu, The preparation of porous nano-TiO_2 with high activity and the discussion of the cooperation photocatalysis mechanism, *Mater. Chem. Phys.*, 2006, **99**, 498–504.

2   A. Sclafani, L. Palmisano and E. Davì, Photocatalytic degradaton of phenol in aqueous polycrystalline TiO_2 dispersions: the influence of Fe^{3+}, Fe^{2+} and Ag^+ on the reaction rate, *J. Photochem. Photobiol. A Chem.*, 1991, **56**, 113–123.

3   C. McManamon, J. O'Connell, P. Delaney, S. Rasappa, J. D. Holmes and M. A. Morris, A facile route to synthesis of S-doped TiO_2 nanoparticles for photocatalytic activity, *J. Mol. Catal. A Chem.*, 2015, **406**, 51–57.

4   Energy Information Administration, *International Energy Outlook 2016-World energy demand and economc outlook*, 2016.

5   P. W. Griffin, G. P. Hammond and J. B. Norman, Industrial energy use and carbon emissions reduction in the chemicals sector: A UK perspective, *Appl. Energy*, 2018, **227**, 587–602.

6   G. P. Hammond and Á. O' Grady, The life cycle greenhouse gas implications of a UK gas supply transformation on a future low carbon electricity sector, *Energy*, 2017, **118**, 937–949.

7   T. L. Lohr, A. Mouat, N. M. Schweitzer, P. C. Stair, M. Delferro and T. Marks, Efficient Catalytic Greenhouse Gas-Free Hydrogen and Aldehyde Formation from Aqueous Alcohol Solutions, *Energy Environ. Sci.*, , DOI:10.1039/C6EE03739A.

8   G. P. Hammond and Á. O'Grady, Indicative energy technology assessment of UK shale gas extraction, *Appl. Energy*, 2017, **185**, 1907–1918.

9   R. deRichter and S. Caillol, Fighting global warming: The potential of photocatalysis against CO_2, CH_4, N_2O, CFCs, tropospheric O_3, BC and other major contributors to climate change, *J. Photochem. Photobiol. C Photochem. Rev.*, 2011, **12**, 1–19.

10   S. G. Newman, K. Lee, J. Cai, L. Yang, W. H. Green and K. F. Jensen, Continuous Thermal Oxidation of Alkenes with Nitrous Oxide in a Packed Bed Reactor, *Ind. Eng. Chem. Res.*, 2015, **54**, 4166–4173.

11   S. Das and W. Wan Daud, Photocatalytic CO_2 transformation into fuel: A review on advances in photocatalyst and photoreactor, *Renewable and Sustainable Ener. Reviews*, 2014, **39**, 765-805.

12   *Energy and carbon for green chemistry*, 2015.

13   IEA, Clean energy. Progress Report. IEA input to the Clean Energy Ministerial, *Oecd /Iea*, 2011, 67.

14   Z. Haiwei and X. Wang, in *2009 International Conference on Management of e-Commerce and e-Government, ICMeCG 2009*, IEEE, 2009, pp. 32–35.

15   United States Environmental Protection Agency, *2012 Toxics Release Inventory National ANalysis Overview*, 2014.

16   T. Ohno, M. Akiyoshi, T. Umebayashi, K. Asai, T. Mitsui and M. Matsumura, Preparation of S-doped TiO2 photocatalysts and their photocatalytic activities under visible light, *Appl. Catal. A Gen.*, 2004, **265**, 115–121.

17   O. Concentrations, P. M. Concentrations, A. T. Concentrations, A. T. Emissions and B. E. Landcover, Volatile Organic Compounds Emissions.

18   V. Chauke and T. Nyokong, Photocatalytic oxidation of 1-hexene using GaPc and InPc octasubstituted derivatives, *J. Mol. Catal. A Chem.*, 2008, **289**, 9–13.

19   X. Lang, X. Chen and J. Zhao, Heterogeneous visible light photocatalysis for selective organic transformations, *Chem. Soc. Rev.*, 2014, **43**, 473–486.

20   L.G. Wade, *Organic Chemistry*, Prentice Hall International, New Jersey, Fourth., 1999.

21   H. Ando, Selective Alkene Production by the Hydrogenation of Carbon Dioxide over Fe-Cu Catalyst, *Energy Procedia*, 2016, **89**, 421–427.

22   J. Atkins, P., Paula, *Elements of Physical Chemistry*, 2009.

23   X. Song, C. Liu, P. Chen, H. Zhang and R. Sun, Natural product-based pesticide discovery: Design, synthesis and bioactivity studies of N-amino-maleimide derivatives, *Molecules*, 2018, **23**, 1–12.

24   N. Yang, D.-M. Yan, Q.-Q. Zhao, J.-R. Chen and W.-J. Xiao, Synthesis of Dihydropyrazoles via Ligand-Free Pd-Catalyzed Alkene Aminoarylation of Unsaturated Hydrazones with Diaryliodonium Salts, , DOI:10.1021/acs.orglett.7b02480.

25   M. S. C. Chan, E. Marek, S. A. Scott and J. S. Dennis, Chemical looping epoxidation, *J. Catal.*, 2018, **359**, 1–7.

26   Markit IHS, Fluoropolymers - Chemical Economics Handbook (CEH) | IHS Markit, https://ihsmarkit.com/products/propylene-chemical-economics-handbook.html, (accessed 29 April 2019).

27   M. Shahid, A. McDonagh, J. H. Kim and H. K. Shon, Magnetised titanium dioxide (TiO₂) for water purification: preparation, characterisation and application, *Desalin. Water Treat.*, 2015, **54**, 979–1002.

28   P. Y. Bruice, *Organic Chemistry*, Prentice Hall, New Jersey, Second., 1998.

29   P. Pichat, J. M. Herrmann, J. Disdier and M. N. Mozzanega, Photocatalytic oxidation

of propene over various oxides at 320 K. Selectivity, *J. Phys. Chem.*, 1979, **83**, 3122–3126.

30   M. S. C. Chan, E. Marek, S. A. Scott and J. S. Dennis, Chemical looping epoxidation, *J. Catal.*, 2018, **359**, 1–7.

31   S. Wang, H. M. Ang and M. O. Tade, Volatile organic compounds in indoor environment and photocatalytic oxidation: State of the art, *Environ. Int.*, 2007, **33**, 694–705.

32   J. E. Lyons and R. A. Sheldon, *Aspects Homogeneous Catal*, UTC, 1986, vol. 108.

33   V. V. Torbina, I. D. Ivanchikova, O. A. Kholdeeva, I. Y. Skobelev and O. V. Vodyankina, Propylene glycol oxidation with tert -butyl hydroperoxide over Cr-containing metal-organic frameworks MIL-101 and MIL-100, *Catal. Today*, 2016, **278**, 97–103.

34   M. M. Heravi, T. B. Lashaki and N. Poorahmad, *Tetrahedron Asymmetry*, 2015, 26, 405–495.

35   H. Kisch, Semiconductor Photocatalysis-Mechanistic and Synthetic Aspects, *Angew. Chemie Int. Ed.*, 2013, **52**, 812–847.

36   Y. Huang, S. S. H. Ho, R. Niu, L. Xu, Y. Lu, J. Cao and S. Lee, *Molecules*, 2016, 21, 56.

37   K.-C. Huang, Z. Zhao, G. E. Hoag, A. Dahmani and P. A. Block, Degradation of volatile organic compounds with thermally activated persulfate oxidation, *Chemosphere*, 2005, **61**, 551–560.

38   P. Gramatica, P. Pilutti and E. Papa, Validated QSAR Prediction of OH Tropospheric Degradation of VOCs: Splitting into Training−Test Sets and Consensus Modeling, *J. Chem. Inf. Comput. Sci.*, 2004, **44**, 1794–1802.

39   G. S. Cheripally, A. Mannava, G. Kumar, R. Gupta, P. Saha, B. Mandal, R. Uppaluri, S. Gumma and A. K. Ghoshal, Measurement and Modeling of Adsorption of Lower Hydrocarbons on Activated Carbon, *J. Chem. Eng. Data*, 2013, **58**, 1606–1612.

40   M. Halecky, J. Rousova, J. Paca, E. Kozliak, W. Seames and K. Jones, Biofiltration of gasoline and diesel aliphatic hydrocarbons, *J. Air Waste Manag. Assoc.*, 2015, **65**, 133–144.

41   T. Prabhat Kumar, M. Anil Kumar and B. Chandrajit, Biofiltration of Volatile Organic Compounds (VOCs) – An Overview, *Res. J. Chem. Sci.*, 2011, **1**, 83–92.

42   A. Maki and J. Mizuguchi, VOC Decomposition System Based upon Heater-Integrated Catalyst Units Using NiO or Cr, *Mater. Trans.*, 2010, **51**, 1361–1363.

43   M. P. GORDON, Advances in Photochemistry: Volume 6, *Photochem. Photobiol.*,

2008, **11**, 145–145.

44   N. J. Turro and G. Schuster, *Photochemical Reactions as a Tool in Organic Syntheses*, 1975, vol. 187.

45   A. Albini, *Photochem. Photobiol. Sci.*, 2016, 15, 319–324.

46   D. O. Draper and S. Sunderland, Examination of the law of grotthus-draper: does ultrasound penetrate subcutaneous fat in humans?, *J. Athl. Train.*, 1993, **28**, 246–250.

47   S. Califano, *Pathways to Modern Chemical Physics*, Springer Berlin Heidelberg, Berlin, Heidelberg, 2012, vol. 9783642281.

48   H. W. Foote, Elements of Physical Chemistry, *Science (80-.).*, 2006, **26**, 588–588.

49   M. Oelgemöller, Solar Photochemical Synthesis: From the Beginnings of Organic Photochemistry to the Solar Manufacturing of Commodity Chemicals, *Chem. Rev.*, 2016, **116**, 9664–9682.

50   H. Görner and H. J. Kuhn, John Wiley & Sons, Ltd, 2007, pp. 1–117.

51   M. Quick, F. Berndt, A. L. Dobryakov, I. N. Ioffe, A. A. Granovsky, C. Knie, R. Mahrwald, D. Lenoir, N. P. Ernsting and S. A. Kovalenko, Photoisomerization dynamics of stiff-stilbene in solution, *J. Phys. Chem. B*, 2014, **118**, 1389–1402.

52   S. Poplata, A. Tröster, Y.-Q. Zou and T. Bach, Recent Advances in the Synthesis of Cyclobutanes by Olefin [2 + 2] Photocycloaddition Reactions., *Chem. Rev.*, 2016, **116**, 9748–815.

53   K. Kabra, R. Chaudhary and R. L. Sawhney, Treatment of Hazardous Organic and Inorganic Compounds through Aqueous-Phase Photocatalysis: A Review, *Ind. Eng. Chem. Res.*, 2004, **43**, 7683–7696.

54   H. Einaga, K. Mochiduki and Y. Teraoka, Photocatalytic Oxidation Processes for Toluene Oxidation over TiO2 Catalysts, *Catalysts*, 2013, **3**, 219–231.

55   M. D. Driessen, a L. Goodman, T. M. Miller, G. a Zaharias and V. H. Grassian, Gas-phase photooxidation of trichloroethylene on TiO_2 and ZnO: Influence of trichloroethylene pressure, oxygen pressure, and the photocatalyst surface on the product distribution, *J. Phys. Chem. B*, 1998, **102**, 549–556.

56   Y. Liu, P. Zhang, B. Tian and J. Zhang, Enhancing the photocatalytic activity of CdS nanorods for selective oxidation of benzyl alcohol by coating amorphous TiO_2 shell layer, *Catal. Commun.*, 2015, **70**, 30–33.

57   V. Paramarta, A. Taufik, L. Munisa and R. Saleh, in *AIP Conference Proceedings*, 2017, vol. 1788, p. 030125.

58   L. Lin, Y. Chai, B. Zhao, W. Wei, D. He, B. He and Q. Tang, Photocatalytic oxidation for degradation of VOCs, *Open J. Inorg. Chem.*, 2013, **03**, 14–25.

59   O. Carp, C. L. Huisman and A. Reller, Photoinduced reactivity of titanium dioxide, *Prog. Solid State Chem.*, 2004, **32**, 33–177.

60   L. Lin, Y. Chai, B. Zhao, W. Wei, D. He, B. He and Q. Tang, Photocatalytic oxidation for degradation of VOCs, *Open J. Inorg. Chem.*, 2013, **03**, 14–25.

61   M. Hussain, N. Russo and G. Saracco, Photocatalytic abatement of VOCs by novel optimized TiO_2 nanoparticles, *Chem. Eng. J.*, 2011, **166**, 138–149.

62   H. Yu, K. Zhang and C. Rossi, Theoretical study on photocatalytic oxidation of VOCs using nano-TiO_2 photocatalyst, *J. Photochem. Photobiol. A Chem.*, 2007, **188**, 65–73.

63   N. Hoffmann, Photochemical Reactions as Key Steps in Organic Synthesis, *Chem. Rev.*, 2008, **108**, 1052–1103.

64   S.-W. Han, J.-H. Lee, J. S. Kim, S.-H. Oh, Y.-K. Park and H. Kim, Gaseous by-products from the TiO_2 Photocatalytic Oxidation of Benzene, *Environ. Eng. Res.*, 2008, **13**, 14–18.

65   M. K. Nayak, J. Singh, B. Singh, S. Soni, V. S. Pandey and S. Tyagi, in *Metal Semiconductor Core-Shell Nanostructures for Energy and Environmental Applications*, Elsevier, 2017, pp. 1–33.

66   S. M. Gupta and M. Tripathi, A review of TiO2 nanoparticles, *Chinese Sci. Bull.*, 2011, **56**, 1639–1657.

67   Y. Zhou, G. Chen, Y.-G. Y. Yu, C. Yan, J. Sun and F. He, Synthesis of metal oxide nanosheets through a novel approach for energy applications, *J. Mater. Chem. A*, 2016, **4**, 781–784.

68   K. Supattarasakda, K. Petcharoen, T. Permpool, A. Sirivat and W. Lerdwijitjarud, Control of hematite nanoparticle size and shape by the chemical precipitation method, *Powder Technol.*, 2013, **249**, 353–359.

69   P. K. Dutta, S. O. Pehkonen, V. K. Sharma and A. K. Ray, Photocatalytic oxidation of arsenic (III): Evidence of hydroxyl radicals, *Environ. Sci. Technol.*, 2005, **39**, 1827–1834.

70   M. Fujihira, Y. Satoh and T. Osa, Heterogeneous photocatalytic oxidation of aromatic compounds on TiO 2, *Nature*, 1981, **293**, 206–208.

71   R. Shi, G. Huang, J. Lin and Y. Zhu, Photocatalytic activity enhancement for Bi_2WO_6 by fluorine substitution, *J. Phys. Chem. C*, 2009, **113**, 19633–19638.

72   Y. Lv, W. Yao, R. Zong and Y. Zhu, Fabrication of Wide–Range–Visible Photocatalyst Bi_2WO_{6-x} nanoplates via Surface Oxygen Vacancies, *Sci. Rep.*, 2016, **6**, 19347.

73   R. Shi, G. Huang, J. Lin and Y. Zhu, Photocatalytic Activity Enhancement for Bi_2WO_6

by Fluorine Substitution, DOI:10.1021/jp906680e.

74   R. M. Cory and G. W. Kling, Interactions between sunlight and microorganisms influence dissolved organic matter degradation along the aquatic continuum, *Limnol. Oceanogr. Lett.*, 2018, **3**, 102–116.

75   A. Di Paola, E. García-López, S. Ikeda, G. Marc, B. Ohtani and L. Palmisano, in *Catalysis Today*, Elsevier, 2002, vol. 75, pp. 87–93.

76   G. I. N. Waterhouse and M. R. Waterland, Opal and inverse opal photonic crystals: Fabrication and characterization, *Polyhedron*, 2007, **26**, 356–368.

77   M. M. Khan, S. F. Adil and A. Al-Mayouf, *J. Saudi Chem. Soc.*, 2015, 19, 462–464.

78   N. Rahimi, R. A. Pax and E. M. A. Gray, *Prog. Solid State Chem.*, 2016, 44, 86–105.

79   M. Grätzel, Photoelectrochemical cells, *Nat. 2001 4146861*.

80   K. Hashimoto, H. Irie and A. Fujishima, A Historical Overview and Future Prospects, *AAPPS Bull.*, 2007, **17**, 12–28.

81   H. Li, H. Wu, J. Xiao, Y. Su, J. Robichaud, R. Brüning and Y. Djaoued, A hierarchically porous anatase TiO_2 coated-WO_3 2D IO bilayer film and its photochromic properties, *Chem. Commun.*, 2016, **52**, 892–895.

82   a Fujishima and K. Honda, Electrochemical photolysis of water at a semiconductor electrode., *Nature*, 1972, **238**, 37–38.

83   C. P. Sajan, S. Wageh, A. A. Al-Ghamdi, J. Yu and S. Cao, TiO_2 nanosheets with exposed {001} facets for photocatalytic applications, *Nano Res.*, 2016, **9**, 3–27.

84   S. Kaneco, H. Kurimoto, Y. Shimizu, K. Ohta and T. Mizuno, Photocatalytic reduction of CO_2 using TiO_2 powders in supercritical fluid CO_2, *Energy*, 1999, **24**, 21–30.

85   M. Li, P. Li, K. Chang, T. Wang, L. Liu, Q. Kang, S. Ouyang and J. Ye, Highly efficient and stable photocatalytic reduction of CO_2 to CH_4 over Ru loaded $NaTaO_3$, *Chem. Commun.*, 2015, 7645–7648.

86   B. Mei, A. Pougin and J. Strunk, Influence of photodeposited gold nanoparticles on the photocatalytic activity of titanate species in the reduction of CO_2 to hydrocarbons, *J. Catal.*, 2013, **306**, 184–189.

87   A. Corma and H. Garcia, Photocatalytic reduction of CO_2 for fuel production: Possibilities and challenges, *J. Catal.*, 2013, **308**, 168–175.

88   M. J. Muñoz-Batista, A. Kubacka, R. Rachwalik, B. Bachiller-Baeza and M. Fernández-García, Green photo-oxidation of styrene over W–Ti composite catalysts, *J. Catal.*, 2014, **309**, 428–438.

89   Y. Ren, Y. Che, W. Ma, X. Zhang, T. Shen and J. Zhao, Selective photooxidation of

styrene in organic–water biphasic media, *New J. Chem.*, 2004, **28**, 1464–1469.

90   M. Z. Guo and C. S. Poon, Photocatalytic NO removal of concrete surface layers intermixed with TiO_2, *Build. Environ.*, 2013, **70**, 102–109.

91   V. N. H. Nguyen, R. Amal and D. Beydoun, Effect of formate and methanol on photoreduction/removal of toxic cadmium ions using TiO_2 semiconductor as photocatalyst, *Chem. Eng. Sci.*, 2003, **58**, 4429–4439.

92   G. Palmisano, E. García-López, G. Marcì, V. Loddo, S. Yurdakal, V. Augugliaro and L. Palmisano, Advances in selective conversions by heterogeneous photocatalysis., *Chem. Commun. (Camb).*, 2010, **46**, 7074–89.

93   J. Wang, P. Yang, B. Cao, J. Zhao and Z. Zhu, Photocatalytic carbon-carbon bond formation with concurrent hydrogen evolution on the Pt/TiO_2 nanotube, *Appl. Surf. Sci.*, 2015, **325**, 86–90.

94   Y. Ma, S. R. Pendlebury, A. Reynal, F. le Formal and J. R. Durrant, Dynamics of photogenerated holes in undoped $BiVO_4$ photoanodes for solar water oxidation, *Chem. Sci.*, 2014, **5**, 2964.

95   P. M. Rao, L. Cai, C. Liu, I. S. Cho, C. H. Lee, J. M. Weisse, P. Yang and X. Zheng, Simultaneously Efficient Light Absorption and Charge Separation in $WO_3/BiVO_4$ Core/Shell Nanowire Photoanode for Photoelectrochemical Water Oxidation, *Nano Lett.*, 2014, **14**, 1099–1105.

96   K. Fuku and K. Sayama, Efficient oxidative hydrogen peroxide production and accumulation in photoelectrochemical water splitting using a tungsten trioxide/bismuth vanadate photoanode., *Chem. Commun. (Camb).*, 2016, **52**, 5406–5409.

97   Y. Liang and J. Messinger, Improving $BiVO_4$ photoanodes for solar water splitting through surface passivation., *Phys. Chem. Chem. Phys.*, 2014, **16**, 12014–20.

98   T. N. Obee and R. T. Brown, TiO2 Photocatalysis for Indoor Air Applications: Effects of Humidity and Trace Contaminant Levels on the Oxidation Rates of Formaldehyde, Toluene, and 1,3-Butadiene, *Environ. Sci. Technol.*, 1995, **29**, 1223–1231.

99   J. Zhao and X. Yang, Photocatalytic oxidation for indoor air purification: a literature review, *Build. Environ.*, 2003, **38**, 645–654.

100   A. Houas, *Appl. Catal. B Environ.*, 2001, 31, 145–157.

101   Y. Kuwahara, J. Aoyama, K. Miyakubo, T. Eguchi, T. Kamegawa, K. Mori and H. Yamashita, TiO_2 photocatalyst for degradation of organic compounds in water and air supported on highly hydrophobic FAU zeolite: Structural, sorptive, and photocatalytic studies, *J. Catal.*, 2012, **285**, 223–234.

102   H. Song, H. Jiang, X. Liu and G. Meng, Efficient degradation of organic pollutant with

WOx modified nano TiO$_2$ under visible irradiation, *J. Photochem. Photobiol. A Chem.*, 2006, **181**, 421–428.

103 W. Y. Teoh, F. Denny, R. Amal, D. Friedmann, L. Mädler and S. E. Pratsinis, Photocatalytic mineralisation of organic compounds: a comparison of flame-made TiO$_2$ catalysts, *Top. Catal.*, 2007, **44**, 489–497.

104 N. Rahimi, R. A. Pax and E. M. A. Gray, Review of functional titanium oxides. I: TiO$_2$ and its modifications, *Prog. Solid State Chem.*, 2016, **44**, 86–105.

105 L. Rimoldi, D. Meroni, E. Falletta, V. Pifferi, L. Falciola, G. Cappelletti and S. Ardizzone, Emerging pollutant mixture mineralization by TiO$_2$ photocatalysts. The role of the water medium, *Photochem. Photobiol. Sci.*, 2017, **16**, 60–66.

106 Y. Paz, Application of TiO$_2$ photocatalysis for air treatment: Patents' overview, *Appl. Catal. B Environ.*, 2010, **99**, 448–460.

107 A. Fujishima, X. Zhang and D. A. Tryk, *Surf. Sci. Rep.*, 2008.

108 R. Portela, S. Suárez, S. B. Rasmussen, N. Arconada, Y. Castro, A. Durán, P. Ávila, J. M. Coronado and B. Sánchez, Photocatalytic-based strategies for H2S elimination, *Catal. Today*, 2010, **151**, 64–70.

109 A. K. L. Sajjad, S. Shamaila, B. Tian, F. Chen and J. Zhang, One step activation of WO$_x$/TiO$_2$ nanocomposites with enhanced photocatalytic activity, *Appl. Catal. B Environ.*, 2009, **91**, 397–405.

110 V. Pfeifer, P. Erhart, S. Li, K. Rachut, J. Morasch, J. Brötz, P. Reckers, T. Mayer, S. Rühle, A. Zaban, I. Mora Seró, J. Bisquert, W. Jaegermann and A. Klein, Energy band alignment between anatase and rutile TiO$_2$, *J. Phys. Chem. Lett.*, 2013, **4**, 4182–4187.

111 A. Di Paola, M. Bellardita, R. Ceccato, L. Palmisano and F. Parrino, Highly active photocatalytic TiO$_2$ powders obtained by thermohydrolysis of TiCl$_4$ in water, *J. Phys. Chem. C*, 2009, **113**, 15166–15174.

112 R. Su, R. Bechstein, L. Sø, R. T. Vang, M. Sillassen, B. Esbjörnsson, A. Palmqvist and F. Besenbacher, How the Anatase-to-Rutile Ratio Influences the Photoreactivity of TiO$_2$, *J. Phys. Chem. C*, 2011, **115**, 24287–24292.

113 T. Khoa Le, D. Flahaut, H. Martinez, H. K. Hung Nguyen and T. K. Xuan Huynh, Study of the effects of surface modification by thermal shock method on photocatalytic activity of TiO$_2$ P25, *Appl. Catal. B Environ.*, 2015, **165**, 260–268.

114 B. Ohtani, O. O. Prieto-Mahaney, D. Li and R. Abe, What is Degussa (Evonic) P25? Crystalline composition analysis, reconstruction from isolated pure particles and photocatalytic activity test, *J. Photochem. Photobiol. A Chem.*, 2010, **216**, 179–182.

115 J. Yu, W. Wang, B. Cheng and B. L. Su, Enhancement of photocatalytic activity of Mesoporous TiO$_2$ powders by hydrothermal surface fluorination treatment, *J. Phys.*

Chem. C, 2009, **113**, 6743–6750.

116   F. J. López-Tenllado, A. Marinas, F. J. Urbano, J. C. Colmenares, M. C. Hidalgo, J. M. Marinas and J. M. Moreno, Selective photooxidation of alcohols as test reaction for photocatalytic activity, *Appl. Catal. B Environ.*, 2012, **128**, 150–158.

117   N. Veronovski, P. Andreozzi, C. La Mesa and M. Sfiligoj-Smole, Stable TiO$_2$ dispersions for nanocoating preparation, *Surf. Coatings Technol.*, 2010, **204**, 1445–1451.

118   T. Ohno, K. Sarukawa, K. Tokieda and M. Matsumura, Morphology of a TiO$_2$ photocatalyst (Degussa, P-25) consisting of anatase and rutile crystalline phases, *J. Catal.*, 2001, **203**, 82–86.

119   A. L. Linsebigler, G. Lu and J. T. Yates, Photocatalysis on TiO$_2$ Surfaces_ Principles, Mechanisms, and Selected Results.pdf, 1995, 735–758.

120   J. W. Ha, Y. W. Do, J. H. Park and C. H. Han, Preparation and photocatalytic performance of nano-TiO$_2$-coated beads for methylene blue decomposition, *J. Ind. Eng. Chem.*, 2009, **15**, 670–673.

121   S. Bogati, A. Georg and W. Graf, Photoelectrochromic devices based on sputtered WO$_3$ and TiO$_2$ films, *Sol. Energy Mater. Sol. Cells*, 2017, **163**, 170–177.

122   K. Kočí, L. Obalová and Z. Lacný, Photocatalytic reduction of CO$_2$ over TiO$_2$ based catalysts, *Chem. Pap.*, 2008, **62**, 1–9.

123   W. Jenks and K. Schmidt-rohr, 2009.

124   Z. Zhang, C.-C. Wang, R. Zakaria and J. Y. Ying, Role of Particle Size in Nanocrystalline TiO$_2$-Based Photocatalysts, *J. Phys. Chem. B*, 1998, **102**, 10871–10878.

125   A. L. Linsebigler, A. L. Linsebigler, J. T. Yates Jr, G. Lu, G. Lu and J. T. Yates, Photocatalysis on TiO$_2$ Surfaces: Principles, Mechanisms, and Selected Results, *Chem. Rev.*, 1995, **95**, 735–758.

126   A. V. Vorontsov, D. V. Kozlov, P. G. Smirniotis and V. N. Parmon, TiO$_2$ photocatalytic oxidation: II. Gas-phase processes, *Kinet. Catal.*, 2005, **46**, 422–436.

127   S. Kuang, L. Yang, S. Luo and Q. Cai, Fabrication, characterization and photoelectrochemical properties of Fe$_2$O$_3$ modified TiO$_2$ nanotube arrays, *Appl. Surf. Sci.*, 2009, **255**, 7385–7388.

128   A. Hajjaji, K. Trabelsi, A. Atyaoui, M. Gaidi, L. Bousselmi, B. Bessais and M. A. El Khakani, Photocatalytic activity of Cr-doped TiO$_2$ nanoparticles deposited on porous multicrystalline silicon films, *Nanoscale Res. Lett.*, 2014, **9**, 1–6.

129   Y. H. Peng, G. F. Huang and W. Q. Huang, Visible-light absorption and photocatalytic

activity of Cr-doped TiO$_2$ nanocrystal films, *Adv. Powder Technol.*, 2012, **23**, 8–12.

130   A. Poorkarimi, A. Karimi-Jashni and S. Javadpour, Optimization of toluene removal over W-doped TiO$_2$ nano-photocatalyst under visible light irradiation, *Environ. Technol. (United Kingdom)*, 2018, **39**, 3135–3148.

131   S. Sathasivam, D. S. Bhachu, Y. Lu, N. Chadwick, S. A. Althabaiti, A. O. Alyoubi, S. N. Basahel, C. J. Carmalt and I. P. Parkin, Tungsten doped TiO$_2$ with enhanced photocatalytic and optoelectrical properties via aerosol assisted chemical vapor deposition, *Sci. Rep.*, 2015, **5**, 10952.

132   O. Avilés-García, J. Espino-Valencia, R. Romero, J. L. Rico-Cerda, M. Arroyo-Albiter and R. Natividad, W and Mo doped TiO$_2$: Synthesis, characterization and photocatalytic activity, *Fuel*, 2017, **198**, 31–41.

133   W. Soontornchaiyakul, T. Fujimura, H. Usami and R. Sasai, Effects of Rh-doping on the photooxidative degradation activity of titanate nanosheets, *RSC Adv.*, 2017, **7**, 21790–21795.

134   X. yu Sun, C. Liu, Z. Chen and Y. qing Ma, The photocatalytic performance of Ta and Rh co-doped TiO$_2$ tuned by the average dopant valence, *Mater. Res. Bull.*, 2018, **100**, 153–160.

135   J. Kuncewicz and B. Ohtani, Rhodium-doped titania photocatalysts with two-step bandgap excitation by visible light - Influence of the dopant concentration on photosensitization efficiency, *RSC Adv.*, 2016, **6**, 77201–77211.

136   D. Y. Lee, M.-H. Lee, B.-Y. Kim and N.-I. Cho, Crystal Structure and Photocatalytic Activity of Al-Doped TiO$_2$ Nanofibers for Methylene Blue Dye Degradation, *J. Nanosci. Nanotechnol.*, 2016, **16**, 5341–5344.

137   C. Y. Tsai, T. H. Kuo and H. C. Hsi, Fabrication of Al-doped TiO$_2$ visible-light photocatalyst for low-concentration mercury removal, *Int. J. Photoenergy*, 2012, **2012**, 1–8.

138   B. Taylor, J. Lauterbach, G. E. Blau and W. N. Delgass, Reaction kinetic analysis of the gas-phase epoxidation of propylene over Au/TS-1, *J. Catal.*, 2006, **242**, 142–152.

139   Z. Zhang, Z. Luo, Z. Yang, S. Zhang, Y. Zhang, Y. Zhou, X. Wang and X. Fu, Band-gap tuning of N-doped TiO$_2$ photocatalysts for visible-light-driven selective oxidation of alcohols to aldehydes in water, *RSC Adv.*, 2013, **3**, 7215–7218.

140   S. A. Ansari, M. M. Khan, M. O. Ansari and M. H. Cho, *New J. Chem.*, 2016, 40, 3000–3009.

141   R. Asahi, T. Morikawa, H. Irie and T. Ohwaki, Nitrogen-Doped Titanium Dioxide as Visible-Light-Sensitive Photocatalyst: Designs, Developments, and Prospects, *Chem. Rev.*, 2014, **114**, 9824–9852.

142 E. Grabowska, A. Zaleska, J. W. Sobczak, M. Gazda and J. Hupka, in *Procedia Chemistry*, Elsevier, 2009, vol. 1, pp. 1553–1559.

143 L. Li, Y. Yang, X. Liu, R. Fan, Y. Shi, S. Li, L. Zhang, X. Fan, P. Tang, R. Xu, W. Zhang, Y. Wang and L. Ma, A direct synthesis of B-doped TiO_2 and its photocatalytic performance on degradation of RhB, *Appl. Surf. Sci.*, 2013, **265**, 36–40.

144 L. G. Devi and R. Kavitha, Enhanced photocatalytic activity of sulfur doped TiO_2 for the decomposition of phenol: A new insight into the bulk and surface modification, *Mater. Chem. Phys.*, 2014, **143**, 1300–1308.

145 M. Humayun, F. Raziq, A. Khan and W. Luo, Modification strategies of TiO_2 for potential applications in photocatalysis: a critical review, *Green Chem. Lett. Rev.*, 2018, **11**, 86–102.

146 S. Ashoka, G. Nagaraju, C. N. Tharamani and G. T. Chandrappa, Ethylene glycol assisted hydrothermal synthesis of flower like ZnO architectures, *Mater. Lett.*, 2009, **63**, 873–876.

147 F. Mighri, V. T. T. Duong, D. T. On and A. Ajji, in *AIP Conference Proceedings*, American Institute of Physics, 2014, vol. 1593, pp. 265–269.

148 K. Pan, Y. Dong, W. Zhou, Q. Pan, Y. Xie, T. Xie, G. Tian and G. Wang, Facile Fabrication of Hierarchical TiO_2 Nanobelt/ZnO Nanorod Heterogeneous Nanostructure: An Efficient Photoanode for Water Splitting, *ACS Appl. Mater. Interfaces*, 2013, **5**, 8314–8320.

149 R. S. Mane, W. J. Lee, H. M. Pathan and S.-H. Han, Nanocrystalline TiO_2/ZnO Thin Films: Fabrication and Application to Dye-Sensitized Solar Cells, *J. Phys. Chem. B*, 2005, **109**, 24254–24259.

150 M. Shang, W. Wang, S. Sun, L. Zhou and L. Zhang, Bi_2WO_6 Nanocrystals with High Photocatalytic Activities under Visible Light, , DOI:10.1021/jp802115w.

151 J. Tang, Z. Zou and J. Ye, Photocatalytic Decomposition of Organic Contaminants by Bi_2WO_6 Under Visible Light Irradiation, *Catal. Letters*, 2004, **92**, 53–56.

152 Q. Xiao, J. Zhang, C. Xiao and X. Tan, Photocatalytic degradation of methylene blue over Co_3O_4/Bi_2WO_6 composite under visible light irradiation, *Catal. Commun.*, 2008, **9**, 1247–1253.

153 J. Tang, Z. Zou and J. Ye, Photocatalytic decomposition of organic contaminants by Bi_2WO_6 under visible light irradiation, .

154 A. Kudo and S. Hijii, H_2 or O_2 Evolution from Aqueous Solutions on Layered Oxide Photocatalysts Consisting of Bi^{3+} with 6s 2 Configuration and d 0 Transition Metal Ions, *Chem. Lett.*, 2003, **28**, 1103–1104.

155 Y. Li, J. Liu, X. Huang and J. Yu, Carbon-modified Bi_2WO_6 nanostructures with

improved photocatalytic activity under visible light, *Dalt. Trans.*, 2010, **39**, 3420–3425.

156 L. Zhang, K. H. Wong, Z. Chen, J. C. Yu, J. Zhao, C. Hu, C. Y. Chan and P. K. Wong, AgBr-Ag-Bi$_2$WO$_6$ nanojunction system: A novel and efficient photocatalyst with double visible-light active components, *Appl. Catal. A Gen.*, 2009, **363**, 221–229.

157 Z. Zhang, W. Wang, W. Yin, M. Shang, L. Wang and S. Sun, Inducing photocatalysis by visible light beyond the absorption edge: Effect of upconversion agent on the photocatalytic activity of Bi$_2$WO$_6$, *Appl. Catal. B Environ.*, 2010, **101**, 68–73.

158 N. Tian, Y. Zhang, H. Huang, Y. He and Y. Guo, Influences of Gd substitution on the crystal structure and visible-light-driven photocatalytic performance of Bi$_2$WO$_6$, *J. Phys. Chem. C*, 2014, **118**, 15640–15648.

159 S. Zhu, T. Xu, H. Fu, J. Zhao and Y. Zhu, Synergetic effect of Bi$_2$WO$_6$ photocatalyst with C$_{60}$ and enhanced photoactivity under visible irradiation, *Environ. Sci. Technol.*, 2007, **41**, 6234–6239.

160 X. Chen, L. Liu, P. Y. Yu and S. S. Mao, Increasing solar absorption for photocatalysis with black hydrogenated titanium dioxide nanocrystals, *Science (80-.).*, 2011, **331**, 746–750.

161 G. Wang, H. Wang, Y. Ling, Y. Tang, X. Yang, R. C. Fitzmorris, C. Wang, J. Z. Zhang and Y. Li, Hydrogen-treated TiO$_2$ nanowire arrays for photoelectrochemical water splitting, *Nano Lett.*, 2011, **11**, 3026–3033.

162 A. Asok, M. N. Gandhi and A. R. Kulkarni, Enhanced visible photoluminescence in ZnO quantum dots by promotion of oxygen vacancy formation, *Nanoscale*, 2012, **4**, 4943–4946.

163 Y. Guo and B. Zu, Zeolite-based Photocatalysts: A Promising Strategy for Efficient Photocatalysis, *J. Thermodyn. Catal.*, , DOI:10.4172/2157-7544.1000e120.

164 T. Ban, S. Kondoh, Y. Ohya and Y. Takahashi, Degradation reaction of monoethanolamine using TS-1 zeolite as a photocatalyst, *Phys. Chem. Chem. Phys.*, 1999, **1**, 5745–5752.

165 G. D. Lee, S. K. Jung, Y. J. Jeong, J. H. Park, K. T. Lim, B. H. Ahn and S. S. Hong, Photocatalytic decomposition of 4-nitrophenol over titanium silicalite (TS-1) catalysts, *Appl. Catal. A Gen.*, 2003, **239**, 197–208.

166 W. S. Lee, M. Cem Akatay, E. A. Stach, F. H. Ribeiro and W. Nicholas Delgass, Gas-phase epoxidation of propylene in the presence of H$_2$ and O$_2$ over small gold ensembles in uncalcined TS-1, *J. Catal.*, 2014, **313**, 104–112.

167 H. Ahsan, *Kaohsiung J. Med. Sci.*, 2011, 27, 358–359.

168 G. Jenzer, T. Mallat, M. Maciejewski, F. Eigenmann and A. Baiker, Continuous

epoxidation of propylene with oxygen and hydrogen on a Pd-Pt/TS-1 catalyst, *Appl. Catal. A Gen.*, 2001, **208**, 125–133.

169   R. Meiers and W. F. Holderich, Epoxidation of propylene and direct synthesis of hydrogen peroxide by hydrogen and oxygen, *Catal. Letters*, 1999, **59**, 161–163.

170   J. Chen, S. J. A. Halin, J. C. Schouten and T. A. Nijhuis, Kinetic study of propylene epoxidation with H_2 and O_2 over Au/Ti-SiO_2 in the explosive regime, *Faraday Discuss.*, 2011, **152**, 321–336.

171   N. Kamiuchi, M. Haneda and M. Ozawa, Propene oxidation over palladium catalysts supported on zirconium rich ceria-zirconia, *Catal. Today*, 2015, **241**, 100–106.

172   Z. Sun, H. Zhang, G. An, G. Yang and Z. Liu, Supercritical CO_2-facilitating large-scale synthesis of CeO_2 nanowires and their application for solvent-free selective hydrogenation of nitroarenes, *J. Mater. Chem.*, 2010, **20**, 1947–1952.

173   W. SHAN, C. LIU, H. GUO, L. YANG, X. WANG and Z. FENG, Synthesis of Zero, One, and Three Dimensional CeO_2 Particles and CO Oxidation over CuO/CeO_2, *Chinese J. Catal.*, 2011, **32**, 1336–1341.

174   M. D. Hernández-Alonso, A. Belén Hungría, A. Martínez-Arias, J. M. Coronado, J. Carlos Conesa, J. Soria and M. Fernández-García, Confinement effects in quasi-stoichiometric CeO2 nanoparticles, *Phys. Chem. Chem. Phys.*, 2004, **6**, 3524–3529.

175   C. Osarinmwian, Existence of three-phase interlines on a cerium dioxide surface, *arXiv Prepr. arXiv1310.2065*.

176   R. Si, Y. W. Zhang, L. P. You and C. H. Yan, Rare-earth oxide nanopolyhedra, nanoplates, and nanodisks, *Angew. Chemie - Int. Ed.*, 2005, **44**, 3256–3260.

177   W. Zhu, K. Tang, J. Li, W. Liu, X. Niu, G. Zhao, X. Ma, Z. Liu, H. Wei and Y. Yang, The effect of copper species in copper-ceria catalysts: structure evolution and enhanced performance in CO oxidation, *RSC Adv.*, 2016, **6**, 46966–46971.

178   D. C. Sayle, S. A. Maicaneanu and G. W. Watson, Atomistic Models for CeO_2 (111), (110), and (100) Nanoparticles, Supported on Yttrium-Stabilized Zirconia, *J. Am. Chem. Soc.*, 2002, **124**, 11429–11439.

179   Y. Shao and Y. Ma, Mesoporous CeO_2 nanowires as recycled photocatalysts, *Sci. China Chem.*, 2012, **55**, 1303–1307.

180   H. De Lasa, B. Serrano and M. Salaices, *Photocatalytic reaction engineering*, 2005.

181   M. Obst and B. König, Solvent-free, visible-light photocatalytic alcohol oxidations applying an organic photocatalyst, *Beilstein J. Org. Chem.*, 2016, **12**, 2358–2363.

182   G. Jones, Origin of catalytic activity in sponge Ni catalysts for hydrogenation of carbonyl compounds, *Catal. Struct. React.*, 2015, **1**, 78–87.

183   X. Li, Y. Li, Y. Huang, T. Zhang, Y. Liu, B. Yang, C. He, X. Zhou and J. Zhang, Organic sponge photocatalysis, *Green Chem.*, 2017, **19**, 2925–2930.

184   Y. Kanda, A. Seino, T. Kobayashi, Y. Uemichi and M. Sugioka, Catalytic Performance of Noble Metals Supported on Mesoporous Silica MCM-41 for Hydrodesulfurization of Benzothiophene, *J. Japan Pet. Inst.*, 2009, **52**, 42–50.

185   R. K. Liew, M. Y. Chong, O. U. Osazuwa, W. L. Nam, X. Y. Phang, M. H. Su, C. K. Cheng, C. T. Chong and S. S. Lam, Production of activated carbon as catalyst support by microwave pyrolysis of palm kernel shell: a comparative study of chemical versus physical activation, *Res. Chem. Intermed.*, 2018, **44**, 3849–3865.

186   M. A. Henderson, Effect of coadsorbed water on the photodecomposition of acetone on TiO_2 (110), *J. Catal.*, 2008, **256**, 287–292.

187   L. Liu, H. Zhao, J. M. Andino and Y. Li, Photocatalytic CO_2 Reduction with H_2O on TiO_2 Nanocrystals: Comparison of Anatase, Rutile, and Brookite Polymorphs and Exploration of Surface Chemistry, *ACS Catal.*, 2012, **2**, 1817–1828.

188   T. Li, W. Zeng, H. Long and Z. Wang, Nanosheet-assembled hierarchical SnO_2 nanostructures for efficient gas-sensing applications, *Sensors Actuators, B Chem.*, 2016, **231**, 120–128.

189   J. He, Q. Zhai, Q. Zhang, W. Deng and Y. Wang, Active site and reaction mechanism for the epoxidation of propylene by oxygen over CuO_x/SiO_2 catalysts with and without Cs+ modification, *J. Catal.*, 2013, **299**, 53–66.

190   M. El-Maazawi, A. N. Finken, A. B. Nair and V. H. Grassian, Adsorption and Photocatalytic Oxidation of Acetone on TiO_2: An in Situ Transmission FT-IR Study, *J. Catal.*, 2000, **191**, 138–146.

191   H. Song, Y. Li, Z. Lou, M. Xiao, L. Hu, Z. Ye and L. Zhu, Synthesis of Fe-doped WO_3 nanostructures with high visible-light-driven photocatalytic activities, *Appl. Catal. B Environ.*, 2015, **166–167**, 112–120.

192   C. Raillard, V. Héquet, P. Le Cloirec and J. Legrand, Kinetic study of ketones photocatalytic oxidation in gas phase using TiO_2-containing paper: effect of water vapor, *J. Photochem. Photobiol. A Chem.*, 2004, **163**, 425–431.

193   N. L. Nagda and H. E. Rector, A critical review of reported air concentrations of organic compounds in aircraft cabins, *Indoor Air*, 2003, **13**, 292–301.

194   A. Fujishima, T. N. Rao and D. A. Tryk, Titanium dioxide photocatalysis, *J. Photochem. Photobiol. C Photochem. Rev.*, 2000, **1**, 1–21.

195   J. J. Testa, M. A. Grela and M. I. Litter, Experimental evidence in favor of an initial one-electron-transfer process in the heterogeneous photocatalytic reduction of chromium(VI) over TiO_2, *Langmuir*, 2002, **17**, 3515–3517.

196   R. Mu, Z. Xu, L. Li, Y. Shao, H. Wan and S. Zheng, On the photocatalytic properties of elongated TiO_2 nanoparticles for phenol degradation and Cr(VI) reduction, *J. Hazard. Mater.*, 2010, **176**, 495–502.

197   T. T. Y. Tan, C. K. Yip, D. Beydoun and R. Amal, Effects of nano-Ag particles loading on TiO2 photocatalytic reduction of selenate ions, *Chem. Eng. J.*, 2003, **95**, 179–186.

198   S. Wang, Z. Ding and X. Wang, A stable $ZnCo_2O_4$ cocatalyst for photocatalytic CO_2 reduction, *Chem. Commun.*, 2015, **51**, 1517–1519.

199   T. Inoue, A. Fujishima, S. Konishi and K. Honda, Photoelectrocatalytic reduction of carbon dioxide in aqueous suspensions of semiconductor powders, *Nature*, 1979, **277**, 637–638.

200   D. Li, X. Fang, H. Liu, H. Lu and Z. Zhang, in *AIP Conference Proceedings*, AIP Publishing LLC , 2018, vol. 1971, p. 020006.

201   A. Kumar, A Review on the Factors Affecting the Photocatalytic Degradation of Hazardous Materials, *Mater. Sci. Eng. Int. J.*, , DOI:10.15406/mseij.2017.01.00018.

202   H. Ghafarian-Zahmatkesh, M. Javanbakht and M. Ghaemi, Ethylene glycol-assisted hydrothermal synthesis and characterization of bow-tie-like lithium iron phosphate nanocrystals for lithium-ion batteries, *J. Power Sources*, 2015, **284**, 339–348.

203   T.-D. Nguyen-Phan and E. W. Shin, Morphological effect of TiO_2 catalysts on photocatalytic degradation of methylene blue, *J. Ind. Eng. Chem.*, 2011, **17**, 397–400.

204   L. Lopez, W. A. Daoud, D. Dutta, B. C. Panther and T. W. Turney, Effect of substrate on surface morphology and photocatalysis of large-scale TiO2 films, *Appl. Surf. Sci.*, 2013, **265**, 162–168.

205   C. Adán, J. Marugán, E. Sánchez, C. Pablos and R. van Grieken, Understanding the effect of morphology on the photocatalytic activity of TiO_2 nanotube array electrodes, *Electrochim. Acta*, 2016, **191**, 521–529.

206   S. A. Hameed, Photo-Degradation of Vat Dye by Bimetallic Photo-Catalysts (Cu-Ni/ TiO_2 and Cu-Ni/ Zno) Under UV and Visible Light Sources, *IOSR J. Environ. Sci.*, 2016, **10**, 1–05.

207   Y. Suyama, M. Otsuki, S. Ogisu, R. Kishikawa, J. Tagami, M. Ikeda, H. Kurata and T. Cho, Effects of light sources and visible light-activated titanium dioxide photocatalyst on bleaching., *Dent. Mater. J.*, 2009, **28**, 693–9.

208   J. S. Kim and T. K. Lee, Effect of humidity on the photocatalytic degradation of trichloroethylene in gas Phase over TiO_2 thin films treated by different conditions, *Korean J. Chem. Eng.*, 2001, **18**, 935–940.

209   T. N. Obee and R. T. Brown, TiO2 Photocatalysis for Indoor Air Applications: Effects of Humidity and Trace Contaminant Levels on the Oxidation Rates of Formaldehyde,

Toluene, and 1,3-Butadiene, *Environ. Sci. Technol.*, 1995, **29**, 1223–1231.

210   M.-G. Jeong, E. J. Park, H. O. Seo, K.-D. Kim, Y. D. Kim and D. C. Lim, Humidity effect on photocatalytic activity of TiO_2 and regeneration of deactivated photocatalysts, *Appl. Surf. Sci.*, 2013, **271**, 164–170.

211   M. Subramanian and A. Kannan, Effect of dissolved oxygen concentration and light intensity on photocatalytic degradation of phenol, *Korean J. Chem. Eng.*, 2008, **25**, 1300–1308.

212   M. Sansotera, F. Persico, V. Rizzi, W. Panzeri, C. Pirola, C. L. Bianchi, A. Mele and W. Navarrini, The effect of oxygen in the photocatalytic oxidation pathways of perfluorooctanoic acid, *J. Fluor. Chem.*, 2015, **179**, 159–168.

213   W. Xu, D. Raftery and J. S. Francisco, Effect of Irradiation Sources and Oxygen Concentration on the Photocatalytic Oxidation of 2-Propanol and Acetone Studied by in Situ FTIR, *J. Phys. Chem. B*, 2003, **107**, 4537–4544.

214   S. Tanaka and U. K. Saha, Effects of pH on photocatalysis of 2,4,6-trichlorophenol in aqueous TiO_2 suspensions, *Water Sci. Technol.*, 1994, **30**, 47–57.

215   B. Zielińska, J. Grzechulska, R. J. Kaleńczuk and A. W. Morawski, The pH influence on photocatalytic decomposition of organic dyes over A11 and P25 titanium dioxide, *Appl. Catal. B Environ.*, 2003, **45**, 293–300.

216   X. Zhu, S. R. Castleberry, M. A. Nanny and E. C. Butler, Effects of pH and Catalyst Concentration on Photocatalytic Oxidation of Aqueous Ammonia and Nitrite in Titanium Dioxide Suspensions, *Environ. Sci. Technol.*, 2005, **39**, 3784–3791.

217   W.-Y. Wang and Y. Ku, Effect of solution pH on the adsorption and photocatalytic reaction behaviors of dyes using TiO_2 and Nafion-coated TiO_2, *Colloids Surfaces A Physicochem. Eng. Asp.*, 2007, **302**, 261–268.

218   B. Ohtani, Preparing Articles on Photocatalysis—Beyond the Illusions, Misconceptions, and Speculation, *Chem. Lett.*, 2008, **37**, 216–229.

219   A. J. Maira, K. L. Yeung, J. Soria, J. M. Coronado, C. Belver, C. Y. Lee and V. Augugliaro, Gas-phase photo-oxidation of toluene using nanometer-size TiO_2 catalysts, *Appl. Catal. B Environ.*, 2001, **29**, 327–336.

220   Q. Guo, C. Zhou, Z. Ma, Z. Ren, H. Fan and X. Yang, Elementary photocatalytic chemistry on TiO_2 surfaces, *Chem. Soc. Rev*, 2016, **45**, 3701.

221   W. H. Zachariasen, General Theory of X-Ray Diffraction in Real Crystals, *Phys. Rev. Lett.*, 1967, **18**, 195–196.

222   A. A. Tahir, M. A. Ehsan, M. Mazhar, K. G. Upul Wijayantha, M. Zeller and A. D. Hunter, Photoelectrochemical and Photoresponsive Properties of Bi_2S_3 Nanotube and Nanoparticle Thin Films, *Chem. Mater*, 2010, **22**, 5084–5092.

223   V. Kumar, S. Kr. Sharma, T. P. Sharma and V. Singh, Band gap determination in thick films from reflectance measurements, *Opt. Mater. (Amst).*, 1999, **12**, 115–119.

224   M. D. Fayer, *Pract. Spectrosc.*, 2001, 26, 709.

225   R. A. Hites, Development of Gas Chromatographic Mass Spectrometry, *Anal. Chem.*, 2016, **88**, 6955–6961.

226   B. D. Fraters, Gildeprint drukkerijen, 2015.

227   Y. Li, H. Yu, W. Song, G. Li, B. Yi and Z. Shao, A novel photoelectrochemical cell with self-organized TiO_2 nanotubes as photoanodes for hydrogen generation, *Int. J. Hydrogen Energy*, 2011, **36**, 14374–14380.

228   T. Horie, M. Sumino, T. Tanaka, Y. Matsushita, T. Ichimura and J. I. Yoshida, Photodimerization of maleic anhydride in a microreactor without clogging, *Org. Process Res. Dev.*, 2010, **14**, 405–410.

229   J. Krishnan and T. Swaminathan, Kinetic modeling of a photocatalytic reactor designed for removal of gas-phase benzene: A study on limiting resistances using design of experiments, *Lat. Am. Appl. Res.*, 2010, **40**, 359–364.

230   A. Banisharif, A. A. Khodadadi, Y. Mortazavi, A. Anaraki Firooz, J. Beheshtian, S. Agah and S. Menbari, Highly active Fe_2O_3-doped TiO_2 photocatalyst for degradation of trichloroethylene in air under UV and visible light irradiation: Experimental and computational studies, *Appl. Catal. B Environ.*, 2015, **165**, 209–221.

231   F. Gérardin, A. Cloteaux, M. Guillemot, M. Faure and J. C. André, Photocatalytic Conversion of Gaseous Nitrogen Trichloride into Available Chlorine—Experimental and Modeling Study, *Environ. Sci. Technol.*, 2013, **47**, 4628–4635.

232   D. M. Baechle, J. D. Demaree, J. K. Hirvonen and E. D. Wetzel, Fluidized Bed Sputtering for Particle and Powder Metallization.

233   S. W. Verbruggen, S. Ribbens, T. Tytgat, B. Hauchecorne, M. Smits, V. Meynen, P. Cool, J. A. Martens and S. Lenaerts, The benefit of glass bead supports for efficient gas phase photocatalysis: Case study of a commercial and a synthesised photocatalyst, *Chem. Eng. J.*, 2011, **174**, 318–325.

234   S. W. Verbruggen, W. Ab, K. Masschaele, E. Moortgat, T. E. Korany, B. Hauchecorne, J. A. Martens and S. Lenaerts, Factors driving the activity of commercial titanium dioxide powders towards gas phase photocatalytic oxidation of acetaldehyde, *Catal. Sci. Technol. Catal. Sci. Technol*, 2012, **2**, 2311–2318.

235   V. A. Patil, J. A. Liburdy and J. Homepage, Turbulent flow characteristics in a randomly packed porous bed based on particle image velocimetry measurements Additional information on Phys. Fluids Turbulent flow characteristics in a randomly packed porous bed based on particle image velocimetry measurements, *Cit. Phys. Fluids*, 2013, **25**, 43304.

236   W. Qiu and Y. Zheng, A comprehensive assessment of supported titania photocatalysts in a fluidized bed photoreactor: Photocatalytic activity and adherence stability, *Appl. Catal. B Environ.*, 2007, **71**, 151–162.

237   N. Veronovski, P. Andreozzi, C. La Mesa and M. Sfiligoj-Smole, Stable TiO_2 dispersions for nanocoating preparation, *Surf. Coatings Technol.*, 2010, **204**, 1445–1451.

238   Y. Huang, S. Ho, Y. Lu, R. Niu, L. Xu, J. Cao and S. Lee, Removal of Indoor Volatile Organic Compounds via Photocatalytic Oxidation: A Short Review and Prospect, *Molecules*, 2016, **21**, 56.

239   V. Puddu, H. Choi, D. D. Dionysiou and G. L. Puma, TiO_2 photocatalyst for indoor air remediation: Influence of crystallinity, crystal phase, and UV radiation intensity on trichloroethylene degradation, *Appl. Catal. B Environ.*, 2010, **94**, 211–218.

240   M. J. López-Muñoz, R. Van Grieken, J. Aguado and J. Marugán, Role of the support on the activity of silica-supported TiO_2 photocatalysts: Structure of the TiO_2/SBA-15 photocatalysts, *Catal. Today*, 2005, **101**, 307–314.

241   S. Murcia-López, V. Vaiano, D. Sannino, M. C. Hidalgo and J. A. Navío, Photocatalytic propylene epoxidation on Bi_2WO_6-based photocatalysts, *Res. Chem. Intermed.*, 2015, **41**, 4199–4212.

242   B. J. Aronson, C. F. Blanford and A. Stein, Solution-Phase Grafting of Titanium Dioxide onto the Pore Surface of Mesoporous Silicates: Synthesis and Structural Characterization, *Chem. Mater.*, 1997, **9**, 2842–2851.

243   M. S. Johnson, E. J. K. Nilsson, E. A. Svensson and S. Langer, Gas-phase advanced oxidation for effective, efficient in situ control of pollution, *Environ. Sci. Technol.*, 2014, **48**, 8768–8776.

244   X. D. Liu, S. Tokura, M. Haruki, N. Nishi and N. Sakairi, Surface modification of nonporous glass beads with chitosan and their adsorption property for transition metal ions, *Carbohydr. Polym.*, 2002, **49**, 103–108.

245   M. Kanemoto, T. Shiragami, C. Pac and S. Yanagida, Semiconductor photocatalysis. 13. Effective photoreduction of carbon dioxide catalyzed by zinc sulfide quantum crystallites with low density of surface defects, *J. Phys. Chem.*, 1992, **96**, 3521–3526.

246   MIT Chemical Engineering, Reactor Design, *MIT OpenCourseWare*, 2010, 1–24.

247   D. W. T. Rippin, Chemical reaction engineering, *Chem. Eng. Sci.*, 1964, **19**, 91.

248   V.-H. Nguyen, S. D. Lin, J. C. S. Wu and H. Bai, Influence of co-feeds additive on the photo-epoxidation of propylene over V–Ti/MCM-41 photocatalyst, *Catal. Today*, 2015, **245**, 186–191.

249   S. Furukawa, T. Shishido, K. Teramura and T. Tanaka, Photocatalytic Oxidation of

Alcohols over TiO_2 Covered with Nb_2O_5, *Acs Catal.*, 2012, **2**, 175–179.

250   M. Keulemans, S. W. Verbruggen, B. Hauchecorne, J. A. Martens and S. Lenaerts, Activity versus selectivity in photocatalysis: Morphological or electronic properties tipping the scale, *J. Catal.*, 2016, **344**, 221–228.

251   P. T. J. Scheepers, L. Van Wel, G. Beckmann, R. B. M. Anzion, A. Cincinelli and T. Martellini, Chemical Characterization of the Indoor Air Quality of a University Hospital: Penetration of Outdoor Air Pollutants, , DOI:10.3390/ijerph14050497.

252   M. I. Stefan, A. R. Hoy and J. R. Bolton, Kinetics and mechanism of the degradation and mineralization of acetone in dilute aqueous solution sensitized by the UV photolysis of hydrogen peroxide, *Environ. Sci. Technol.*, 1996, **30**, 2382–2390.

253   Z. Han, V. W. C. Chang, L. Zhang, M. S. Tse, O. K. Tan and L. M. Hildemann, Preparation of TiO_2-Coated Polyester Fiber Filter by Spray-Coating and Its Photocatalytic Degradation of Gaseous Formaldehyde, *Aerosol Air Qual. Res.*, 2012, **12**, 1327–1335.

254   M. El-Maazawi, A. N. Finken, A. B. Nair and V. H. Grassian, Adsorption and photocatalytic oxidation of acetone on TiO_2: An in situ transmission FT-IR study, *J. Catal.*, 2000, **191**, 138–146.

255   H. Sakai, Y. Kubota, K. Yamaguchi, H. Fukuoka and K. Inumaru, Photocatalytic decomposition of 2-propanol and acetone in air by nanocomposites of pre-formed TiO_2 particles and mesoporous silica, *J. Porous Mater.*, 2013, **20**, 693–699.

256   W. Xu and D. Raftery, In situ solid-state nuclear magnetic resonance studies of acetone photocatalytic oxidation on titanium oxide surfaces, *J. Catal.*, 2001, **204**, 110–117.

257   J. M. Coronado, S. Kataoka, I. Tejedor-Tejedor and M. A. Anderson, Dynamic phenomena during the photocatalytic oxidation of ethanol and acetone over nanocrystalline TiO_2: Simultaneous FTIR analysis of gas and surface species, *J. Catal.*, 2003, **219**, 219–230.

258   R. M. Lambert, F. J. Williams, R. L. Cropley and A. Palermo, Heterogeneous alkene epoxidation: Past, present and future, *J. Mol. Catal. A Chem.*, 2005, **228**, 27–33.

259   F. Minisci, C. Gambarotti, M. Pierini, O. Porta, C. Punta, F. Recupero, M. Lucarini and V. Mugnaini, Molecule-induced homolysis of N-hydroxyphthalimide (NHPI) by peracids and dioxirane. A new, simple, selective aerobic radical epoxidation of alkenes, *Tetrahedron Lett.*, 2006, **47**, 1421–1424.

260   A. Seubsai, M. Kahn and S. Senkan, New Catalytic Materials for the Direct Epoxidation of Propylene by Molecular Oxygen, *ChemCatChem*, 2011, **3**, 174–179.

261   J. Huang, T. Akita, J. Faye, T. Fujitani, T. Takei and M. Haruta, Propene epoxidation with dioxygen catalyzed by gold clusters, *Angew. Chemie - Int. Ed.*, 2009, **48**, 7862–

7866.

262   O. Sacco, M. Stoller, V. Vaiano, P. Ciambelli, A. Chianese and D. Sannino, Photocatalytic Degradation of Organic Dyes under Visible Light on N-Doped, *Int. J. Photoenergy*, 2012, **2012**, 1–8.

263   T. A. Nijhuis and B. M. Weckhuysen, The role of water in the epoxidation over gold–titania catalysts, *Chem. Commun.*, 2005, 6002.

264   M. Ojeda and E. Iglesia, Catalytic epoxidation of propene with H_2O–O_2 reactants on Au/TiO_2, *Chem. Commun.*, 2009, **2**, 352–354.

265   T. Thömmes, S. Zürcher, A. Wix, A. Reitzmann and B. Kraushaar-Czarnetzki, Catalytic vapour phase epoxidation of propene with nitrous oxide as an oxidant. I. Reaction network and product distribution, *Appl. Catal. A Gen.*, 2007, **318**, 160–169.

266   V.-H. Nguyen, H.-Y. Chan, J. C. S. Wu and H. Bai, Direct gas-phase photocatalytic epoxidation of propylene with molecular oxygen by photocatalysts, *Chem. Eng. J.*, 2012, **179**, 285–294.

267   F. Amano, T. Yamaguchi and T. Tanaka, Photocatalytic oxidation of propylene with molecular oxygen over highly dispersed titanium, vanadium, and chromium oxides on silica, *J. Phys. Chem. B*, 2006, **110**, 281–288.

268   F. Amano, T. Tanaka and T. Funabiki, Steady-State Photocatalytic Epoxidation of Propene by O_2 over V_2O_5 /SiO_2 Photocatalysts, *Langmuir*, 2004, **20**, 4236–4240.

269   H. Yoshida, C. Murata and T. Hattori, Screening Study of Silica-Supported Catalysts for Photoepoxidation of Propene by Molecular Oxygen, *J. Catal.*, 2000, **194**, 364–372.

270   J. Tang, Z. Zou and J. Ye, Photocatalytic decomposition of organic contaminants by Bi_2WO_6 under visible light irradiation, *CATAL LETT , 92   53 - 56.   .*

271   C. Belver, C. Adan and M. Fernandez-Garcia, *Catalysis today.*, Elsevier Science Publishers, 1987, vol. 143.

272   D. Kang, Y. Park, J. C. Hill and K. S. Choi, Preparation of Bi-based ternary oxide photoanodes $BiVO_4$, Bi_2WO_6, and $Bi_2Mo_3O_{12}$ using dendritic Bi metal electrodes, *J. Phys. Chem. Lett.*, 2014, **5**, 2994–2999.

273   X. P. Jiang, X. L. Fu, C. Chen, N. Tu, M. Z. Xu, X. H. Li, H. Shao and Y. J. Chen, High performance Aurivillius type $Na_{0.5}Bi_{4.5}Ti_4O_{15}$ piezoelectric ceramics with neodymium and cerium modification, *J. Adv. Ceram.*, 2015, **4**, 54–60.

274   J. Tian, Y. Sang, G. Yu, H. Jiang, X. Mu and H. Liu, A Bi_2WO_6-based hybrid photocatalyst with broad spectrum photocatalytic properties under UV, visible, and near-infrared irradiation, *Adv. Mater.*, 2013, **25**, 5075–5080.

275   G. Colón, S. Murcia López, M. C. Hidalgo and J. A. Navío, Sunlight highly photoactive Bi_2WO_6-TiO_2 heterostructures for rhodamine B degradation, *Chem. Commun.*, 2010, **46**, 4809–4811.

276   F. Amano, K. Nogami, R. Abe and B. Ohtani, Preparation and Characterization of Bismuth Tungstate Polycrystalline Flake-Ball Particles for Photocatalytic Reactions, *J. Phys. Chem. C*, 2008, **112**, 9320–9326.

277   M. Yan, Y. Wu, Y. Yan, X. Yan, F. Zhu, Y. Hua and W. Shi, Synthesis and Characterization of Novel $BiVO_4$/Ag_3VO_4 Heterojunction with Enhanced Visible-Light-Driven Photocatalytic Degradation of Dyes, *ACS Sustain. Chem. Eng.*, 2016, **4**, 757–766.

278   Y. Jia, S. Zhan, S. Ma and Q. Zhou, Fabrication of TiO2-Bi_2WO_6 Binanosheet for Enhanced Solar Photocatalytic Disinfection of E. coli: Insights on the Mechanism, *ACS Appl. Mater. Interfaces*, 2016, **8**, 6841–6851.

279   R. W. Wolfe, R. E. Newnahm and M. I. Kay, Crystal structure of Bi_2WO_6, *Solid State Commun.*, 1969, **7**, 1797–1801.

280   G. N. Rocha, L. F. L. Melo, S. M. Dantas, A. P. Ayala, A. S. B. Sombra, A. F. L. Almeida, A. S. De Menezes and P. B. A. Fechine, Preparation and study of bismuth rare-earth tungstate composite screen-printed thick films, *J. Electron. Mater.*, 2013, **42**, 752–760.

281   M. Perez, *Scr. Mater.*, 2005, 52, 709–712.

282   F. Amano, K. Nogami, R. Abe and B. Ohtani, Preparation and Characterization of Bismuth Tungstate Polycrystalline Flake-Ball Particles for Photocatalytic Reactions, *J. Phys. Chem. C*, 2008, **112**, 9320–9326.

283   D. He, L. Wang, D. Xu, J. Zhai, D. Wang and T. Xie, Investigation of photocatalytic activities over Bi_2WO_6/$ZnWO_4$ composite under UV light and its photoinduced charge transfer properties, *ACS Appl. Mater. Interfaces*, 2011, **3**, 3167–3171.

284   Y. Yang, J. Cui, H. Jin and F. Cao, A three-dimensional (3D) structured Bi_2WO_6-palygorskite composite and their enhanced visible light photocatalytic property, *Sep. Purif. Technol.*, 2018, **205**, 130–139.

285   Z. Liu, F. Chen, Y. Gao, Y. Liu, P. Fang and S. Wang, A novel synthetic route for magnetically retrievable Bi_2WO_6 hierarchical microspheres with enhanced visible photocatalytic performance, *J. Mater. Chem. A*, 2013, **1**, 7027.

286   S. Girish Kumar and K. S. R. Koteswara Rao, Tungsten-based nanomaterials (WO_3 & Bi_2WO_6): Modifications related to charge carrier transfer mechanisms and photocatalytic applications, *Appl. Surf. Sci.*, 2015, **355**, 939–958.

287   V.-H. Nguyen, H.-Y. Chan, J. C. S. Wu and H. Bai, Direct gas-phase photocatalytic epoxidation of propylene with molecular oxygen by photocatalysts, *Chem. Eng. J.*,

2011, **179**, 285–294.

288   S. J. Khatib and S. T. Oyama, Direct Oxidation of Propylene to Propylene Oxide with Molecular Oxygen: A Review, *Catal. Rev. - Sci. Eng.*, 2015, **57**, 306–344.

289   D. M. Perez Ferrandez, M. H. J. M. de Croon, J. C. Schouten and T. A. Nijhuis, Gas-Phase Epoxidation of Propene with Hydrogen Peroxide Vapor, *Ind. Eng. Chem. Res.*, 2013, **52**, 10126–10132.

290   D. H. Wells, A. M. Joshi, W. N. Delgass and K. T. Thomson, A quantum chemical study of comparison of various propylene epoxidation mechanisms using H_2O_2 and TS-1 catalyst, *J. Phys. Chem. B*, 2006, **110**, 14627–14639.

291   H. QI, D. zhi SUN and G. qing CHI, Formaldehyde degradation by $UV/TiO_2/O_3$ process using continuous flow mode, *J. Environ. Sci.*, 2007, **19**, 1136–1140.

292   V. Nguyen, J. C. S. Wu and H. Bai, Temperature effect on the photo-epoxidation of propylene over V–Ti/MCM-41 photocatalyst, *Catal. Commun.*, 2013, **33**, 57–60.

293   M. Kim, Tae Won and Lee, Effect of pH and temp for photocatlytic degradation.pdf, *j. Adv. Eng Tech*, 2010, **3**, 193–198.

294   T. Hirakawa, J. K. Whitesell and M. A. Fox, Effect of Temperature and Pressure in the Photocatalytic Oxidation of n -Octanol on Partially Desilanized Hydrophobic TiO_2 Suspended in Aerated Supercritical CO_2 †, *J. Phys. Chem. B*, 2004, **108**, 10213–10218.

295   W. Xu, D. Raftery and J. S. Francisco, Effect of Irradiation Sources and Oxygen Concentration on the Photocatalytic Oxidation of 2-Propanol and Acetone Studied by in Situ FTIR, *J. Phys. Chem. B*, 2003, **107**, 4537–4544.

296   T. R. Pope, M. N. Lassig, G. Neher, R. D. Weimar and T. T. Salguero, Chromism of Bi_2WO_6 in single crystal and nanosheet forms, *J. Mater. Chem. C*, 2014, **2**, 3223–3230.

297   X. Yan, Y. Li and T. Xia, Black Titanium Dioxide Nanomaterials in Photocatalysis, *Int. J. Photoenergy*, 2017, **2017**, 1–16.

298   X. Yang, C. Salzmann, H. Shi, H. Wang, M. L. H. Green and T. Xiao, The role of photoinduced defects in TiO_2 and its effects on hydrogen evolution from aqueous methanol solution, *J. Phys. Chem. A*, 2008, **112**, 10784–10789.

299   G. Arnaoutakis, M. Cazzanelli, Z. El Koura and A. Miotello, *Charge Carrier Recombination Dynamics of Semiconductor Photocatalysts APPLICATION NOTE*, 2016.

300   B. Viswanathan, H. Katsumata, G. Magesh, B. Viswanathan, R. P. Viswanath and T. K. Varadarajan, *Photocatalytic routes for chemicals*, 2007, vol. 661.

301 D. A. Ruddy and T. D. Tilley, Highly selective olefin epoxidation with aqueous H_2O_2 over surface-modified TaSBA15 prepared via the TMP method, *Chem. Commun.*, 2007, **0**, 3350.

302 M. Guidotti, C. Pirovano, N. Ravasio, B. Lázaro, J. M. Fraile, J. A. Mayoral, B. Coq and A. Galarneau, The use of H_2O_2 over titanium-grafted mesoporous silica catalysts: a step further towards sustainable epoxidation, *Green Chem.*, 2009, **11**, 1421.

303 C. Ramachandran, H. Du, Y. Kim, M. Kung, R. Snurr and L. Broadbelt, Solvent effects in the epoxidation reaction of 1-hexene with titanium silicalite-1 catalyst, *J. Catal.*, 2008, **253**, 148–158.

304 W. Fan, P. Wu and T. Tatsumi, Unique solvent effect of microporous crystalline titanosilicates in the oxidation of 1-hexene and cyclohexene, *J. Catal.*, 2008, **256**, 62–73.

305 G. Langhendries, D. E. De Vos, G. V. Baron and P. A. Jacobs, Quantitative Sorption Experiments on Ti-Zeolites and Relation with α-Olefin Oxidation by H_2O_2, *J. Catal.*, 1999, **187**, 453–463.

306 A. Agarwala and D. Bandyopadhyay, The Radical Versus Non-radical Reactive Intermediates in the Iron(III) Porphyrin Catalyzed Oxidation Reactions by Hydroperoxides, Hydrogen Peroxide and Iodosylarene, *Catal. Letters*, 2008, **124**, 256–261.

307 Y. Ding, Q. Gao, G. Li, H. Zhang, J. Wang, L. Yan and J. Suo, Selective epoxidation of cyclohexene to cyclohexene oxide catalyzed by Keggin-type heteropoly compounds using anhydrous urea-hydrogen peroxide as oxidizing reagent and acetonitrile as the solvent, *J. Mol. Catal. A Chem.*, 2004, **218**, 161–170.

308 E. Klemm, E. Dietzsch, T. Schwarz, T. Kruppa, A. L. De Oliveira, F. Becker, G. Markowz, S. Schirrmeister, R. Schütte, K. J. Caspary, F. Schüth and D. Hönicke, Direct gas-phase epoxidation of propene with hydrogen peroxide on TS-1 zeolite in a microstructured reactor, *Ind. Eng. Chem. Res.*, 2008, **47**, 2086–2090.

309 D. M. Perez Ferrandez, M. H. J. M. de Croon, J. C. Schouten and T. A. Nijhuis, Gas-Phase Epoxidation of Propene with Hydrogen Peroxide Vapor, *Ind. Eng. Chem. Res.*, 2013, **52**, 10126–10132.

310 A. Phaniendra, D. B. Jestadi and L. Periyasamy, Free radicals: properties, sources, targets, and their implication in various diseases., *Indian J. Clin. Biochem.*, 2015, **30**, 11–26.

311 A. Samuni, G. Czapski and D. Meisel, Hydroperoxyl Radical Reactions. I. Electron Paramagnetic Resonance Study of the Gomplexation of H02 with Some Metal Ions, *J. Am. Chem. Soc*, 1970, **74**, 2207.

312 S. Bhattacharjee and J. A. Anderson, Comparison of the epoxidation of cyclohexene, dicyclopentadiene and 1,5-cyclooctadiene over LDH hosted Fe and Mn sulfonato-

salen complexes, *J. Mol. Catal. A Chem.*, 2006, **249**, 103–110.

313   V. I. Kopp and A. Z. Genack, Kopp and Genack Reply:, *Phys. Rev. Lett.*, 2003, **91**, 259402.

314   H. Martínez, M. F. Cáceres, F. Martínez, E. A. Páez-Mozo, S. Valange, N. J. Castellanos, D. Molina, J. Barrault and H. Arzoumanian, Photo-epoxidation of cyclohexene, cyclooctene and 1-octene with molecular oxygen catalyzed by dichloro dioxo-(4,4′-dicarboxylato-2,2′-bipyridine) molybdenum(VI) grafted on mesoporous TiO2, *J. Mol. Catal. A Chem.*, 2016, **423**, 248–255.

315   M. Vandichel, K. Leus, P. Van Der Voort, M. Waroquier and V. Van Speybroeck, Mechanistic insight into the cyclohexene epoxidation with VO(acac)2 and tert-butyl hydroperoxide, *J. Catal.*, 2012, **294**, 1–18.

316   X. Deng, Y. Wang, L. Shen, H. Wu, Y. Liu and M. He, Low-Cost Synthesis of Titanium Silicalite-1 (TS-1) with Highly Catalytic Oxidation Performance through a Controlled Hydrolysis Process, *Ind. Eng. Chem. Res.*, 2013, **52**, 1190–1196.

317   J. H. Zhang, M. B. Yue, X. N. Wang and D. Qin, Synthesis of nanosized TS-1 zeolites through solid transformation method with unprecedented low usage of tetrapropylammonium hydroxide, *Microporous Mesoporous Mater.*, 2015, **217**, 96–101.

318   R. Kumar, G. C. G. Pais, B. Pandey and P. Kumar, Hydroxy-assisted chemo- and stereo-selective epoxidation catalysed by a titanium silicate molecular sieve (TS-1)/H2O2 system, *J. Chem. Soc. Chem. Commun.*, 1995, 1315.

319   R. B. Khomane, B. D. Kulkarni, a Paraskar and S. R. Sainkar, Synthesis, characterization and catalytic performance of titanium silicalite-1 prepared in micellar media, *Mater. Chem. Phys.*, 2002, **76**, 99–103.

320   H. Du, M. Fang, J. Chen and W. Pang, Synthesis and characterization of a novel layered titanium silicate JDF-L1, *J. Mater. Chem.*, 1996, **6**, 1827.

321   Q. Zhao, P. Li, D. Li, X. Zhou, W. Yuan and X. Hu, Synthesis and characterization of titanium silicate-1 supported on carbon nanofiber, *Microporous Mesoporous Mater.*, 2008, **108**, 311–317.

322   P. Pędziwiatr, F. Mikołajczyk, D. Zawadzki, K. Mikołajczyk and A. Bedka, Decomposition of hydrogen peroxide - kinetics and review of chosen catalysts, *Acta Innov.*, 2018, 45–52.

323   C. N. Satterfield and T. W. Stein1, *Decomposition of Hydrogen Peroxide Vapor on Relatively Inert Surfaces*, UTC, 2018, vol. 49.

324   S. Kwon, N. M. Schweitzer, S. Park, P. C. Stair and R. Q. Snurr, A kinetic study of vapor-phase cyclohexene epoxidation by H_2O_2 over mesoporous TS-1, *J. Catal.*, 2015, **326**, 107–115.

325 C. W. Yoon, K. F. Hirsekorn, M. L. Neidig, X. Yang and T. D. Tilley, Mechanism of the Decomposition of Aqueous Hydrogen Peroxide over Heterogeneous TiSBA15 and TS-1 Selective Oxidation Catalysts: Insights from Spectroscopic and Density Functional Theory Studies, *ACS Catal.*, 2011, **1**, 1665–1678.

326 C. M. Lousada, A. J. Johansson, T. Brinck and M. Jonsson, Mechanism of H_2O_2 Decomposition on Transition Metal Oxide Surfaces, *J. Phys. Chem. C*, 2012, **116**, 9533–9543.

327 S. Kwon, N. M. Schweitzer, S. Park, P. C. Stair and R. Q. Snurr, A kinetic study of vapor-phase cyclohexene epoxidation by H2O2 over mesoporous TS-1, *J. Catal.*, 2015, **326**, 107–115.

328 T. A. Nijhuis and B. M. Weckhuysen, The role of water in the epoxidation over gold-titania catalysts, *Chem. Commun.*, 2005, 6002–6004.

329 H. Shima, T. Tatsumi and J. N. Kondo, Direct FT-IR observation of oxidation of 1-hexene and cyclohexene with H_2O_2 over TS-1, *Microporous Mesoporous Mater.*, 2010, **135**, 13–20.

330 H. Li, B. Xu, B. Deng, X. Yan and Y. Zheng, Epoxidation of 1-hexene with hydrogen peroxide over nitrogen-incorporated TS-1 zeolite, *CATCOM*, 2014, **46**, 224–227.

331 A. M. Joshi, W. N. Delgass and K. T. Thomson, Comparison of the catalytic activity of Au 3, Au 4+, Au 5, and Au 5- in the gas-phase reaction of H_2 and O_2 to form hydrogen peroxide: A density functional theory investigation, *J. Phys. Chem. B*, 2005, **109**, 22392–22406.

332 R. R. Sever and T. W. Root, DFT Study of Solvent Coordination Effects on Titanium-Based Epoxidation Catalysts. Part Two: Reactivity of Titanium Hydroperoxo Complexes in Ethylene Epoxidation, *J. Phys. Chem. B*, 2003, **107**, 4090–4099.

333 M. Ojeda and E. Iglesia, Catalytic epoxidation of propene with H_2O–O_2 reactants on Au/TiO 2, *Chem. Commun.*, 2009, 352–354.

334 O. Carp, C. L. Huisman and A. Reller, Photoinduced reactivity of titanium dioxide, *Prog. Solid State Chem.*, 2004, **32**, 33–177.

335 T. Inoue, A. Fujishima, S. Konishi and K. Honda, *Nature*, 1979, 277, 637–638.

336 X. Lang, X. Chen and J. Zhao, Heterogeneous visible light photocatalysis for selective organic transformations, *Chem. Soc. Rev.*, 2014, **43**, 473–486.

337 Y. Ren, Y. Che, W. Ma, X. Zhang, T. Shen and J. Zhao, Selective photooxidation of styrene in organic–water biphasic media, *New J. Chem.*, 2004, **28**, 1464–1469.

338 S. R. Taffarel, M. A. Lansarin and C. C. Moro, *Styrene Photocatalytic Degradation Reaction Kinetics*, 2011, vol. 22.

339　M. A. Katkar, S. N. Rao and H. D. Juneja, Green epoxidation of 1-hexene: O_2 utilizing cis-MoO2 Schiff base complex, *RSC Adv.*, 2012, **2**, 8071.

340　V.-H. Nguyen, S. D. Lin, J. Chi, -Sheng Wu and H. Bai, Artificial sunlight and ultraviolet light induced photo-epoxidation of propylene over V-Ti/MCM-41 photocatalyst, *Beilstein J. Nanotechnol*, 2014, **5**, 566–576.

341　T. Ohno, K. Nakabeya and M. Matsumura, Epoxidation of olefins on photoirradiated titanium dioxide powder using molecular oxygen as an oxidant, *J. Catal.*, 1998, **176**, 76–81.

342　G. Ren, Y. Gao, J. Yin and H. Liu, Synthesis of High-Activity TiO_2/WO_3 Photocatalyst via Environmentally Friendly and Microwave Assisted Hydrothermal Process, *J.Chem.Soc.Pak*.

343　J. Li, J. Xu, W. L. Dai, H. Li and K. Fan, One-pot synthesis of twist-like helix tungsten-nitrogen-codoped titania photocatalysts with highly improved visible light activity in the abatement of phenol, *Appl. Catal. B Environ.*, 2008, **82**, 233–243.

344　Y. P.Yanachawakul, N. Leepipatpiboon and N. Sunsandee, *Chemical engineering journal.*, Elsevier Science Pub. Co, 2012, vol. 193–194.

345　S. J. Khatib and S. T. Oyama, Direct Oxidation of Propylene to Propylene Oxide with Molecular Oxygen: A Review, *Catal. Rev.*, 2015, **57**, 306–344.

346　K. E. O'Shea, E. Pernas and J. Saiers, The Influence of Mineralization Products on the Coagulation of TiO 2 Photocatalyst, *Langmuir*, 1999, **15**, 2071–2076.

347　M. Bellardita, M. Addamo, A. Di Paola and L. Palmisano, Photocatalytic behaviour of metal-loaded TiO2 aqueous dispersions and films, *Chem. Phys.*, 2007, **339**, 94–103.

348　V. Chauke and T. Nyokong, Photocatalytic oxidation of 1-hexene using GaPc and InPc octasubstituted derivatives, *J. Mol. Catal. A Chem.*, 2008, **289**, 9–13.

349　N. Azizi and M. R. Saidi, Highly Chemoselective Addition of Amines to Epoxides in Water, *Org. Lett.*, 2005, **7**, 3649–3651.

350　H. Varshney, A. Ahmad and A. Rauf, Ring Opening of Epoxy Fatty Esters by Nucleophile to Form the Derivatives of Substituted Amino Alcohol, *Food Nutr. Sci.*, 2013, **04**, 21–24.

351　U. R. Pillai and E. Sahle-Demessie, Selective oxidation of alcohols in gas phase using light-activated titanium dioxide, *J. Catal.*, 2002, **211**, 434–444.

352　C.-J. Li and L. Chen, Organic chemistry in water, *Chem. Soc. Rev.*, 2006, **35**, 68–82.

353　S. W. Depner, K. R. Kort, C. Jaye, D. A. Fischer and S. Banerjee, Nonhydrolytic Synthesis and Electronic Structure of Ligand-Capped CeO_2 $-\delta$ and CeOCl Nanocrystals, *J. Phys. Chem. C*, 2009, **113**, 14126–14134.

354 M. Sun, G. Zou, S. Xu and X. Wang, Effect of structure of CeOHCO$_3$ precursor of CeO$_2$ on its catalytic performance, *Chinese J. Catal.*, 2012, **33**, 1318–1325.

355 S. K. Sahoo, M. Mohapatra, A. K. Singh and S. Anand, Hydrothermal synthesis of single crystalline nano CeO$_2$ and its structural, optical, and electronic characterization, *Mater. Manuf. Process.*, 2010, **25**, 982–989.

356 P. Pal, S. K. Pahari, A. Sinhamahapatra, M. Jayachandran, G. V. M. Kiruthika, H. C. Bajaj and A. B. Panda, CeO$_2$ nanowires with high aspect ratio and excellent catalytic activity for selective oxidation of styrene by molecular oxygen, *RSC Adv.*, 2013, **3**, 10837.

357 W. Weng, M. A. L. Cordeiro, D. G. Stroppa, C. J. Kiely and E. R. Leite, Understanding the Growth Mechanism of CeO$_2$ Nanocrystals by Comparison of Experimental and Simulated HAADF-STEM Images, *Microsc. Microanal.*, 2014, **20**, 178–179.

358 D. C. Sayle, S. A. Maicaneanu and G. W. Watson, Atomistic models for CeO2(111), (110), and (100) nanoparticles, supported on yttrium-stabilized zirconia, *J. Am. Chem. Soc.*, 2002, **124**, 11429–11439.

359 A. Trovarelli, To cite this article: Alessandro Trovarelli (1999) Structural and Oxygen Storage/Release Properties of CeO$_2$-Based Solid Solutions, *Comments Inorg. Chem.*, **20**, 263–284.

360 M. Hosseini-Zori, Co-doped TiO$_2$ nanostructures as a strong antibacterial agent and self-cleaning cover: Synthesis, characterization and investigation of photocatalytic activity under UV irradiation, *J. Photochem. Photobiol. B Biol.*, 2018, **178**, 512–520.

361 S. K. Pahari, P. Pal, A. Sinhamahapatra, A. Saha, C. Santra, S. C. Ghosh, B. Chowdhury and A. B. Panda, Efficient oxidation of hydrocarbons over nanocrystalline Ce 1−x Sm x O 2 (x = 0–0.1) synthesized using supercritical water, *RSC Adv.*, 2015, **5**, 45144–45151.

362 H. X. Mai, L. D. Sun, Y. W. Zhang, R. Si, W. Feng, H. P. Zhang, H. C. Liu and C. H. Yan, Shape-selective synthesis and oxygen storage behavior of ceria nanopolyhedra, nanorods, and nanocubes, *J. Phys. Chem. B*, 2005, **109**, 24380–24385.

363 A. Nodzewska and M. Watkinson, Remarkable increase in the rate of the catalytic epoxidation of electron deficient styrenes through the addition of Sc(OTf) 3 to the MnTMTACN catalyst †, *Chem. Commun*, 2018, **54**, 1461.

364 M. D. Guillén and E. Goicoechea, Detection of Primary and Secondary Oxidation Products by Fourier Transform Infrared Spectroscopy (FTIR) and 1 H Nuclear Magnetic Resonance (NMR) in Sunflower Oil during Storage, *J. Agric. Food Chem.*, 2007, **55**, 10729–10736.

365 L. Zhang, Z. Zhang, X. He, F. Zhang and Z. Zhang, Regulation of the products of styrene oxidation, *Chem. Eng. Res. Des.*, 2017, **120**, 171–178.

366   J. Pei, Y. Tan, H. R. Tan, C. Boothroyd, Y. L. Foo, C. Bin He and M. Lin, Three-Dimensional Structure of CeO$_2$ Nanocrystals, *J. Phys. Chem. C*, 2011, **115**, 3544–3551.